The Optimal Application of Common Control Techniques to Permanent Magnet Synchronous Motors

William Treharne

Balliol College

University of Oxford

A thesis submitted for the degree of

Doctor of Philosophy

September 2011

Statement of Originality

The work presented in this thesis was carried out between October 2007 and September 2011 under the supervision of Dr Malcolm McCulloch.

The author wishes to declare that, except for commonly understood and accepted ideas or where reference is made to the work of others, the work in this thesis is his own, and includes nothing which is the outcome of work done in collaboration. It has not been submitted in part, or in whole, to any other university for a degree, diploma or other qualification.

W. Treharne

Balliol College

September 2011

This thesis is dedicated to

my wife, Rebecca, and my parents, Janet and David,

for their unending support and encouragement

Acknowledgements

I wish to thank Dr Malcolm McCulloch for his support throughout the course of my DPhil. His advice, feedback and enthusiasm for the subject has been of great help and working with him has been a pleasure.

I would also like to extend my thanks to the members of the Electrical Power Group who helped make the research experience highly enjoyable. In particular, I would like to thank Tim Woolmer and Marcus Leong for their support. For their very generous loan of a motor test rig, I would like to thank Oxford YASA Motors, without which much of this work would not have been possible.

Finally, I would like to thank my loving family for their encouragement and support throughout the long preparation of this thesis.

Abstract

Permanent magnet synchronous motors are finding ever increasing use in hybrid and electric vehicles. This thesis develops a new control strategy for Permanent Magnet Synchronous Motors (PMSMs) to reduce the motor and inverter losses compared to conventional control techniques. The strategy utilises three common control modes for PMSMs; brushless DC with 120°E conduction, brushless DC with 180°E conduction, and brushless AC control.

The torque and power output for each control mode is determined for an example motor system using a three phase axial flux YASA motor and an IGBT inverter. The loss components for the motor and inverter are also estimated using a combination of analytical and simulation techniques and results are then validated against experimental measurements. Efficiency maps for each control mode have been used to determine an optimal mode utilisation strategy, which minimises the total system losses and maximises the available motor torque output.

The proposed control strategy switches between the three control modes without interruption of motor torque to maximise the system efficiency for the instantaneous operating speed and demanded torque output. The benefits of the new strategy are demonstrated using an example vehicle over a simulated drive cycle. This yields a 10% reduction in losses compared to conventional brushless AC control.

Contents

List of Figures

List of Tables

Nomenclature

$\eta_{inverter}$	Inverter efficiency
η_{motor}	Motor efficiency
ω_e	Electrical speed
ω_m	Mechanical speed
θ_e	Electrical angle
d	PWM duty
e_{ph}	Phase back EMF voltage
i_d	Direct current component
i_q	Quadrature current component
i_{dmd}	Demanded current
i_{max}	Maximum phase current
$i_{ph,RMS}$	RMS phase current
i_{ph}	Instantaneous phase current
k	Back EMF constant ($\mathrm{V}/(\mathrm{rad}/\mathrm{s})$)
k_T	Motor torque constant ($\mathrm{N\,m}/\mathrm{A}$)
L	Motor phase inductance

n_{pp}	Number of motor pole pairs
$P_{inverter}$	Inverter power
P_{loss}	Loss component power
P_{motor}	Motor power
R	Motor phase resistance
T	Motor torque
T_{dmd}	Motor torque demand
V_d	Direct voltage component
V_q	Quadrature voltage component
V_{dc}	DC link voltage
°E	Electrical degrees
°M	Mechanical degrees
UCDS	Unified Cycle Driving Schedule
ACIM	AC Induction Motor
BLAC	Brushless AC
BLDC	Brushless DC
BLDC-120	Brushless DC control with 120°E commutation
BLDC-180	Brushless DC control with 180°E commutation
EMF	Electromotive Force
FOC	Field Oriented Control

ICE	Internal Combustion Engine
IGBT	Insulated Gate Bipolar Transistor
MOSFET	Metal Oxide Semiconductor Field Effect Transistor
PMSM	Permanent Magnet Synchronous Motor
RMS	Root Mean Square
SMPMSM	Surface Mounted Permanent Magnet Synchronous Motor
SRM	Switched Reluctance Motor
SVM	Space Vector Modulation
YASA	Yokeless and Segmented Armature

1

Introduction

This thesis develops a new control strategy for permanent magnet synchronous motors (PMSMs) to minimise the system losses for vehicle applications. Three common control modes for PMSMs are examined; brushless DC with 120°E conduction (BLDC-120), brushless DC with 180°E conduction (BLDC-180), and brushless AC (BLAC). The torque and power output for each control mode are determined for an example system. The loss components for the motor and inverter are also estimated using a combination of analytical and simulation techniques. The results of this are validated against experimental measurements. Efficiency maps for each control mode have then been used to determine an optimal control strategy, which minimises the total system losses and maximises the available torque output.

The comparison between different motor control modes is made with an emphasis on application to hybrid and electric vehicles. However, the techniques described could be applied to permanent magnet synchronous motors on different scales and for different applications.

This chapter will give an overview of motors and drives for vehicle applications before discussing the structure of the thesis.

1.1 Motivation for the Thesis

Climate change through the emission of carbon dioxide has led to increasingly strict tailpipe emissions legislation for new road cars in recent years. Mandatory EU legislation now requires average CO_2 emission to be no higher than $130\,\mathrm{g/km}$ by 2015 and no higher than $95\,\mathrm{g/km}$ by 2020 [24]. The increasing costs of fuels and rising vehicle duty for less fuel efficient vehicles has also led to an increased consumer demand for more economical cars [25].

Hybrid and electric vehicles are often proposed as a way of addressing both of these issues. Many automotive manufacturers have now started developing hybrid and electric vehicles that make use of motor and battery technologies to enable regenerative braking [26]. As a result, these hybrids typically achieve greater fuel economy than conventional internal combustion engine powered vehicles [27].

Consumer uptake of these vehicles is currently low in comparison to more conventionally powered vehicles [1]. However, the global sales of such vehicles are predicted to grow rapidly as the barriers to mass adoption are overcome [1], as shown in Figure 1.1.

There are currently many issues which are preventing the wider uptake of hybrid and electric vehicles which must be overcome if the vehicle sales growth predictions are to be met. Of particular concern to potential buyers of electrics vehicles is the purchase price and vehicle range on a single charge [28].

The efficiency of the vehicle drivetrain is critical to both of these issues. Improvements to the drivetrain efficiency will help maximise the range that can be achieved from a given size vehicle battery. Lower losses will also lead to reduced cooling requirements and therefore the size, and more importantly the mass, of the ancillary components will be

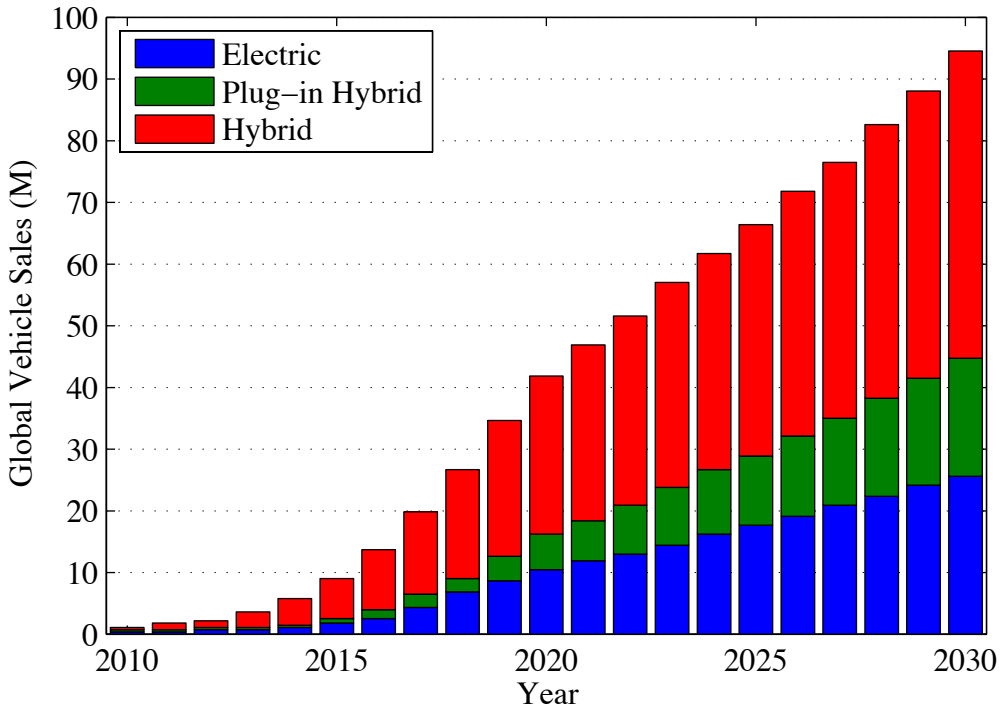

Figure 1.1: Projected growth in the global sales of hybrid and electric vehicles [1].

reduced [29]. The resulting decrease in the total vehicle weight will reduce the power requirements of the vehicle's motor(s) to accelerate the vehicle and hence the power requirements of the battery.

The iterative process of mass reduction resulting in reduced power requirements, and in turn yielding further weight savings is known as mass decompounding [29]. Application of this principal to electric vehicles, together with a design emphasis on maximising the drivetrain efficiency, will result in a lighter vehicle with a smaller and less expensive battery and a lower total cost.

1.2 Hybrid Drivetrain Topologies

Electrical hybrid systems are finding their way into an ever growing number of commercially available vehicles. Typically these involve the use of an electric motor coupled to the vehicle's internal combustion engine or drivetrain [26]. There are a number of topologies

that could be used for a hybrid electric vehicle drivetrain and are often classified as series or parallel hybridisations [30].

Series hybrid vehicles typically use an internal combustion engine to drive a generator which supplies the average power requirement for the vehicle [30]. The transient energy demands are then met by the hybrid's other power sources, such as a battery or ultracapacitor bank. The mechanically isolated engine is then able to run under its most economical operating conditions, rather than operating over a wide range of speed and torque outputs. However, this topology carries the disadvantages of the added weight of a generator and the losses of an additional energy conversion stage [31].

Parallel hybrids have a drivetrain which allows the vehicle's wheels to be driven from its multiple power sources either separately or simultaneously [31]. Parallel hybrids tend to be more efficient than series hybrids for motorway driving as there are fewer power conversions that take place and allow the vehicle to continue operating if one of the power sources fails [31, 32]. However, when this type of drivetrain is used with an internal combustion engine, it does not allow the engine to be optimised for single speed running, unlike for series hybrids [31]. Series hybrids are therefore able to achieve lower fuel consumption in city driving conditions where the vehicle is frequently stopping and starting [32].

It is also possible to have a combined hybrid by adding a mechanical link between the internal combustion engine and the electric motor(s) of a series hybrid [33]. Also known as series-parallel hybrids [34], these drivetrains allow the vehicle to operate as a series or parallel hybrid to make use of the advantages of both modes of operation.

All of the drivetrain topologies described above will allow a vehicle to make use of regenerative braking, and potentially improve the vehicle fuel economy compared to a conventional internal combustion engined vehicle [30]. Regardless of the topology chosen, the efficiency of the electric motor(s) and the associated inverter(s) must be maximised in order to increase the vehicle fuel economy and reduce CO_2 emissions.

1.3 Electric Motors Suitable for Vehicle Traction Applications

Electric motors are a key technology for hybrid and electric vehicles. They can be used for propulsion but also as a generator under braking where the resultant torque slows the vehicle and the electrical energy generated can be stored for subsequent reuse [26]. The location of the electric motors in the vehicle, and method of energy storage used varies depending on the application.

The basic requirements of electric motors for vehicle traction applications include high torque and high power density, high efficiency over a wide speed and torque range, and high reliability and robustness [35]. Cost is also a major consideration for commercial applications [36]. Out of the large number of available motor technologies, there are three in particular that show the greatest potential for use in hybrid and electric vehicles [26, 35]. The following section discusses the suitability of three common motor types.

1.3.1 Induction Machines

AC Induction Motors (ACIMs) are widely used in industrial applications and are a mature technology with low cost and high reliability [37]. With digital microprocessor control, it is possible to separate the torque and field control for the motor allowing extended speed operation through flux weakening [26]. However, the drives required to power this type of motor often have high losses, low efficiency and complex control, which with the poor specific power of induction motors, has limited their application in the automotive sector [38]. There are however a number of examples of electric vehicles in production which make use of induction motors, such as the Tesla Roadster and the Mini E [39].

1.3.2 Switched Reluctance Machines

Switched Reluctance Motors (SRMs) offer the advantages of a simple rotor construction without magnets or windings, which is desirable for high speed or high temperature operation [35]. The lack of any permanent magnetic field results in low losses when the motor is rotating at no-load. Some input current is still needed at no-load to overcome the mechanical losses of the machine, giving rise to small resistive and magnetic losses. This type of motor suffers from high torque ripple from the rotor shape required to give the varying magnetic reluctance with rotor position [37, 38]. They also require a non-standard inverter topology [38].

1.3.3 Permanent Magnet Machines

Permanent magnet synchronous motors are finding ever increasing use in electric and hybrid vehicles because they offer both high efficiencies and high torque densities [38]. They are normally operated as either brushless DC (BLDC) machines, using rectangular phase current waveforms, or as brushless AC (BLAC) machines, using sinusoidal phase currents waveforms [40]. BLDC is usually applied to machines with a trapezoidal back electromotive force (EMF), and BLAC to machines with a sinusoidal back EMF [35, 41]. However, the back EMF shape of a permanent magnet motor is never perfectly trapezoidal or sinusoidal [42], and either control mode can be applied regardless of the back EMF waveform shape [43].

Permanent magnet synchronous motors offer the highest specific power and highest efficiency of any of the motor technologies which has led to their use in the majority of commercially available hybrid and electric vehicles[35, 38]. The use of high energy product rare-earth permanent magnets instead of secondary windings or induced magnetic fields contributes to their high efficiency [36].

However, the field produced by the permanent magnets is not as easy to control as for switched reluctance or induction machines. The magnetic field is always present and

Table 1.1: Magnetic properties of commercially available permanent magnet compounds [9].

Magnet Compound	B_r (T)	H_{ci} (kA m^{-1})	$(BH)_{max}$ (kJ m^{-3})	T_c (°C)
$Nd_2Fe_{14}B$ (sintered)	1.15-1.43	876-2388	255-394	320
$Nd_2Fe_{14}B$ (bonded)	0.2-0.7	720-1200	8-81	360-470
$SmCo_5$ (sintered)	0.8	1194	135	740
Sm_2Co_{17} (sintered)	1.0	1432	200	820
Alnico	0.83-1.25	-	44	850
Sintered ferrite	0.2-0.44	210-310	6.5-36.6	460

can only be suppressed though the application of an opposing stator field [44]. Once the motor has reached base speed and there is no further voltage available from the power supply to overcome the motor's back EMF, some of the inverter's available current must be used for field weakening to further increase the motor speed [45]. The field weakening current does not contribute to torque production, yet creates additional system losses, resulting in a reduced efficiency [46]. Field weakening of permanent magnet machines combined with high operating temperatures can also lead to irreversible demagnetisation of the permanent magnets [47]. This causes a reduction in the specific motor torque, and a reduced efficiency from the increased phase currents needed to produce a given torque output. Field weakening performance will be further discussed in Chapter 4.

Table 1.1 gives some properties of commonly used magnet materials in the construction of PMSMs. Rare earth magnets are compounds of rare earth (lanthanide group) metals with transition metals such as iron and cobalt. Neodymium-Iron-Boron magnets offer a higher remanent flux density than Samarium-Cobalt magnets as well as a higher coercivity and energy product [9]. This makes them well suited for applications where maximising torque density is of high importance [47]. However, Samarium-Cobalt magnets have significantly higher curie temperature, making them better suited to high temperature applications [47], and in designs where the rotor cannot be easily cooled.

Table 1.2: A comparison of the performance of common motor technologies taken from openly available manufacturers' information [10–16].

Electric motor technology	Specific power (kW/kg)	Specific torque (N m/kg)	Peak efficiency (%)	Cost (€/kW)
PMSM	0.66-3.20	1.47-22	92.5-97	-
ACIM	0.56-2.13	1.43-3.70	90-90.5	2.02-7.64
SRM	0.56-2.27	1.33	93-94	-

1.3.4 A Comparison of Motor Technology

Table 1.2 provides some motor performance figures for the motor technologies described above. While many motor manufacturers do not disclose the performance data for their products, the data collected from literature and product datasheets allows a basic comparison to be made. It should be noted that Table 1.2 includes data for a permanent magnet machine featuring liquid cooled stator windings. Higher specific torques than stated may be achievable for induction and switched reluctance machines using similar cooling techniques, although performance figures for such machines could not be obtained.

It can be seen that permanent magnet synchronous motors offer superior performance to both induction and switched reluctance motors in terms of the specific power, the specific torque and the peak efficiency. Achieving a high motor specific torque and specific power is important for reducing the overall mass of hybrid and electric vehicles, aiding mass decompounding and improving the vehicle fuel economy or range [29]. Furthermore, the superior efficiency offered by PMSMs makes them an ideal choice for application to electric vehicles where efficiency is to be maximised.

1.4 Power Electronics

In order to drive permanent magnet synchronous motors for vehicle applications, an inverter is needed to control the supply of electrical power to the motor. The inverter is

also required to control the motor phase currents in response to a torque demand provided by a high level vehicle control system [48].

The most commonly used inverter topology is three half-bridges with free-wheeling diodes [49]. While it is possible to create motors and inverters with more than three phases, components for such systems are not as commonly available and require more complicated controllers than for three phase systems [50]. The increased number of inverter sensors, additional gate-driver electronics and microcontroller processing power needed to drive a motor with more than three phases would necessitate a significant performance advantage over a similar three phase motor system to justify the additional cost.

Power electronics modules with three-phase topologies are commonly available with both MOSFETs and IGBTs as the switching devices. Both devices are widely used in motor inverters, but the most suitable device is highly dependent on the application. The operating voltage, current capability, switching frequency, thermal requirements, size and cost must all be taken into consideration [51].

MOSFETs switch faster than IGBTs and as a result will have lower switching losses for a given operating voltage and current. This makes MOSFETs better suited to applications where high switching frequencies are required [51]. When driving motors to high speeds it is necessary to maintain a switching frequency which is at least an order of magnitude higher than the fundamental electrical frequency of the motor [52]. This ensures a sufficient number of PWM duty adjustments can be made during the electrical cycle to produce the required phase current waveform. IGBTs are preferred for applications with switching frequencies below 20 kHz and MOSFETs for switching frequencies above 200 kHz [51].

Switching and conduction losses increase with the rated device breakdown voltage. For operating voltages below 250 V MOSFETs are an obvious choice as IGBTs with ratings below 600 V are uncommon [53]. Above 1000 V, the conduction losses for MOSFETs cannot compete with that of IGBTs [53]. For intermediate operating conditions, it is necessary to perform an analysis of the inverter losses over the expected operating range to

determine which type of device is most appropriate for the application under consideration.

1.5 Scope of the Thesis

It has been shown that permanent magnet synchronous motors offer superior specific torque and power and higher peak efficiencies than other motor technologies [35, 38]. These characteristics are well suited for application to high efficiency vehicles [35]. The topologies and materials used in the construction of PMSMs have been widely explored in the literature with the aim of improving the system efficiency [15, 37, 54]. Less widely examined is the influence of motor control schemes on the motor performance, as will be shown in Chapter 3. This thesis will therefore focus on developing a motor control strategy to improve motor performance. The analysis carried out in Chapters 4 and 5 ultimately lead to the following goals for an improved control strategy:

1. Use of the control strategy results in an improved system efficiency.
2. Use of the control strategy maximises the available motor torque.

The following constraints have been applied to the development of a new control system in order to minimise the development costs and utilise resources available to the author:

1. The controller can be applied to a motor and inverter system available for testing and collection of experimental results.
2. Techniques for analysing performance will be limited to those which can make use of available test equipment and data.
3. The controller can be implemented without making any changes to existing motor or inverter hardware.

To work within these constraints, the theoretical and experimental examples given in the rest of this thesis are based on a motor and inverter system available to the author,

shown schematically in Figure 1.2. However, the analysis conducted in this thesis could have been performed on any permanent magnet synchronous motor with a suitable inverter.

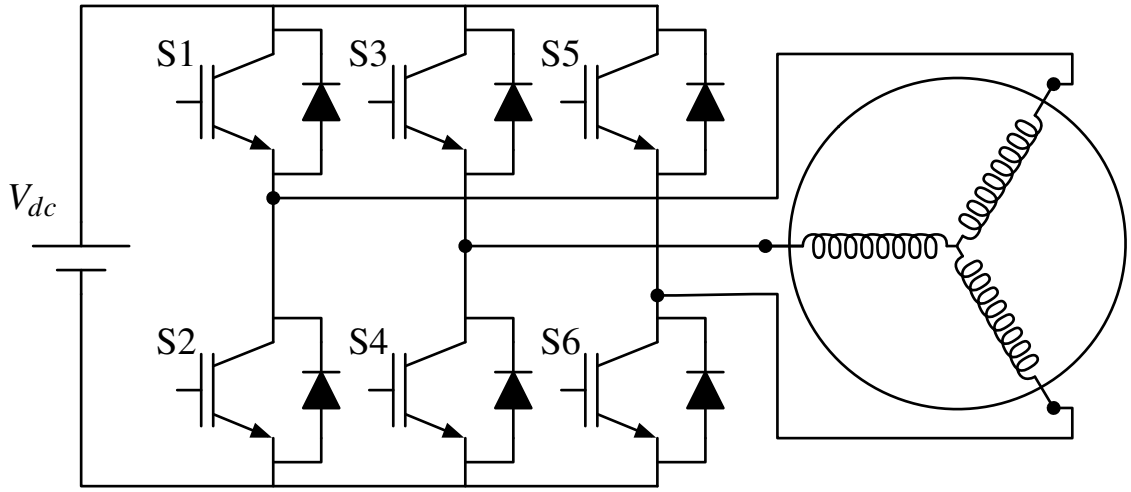

Figure 1.2: Schematic of the three-phase motor and inverter system used in this thesis.

The example system uses a 500 N m three-phase, star connected brushless permanent magnet Yokeless and Segmented Armature (YASA) motor illustrated in Figure 1.3. The new axial flux permanent magnet motor topology developed by Oxford University offers a higher torque density and efficiency than many commercially available motors [15]. The motor uses concentrated, non-overlapping windings that minimises end windings and hence gives lower copper losses [55]. The motor construction also makes use of Neodymium-Iron-Boron magnets on the rotors and high resistivity soft magnetic composite stator pole pieces to minimise the stator eddy current losses[15]. The motor has been designed for use in automotive applications and its specification is given in Table 1.3. Surface Mounted Permanent Magnet Synchronous Motors (SMPMSMs, where the magnets are mounted on the surface of the rotor), such as the YASA motor, generally have lower full load iron losses than internal magnet rotor constructions [35]. Therefore, the analysis carried out in this thesis will be limited to SMPMSMs.

A Semikron Advanced Integration (SKAI) three phase IGBT inverter will be used to drive the motor as it offers a close match to the 300 A peak current rating of the motor. It also contains the phase current, DC link voltage and IGBT temperature sensors needed to

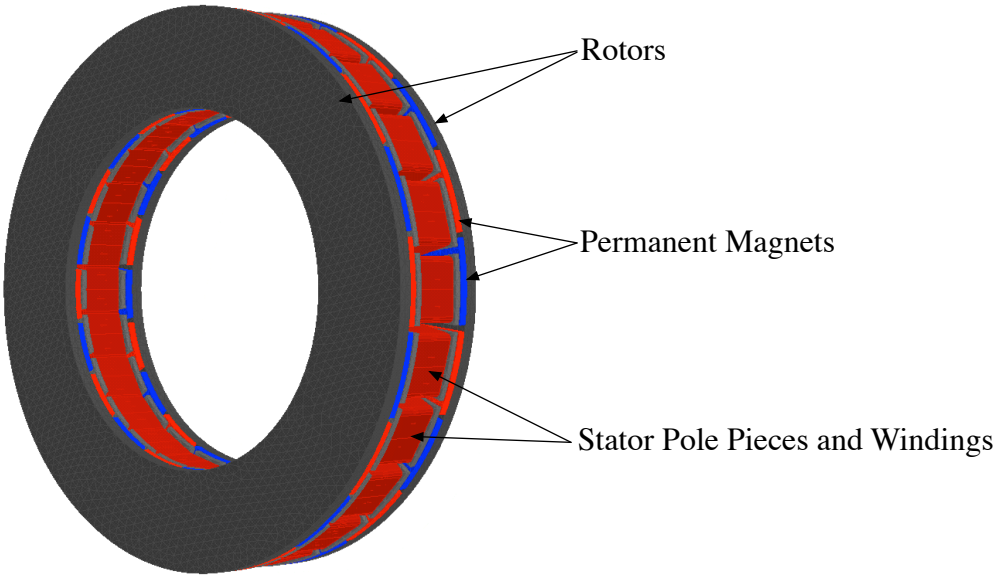

Figure 1.3: A CAD model of a 500 N m YASA motor.

Table 1.3: Specification of the 500 N m YASA motor.

Rated peak torque output	500 N m
Maximum speed	2500 rpm[a]
Rated peak phase current ($I_{ph,max}$)	300.0 A
Nominal DC link voltage (V_{dc})	400 V
Number of pole pairs (n_{pp})	10
Number of stator pole pieces	24
Number of phases	3
Phase inductance (L_{ph})	231.0 µH
Phase resistance (R_{ph}, at 60 °C)	27.0 mΩ
Phase back EMF constant (k)	0.1103 V s (Volts per electrical rad/s)
Number of coil turns per pole piece	45
Dry weight	23.0 kg
Outer diameter	344 mm
Cooling method	Oil cooled stator windings

[a]The maximum speed is limited by the bearings used in the prototype motor design.

Table 1.4: Specification of the Semikron SKAI inverter for a 125 °C junction temperature [17].

Rated continuous RMS phase current	300 A
Semiconductor voltage rating	1200 V
Maximum operating voltage	900 V
Number of phase outputs	3
Maximum junction temperature	150 °C
DC link capacitance	1.0 mF
IGBT collector-emitter threshold voltage ($V_{CE,0}$)	0.85 V
IGBT on-state resistance (r_{CE})	3.1 mΩ
IGBT switching energy dissipation ($E_{on} + E_{off}$)	101 mJ (at V_{rated} = 600 V, I_{rated} = 400 A
IGBT switching energy current exponent ($k_{I,IGBT}$)	0.992[a]
IGBT switching energy voltage exponent ($k_{V,IGBT}$)	1.398[a]
Diode forward threshold voltage (V_{TO})	0.80 V
Diode on-state resistance (r_T)	1.87 mΩ
Diode switching energy dissipation ($E_{on} + E_{off}$)	32 mJ (at V_{rated} = 600 V, I_{rated} = 400 A
Diode switching energy current exponent ($k_{I,diode}$)	0.607[a]
Diode switching energy voltage exponent ($k_{V,diode}$)	0.597[a]
Maximum switching frequency	15 kHz
Weight	8.2 kg

[a]Voltage and current exponents have been calculated from the datasheets of devices with similar characteristics to the SKAI 3001GD12 1452 W Inverter.

monitor and control the inverter. The power electronics have a rated breakdown voltage of 1200 V and a maximum operating voltage of 900 V. This will allow the inverter to be driven from 400 V DC link voltage, in the range representative of many vehicle battery voltages [54].

The inverter is controlled by an integrated Texas Instruments TMS320F2810 DSP. This microcontroller is accessible for reprogramming and allows the development of control strategies using the on-board peripherals such as ADCs and hardware PWM generation. The specification of the inverter is given is Table 1.4.

1.6 Organisation of the Thesis

This thesis consists of a number of chapters looking at different aspects of permanent magnet motor systems. Each chapter attempts to answer a specific question relating to the control, or operation of the motor and inverter. The answers to these questions lead towards a new permanent magnet synchronous motor control strategy, which makes use of the most desirable characteristics of the three motor control modes considered.

In order to determine the efficiency maps for a motor and inverter, the loss mechanisms which reduce the system efficiency must first be understood. Chapter 2 asks the question: "What are the loss mechanisms for permanent magnet synchronous motor systems?" Each of the loss components for the motor and inverter are identified and discussed.

To determine the implications of different motor control modes on the performance of permanent magnet synchronous motors and to see how control strategies can be improved, the conventional control techniques must first be understood. Chapter 3 tries to ascertain: "How are permanent magnet motors controlled?" Six step commutation for BLDC-120 and BLDC-180 operation is compared with space vector modulation techniques for BLAC machines. Accurate knowledge of the motor position is essential for good control, so a number of motor position sensing methods are evaluated. A new method of extrapolating a low resolution position sensor output is also presented.

To compare the performance of different control modes, the maximum torque and power output for the motor over the required speed range must be determined. The issues of field weakening are addressed in Chapter 4, which explores the question: "What is the maximum torque output available from a permanent magnet synchronous motor?" The need for an extended speed range for electric vehicles is explained and the methods for achieving this are described. A number of motor operating regions have been identified and the equations governing the behaviour are determined. The effects of the motor parameters on the system performance beyond base speed are then investigated. Finally, the maximum torque curves for the three control modes are compared for the example motor system.

System efficiency is the focus of Chapter 5 by trying to establish: "What is the most efficient way to drive a permanent magnet motor?" This question is answered by examining the loss components for both the motor and the inverter while running under BLDC-120, BLDC-180 and BLAC control. A comparison is made using simulated and experimental results for the example system for which efficiency maps have been determined. A control mode utilisation yielding the optimal operating efficiency is then presented.

Once the mechanical performance and efficiency maps have been determined for each of the control modes of interest, a new control technique can be developed which seeks to utilise the desirable characteristics of each control mode. Chapter 6 looks to determine: "How can the benefits of BLDC and BLAC control modes be combined?" A method of switching between the control modes is described and demonstrated experimentally. A method of gradually transitioning between the control modes is also presented.

The final chapter reviews the contents of this thesis and describes the specific contribution made. Ideas for further work are then discussed.

2

Loss Mechanisms in Permanent Magnet Motor Systems

2.1 Introduction

This thesis will aim to identify an optimal control method for brushless permanent magnet machines, which maximises the energy efficiency for a motor system. Before the losses can be analysed for a particular control method, the mechanisms that give rise to losses must be understood. This chapter discusses the loss mechanisms in both the motor and the inverter so the total losses can be calculated and minimised. The examples presented in this chapter are based on a brushless AC machine, but the loss mechanisms described and the equations given are equally applicable to permanent magnet machines with non-sinusoidal back EMFs and to control strategies with non-sinusoidal phase currents. In subsequent chapters, these loss mechanisms will be determined for the example motor system.

2.2 Motor Loss Mechanisms

Motor losses can be divided into resistive losses affecting the motor windings, magnetic losses which affect the components that form the magnetic circuit of the machine, and mechanical losses affecting moving parts of the machine. The losses change with motor speed and output torque.

2.2.1 Winding Losses

The stator windings of a permanent magnet synchronous motor are used to produce a magnetic field which interacts with that of the permanent magnets on the rotor. This interaction produces a torque on the machine's output shaft [56]. Ampere's Law shows there is a direct relationship between the strength of the magnetic field produced by the windings and the current that flows through the windings:

$$\int \mathbf{J} \cdot \mathrm{d}\mathbf{A} = \oint \mathbf{H} \cdot \mathrm{d}\mathbf{l} \tag{2.1}$$

Therefore, by increasing the number of Ampere-turns on a stator winding the motor torque output can be increased. However, the volume available for stator windings in a machine will be constrained by the packaging and weight requirements of the application. The current density of the windings is also constrained by the resistive losses and the cooling capability of the motor design [57]. Overheating of the motor windings could lead to breakdown of the insulation and winding turns becoming short-circuited [58]. Winding wire products with insulation temperature classes in excess of 200 °C are available [59].

Motor windings have a finite electrical resistance and so any currents flowing through the stator coils will give rise to resistive power losses. At low motor speeds, the winding losses dominate over other motor losses, such as hysteresis and eddy current losses, which are frequency dependant [60]. In general, the power P_{loss} dissipated by a piece of wire with resistance R carrying a current I is given by:

$$P_{loss} = I^2 R \tag{2.2}$$

The resistance of a metal wire increases with temperature θ and can be approximated using Equation 2.3 where $R(20^\circ)$ is the resistance at 20°C and (α) is the temperature coefficient of resistance. Table 2.1 shows the physical and electrical properties of some common metals. For copper windings, the resistance (and hence the winding resistive loss) is 32 % higher at 200 °C than at 100 °C. While the higher temperature may be within the operating limits of the winding insulation, it is desirable to minimise the operating temperature in order to minimise the winding losses and maximise the motor efficiency.

$$R(\theta) = R(20^\circ)(1 + (\theta - 20)\alpha) \tag{2.3}$$

The relatively low resistivity of copper makes it a popular choice for use in electrical machine windings. However, the increasing price of copper relative to aluminium [61] and the lower density of aluminium makes it a potential choice for lightweight applications. The weight saving over copper windings would have to be evaluated against the decrease in system efficiency from the additional losses, and the impact this would have on the vehicle's design and performance. A direct replacement of copper windings for aluminium windings of the same cross-sectional area would result in a 53.7 % increase in the DC winding resistance but a 69.6 % reduction in the mass of the windings. Alternatively, if the cross-section of the aluminium windings were increased to give the same resistance as the copper windings, (provided that sufficient stator slot volume was available) a mass saving of 53.3 % for the windings could be achieved.

Careful selection of the motor winding configuration can lead to a reduction in the winding losses. Concentrated windings, where the winding coils only span a single stator tooth, are preferable to distributed spanning multiple teeth as this minimises the length (and material cost) of the end windings [62], as shown in Figure 2.1. The end windings add to

Table 2.1: Physical and electrical properties of possible motor winding materials [18, 19]

Material	Resistivity (Ω m)	Temperature Coefficient ($^{\circ}C^{-1}$)	Density (kg/m^3)
Aluminium	2.65×10^{-8}	3.8×10^{-3}	2712
Copper	1.724×10^{-8}	4.29×10^{-3}	8930
Iron	9.71×10^{-8}	6.41×10^{-3}	7850
Nickel	6.85×10^{-8}	6.41×10^{-3}	8800
Silver	1.59×10^{-8}	6.1×10^{-3}	10490

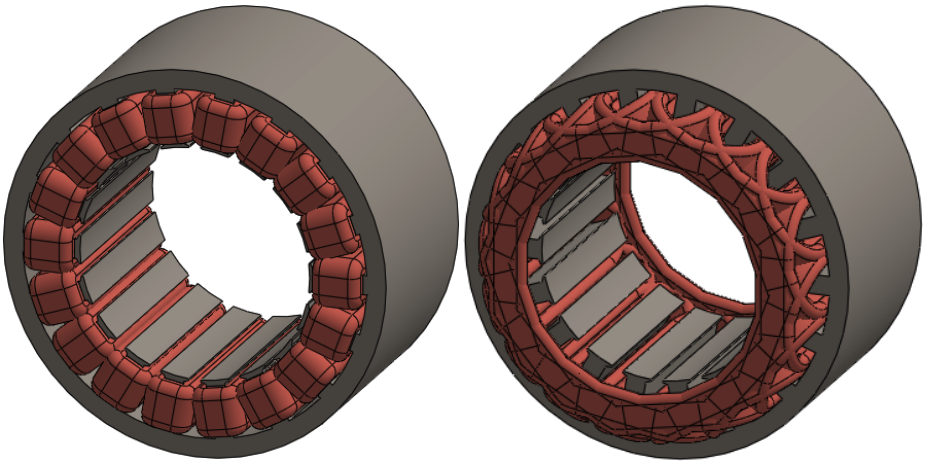

(a) Non-overlapping concentrated windings (b) Overlapping distributed windings

Figure 2.1: Radial flux permanent magnet machine winding configurations.

the overall coil length increasing the total resistance, but do not contribute toward useful torque production [54].

The resistance of a conductor also increases with the frequency the current it is carrying as a result of the skin effect and the proximity effect [63]. The skin depth δ of a conductor can be calculated using Equation 2.4 where ρ and $\mu$are the resistivity and permeability of the conductor and f is the frequency of the current. The AC resistance R_{ac} can then be calculated from the DC resistance R_{dc} using Equation 2.5. The skin effect correction factor k_s can be approximated using Equation 2.6 for $r_o/\delta < 1.7$ where r_o is the conductor radius [64]. The proximity effect correction factor k_x can be approximated for a coil winding using Equation 2.7 where p is the number of winding layers and Δ is the ratio of the winding layer thickness to the skin depth [64].

$$\delta = \sqrt{\frac{\rho}{\pi f \mu}} \tag{2.4}$$

$$R_{ac} = R_{dc} k_s k_x \tag{2.5}$$

$$k_s = 1 + \frac{(r_o/\delta)^4}{48 + 0.8(r_o/\delta)^4} \tag{2.6}$$

$$k_x = 1 + \frac{5p^2 - 1}{45}\Delta^4 \tag{2.7}$$

For machines operating at high electrical frequencies, it is possible to employ a Litz wire for the windings to reduce the losses resulting from the skin effect and the proximity effect [65]. A Litz wire consists of many insulated, small cross-section wires and is used in place of a single solid wire with a larger cross-sectional area. A Litz wire will have a lower resistance than a solid wire with the same total cross-sectional area at high frequencies. This suggests a smaller conductor volume could be used to achieve the same total resistance. However, the same slot fill factor cannot be achieved as for a solid wire [66] because of the additional spacing and insulation between the wire elements. The use of a Litz wire will also give an inferior thermal conductivity to a solid wire, reducing the heat rejection to an external coolant [67].

The total average resistive losses for a three phase motor can be calculated from Equation 2.8 where $I_{Ph,RMS}$ is the RMS phase current and $R_{Ph,W}$ is the phase winding resistance. The resistance of the phase cables connecting the motor to the inverter, $R_{Ph,C}$, should also be taken into consideration when calculating the resistive losses, as shown in Figure 2.2. Equation 2.8 will be applied to the simulated phase currents for the YASA motor in Chapter 5 to estimate the winding losses.

$$P_{loss,R} = \frac{3}{2} I_{Ph,RMS}^2 (R_{Ph,W} + R_{Ph,C}) \tag{2.8}$$

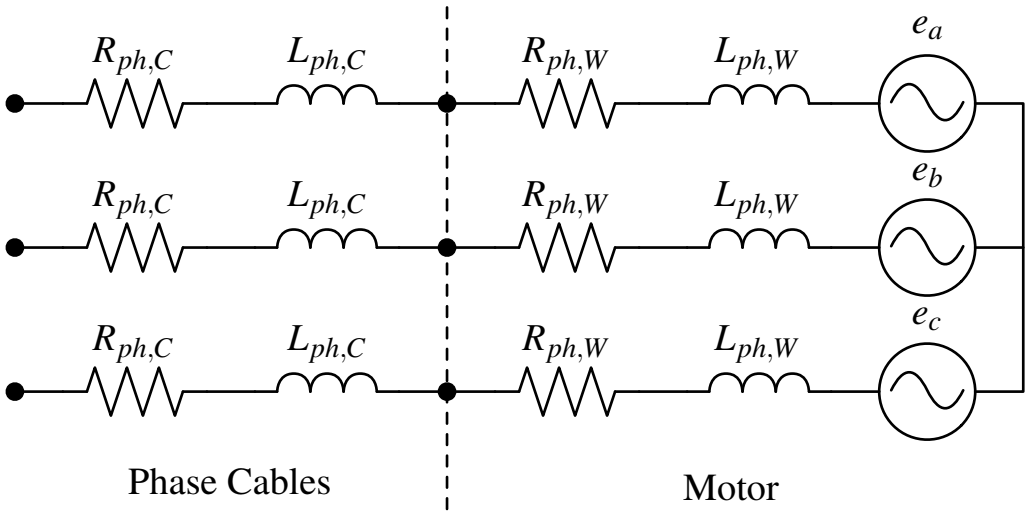

Figure 2.2: Motor equivalent circuit model as seen by the inverter.

2.2.2 Eddy Current Losses

When a conductor is subjected to a time varying magnetic field, it causes circulating currents to flow through the material [68]. As all of the active magnetic materials in a motor have a finite resistivity, the circulating currents dissipate energy through resistive losses [56]. This is illustrated in Figures 2.3 to 2.5 which shows the location of the eddy currents in a 500 N m YASA motor. The colours of the motor components indicate the eddy current densities, while the arrows show the direction of eddy current flow. In each case the eddy currents are concentrated around locations where there is a large rate of change of the magnetic field. For the rotor back iron (Figure 2.3) this is between the permanent magnets.

The permanent magnets in Figure 2.4 have been cut into four sections to reduce the length of the eddy current paths and reduce the overall losses [69, 70] by approximately 75 %. The eddy currents circulate around the gaps between two adjacent pole pieces where the rate of change of magnetic flux is highest. Eddy current losses on the rotor can be further

reduced by insulating the permanent magnets from the rotor, breaking the eddy current path between the two components. Minimising the eddy current losses in the permanent magnets is important to prevent overheating and permanent demagnetisation [71].

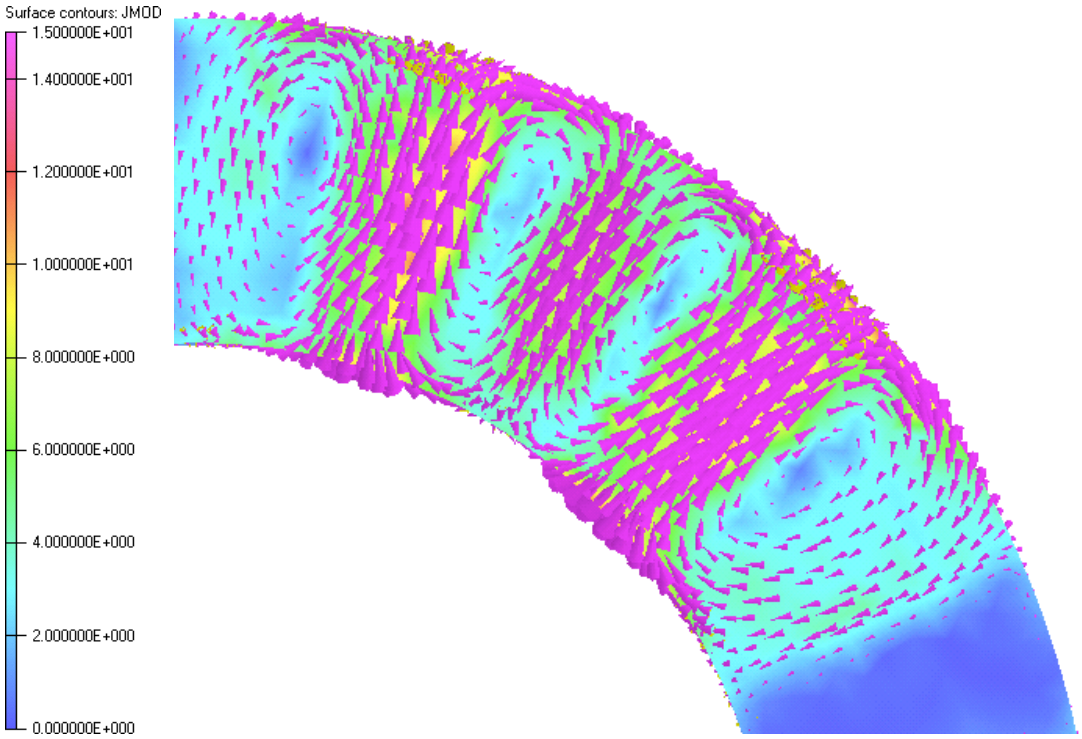

Figure 2.3: Eddy current paths in the rotor back iron of the YASA motor for BLDC-120 control with a 212 A RMS phase current at 500 rpm (JMOD in A/mm^2).

It is common practice in radial flux machines to assemble the stator from a stack of laminations to increase the resistance seen by the eddy currents and reduce the total losses [72]. Eddy current losses can be further reduced by decreasing the lamination thickness, using a lamination material with a higher resistivity or decreasing the amplitude of the magnetic field seen by the materials in the flux path [42]. However, reducing the peak magnetic field strength will also reduce the torque density of the machine which is highly undesirable for automotive applications [35].

The stator pole pieces in Figure 2.5 are made of a powdered iron material to help reduce the eddy current losses. The individual iron grains are insulated from one another giving the components a very high resistivity [73]. This is analogous to having very thin laminations

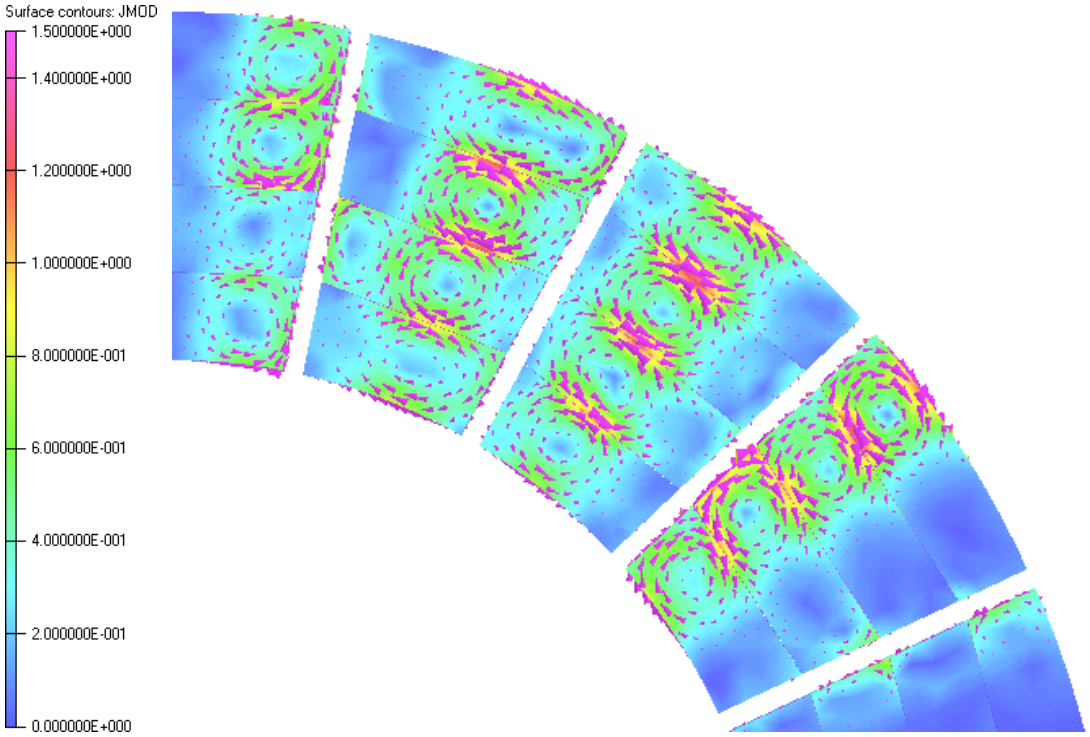

Figure 2.4: Eddy current paths in the permanent magnets of the YASA motor for BLDC-120 control with a 212 A RMS phase current at 500 rpm (JMOD in A/mm^2).

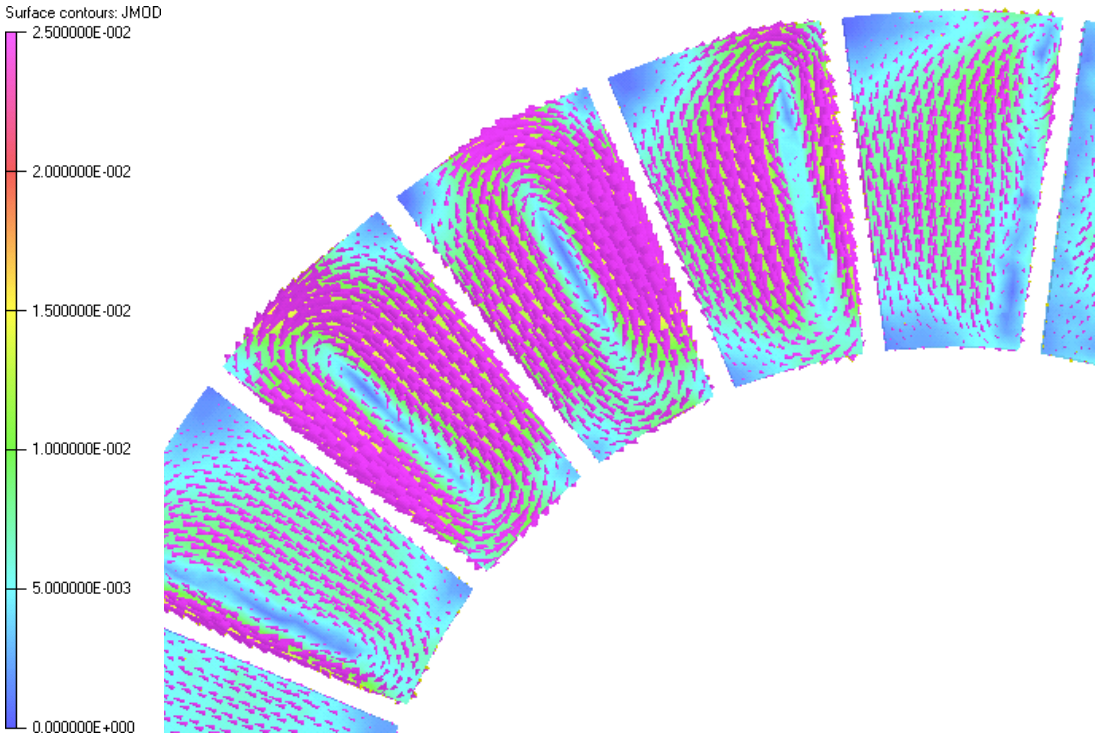

Figure 2.5: Eddy current paths in the stator pole pieces of the YASA motor for BLDC-120 control with a 212 A RMS phase current at 500 rpm (JMOD in A/mm^2).

on a radial flux machine. However, the powdered iron material also allows complex three-dimensional shapes to be formed for axial flux machines [15]. The eddy currents in the figure can be seen to circulate around the gaps between the permanent magnets.

The mild steel rotor discs shown in Figure 2.3 have a much higher conductivity ($5.0 \times 10^6\,\mathrm{S/m}$) than the soft magnetic composite pole pieces ($384\,\mathrm{S/m}$) and consequently have much higher eddy current losses. The losses for the rotors could be further decreased by increasing the number of magnet segmentations [69, 74] or by changing the rotor material for one with a lower conductivity. However, the effects of any changes to the magnetic properties of the rotor material on the motor torque output would also need to be considered. Minimising the losses will help reduce the requirements of the cooling system and the overall system weight [29].

The eddy current losses in all of the components that form the machine's magnetic circuit will increase with motor speed and the amplitude of the motor phase currents as both factors contribute to the rate of change of flux density [71]. The relationship is non-linear and highly dependent on the shape of the motor phase currents. For non-sinusoidal phase currents, the additional harmonic content will contribute towards the total eddy current losses.

A simple empirical formula for determining eddy current losses in a PMSM is given by Equation 2.9 [75, 76]. f_e is the motor electrical frequency, B_{max} is the amplitude of the magnetic field strength and k_{eddy} is the constant of proportionality. However, this equation can only be applied to simple cases with sinusoidal phase currents [76]. It does not take into account the additional losses resulting from the additional harmonic content in the motor phase currents when under BLDC control.

$$P_{eddy} = k_{eddy} f_e^2 B_{max}^2 \tag{2.9}$$

An analytical method for estimating the eddy current losses in magnetic materials is

presented in [68]. This method does not take into account the non-linear material properties and is difficult to apply to motors with complex three dimensional geometries. An analytical method for determining the rotor eddy current losses in SMPMSMs is proposed in [77]. This 2D analytical method is shown to give good agreement to experimental measurements, but the method does not take into account the effect of stator slotting which can give rise to additional losses from the variation of the magnet working point [78]. The 2D nature of the method also limits its applicability to axial flux machines with 3D flux paths.

Modern magnetic Finite Element Analysis (FEA) tools, such as Opera [8], which has been used in this thesis, can address many of the issues described above. Complex, time stepping motor models can be generated with non-linear magnetic properties and arbitrary phase current waveforms. This allows the eddy currents losses to be determined to a higher level of accuracy than with analytical techniques [73]. A more detailed analysis of eddy current losses in the YASA machine is carried out in Chapter 5 where a finite element analysis has been used to estimate the total losses.

2.2.3 Hysteresis Losses

The ferromagnetic components of a PMSM which form part of the magnetic circuit are exposed to time-varying magnetic fields as the motor rotates and the phase currents change. Energy is dissipated as the materials are re-magnetised and their atomic dipoles align themselves with the directions of the applied magnetic field [56]. As brushless machines are synchronous, the permanent magnets and rotors rotate with the applied magnetic field. As a result, they are exposed to relatively small changes and slow changes in magnetic flux density in comparison to the stator and for this reason, rotor hysteresis losses are often neglected [79]. The hysteresis losses in the motor are therefore dominated by the losses of the stator.

Hysteresis losses can be split into major and minor loop losses as illustrated by

Figure 2.6. If a material experiences a periodic flux density waveform that monotonically increases to a maximum value before monotonically decreasing to a minimum which is symmetric about zero, the B-H curve will trace a major loop. However, if the material experiences small excursions from the major loop as a result small reversals in the flux density, additional hysteresis losses will be caused by the resulting minor loops [80].

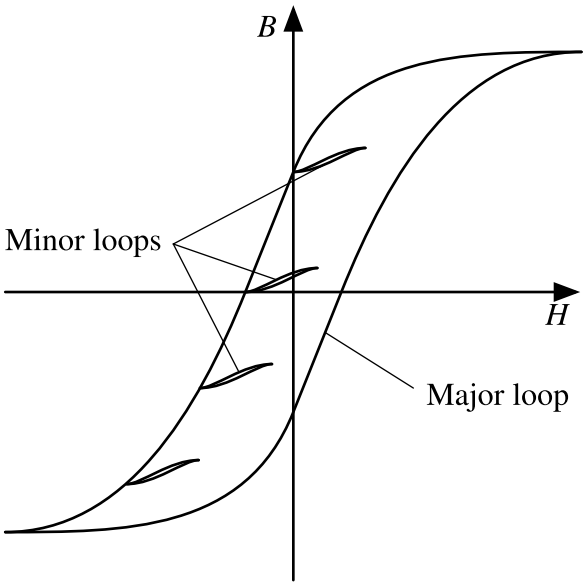

Figure 2.6: Major and minor B-H hysteresis loops for a magnetic material.

The hysteresis losses can be approximated empirically using Equation 2.10 where f_e is the motor electrical frequency, B_{max} is the amplitude of the magnetic field strength and k_{hys} is the constant of proportionality [81]. β is normally in the range of 1.8 to 2.2 [76] and can be determined from Finite Element Analysis (FEA) results [82]. This method assumes that there are no re-entrant minor hysteresis loops and that the flux density value used is the amplitude of the fundamental flux component. The equation shows that hysteresis losses can be reduced by decreasing the number of rotor pole pairs to give a lower electrical frequency for a given shaft speed [42]. However, the effect of changing the number of pole pairs on other aspects of the motor's performance such as the back EMF shape and specific torque output must also be considered.

$$P_{hys} = k_{hys} f_e B_{max}^{\beta} \tag{2.10}$$

A harmonic analysis on the stator flux density is used in [76] to estimate the eddy current losses in a PMSM, but the analysis is not extended to determine hysteresis losses. Instead, Equation 2.10 is used and the assumptions of sinusoidal flux waveforms and no minor hysteresis loops is made. The measurement of material hysteresis loops is proposed in [83] for many flux amplitudes and frequencies. The results are then used to determine fitting parameters for a Preisach distribution function for use in a FEA. However, this requires many measurements from a real motor, which is not practical for motor constructions where measurement windings cannot be inserted. In [84], the losses associated with each harmonic component of the stator flux density waveform are calculated from FEA results. The technique is shown to offer improvements in the iron loss estimation of a PMSM of up to 28.4 % over the technique given in [81].

In order to accurately estimate the hysteresis losses for non-sinusoidal flux waveforms, it is necessary to consider both the major and minor hysteresis loops resulting from the harmonic content of the motor phase currents and motor geometry. Magnetic FEA software now allows material hysteresis loss data to be input into motor models for calculation of both major and minor loop hysteresis losses [85]. However, such tools were unavailable at the time of carrying out the analysis presented in this thesis. Therefore, the following method based on [84] will be used to estimate the hysteresis losses for the YASA motor. First, the harmonic content of the stator flux variation will be analysed using the flux density waveforms determined though a magnetic FEA of the motor at the required operating point. The hysteresis losses associated with each harmonic component will then be calculated from the material loss data provided by the manufacturer, such as in Figure 2.7. This will give an improvement in accuracy over the method in [81] using the peak flux density and frequency alone.

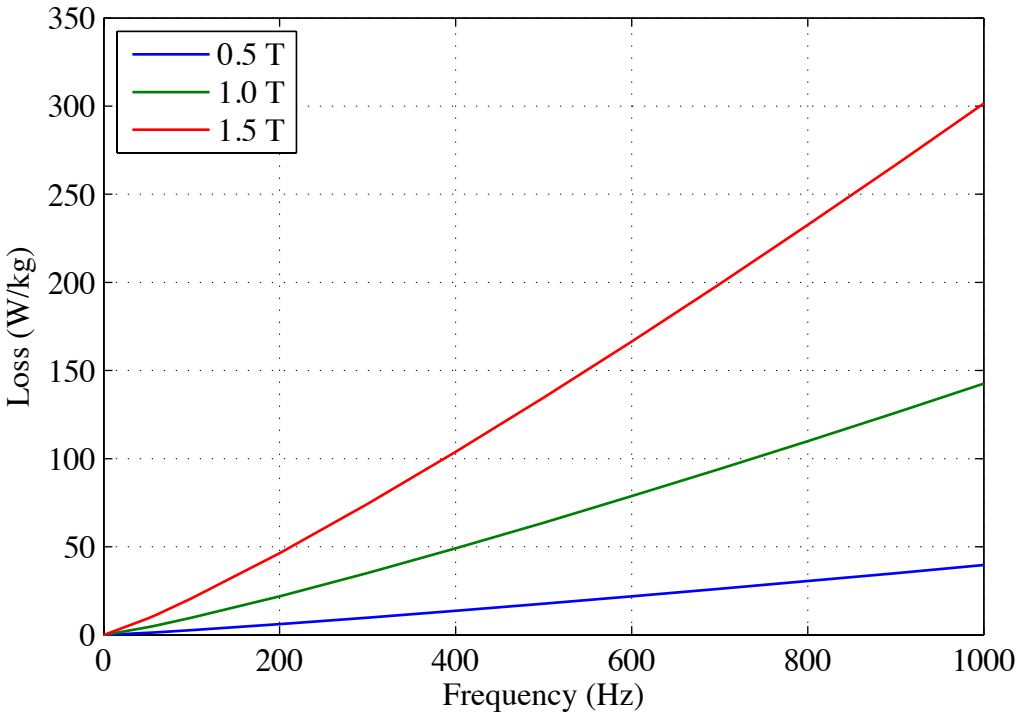

Figure 2.7: Hysteresis losses for the Somaloy 3P HR material with varying field strength amplitudes and frequencies [2].

2.2.4 Mechanical Losses

All motors suffer from mechanical losses resulting from bearing friction and windage losses. Windage losses are caused by shearing of the air in the air gap and are more significant in machines with narrow air gaps and high rotor speeds [56]. The windage losses for an axial flux motor can be estimated using Equation 2.11, where ρ is the air density, D_{in} is the inner rotor diameter, D_{out} is the outer rotor diameter and k_{drag} is the constant of proportionality [86].

$$P_{drag} = k_{drag} \rho \omega_m^3 \left(D_{out}^5 - D_{in}^5 \right) \tag{2.11}$$

Bearing losses depend on the type of bearing, lubricants and seals used and will be higher for large diameter bearings used in large machines [87]. As with the windage losses,

the bearing losses are not affected by the motor load and increase with the mechanical speed. The bearing loss can be approximated by the following equation [75]:

$$P_{bearing} = k_{bearing}\omega_m^2 \tag{2.12}$$

2.3 Inverter Loss Mechanisms

All of the power delivered to an electric motor (when motoring) is supplied by the inverter power electronics. It is therefore essential to understand the associated loss components when evaluating different motor control strategies with the objective of minimising the total system losses. The cooling of the power electronics modules is critical to ensure that they are operated within their thermal limits to avoid permanent damage [88]. An understanding of the inverter losses is therefore also key to specifying a suitable cooling system.

The loss mechanisms of IGBTs and their anti-parallel diodes can be separated into conduction losses, which act all the time a current is flowing through the device, and switching losses which act during the transition period when a device switches between on and off states [58]. The loss mechanisms described are applicable to all power electronics topologies, but this thesis will concentrate on the standard three-phase, two-level inverter shown in Figure 2.8.

2.3.1 Conduction Losses

Energy is dissipated by the power electronic devices all the time they are conducting as a result of the small voltage drops across the devices [4]. The IGBT on-state voltage drop can be approximated by a linear relationship consisting of an IGBT collector-emitter threshold voltage V_{CEO} and the voltage drop from the on-state resistance r_{CE}. A similar relationship can be used for the inverse diodes with a threshold voltage V_{TO} and on-state resistance

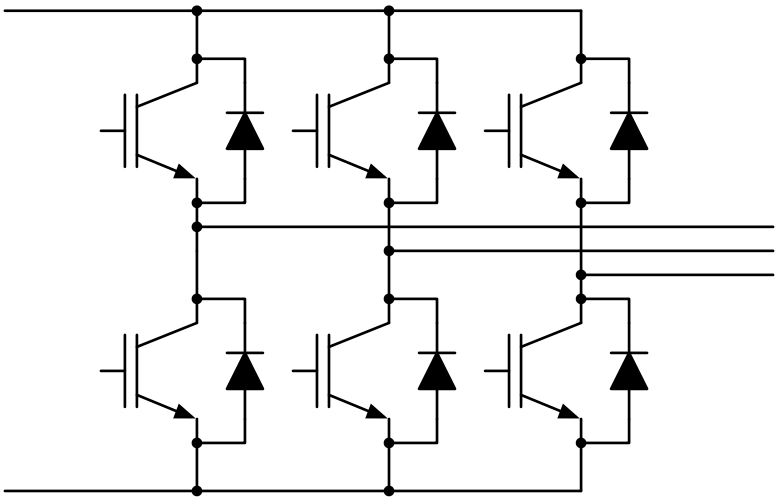

Figure 2.8: The three-phase, two-level inverter topology.

r_T. The power dissipated by the devices is a function of the device currents and can be calculated using Equations 2.13 and 2.14 where i_{IGBT} and i_{diode} are the IGBT and diode currents respectively [89].

$$P_{c,IGBT} = i_{IGBT} V_{CEO} + i_{IGBT}^2 r_{ce} \tag{2.13}$$

$$P_{c,diode} = i_{diode} V_{TO} + i_{diode}^2 r_T \tag{2.14}$$

For brushless AC drives, the IGBTs in each inverter leg are typically switched in antiphase, so only one of the two IGBTs will be conducting at any one time [90]. The inverter leg output voltage is switched between the two DC link voltage rails for varying pulse widths to create a pseudo-sinusoidal output voltage. When the phase current is positive, the top IGBT and bottom diode conduct. When the phase current is negative, the bottom IGBT and top diode conducts.

Figures 2.10 to 2.12 show the voltages and currents in an inverter leg (Figure 2.9) for an example motor operating at 250 rpm with a 100 V DC link supply. As the direction of the phase current changes from positive to negative, it can be seen that the IGBT and diode pair carrying the current changes.

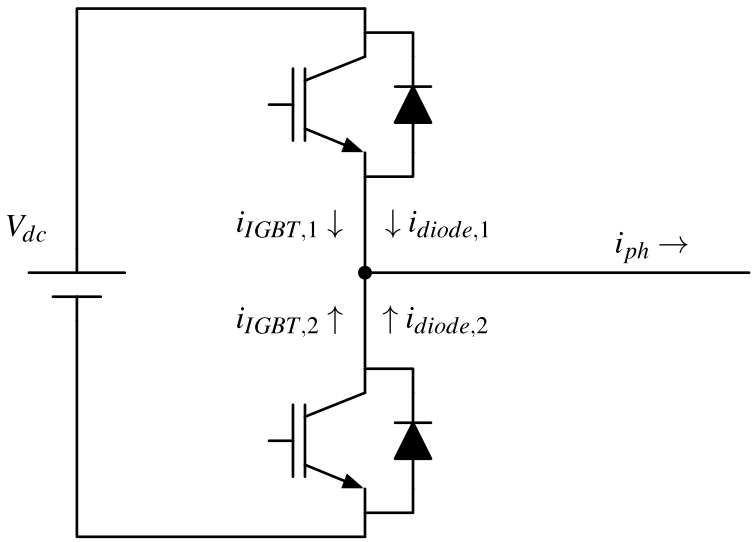

Figure 2.9: Phase current components in an inverter leg.

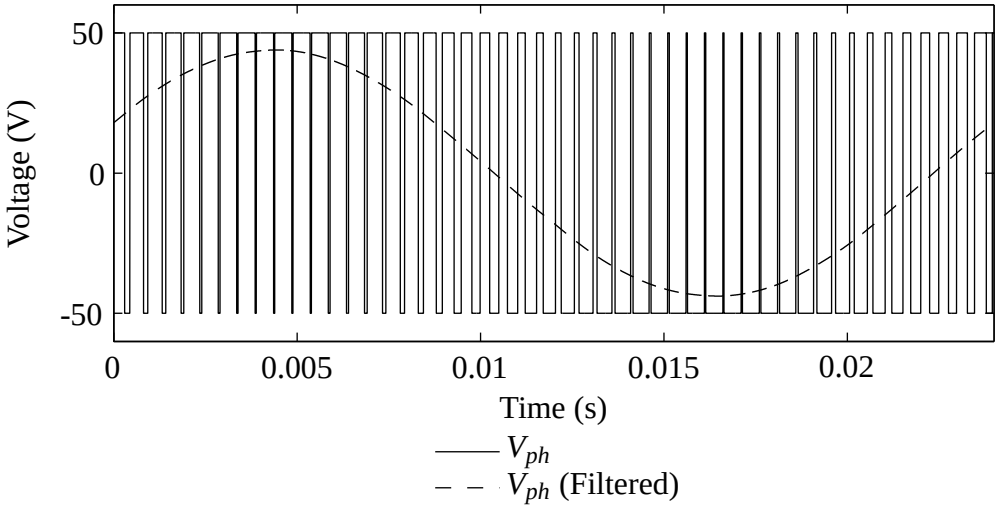

Figure 2.10: Inverter phase voltage for sine wave Pulse Width Modulation.

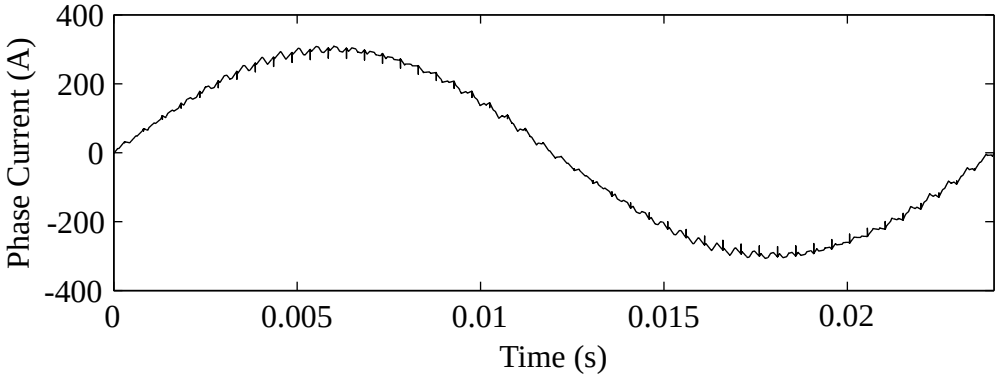

Figure 2.11: Motor phase current (i_{ph}) for sine wave Pulse Width Modulation.

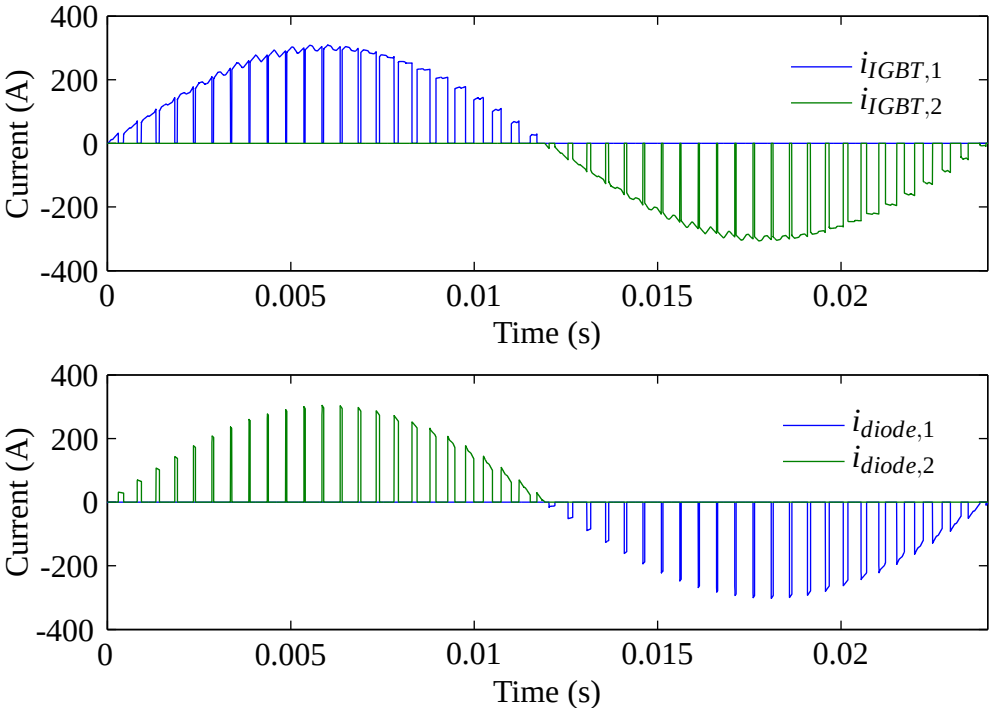

Figure 2.12: IGBT and diode currents for sine wave Pulse Width Modulation.

Figure 2.13 shows the instantaneous IGBT and diode conduction losses for an inverter leg whose characteristics are given in Table 1.4 for a peak phase current of 300 A. The same inverter is used in the experimental sections in the remainder of this thesis. When motoring, the IGBTs conduct for more of the time than the diodes and as a result, the average conduction losses over an electrical cycle are higher for the IGBTs than the diodes. For the example shown for the motor producing 500 N m of torque at 250 rpm, the cycle average losses are 125.2 W for each IGBT and 20.6 W for each diode.

When the motor is regenerating, the phase of the sinusoidal voltage applied by the inverter with respect to the phase current is different from when motoring. This results in the diodes conducting for more time than the IGBTs and the diode conduction losses dominating. For the example system, a braking torque of 500 N m at 250 rpm creates 53.6 W of conduction losses in each IGBT and 76.2 W in each diode (as determined through the motor simulation used in Chapter 5). The difference in the total conduction losses has changed by 16.0 W. It is therefore important to consider the phase of the applied voltage

with respect to the phase current when calculating the conduction losses.

A derivation of analytical equations for determining the switching and conduction losses in a voltage source inverter is presented in [89]. The equations given are dependant on the modulation scheme used and sinusoidal phase currents have been assumed. This method is more difficult to apply to non-sinusoidal phase currents and arbitrary modulation schemes. Therefore, the analysis of inverter losses in this thesis will apply Equations 2.13 and 2.14 to device currents determined through a simulation of the motor control system. The instantaneous losses will be averaged over an electrical cycle under steady state conditions to determine the losses at a particular operating point.

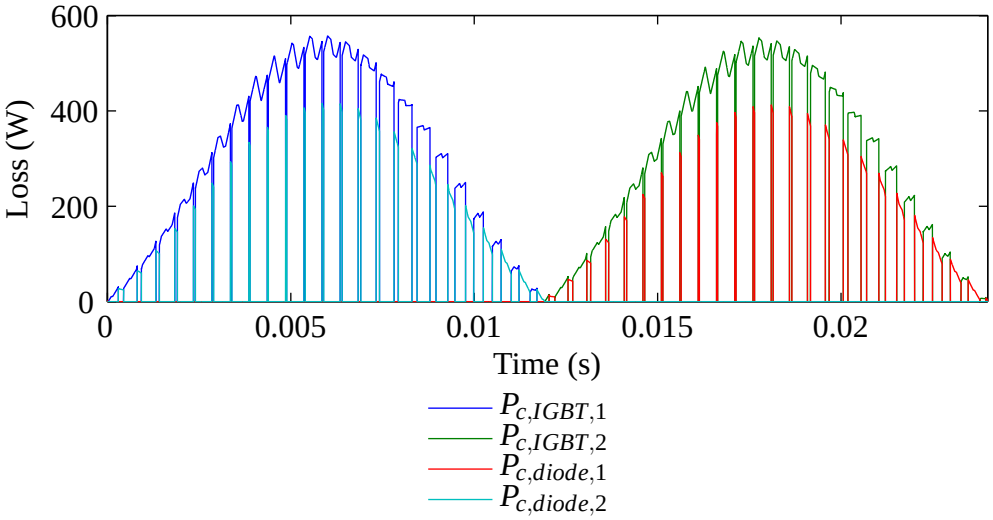

Figure 2.13: Instantaneous IGBT and diode conduction losses for sine wave Pulse Width Modulation.

2.3.2 Switching Losses

Switching losses result from the energy that is dissipated during the finite time taken for IGBTs and diodes to turn on and off [4]. For the inverter used for the experiments in the following chapters, the IGBTs have a turn-on time of 177 ns and a turn-off time of 600 ns when switching 600 V and 600 A with a 2 Ω gate resistance [20]. During the transitional period for turn-on, the IGBT collector-emitter voltage falls from the DC-link voltage to the

on-state voltage drop, while the collector current increases from zero to the on-state current, as shown in Figure 2.14. During turn-off the voltage rises to the DC-link voltage while the collector current falls to zero. While the collector-emitter voltage transitions between the two levels, energy is dissipated by the IGBT as a result of the simultaneous current flow and voltage drop, as shown in Figure 2.14.

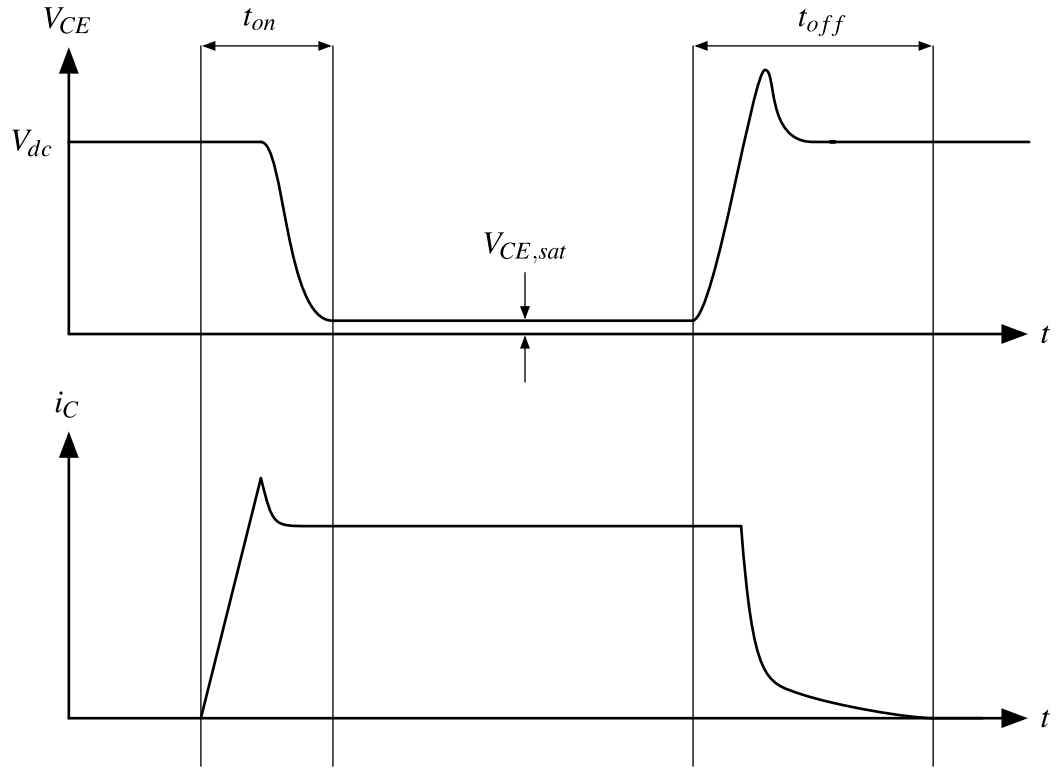

Figure 2.14: IGBT voltage and current during turn-on and turn-off [3].

The free-wheeling diodes in an inverter also suffer from power dissipation during turn-off. As the forward voltage across the diode becomes negative following a period of diode conduction, a negative current is required to sweep out the excess carriers in the diode before it will block a negative voltage [4]. As with IGBTs, the simultaneous current flow (illustrated in Figure 2.15) and applied voltage results in power dissipation. For the free-wheeling diodes in the SKAI inverter, the reverse recovery current can reach 420 A when the inverter is switching 600 V and 600 A [20].

The IGBT switching losses can be reduced by increasing the drive strength of the IGBT

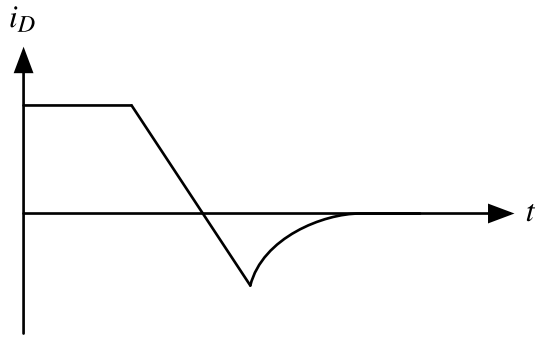

Figure 2.15: Free-wheeling diode current during turn-off [4].

gate driver, resulting in faster switching and lower energy dissipation. However, there is a practical limit to the switching speed of the IGBTs imposed by the voltage overshoot during turn-off [3]. The high rate of change of current can cause large voltage transient from parasitic inductances in the inverter and can potentially destroy the device [91].

The effect of the gate drive resistance on IGBT switching speed and the resulting switching losses is investigated in [3], where the losses have been calculated from the measured IGBT current and voltage drop. It is not possible to modify the gate drive circuit of the SKAI inverter and the IGBT and diodes are inaccessible inside the unit, preventing characterisation of their losses during operation. Therefore, the inverter switching losses, estimated in the following chapters, will be determined from data provided by the manufacturer. The switching losses can be estimated using Equation 2.15 for an IGBT with a switching frequency f_s, turn-on energy E_{on} and turn-off energy E_{off} [4].

$$P_s = f_s(E_{on} + E_{off}) \tag{2.15}$$

The turn-on and turn-off energies change with the device current (i) and DC-link voltage (V_{dc}) and the IGBT switching losses can be approximated using Equation 2.16. A similar relationship can used to estimate the diode switching losses using Equation 2.17 where E_{rr} is the diode reverse recovery energy dissipated when the diode turns off [89]. The constants in Equations 2.16 and 2.17 can be obtained from manufacturers datasheets and are given for the SKAI inverter in Table 1.4.

$$P_{s,IGBT} = f_s(E_{on} + E_{off}) \left(\frac{i}{I_{rated}}\right)^{k_{I,IGBT}} \left(\frac{V_{dc}}{V_{rated}}\right)^{k_{V,IGBT}} \tag{2.16}$$

$$P_{s,diode} = f_s E_{rr} \left(\frac{i}{I_{rated}}\right)^{k_{I,diode}} \left(\frac{V_{dc}}{V_{rated}}\right)^{k_{V,diode}} \tag{2.17}$$

Figure 2.16 shows how the instantaneous switching losses for the IGBTs and diodes in the Semikron SKAI inverter change over an electrical cycle for a peak phase current of 300 A. The switching losses can be reduced by lowering the PWM switching frequency. However, a reduction in switching frequency will increase the amplitude of the ripple on the phase currents which will potentially increase other loss components from the increased harmonic content [92]. This would also decrease the number of PWM voltage pulses per cycle available to create the desired phase current profile. Furthermore, low switching frequencies are undesirable for electric vehicles because of the high pitched audible sound produced.

It can be seen that for a 2 kHz switching frequency, the total switching losses (85.7 W cycle average) account for a much smaller proportion of the total inverter losses than the conduction losses (291.2 W cycle average). At a switching frequency of 10 kHz, the cycle average switching losses will increase to 428.7 W. This indicates that it is desirable to reduce the inverter switching frequency when possible to maximise the system efficiency.

Changes to the inverter switching frequency will not be considered further in this thesis as the influence of the switching frequency on switching losses is well understood. A fixed switching frequency will therefore be used in the simulated and experimental examples. The thesis will instead focus on the effect of control modes on the system losses as will be discussed in the next chapter.

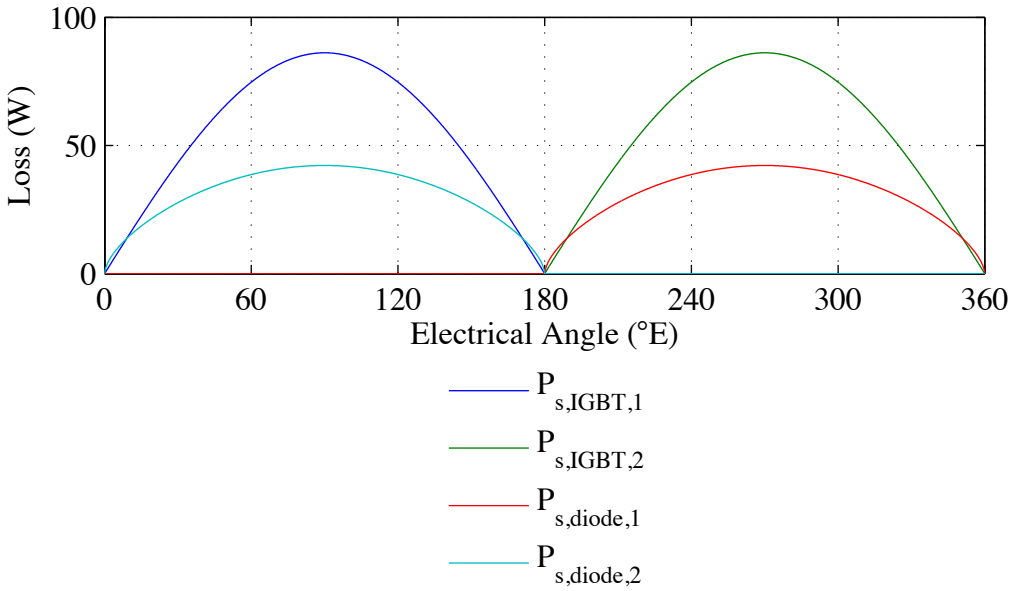

Figure 2.16: Average IGBT and diode switching losses for sine wave Pulse Width Modulation with a 2 kHz switching frequency, peak phase current of 300 A and a DC link voltage of 400 V.

2.3.3 Device Ratings

When selecting power electronics devices for a particular application, it is important to select devices with appropriate ratings to minimise system losses. Table 2.2 shows the characteristics of a range of IGBT modules with 600 V, 1200 V and 1700 V ratings. The IGBT switching energies and inverse diode reverse recovery energies have been normalised for operation at a DC link voltage of 400 V and a phase current of 100 A.

The device characteristics show an increase in the IGBT collector-emitter voltage and on state resistance with increasing blocking voltages. For the inverse diodes the trend for the forward voltage drop is less obvious, but an increase in the on state resistance with increasing blocking voltages can be seen. These characteristics both contribute towards conduction losses and it is therefore important to select devices with the lowest blocking voltage possible in order to minimise the conduction losses. However, the large steps in the available voltage ratings can make it difficult to match the chosen supply voltage to an optimally sized inverter.

Table 2.2: Comparison of IGBT module characteristics from the Semikron SEMITRANS IGBT product range (V_{dc} = 400 V, i_{Ph} = 100 A) [20].

V_{rated}	$I_{c,rated}$	V_{CEO}	r_{CE}	$E_{on}+E_{off}$	V_{FO}	r_F	E_{rr}
600 V	195 A	0.85 V	5.7 mΩ	4.8 mJ	0.95 V	3.0 mΩ	1.2 mJ
600 V	390 A	0.85 V	2.7 mΩ	3.2 mJ	0.95 V	1.5 mΩ	1.8 mJ
600 V	760 A	0.85 V	1.4 mΩ	3.2 mJ	0.95 V	0.8 mΩ	2.2 mJ
1200 V	260 A	0.90 V	7.3 mΩ	5.4 mJ	0.80 V	5.3 mΩ	2.3 mJ
1200 V	470 A	0.90 V	3.7 mΩ	5.5 mJ	0.80 V	2.7 mΩ	1.9 mJ
1200 V	660 A	0.90 V	2.8 mΩ	5.2 mJ	0.80 V	2.0 mΩ	2.1 mJ
1700 V	160 A	0.90 V	15.0 mΩ	14.4 mJ	0.90 V	7.0 mΩ	4.0 mJ
1700 V	260 A	0.90 V	10.0 mΩ	13.7 mJ	0.90 V	5.3 mΩ	2.8 mJ
1700 V	430 A	0.90 V	5.2 mΩ	15.8 mJ	0.90 V	3.0 mΩ	4.3 mJ

It is also apparent that the device on-state resistances decrease as current ratings increase. Therefore, using devices with higher than required current ratings would be advantageous for minimising conduction losses. However, this might not be practical for applications constrained by cost, packaging volume and weight such as in automotive applications.

The IGBT switching energies and the diode reverse recovery energies both increase with the voltage rating, but do not vary significantly with the rated current. Therefore, to minimise the inverter switching losses, IGBT modules with the lowest possible voltage rating for the application should be used.

2.3.4 Low Speed Operation

The low mass of the IGBT and diode devices on the module substrate combined with the thermal resistance to the power electronics heat sink can cause the device temperatures to rise rapidly when carrying large currents [93]. At motor speeds where the thermal time constant of the power electronics is smaller than the electrical cycle period of the motor, it may be necessary to limit the maximum motor phase currents to prevent overheating of the inverter. This is because the frequency of the motor phase currents is not high

Table 2.3: IGBT simple thermal model parameters

Device Property	Symbol	Value
IGBT to heat sink thermal resistance	R_{th}	$0.065\,\mathrm{K\,W^{-1}}$
IGBT specific heat capacity	c	$0.71\,\mathrm{J\,g^{-1}\,K^{-1}}$
IGBT mass	m	$10\,\mathrm{g}$
Heat sink temperature	$T_{heatsink}$	$50.0\,^{\circ}\mathrm{C}$

enough for the heating effects resulting from the inverter losses to be spread equally over all three phases. The thermal cycling of the IGBTs causes internal stresses from the different thermal expansion coefficients of the wire and device substrate and can ultimately lead to failure through fatigue [94].

This effect is illustrated in Figure 2.17, which approximates the temperature variation of a single IGBT in a three phase inverter during an electrical cycle for three different motor speeds. The IGBT temperature variation has been estimated using a simple thermal model consisting of the IGBT mass connected to a heat sink at constant temperature through a thermal resistance. The rate of temperature change has been calculated using Equation 2.18 and the model parameters in Table 2.3. The IGBT losses (P_{loss}) have been estimated using Equations 2.16 and 2.13 for a sinusoidal phase current with an amplitude of 400 A with a 10 kHz PWM frequency.

$$P_{loss}(t) - R_{th}(T_{IGBT}(t) - T_{heatsink}) = mc\frac{dT_{IGBT}(t)}{dt} \tag{2.18}$$

At 10 rpm, the IGBT junction temperature peaks at 138 °C, which is dangerously close to the 150 °C operating limit [17] and has an 88 °C temperature range over the electrical cycle. At 100 rpm the peak temperature for the same current amplitude has fallen to 90 °C and the temperature range to 21 °C. At 1000 rpm, the peak temperature is 78 °C with only 3 °C variation.

It will not be necessary to reduce the current limit at low speeds for the example system used in this thesis as the motor phase peak current limit of 300 A is less than the 424 A rated

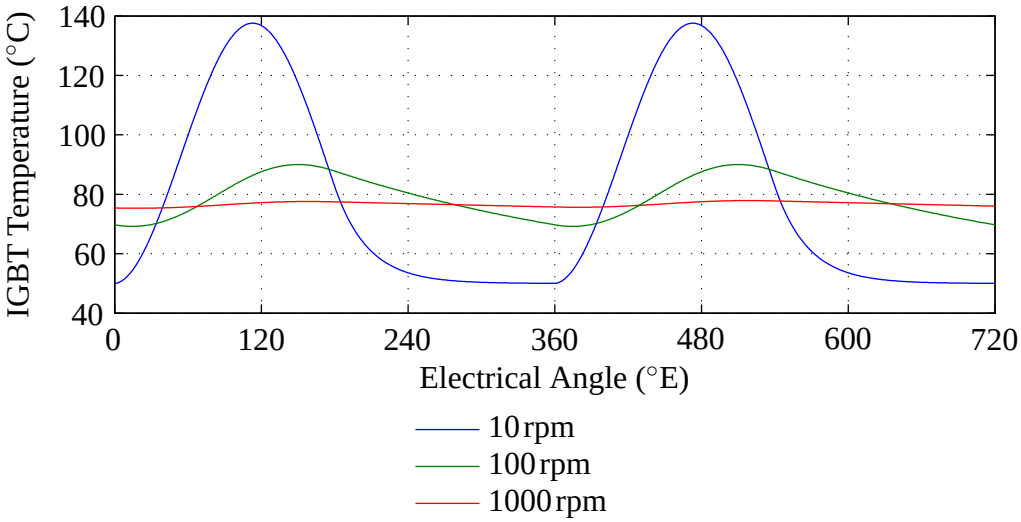

Figure 2.17: The approximated IGBT temperature variation for a 400 A sinusoidal phase current at different motor speeds.

continuous current output of the inverter [17].

2.4 Summary

In this chapter, a discussion has been given on each of the major loss components for motor and inverter systems. The motor efficiency will be reduced by resistive winding losses from the phase currents and eddy current and hysteresis losses from the time varying magnetic fields in the machine. Mechanical windage and bearing losses also act on the motor when rotating. The inverter will suffer from conduction and switching losses from the non-ideal behaviour of the IGBTs and diodes. Techniques for determining the losses in motors and inverters have also been given, and the methods that will be used for the analysis of losses for the example motor system in this thesis have been selected.

The motor winding losses, the inverter switching losses and the inverter conduction losses will be predicted from the component parameters and motor phase currents using simple analytical equations. These equations can be directly applied to the phase currents from the motor simulation used in Chapter 4. The motor eddy current losses will be determined through a finite element analysis of the motor to give a more accurate estimate

than some of the analytical techniques presented in the literature. The hysteresis losses cannot be directly determined using the FEA software available to the author. Instead, a harmonic analysis of the motor component flux densities will be used to calculate the losses from the available component material data.

The selection of suitably rated power electronic devices for a particular application has been discussed. It was shown that use of devices with the lowest possible blocking voltage and highest possible current rating with give the lowest inverter losses. Finally, it was shown that at low motor speeds, it may be necessary to reduce the maximum motor phase current to avoid excessive thermal cycling of the power electronics.

3

Control of Permanent Magnet Synchronous Motors

3.1 Introduction

Motor performance is highly dependent on the strategy used to control the motor. The control strategy used determines the shape of motor phase current waveforms and hence the motor and inverter losses [89]. The choice of control strategy can also affect the torque and power output of the motor [35]. Before these issues can be explored further, it is necessary to understand how permanent magnet synchronous motors are normally controlled. The following chapter will introduce three well established methods: Brushless DC with 120°E conduction (BLDC-120), Brushless DC with 180°E conduction (BLDC-180), and Brushless AC (BLAC).

3.2 Brushless DC Control

Six-step commutation is usually associated with the control of brushless DC machines characterised by a trapezoidal back EMF [35]. The inverter switching pattern is changed every 60°E, as shown in Figure 3.1 where S1 to S6 are the switching signals applied to the six inverter switching devices indicated in Figure 1.2. e_a, e_b and e_c are the phase back EMFs of the motor and i_a, i_b and i_c are the resulting phase currents.

Two variations of six-step commutation are commonly employed and differ by the duration for which current flows in each motor phase. For 120°E conduction (BLDC-120, shown in Figure 3.1), each motor phase is active for 120°E at a time followed by a 60°E inactive period. This ideally results in a rectangular current waveform where only two of the motor phases are conducting at any instant [52]. The width of the pulses applied to the inverter switches is modulated to control the amplitude of the phase currents.

The instantaneous torque output of a PMSM is given by Equation 3.1. In order to maximise the motor torque output for a given phase current amplitude for BLDC-120 control, the motor phase currents must be aligned with the nominally flat parts of the back EMF waveforms for their respective phases. Ideally, this would result in a ripple free output torque. However, real motors do not show a constant phase back EMF during the 120°E conduction period [35]. The inductance of the motor windings also limits the rate of change of the phase currents and prevents the ideal step changes shown in Figure 3.1. These non-idealities gives rise to torque ripple on the motor output [35].

$$T = \frac{\sum i_{ph} e_{ph}}{\omega_m} \tag{3.1}$$

Brushless DC control with 180°E conduction (BLDC-180) operates in a similar way to BLDC-120 control, except that the active duration of each switching device is extended to span 180°E. This increases the amount of power that can be delivered to the motor by the inverter and results in all three motor phase conducting simultaneously [95]. However, the

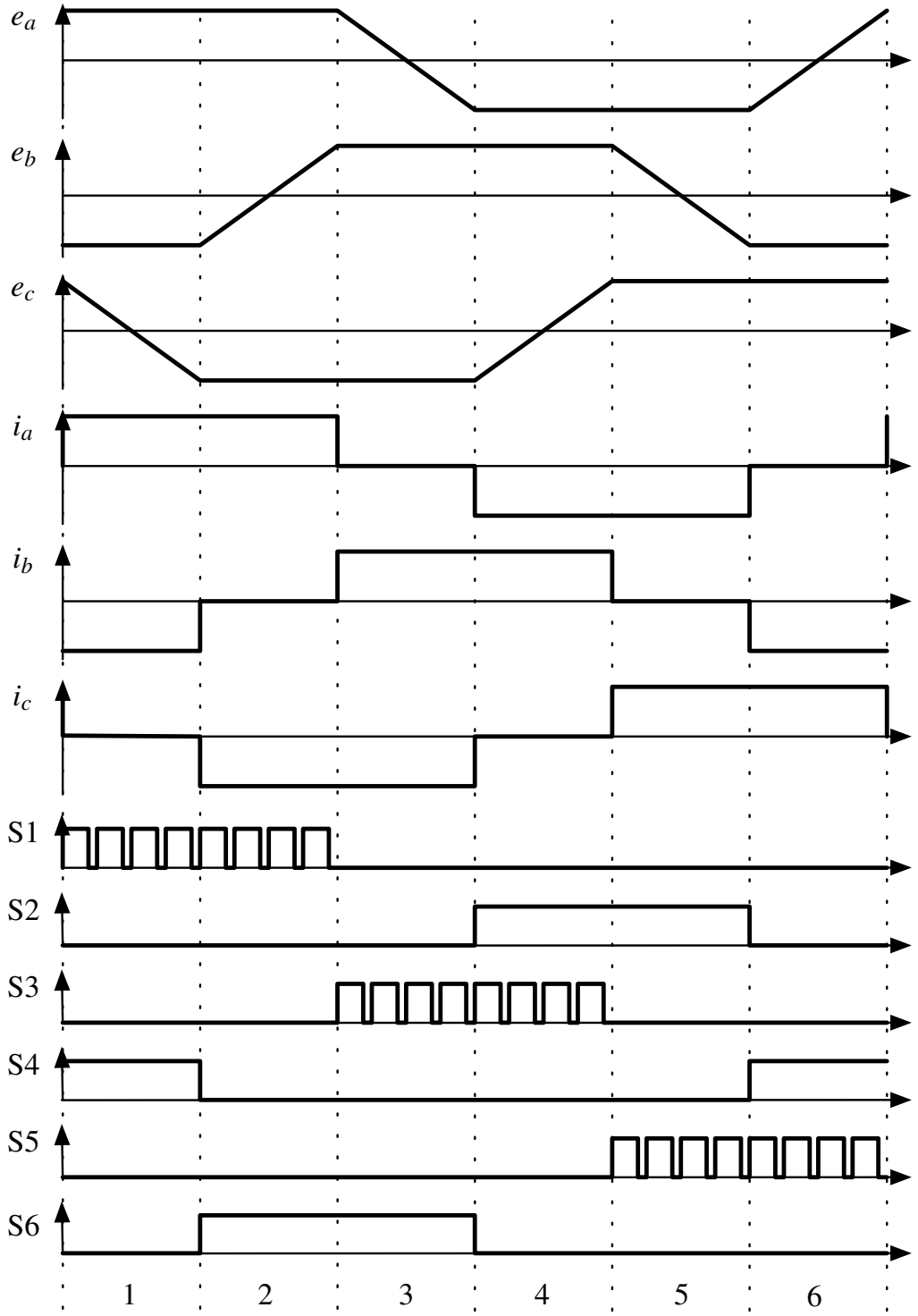

Figure 3.1: The ideal motor back EMF, phase currents and inverter switching pattern for six step commutation under BLDC-120 control.

resulting phase currents do not show the characteristic rectangular waveforms of BLDC-120 control, as shown in Figure 4.26.

Figure 3.2 shows a possible control system for BLDC control [96]. The motor phase currents are measured and the maximum phase current is compared to a demand value. The demand current is proportional to the required motor torque. The current error is input to a Proportional-Integral (PI) controller which adjusts the duty cycle of the PWM signals applied to the inverter. The motor position is needed to determine which inverter phases to switch. A low resolution position sensor can be used as the controller only needs the motor position in 60°E steps. The position sensor output for a BLDC-180 controller must be offset from that of a BLDC-120 controller by 30°E as the conduction period starts 30°E earlier and ends 30°E later. Positions sensing techniques will be discussed further at the end of this chapter.

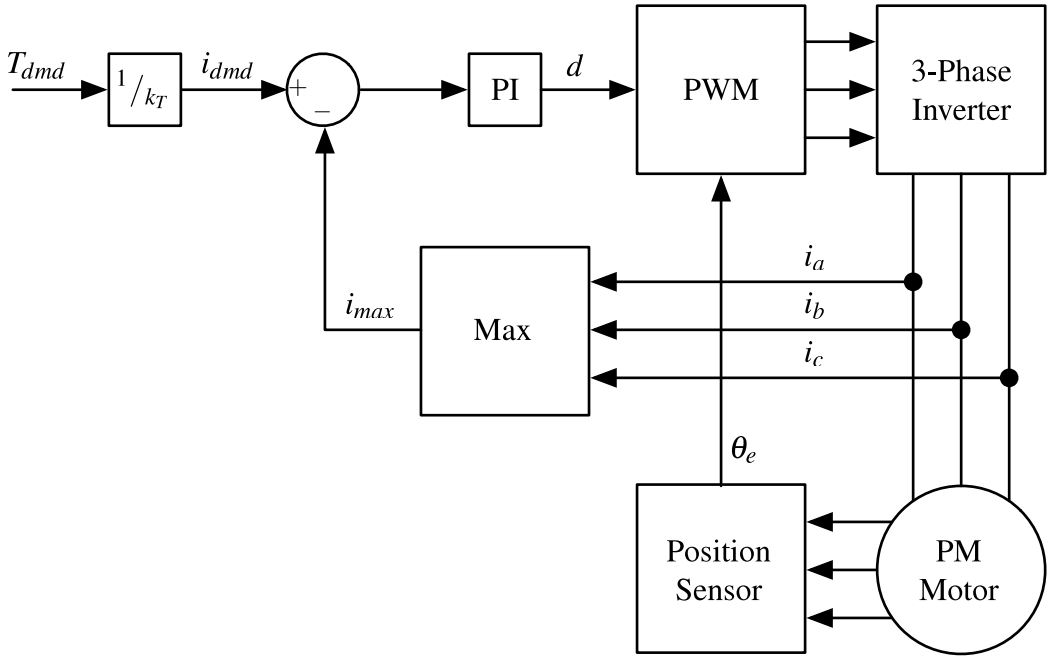

Figure 3.2: A closed loop current control system for six-step commutation control.

3.3 Brushless AC Control

Permanent magnet synchronous motors with a sinusoidal back EMF are usually driven with sinusoidal phase currents [35]. Field Oriented Control (FOC) makes use of mathematical transforms to separate the torque and magnetic field components of the phase currents [97], as shown in Figure 3.3. The three phase currents are measured and transformed into an orthogonal two phase stationary reference frame using the Clarke transform given in Equation 3.2.

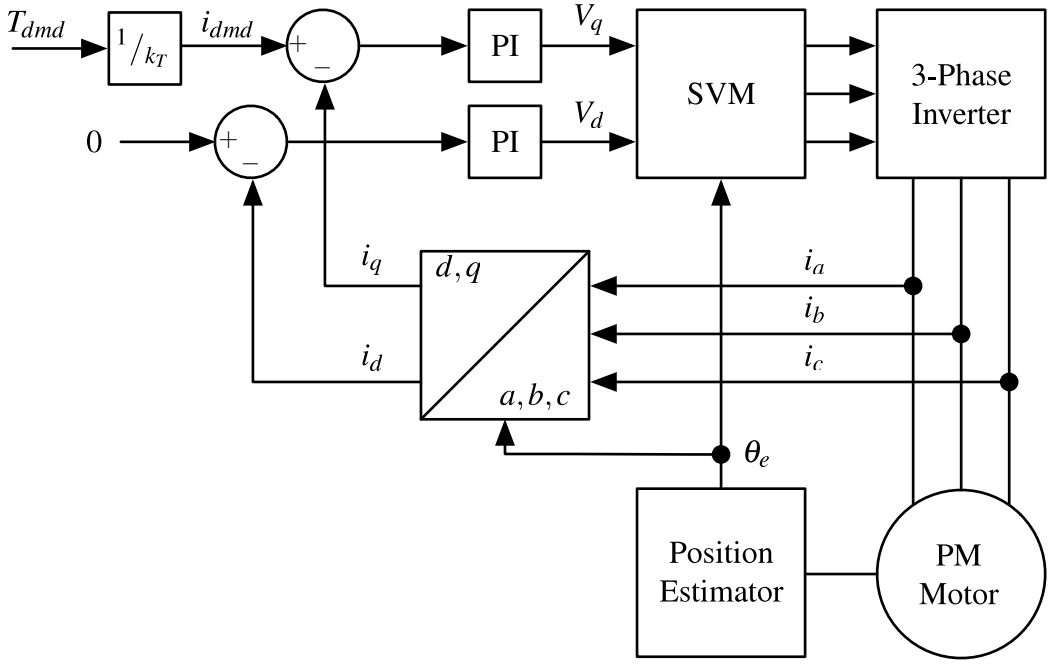

Figure 3.3: A field oriented control system for a permanent magnet synchronous motor [5].

$$\begin{bmatrix} i_\alpha \\ i_\beta \end{bmatrix} = \begin{bmatrix} 1 & 0 & 0 \\ 0 & \frac{1}{\sqrt{3}} & -\frac{1}{\sqrt{3}} \end{bmatrix} \begin{bmatrix} i_a \\ i_b \\ i_c \end{bmatrix} \tag{3.2}$$

$$\begin{bmatrix} i_d \\ i_q \end{bmatrix} = \begin{bmatrix} \cos(\omega t) & \sin(\omega t) \\ -\sin(\omega t) & \cos(\omega t) \end{bmatrix} \begin{bmatrix} i_\alpha \\ i_\beta \end{bmatrix} \tag{3.3}$$

A Park transform is then applied to change the phase currents to a rotating reference

frame fixed to the rotor given by Equation 3.3. This second transform changes the motor currents into two DC components; a direct component proportional to the motor field strength, and a quadrature component proportional to the motor torque. These two components can be controlled by separate PI controllers to produce direct and quadrature voltage components. These voltage components are then transformed back to the stationary reference frame to determine the required voltage waveforms to control the motor currents. Unlike with six-step commutation, the rotor position must be known accurately for field oriented control in order to produce highly sinusoidal phase currents [98].

Space Vector Modulation (SVM) is a technique for calculating the PWM duty cycles used to produce sinusoidal inverter output voltages. The switches in each leg of the three phase inverter are always switched with complementary PWM signals. This gives eight possible switching vectors, six with non-zero voltages and two with zero voltages. The vectors can be plotted on the two dimensional α,β-plane as shown in Figure 3.4.

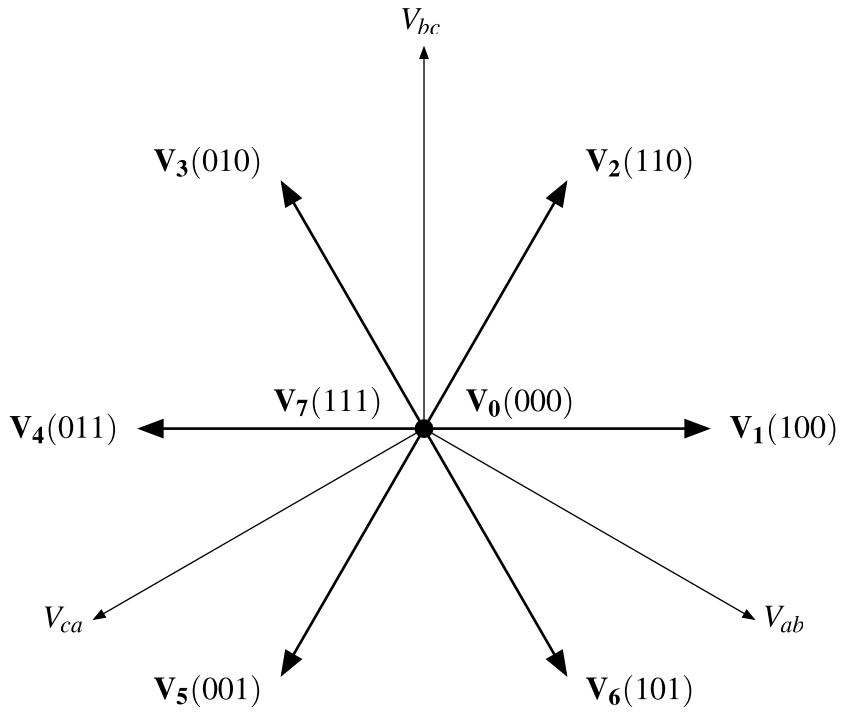

Figure 3.4: The eight Space Vector Modulation voltage vectors shown in the α,β-plane.

The space vector modulation technique attempts to create the desired reference voltage

vector (calculated by the field oriented controller) at the inverter output. For a fixed amplitude sinusoidal voltage output, the reference voltage will trace out a circle on the α,β-plane. As it does so it will pass through six space vector sectors bounded by the six non-zero voltage vectors, as shown in Figures 3.5. In each sector, the reference voltage can be produced by modulating between the two bounding non-zero voltage vectors and one or both of the zero voltage vectors. A detailed explanation for the production of a reference voltage from the eight space vectors can be found in [99].

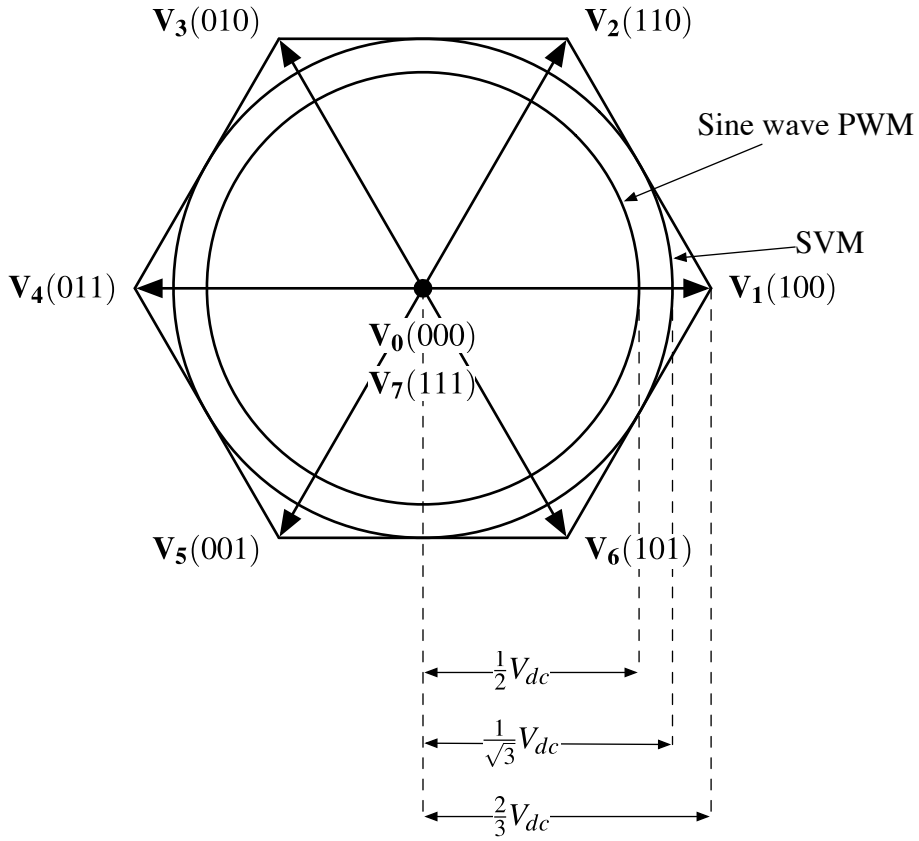

Figure 3.5: Comparison of achievable phase voltage circles for sine wave PWM and space vector PWM.

The use of space vector modulation results in a non-sinusoidal PMW duty being applied to each inverter phase, as shown in Figure 3.6. However, the resulting line-to-line voltages are sinusoidal. Furthermore, the unusual PWM duty waveform applied to each inverter phase provides a 15.5% improvement in the DC link voltage utilisation over conventional sine wave PWM [100] as shown in Figure 3.5. SVM allows the amplitude of the line-to-

line inverter voltage to reach the DC link voltage (a phase voltage of $V_{dc}/\sqrt{3}$), whereas sine wave modulation can only achieve a maximum phase voltage of $V_{dc}/2$. This improvement in DC link voltage utilisation will allow the motor to run to a higher speed before field weakening is needed, reducing the system losses associated with field weakening.

It is possible to further increase the voltage applied to the motor by over modulating the space vector PWM. However, this introduces harmonics into the voltage output and hence the motor phase currents [101]. As a consequence of the increased harmonic content of the motor phase currents, the motor losses could also be increased.

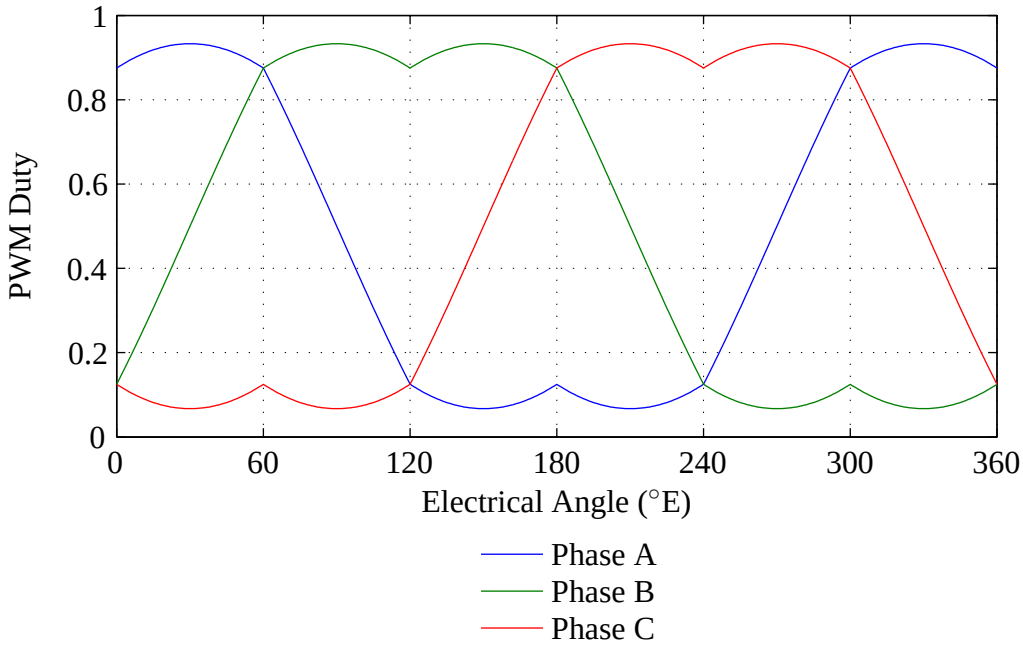

Figure 3.6: Phase PWM duty cycle waveforms for space vector modulation.

3.4 A Comparison of Motor Performance Under BLDC and BLAC Control

Permanent magnet synchronous motors with sinusoidal back EMFs are usually operated with BLAC control, and motors with trapezoidal back EMFs are usually operated with BLDC control in order to minimise the output torque ripple and maximise the torque

density [35]. However, it is possible to operate sinusoidal and trapezoidal back EMF machines under either BLDC or BLAC control, as shown in [40, 102].

The application of BLDC and BLAC control to motors with an internal permanent magnet rotor and a sinusoidal back EMF is compared in [40] and [35]. It is shown that the highest torque per RMS current is achieved using BLAC control below base speed and BLDC-180 in the field-weakening region (field weakening is discussed further in Chapter 4). Changing between the control modes to maximise torque is suggested, but the effect on the system efficiency is not examined.

A finite element analysis of radial flux PMSMs is performed in [103] under both BLAC and BLDC-120 control to analyse the effect on mechanical vibration. It is shown that the high order vibration is higher under BLDC control than BLAC control. Again, the change in efficiency is not considered.

The rotor eddy current losses for a PMSM under BLAC and BLDC-120 control is compared in [104]. It is shown that BLAC control gives the lowest eddy current losses, while the losses under BLDC-120 control can be minimised with a phase advance angle of 20°E for the motor under test. The paper does not consider the losses in the motor stator or in the inverter.

The performance of PMSMs with non-sinusoidal back EMFs under BLDC-120, BLAC and non-sinusoidal harmonic injection (NSHI) control is examined in [105]. Resistive and iron losses are shown to be generally lower for BLAC than BLDC-120 control over a limited number of speed and torque operating points. It is inferred that the inverter losses should also be lower for BLAC control, but this is not quantified.

A high level analytical comparison of BLAC and BLDC-120 control of sinusoidal and trapezoidal back EMF motors is made in [106]. A theoretical 33 % higher power rating is shown to be possible for BLDC-120 control of a machine with trapezoidal back EMF than for BLAC control of a sinusoidal back EMF machine, using an inverter of given current and voltage rating. However, the analysis assumes ideal phase current waveforms and does

not take into account the current ripple associated with BLDC control of real motors.

The effect of the motor control mode on the torque performance of PMSMs has been widely discussed in the literature [35, 40, 102, 106]. However, it is apparent that further investigations into the losses resulting from the motor control mode used, are needed to devise an improved control strategy and improve the efficiency of the system as a whole. The remaining chapters of this thesis will further compare the performance of PMSMs under BLDC and BLAC control with particular attention to the resulting losses in the motor and inverter.

3.5 Position Sensing Techniques

All of the control techniques described above require knowledge of the motor position. This section compares some common position sensing techniques and proposes an alternative method.

3.5.1 Low Resolution Position Sensors

Low resolution position sensing techniques typically use an array of sensors with a binary output to determine the rotor angle. For BLDC control of three-phase machines, three sensors are usually arranged with a spacing of either 60°E or 120°E. This provides an output change every 60°E of rotor rotation, which is sufficient for six-step commutation [107]. The low costs associated with low resolution sensors makes them an attractive choice for applications where high accuracy position measurement is not needed [108].

For surface mounted permanent magnet machines, Hall effect sensors can be placed on the motor stator close to the rotor and detect the rotor position from the polarity of the magnetic field produced by the permanent magnets. However, the Hall effect sensors are susceptible to the magnetic field produced by the stator currents which can result in erroneous outputs [109]. An alternative configuration is to move the Hall sensors away

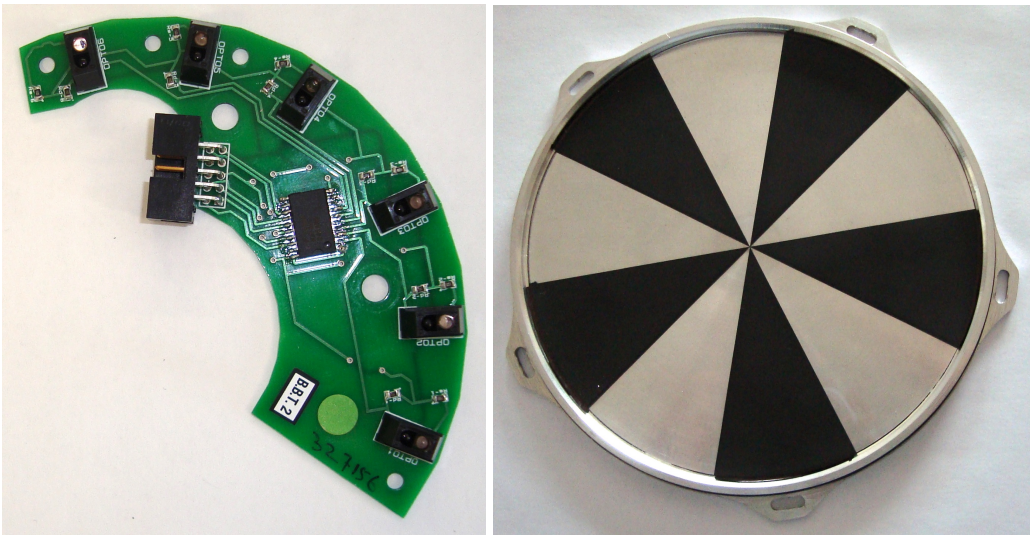

(a) Optical sensor array. (b) Optical sensor reflective pattern.

Figure 3.7: Optical position sensor components.

from the stator windings and use a separate set of permanent magnets attached to the rotor shaft to trigger the Hall sensors [52].

In [107], it is shown that inaccurate placement of the Hall effect sensors results in increased torque ripple from an unbalanced operation of the motor and inverter. A signal filtering technique is proposed to mitigate the effect of misplaced sensors.

Optical sensors can be used to produce a similar output to Hall switches but are less sensitive to electromagnetic interference allowing greater placement flexibility. Each sensor consists of an infra-red LED and a photo-transistor and the output state is controlled by allowing or preventing the infra-red light reaching the photo-transistor. Figure 3.7(a) shows an array of optical sensors used for a vehicle wheel motor and is attached to the stator assembly. Figure 3.7(b) shows the corresponding sensor pattern which is attached to the rotor assembly. The rotor pattern is divided into reflective and non-reflective sections with an equal span to the permanent magnet arcs.

3.5.2 High Resolution Position Sensors

Absolute encoders typically use an array of optical sensors to produce a digital position measurement and can offer resolutions in excess of 4096 pulses per mechanical revolution [110]. Absolute encoders can provide the required position resolution for BLAC control, but they are too expensive and not robust enough for automotive applications [43].

Electrical resolvers are rotating electrical transformers which produce a modulated sine and cosine of the rotor angle [111], as shown in Figure 3.8. The sin and cosine signals are demodulated and converted to a digital angle for use by the motor controller, either in hardware or software. Resolvers offer a robust and accurate position measurement suitable for use in PMSMs [112].

The use of a software based resolver to digital conversion is proposed in [111] and [112] as an alternative to expensive hardware based solutions. However, software implementations require the use of high sampling rate analogue to digital converters on the motor controller processor with additional processing to perform the conversion.

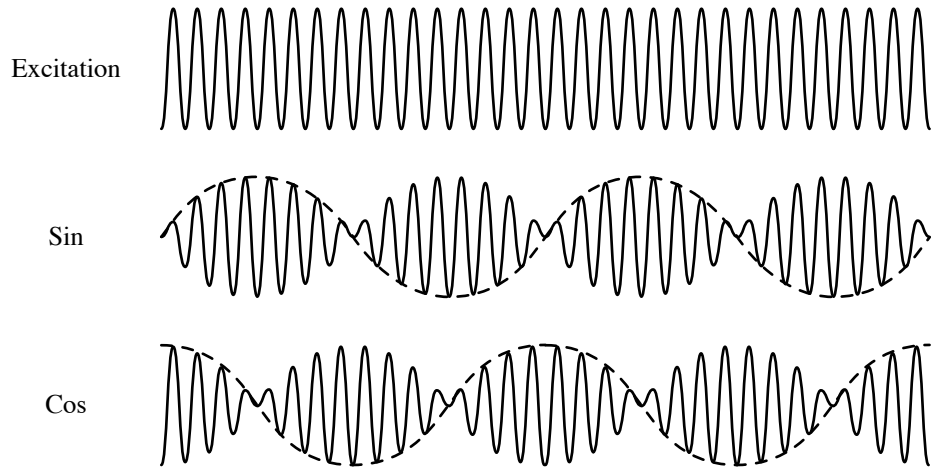

Figure 3.8: Resolver excitation input signal and modulated output signals.

3.5.3 Sensorless Control

Sensorless control techniques estimate the rotor position without the use of a dedicated position sensor. Instead, motor parameters from other sensors, such as stator voltages or phase currents, are used to deduce to position [113].

Sensorless techniques suffer from poor starting and low speed performance, and sensitivity to variation of motor parameters [108]. If the estimated rotor position is incorrect, the motor phase currents will not be correctly aligned with the motor back EMF to produce maximum torque. A misalignment of 30°E would reduce the output torque by 13%, as shown in Figure 3.9. A position sensor misalignment of more than 90°E would result in the motor torque direction being reversed.

In many applications, it may be possible for the motor to operate with a reduced torque output or even rotate in the wrong direction initially. However, this is not possible for direct drive vehicle motors where full motor torque must be available from start-up [114]. Therefore, sensorless control will not be considered further in this thesis.

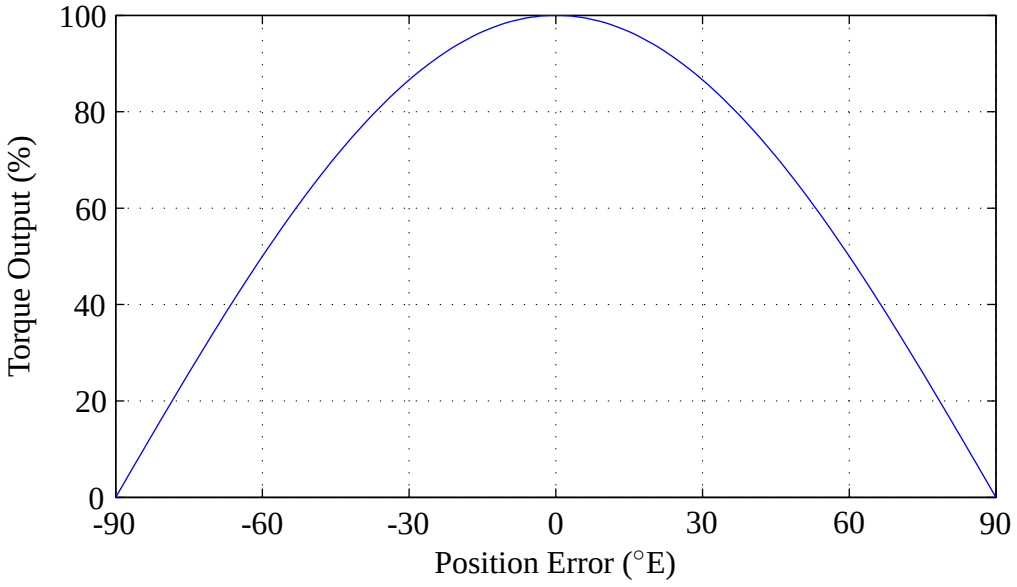

Figure 3.9: Available torque as a proportion of the maximum torque for position sensor misalignment.

3.5.4 Position Sensing for the YASA Motor

For the purpose of comparing different motor control strategies, including BLAC control, the position sensing technique used for the experimental work in this thesis must provide a sufficient resolution position output for the control strategies being considered. However, the brushless YASA motor under test is only fitted with three optical position sensors which provide a 60°E resolution on the rotor position. The construction of the motor means it is not feasible to add a higher resolution position sensor to the motor without alterations to the mechanical design. Therefore, a method of producing a high resolution position measurement using the available low resolution position sensors is needed. In [43, 108, 115–118], the use of low cost, low resolution sensors (such as Hall sensors) combined with software based extrapolation techniques is suggested as an alternative to high resolution position sensors. The methods described provide better starting and low speed control than with sensorless techniques [43].

The method in [108] uses the low resolution sensor outputs to give the true position at the six points during the electrical cycle at the instant when the sensor output changes. The position error is therefore reset every 60°E as is the case in [43]. At points in between, the motor speed and time since the position sensor output last changed is used to estimate the change in angle. The motor speed is determined from the time taken to complete an electrical cycle. However, when the motor is first started, its position is not known with sufficient accuracy to be correctly operated in BLAC mode. The method in [108] also compensates for the change in Hall sensor output transition angle as a result of the armature reaction at high loads and can estimate the rotor position to within 5.4°E of the true angle.

A Taylor series approximation for the first derivative of the motor speed is used in [115] to improve the accuracy of the angle tracking between Hall sensor output changes. A vector-tracking observer is applied to the Hall sensor outputs in [118], which models the response of the mechanical system. However, this places a dependence on knowledge of the mechanical system to which the motor is connected. It is also desirable to minimise

the complexity of any additional processing required by the motor controller to avoid overloading [119].

The use of three Hall effect sensors is suggested in [116] to determine the initial rotor position to within $\pm 30\,^{\circ}$E of the true position. The controller attempts to start the motor using space vector modulation (SVM) with the initial position estimate. However, the uncertainty in the rotor position limits the motor torque to between 86.6 % and 100 % of the maximum at start up. This is undesirable for vehicle applications as high starting torques are required [43].

The proposed new technique that will be applied to the YASA motor is shown diagrammatically in Figure 3.10. The three optical position sensors in the motor have been carefully aligned so their outputs change at precisely known rotor angles. The outputs from the position sensors ($p_{1,2,3}$) are input to a look-up table which provides the control system with an initial position measurement (θ_p) that changes in $60\,^{\circ}$E steps. Each time the estimated position changes, the motor speed (ω_p) is calculated from the time delay since the last position update.

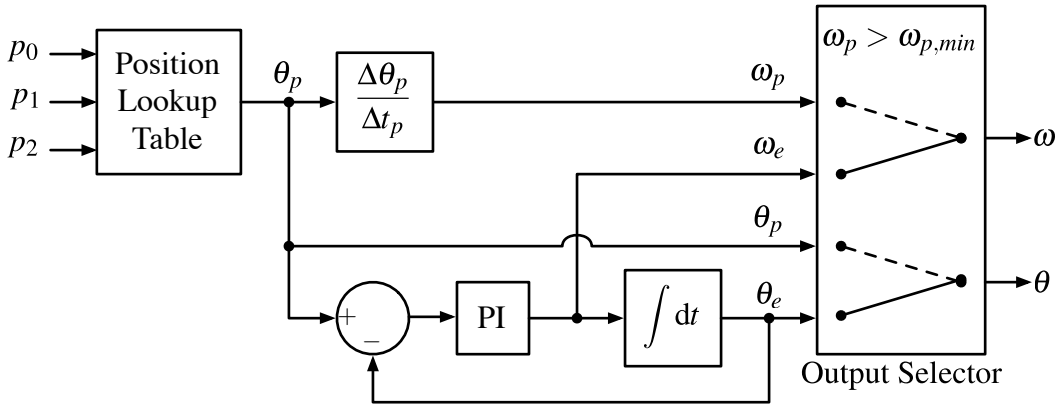

Figure 3.10: The proposed position extrapolation technique.

A PI controller is used to improve on the initial speed and position measurements. The integral of the speed output from the PI controller (ω_e) gives a second position estimate (θ_e). This estimated position is compared to the position sensor output and the error is fed back to the PI controller input. The PI controller therefore adjusts the estimated motor

speed to control the error in the estimated motor position to zero.

When starting up, the motor controller uses the output of the position sensors directly to give the true rotor position to within $\pm 30\,^{\circ}\mathrm{E}$. This allows the motor to start with at least 87 % of its maximum torque as in [116]. At speeds below 50 rpm ($\omega_{p,min}$), it is difficult to extrapolate the motor position as the position sensor output changes infrequently and the estimated position can drift from the true position. Therefore, the position sensor output is used until the motor reaches 50 rpm. Beyond this speed, the extrapolated position and speed are used. When changing from the initial position and speed estimates to the extrapolated estimates, the outputs of the PI controller and integrator blocks are reset to ω_p and θ_p respectively. This ensures no sudden changes in the values passed to the motor controller.

The PI controller is manually tuned to give acceptable position tracking. Setting the controller gains too low can result in a poor transient response and the extrapolated position drifting unacceptably from the true position. Alternatively, if the gains are set too high, the PI controller will over compensate for the position feedback error resulting in a fluctuating motor speed and position estimate.

A proportional gain of $0.1\,\mathrm{rpm}/^{\circ}\mathrm{E}$ and an integral gain of $200\,\mathrm{rpm}/^{\circ}\mathrm{E}/\mathrm{s}$ have been selected for the motor under test. Figures 3.11 and 3.12 show the simulated steady state performance of the proposed position extrapolation technique with a 10 kHz update frequency. The position estimation algorithm can be seen to track the true motor position to within $1\,^{\circ}\mathrm{E}$ of the true position.

The angle tracking algorithm also responds well to fast changes in the motor speed. Figures 3.13 and 3.14 show how the estimated motor angle and speed follow a simulated sinusoidal variation in motor speed. Even for accelerations in excess of $1200\,\mathrm{rpm}/\mathrm{s}$, the estimated position is never more than $10\,^{\circ}\mathrm{E}$ away from the true rotor position. This would result in a worst case torque output reduction of 1.5 % from the theoretical maximum. The estimated motor speed is also always within 5 rpm of the true motor speed. The UCDS vehicle drive cycle used in Chapter 6 requires a maximum vehicle wheel acceleration

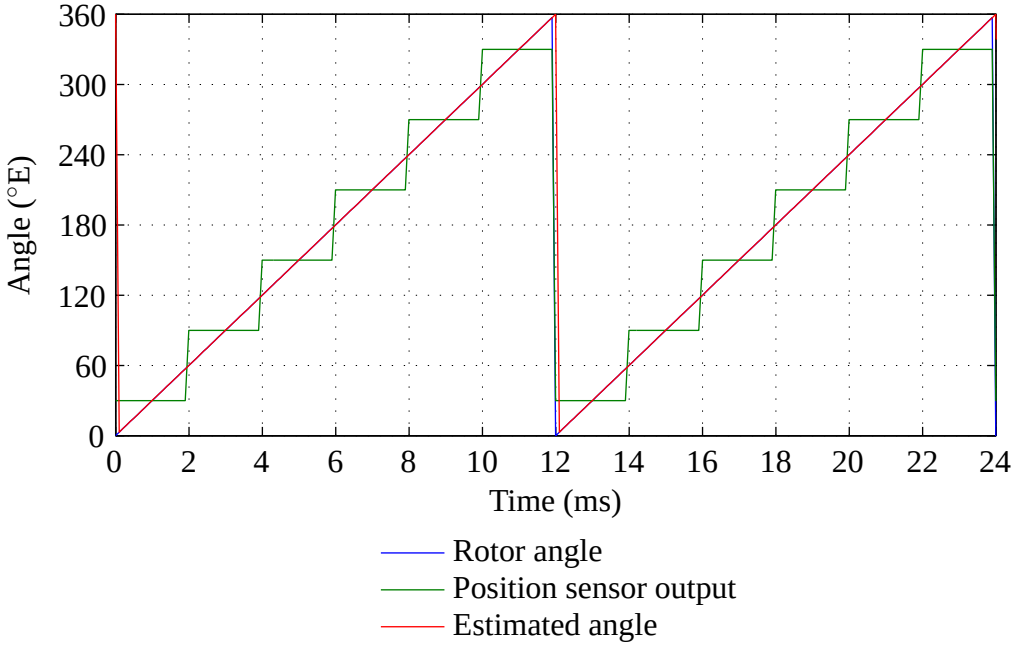

Figure 3.11: Estimated rotor angle for steady state operation at 500 rpm.

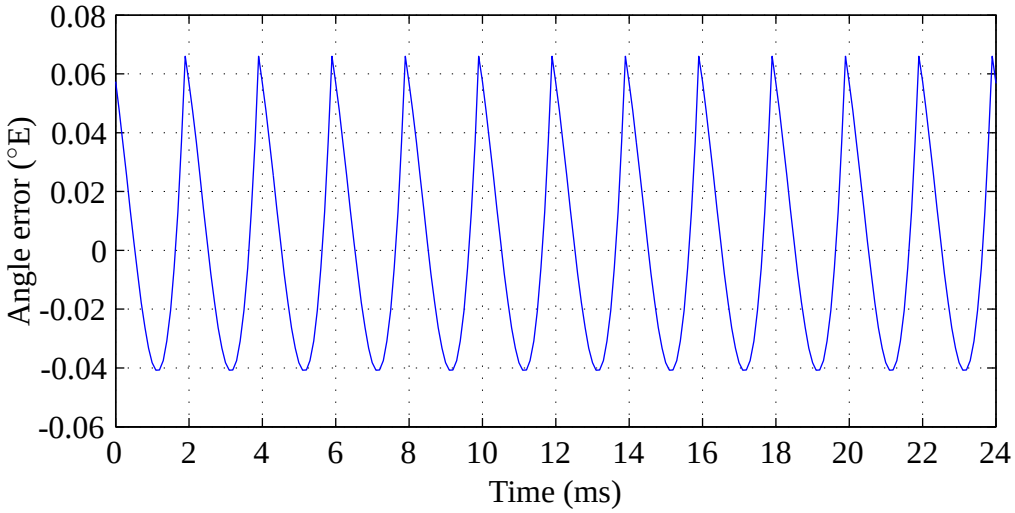

Figure 3.12: Estimated rotor angle error for steady state operation at 500 rpm.

of only 125 rpm/s for a 0.3 m rolling radius. This method will therefore give sufficient accuracy for estimating the motor position and speed for both steady state and transient operation of the YASA motor.

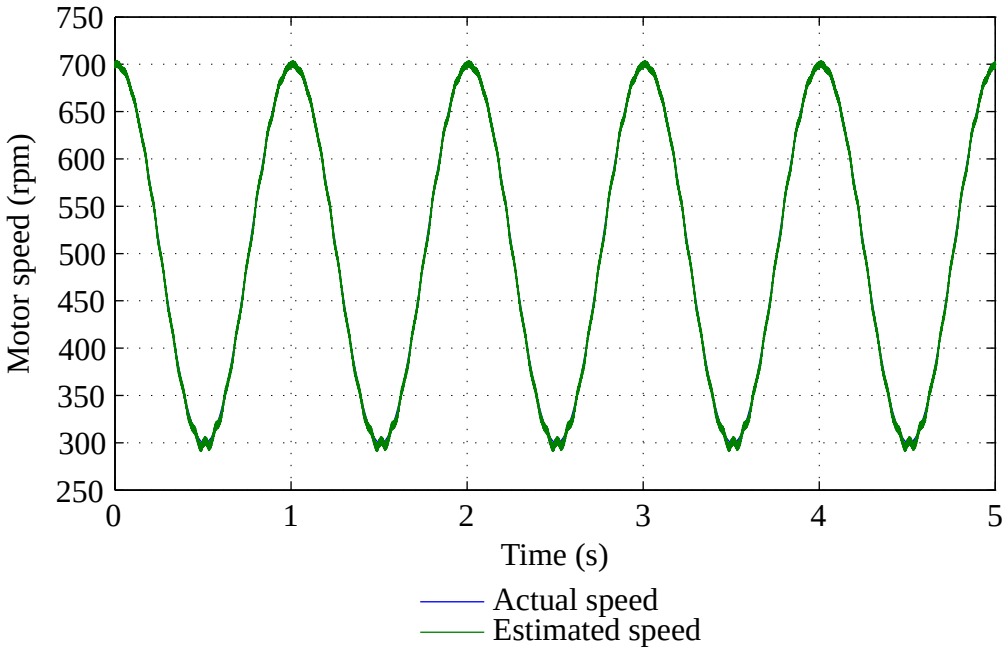

Figure 3.13: Estimated motor speed for 500 rpm average speed with a 200 rpm 1 Hz component.

3.6 Summary

This chapter has introduced the most commonly used control schemes for permanent magnet synchronous motors. An overview of six step commutation with 120°E (BLDC-120) and 180°E (BLDC-180) conduction angles was given. Field oriented control for machines with a sinusoidal back EMF (BLAC) was also examined and shown to be more computationally demanding to implement but potentially offered a smoother torque output.

A review of the literature has found evidence of the torque performance of BLDC and BLAC control modes being compared, but little comparing the resulting losses for both the motor and inverter in detail. The three control modes will therefore be examined further in the following chapters to compare their efficiency and torque output.

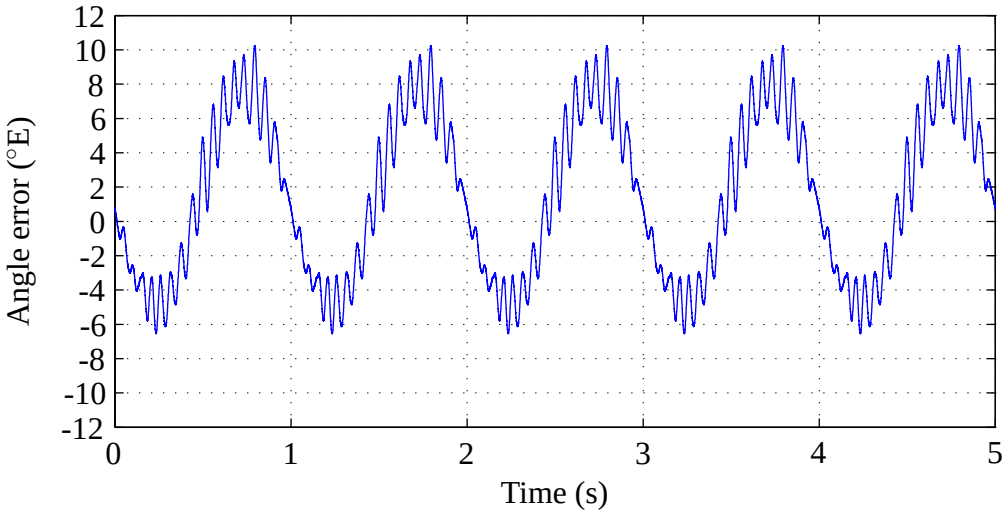

Figure 3.14: Estimated rotor angle error for 500 rpm average speed with a 200 rpm 1 Hz component.

A review of common position sensing techniques was also given. High resolution position sensors such as resolver and encoders were shown to offer the position resolution required for BLAC control but at a greater cost than low resolution sensors such as Hall-effect or optical sensors. A new method of producing a high resolution output from several low resolution sensors was presented. The proposed technique would allow a motor to be started with at worst case 87 % of the theoretical maximum torque.

4

Maximum Torque Output of PM Motors

4.1 Introduction

High torque and power density and high efficiency are key requirements of electric motors when applied to hybrid and electric vehicles [35]. To compare the efficiencies of PMSMs under BLDC and BLAC control, it is first necessary to determine the operating range that can be achieved by each control mode. This will provide the limits for the range over which the system efficiency needs to be determined. This chapter will investigate the maximum torque and power performance of each control mode. An overview of field weakening will be given to explain how the operating speed range of PMSMs can be maximised. The effect of motor characteristics on the theoretical operating range will then be explored to determine ideal characteristics of PMSM. Finally the maximum operating envelope for the example motor and inverter system will be determined for each of the three control modes.

4.2 Extending the Operating Range Through Field Weakening

To determine the maximum operating range of PMSM, it is important to understand the limits imposed by the driving inverter. Figure 4.1 shows the per phase equivalent circuit model for a permanent magnet synchronous motor which can be described by Equation 4.1 and 4.2. At motor speeds where the back EMF (e) is much smaller than the DC link voltage, the phase voltage (V) applied to the motor can be set to an amplitude which controls the phase current (I) to the level that provides the rated torque output. The phase currents can also be controlled to be in-phase with the phase back EMFs to maximise the motor torque output per unit current. As the motor speed increases, so must the amplitude of the applied voltage in order to maintain the same phase current in response to the increasing back EMF and increased impedance from the phase inductance (L).

$$V = I(R + j\omega L) + e \tag{4.1}$$

$$e = k\omega \tag{4.2}$$

When the amplitude of the voltage applied by the inverter reaches the limit for the available DC link voltage, the phase current can no longer be maintained at the amplitude required for rated torque while in phase with the back EMF. The motor speed at which this occurs is known as the base speed, ω_b. If the motor speed increases further with the phase currents controlled to be in phase with the back EMF, the maximum current achievable will start to decrease and the torque output will be reduced. Field weakening is a technique employed beyond the base speed that increases the available torque output relative to without field weakening.

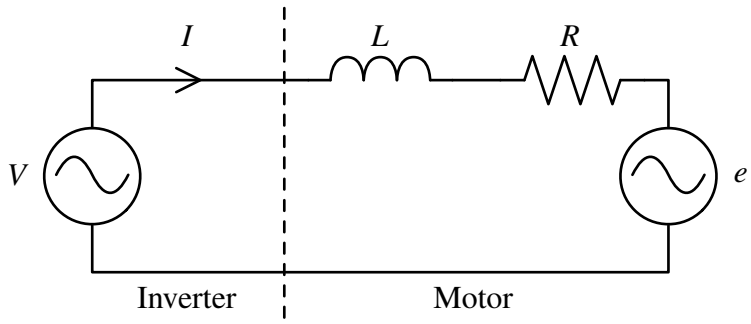

Figure 4.1: Single phase equivalent circuit model for a PMSM.

4.2.1 The Advantages of Field Weakening

Extended Speed Range

Field weakening allows the inverter voltage limitation to be overcome by using some of the inverter's available current to oppose the rotor magnetic field. This allows the motor to supply torque to higher speeds than without field weakening, as shown in Figure 4.2.

Field weakening results in a constant torque region for speeds less than the base speed. Once the base speed has been reached, the diversion of some of the inverter current to oppose the rotor field allows a larger current component in phase with the back EMF to be produced and a higher torque output as a result. Beyond base speed, the power output of the motor is nominally constant.

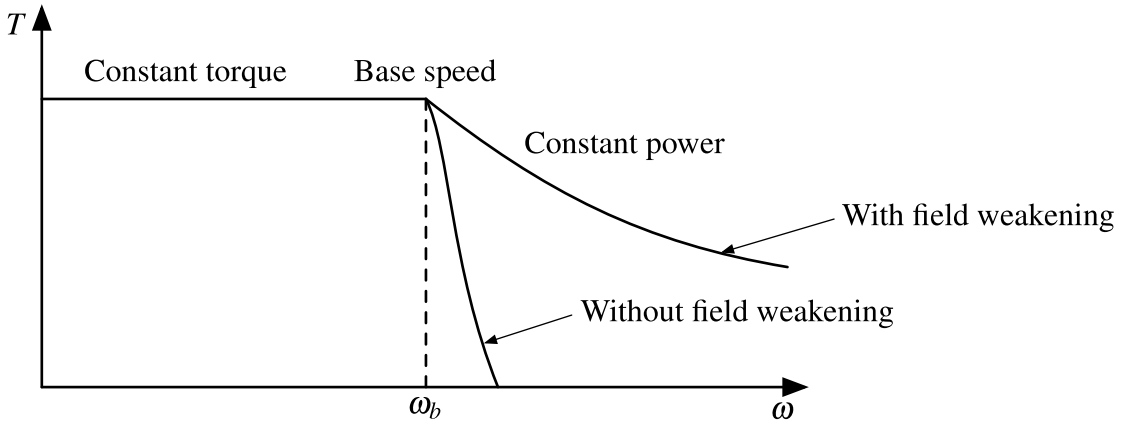

Figure 4.2: Maximum motor torque output with and without field weakening.

Reduced Inverter Requirements

It is possible to design a motor and inverter to operate entirely within the constant torque region for a particular application. However, this may result in the inverter being over sized for the vehicle power requirements. For example, if a system is designed to operate without field weakening, the motor must be wound to give a back EMF which is lower than the maximum inverter output voltage across the required speed range. Consequently, the motor would be capable of producing full torque across the entire speed range and would achieve maximum power at top speed. The inverter must be capable of supplying enough current to achieve the required low speed torque. However, unless the vehicle power supply is capable of producing sufficient power, the theoretical peak motor power operating point would never be reached.

Conversely, if the system has been designed to allow for field weakening, the motor can be wound to give a higher back EMF constant as the back EMF can be overcome at high speeds. Furthermore, a lower phase current amplitude will be required to give the same torque output at low speeds. This allows the size of the inverter to be reduced as the power electronics size generally increases with the current carrying capability. This also allows the cost and weight of the system to be reduced. The motor can be designed so the motor power available in the constant power region matches the power available from the power supply. This will maximise the power supply utilisation and minimise the inverter requirements.

Simplified Vehicle Drivetrains

An alternative to the use of field weakening to extend the motor speed range in vehicles, is the use of multi-speed gearboxes. By changing the ratio of the gearing between the motor and the wheels, the maximum wheel speed can be increased, albeit with a lower maximum torque at the higher speeds.

The use of a gearbox will introduce additional mechanical losses to the system.

However, the improvement in motor and inverter efficiency without field weakening would also need to be considered (as discussed in the following section). The use of a multi-speed gearbox would introduce an interruption in the torque provided to the wheels of the vehicle while gear changes take place. Furthermore, additional cost, complexity and weight can be avoided if field weakening is utilised instead of multi-speed gearboxes. For these reasons, the use of multi-speed gearboxes will not be considered further.

4.2.2 The Disadvantages of Field Weakening

Reduced High Speed Torque Output and System Efficiency

The torque produced by a permanent magnet motor is given by Equation 4.3 and the voltages applied to the motor by Equations 4.4 and 4.5 where k is the motor back EMF constant and n_{pp} is the number of pole pairs [120]. When operating above the base speed, a field weakening current (negative i_d) is required to keep the applied voltage within the voltage limits of the inverter, as shown in Figure 4.3.

$$T = \frac{3}{2} n_{pp}(k i_q + (L_d - L_q) i_d i_q) \tag{4.3}$$

$$V_d = R i_d + \frac{d}{dt}(L_d i_d + k) - \omega L_q i_q \tag{4.4}$$

$$V_q = R i_q + \frac{d}{dt}(L_q i_q) + \omega L_d i_d + k\omega \tag{4.5}$$

For surface mounted permanent magnet motors, the difference between direct and quadrature axis inductances is negligible so the direct current, i_d, has no influence over the motor torque output. However, the limited inverter current means that direct current component required for field weakening will detract from the available quadrature current and reduce the maximum motor torque output beyond the base speed. The current available

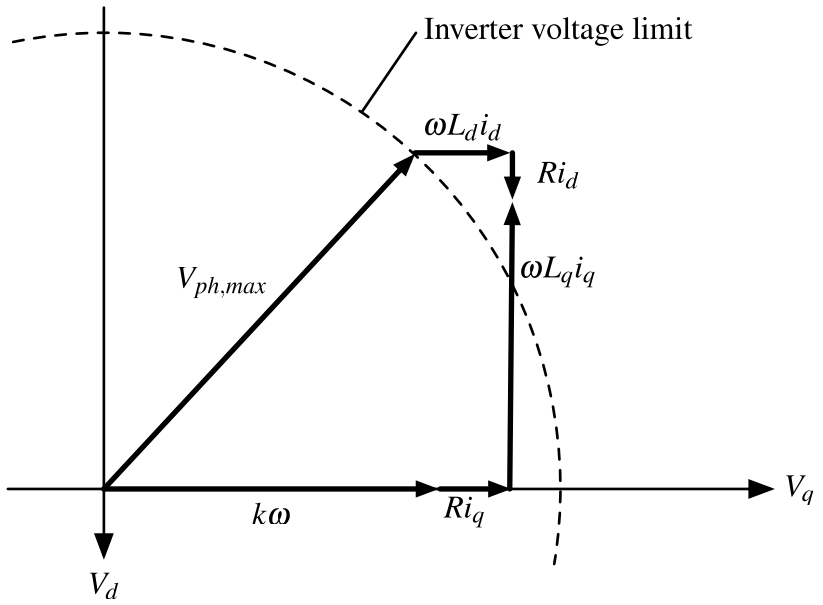

Figure 4.3: Voltage vectors for field weakening operation.

for torque production is given by the following equation where $I_{ph,max}$ is the maximum phase current available from the inverter:

$$i_q = \pm\sqrt{I_{ph,max}^2 - i_d^2} \tag{4.6}$$

The direct current results in the generation of losses in both the motor and inverter, even if not contributing to the torque output in SMPMSMs. As a result, the system efficiency will be reduced relative to if a higher supply voltage was available and a field weakening current was not required. The higher the required motor speed beyond the base speed, the greater the field weakening current required and the greater the reduction in the torque output and the system efficiency.

For interior permanent magnet motors or for designs which feature some rotor saliency, the direct and quadrature inductance will be different. This results in some reluctance torque being produced from the direct current. Furthermore, the higher direct axis inductance means less field weakening current is required to stay within the inverter voltage limitation. However, the system losses will still increase as a result of field weakening

operation.

In addition to reducing the system efficiency, the use of field weakening could also impact on the vehicle level efficiency. The reduced torque output beyond base speed affects braking (generating) torques in addition to motoring torques as the quadrature current is still limited by Equation 4.6. The reduced braking torques available from a field weakened system (compared to a system capable of delivering full torque across the speed range) could result in a reduced energy recovery during regenerative braking. If the motor is not able to produce all of the braking torque required to decelerate a vehicle, mechanical braking will be required to produce the shortfall in torque and energy will be lost.

Potentially Dangerous Failure Modes

Another disadvantage is the potential safety implications of operating far beyond the base speed of the system. Through field weakening, it is possible to drive a motor to speeds where the line-to-line back EMF is in excess of the DC link voltage. Under these circumstances, if a fault condition resulted in the inverter being disabled, the high back EMF would cause an unregulated current to flow through the free-wheeling diodes of the inverter back into the power source. The current could exceed the system ratings causing permanent damage to the motor or inverter. However, a potentially more serious consequence for vehicle applications would be the resulting uncontrolled braking torque produced by the motor.

To ensure the inverter is fail safe, the vehicle could be designed such that the no-load DC link voltage (V_{dc0}) is greater than the motor line-to-line back EMF at the top vehicle speed (ω_{max}), as given by Equation 4.7. Therefore, if the inverter is disabled the DC link voltage will rise up to the no load voltage and no current will flow through the inverter, allowing the motor to freewheel.

$$V_{dc0} \geq \sqrt{3} k \omega_{max} \tag{4.7}$$

For the purposes of comparing the performance of control strategies over the full theoretical operating range, this constraint will not be used. However, this failure mode would need to be taken into account on real vehicles. One possible prevention method would be to use contactors between the power supply and inverter, which could be opened under fault conditions to prevent current flow [121].

Potential Demagnetisation of the Permanent Magnets

The permanent magnets in a PMSM can become partially demagnetised if a sufficiently large field weakening current is applied to the motor [35]. This would result in a lower motor torque output for a given phase current because of the reduced permanent magnet field. The motor efficiency would also decrease as higher phase currents would be needed to achieve a given torque following a partial demagnetisation. As the magnet temperature increases, the amount of field weakening required to cause demagnetisation is reduced [122]. Therefore, it must be ensured that the motor is capable of withstanding the field weakening currents required to achieve the desired extended speed range at the maximum operating temperature [35].

4.2.3 Comparison of System Performances

To further explore the advantages of field weakening, the following example is given where possible design variations of the 500 N m YASA motor are compared. Starting with the characteristics of the real motor given in Table 4.1, the number of stator winding coil turns will be varied to change the motor parameters without changing the geometry of any of the magnetic components. The following approximations will be made to estimate the effect of the number of turns on each motor parameter where n is the number of turns:

$$L_{ph} = L_{ph,0} \left(\frac{n}{n_0} \right)^2 \tag{4.8}$$

Table 4.1: Example motor characteristics used in a performance comparison for different numbers of winding turns.

Characteristic	Symbol	Real Machine	Design 1	Design 2
Maximum phase voltage	$V_{ph,max}$	230.9 V	230.9 V	230.9 V
Number of turns per coil	n	45	38	83
Maximum phase current	$I_{ph,max}$	300.0 A	355.3 A	162.7 A
Phase inductance	L_{ph}	231.0 µH	164.7 µH	785.9 µH
Back EMF constant	k	0.1103 V s	0.0931 V s	0.2034 V s
Base speed	ω_b	1693 rpm	2005 rpm	918 rpm

$$R_{ph} = R_{ph,0}\left(\frac{n}{n_0}\right)^2 \tag{4.9}$$

$$k = k_0\left(\frac{n}{n_0}\right) \tag{4.10}$$

$$I_{ph,max} = I_{ph,max,0}\left(\frac{n_0}{n}\right) \tag{4.11}$$

For a fixed stator slot volume, a constant winding current density and slot fill factor will be assumed to simplify the comparison and the issues of incomplete winding layers and wire shape on packing will be ignored. Therefore, the conductor cross sectional area and hence the maximum phase current are inversely proportional to the number of turns. While this approximation does not provide a perfect comparison of practical machines, it allows the general trends relating to machine parameters to be observed.

If the motor being designed is to be used in an application that requires a peak torque of 500 N m, a peak power output of 50 kW available from 1000 rpm to a top speed of 2000 rpm, and a DC link voltage of 400 V, a range of winding turn numbers are possible. Table 4.1 describes two possible designs that meet the design criteria. Design 1 has the highest number of turns possible that allows full torque to be achieved to the top speed without using field weakening. Any more turns would reduce the base speed to less than

the required maximum speed, and any fewer turns would increase the current requirement per unit torque unnecessarily. Design 2 has the highest number of turns possible that meets the power requirement and makes use of field weakening. Any more turns would cause the power output at 2000 rpm to fall below 50 kW and any fewer turns would again increase the current requirement per unit torque unnecessarily. The two designs therefore meet the design criteria, one with and one without field weakening, while minimising the inverter current requirement.

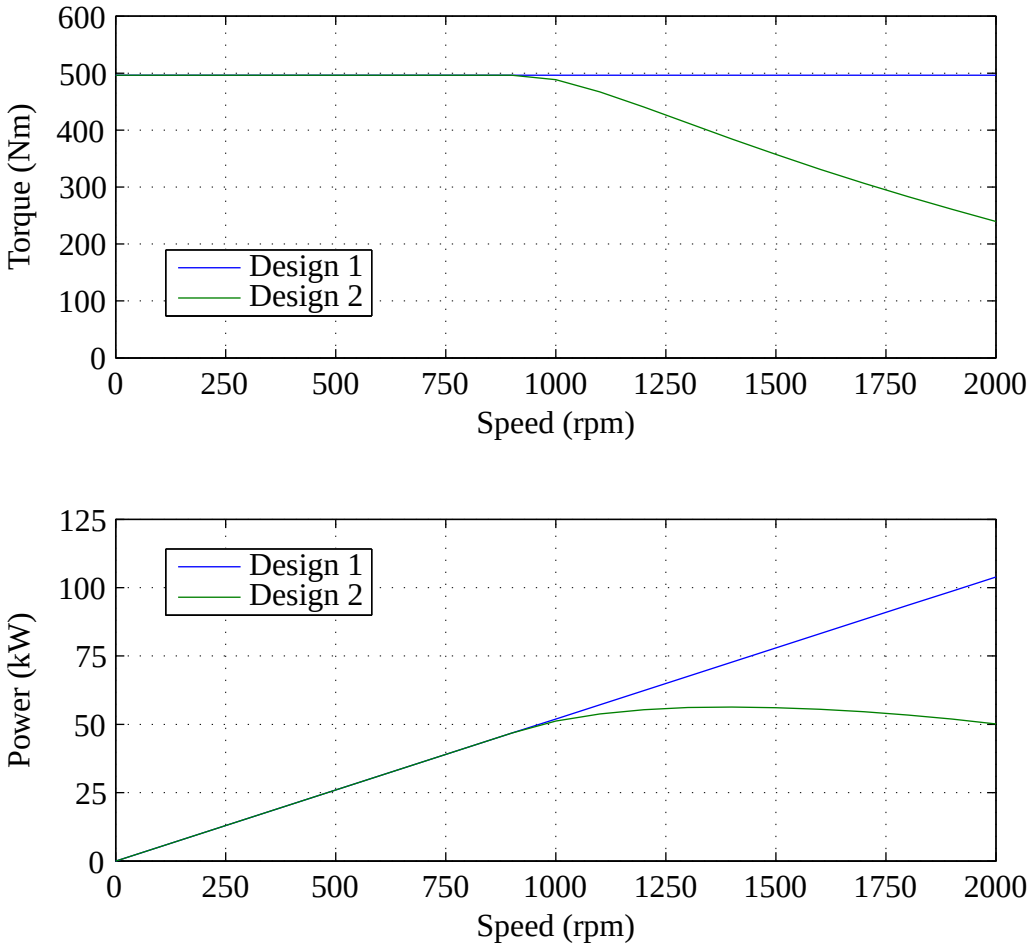

Figure 4.4: Motor torque and power output for two example machine designs with different winding configurations.

While both designs meet the design requirements of the application, they offer quite different performance, as shown in Figure 4.4 for BLAC control. The torque curves have been determined using the analytical equations derived in the following sections of this

chapter. Below the base speed for the second design (918 rpm), the efficiencies of the two machines will be identical. The reduced phase current for Design 2 will be balanced by the increased phase resistance to give the same copper losses (neglecting frequency effects) as for Design 1. The geometry of magnetic components and the number of ampere-turns is assumed to be identical from the above equations, so the iron losses will also be the same. However, beyond the base speed for Design 2, the required field weakening currents will always give a lower efficiency for the second design compared to the first for a given speed and torque as a result of the field weakening current required.

Despite the lower efficiency given by Design 2, it has the advantage of a 54 % reduction in the required maximum phase current. This would allow the size, weight and cost of the inverter to be reduced, all of which are major considerations for automotive applications.

4.3 Methods of Achieving an Extended Speed Range

In order to achieve an extended speed range for any of the control modes, it is necessary to produce a field weakening current. This current opposes the back EMF allowing higher motor speeds to be achieved within the inverter voltage limit. The following section explains how field weakening is achieved for the BLDC and BLAC control modes.

Below the base speed, the inverter voltage is adjusted to keep the motor phase currents in phase with the back EMF to maximise the motor torque output and efficiency. All of the current is along the quadrature axis. Beyond the base speed, the phase currents must be advanced with respect to the back EMF. This introduces a field weakening direct current component.

4.3.1 Commutation Advance

For the BLDC control modes, the direct axis current is achieved by advancing the commutation point [102] beyond base speed to shift the phase currents, as shown in

Figure 4.5. In its simplest form, the optimal phase advance angle θ_a which maximises the available torque can be determined from a look-up table as a function of motor speed and torque demand. The greater the motor speed and torque demand, the larger the advance angle needed to achieve the demand.

Alternatively, the phase advance angle can be adjusted by a PI controller. Once the inverter becomes voltage limited, a PI controller can adjust the advance angle to control the phase currents to the demanded amplitude.

4.3.2 Direct Axis Current Control

For BLAC control, the direct current can be changed simply by varying the direct current demand input to the field oriented control system. It is however, necessary to determine the amount of field weakening current required for the motor speed and quadrature current demand. Figure 4.6 shows one method of determining the required field weakening current in the extended speed range. In addition to the two current PI controllers used in the standard field oriented control system, a third PI controller is used with the phase voltage error as an input to control the direct current demand.

Below the base speed, the demanded phase voltage, V_{ph} (given by Equation 4.12), is less than the phase voltage limit, $V_{ph,max}$ and the PI controller will demand zero direct current. Once the phase voltage limit has been reached, the demanded phase voltage starts to exceed this and the PI controller will start to demand a more negative direct current until the demanded phase voltage is brought back to the voltage limit.

$$V_{ph} = \sqrt{V_d^2 + V_q^2} \tag{4.12}$$

The direct phase current is limited to a negative value between zero and the phase current limit. As the magnitude of the direct current is increased, the quadrature current must be reduced to ensure the inverter stays within the phase current limit as given by

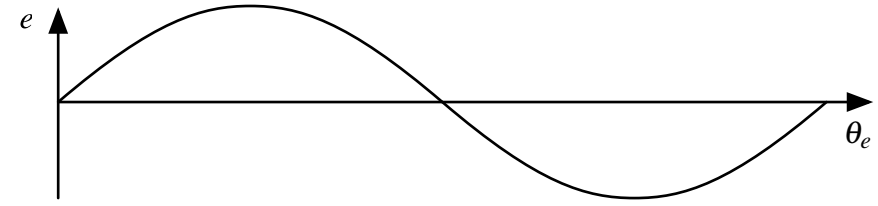

(a) Phase back EMF

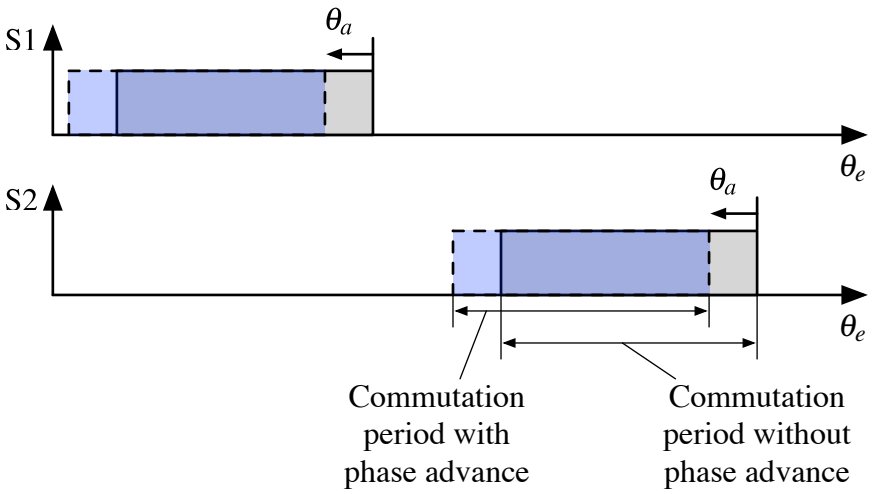

(b) BLDC-120 commutation advance

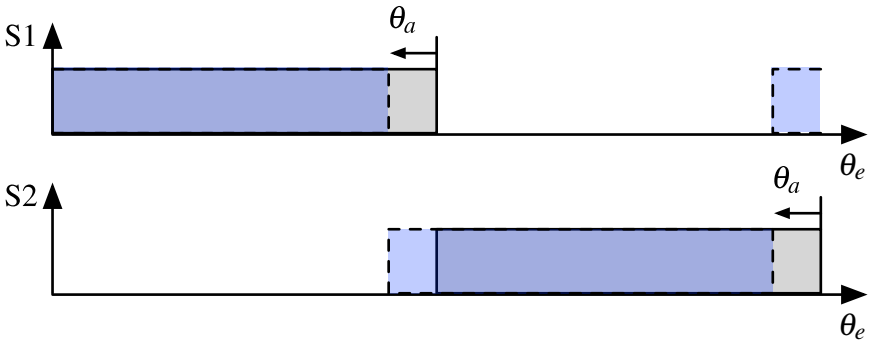

(c) BLDC-180 commutation advance

Figure 4.5: Advancing of switching signals above base speed for BLDC control modes.

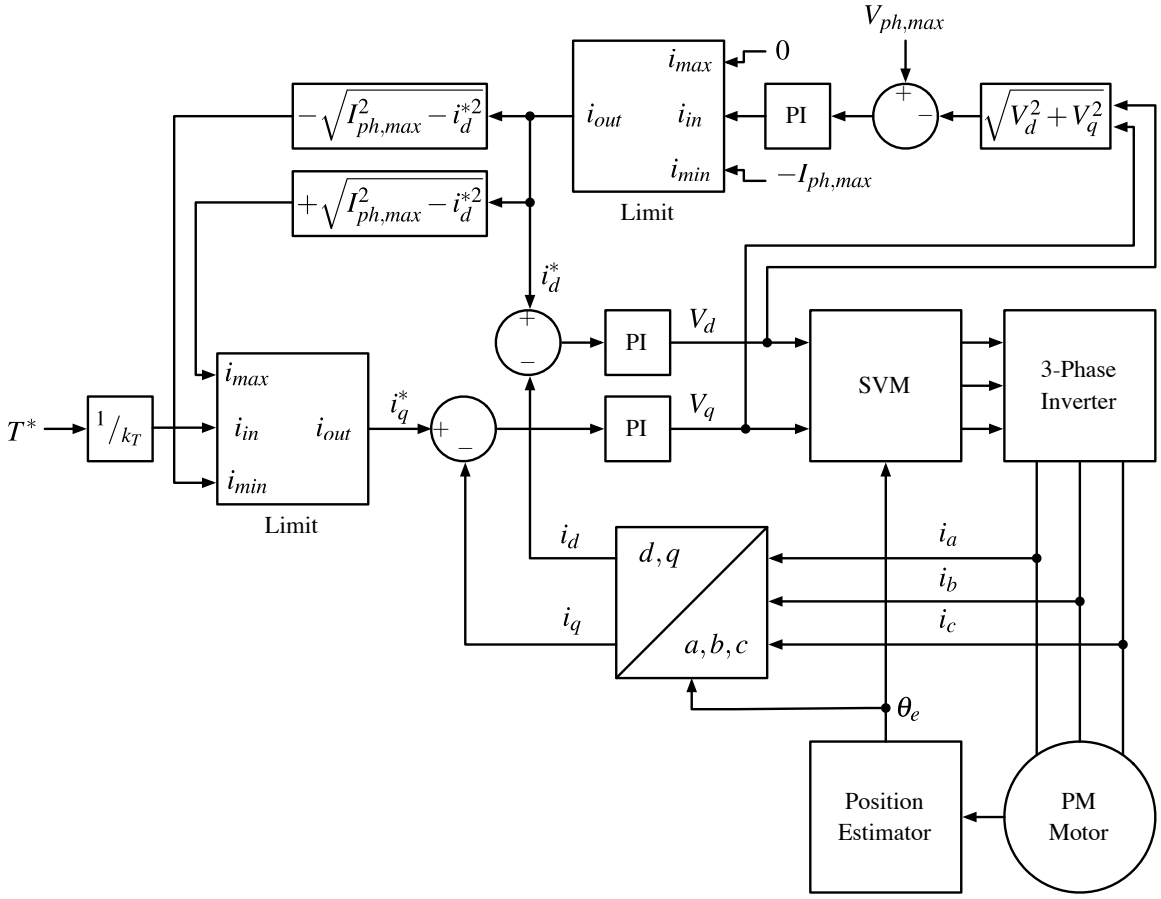

Figure 4.6: Field Oriented Control with field weakening operation.

Equation 4.6.

4.4 Analytical Prediction of Machine Performance

The electrical characteristics of a motor have a strong impact on the mechanical power and torque output, particularly when operating in the extended speed range. When designing a motor system to maximise the efficiency and torque performance, the effect of the electrical parameters must be understood. This section determines the equations that describe the performance of permanent magnet electrical machines in terms of their electrical characteristics.

With knowledge of the motor characteristics, it is possible to predict the full operating range of the motor for a given supply voltage and maximum phase current. The equations determined in this section will be used to verify the torque predicted by the simulated motor model at the end of this chapter. The analysis carried out in this section has been performed for a PMSM under BLAC control only, as the sinusoidal voltages and currents can be analysed using simple phasor diagrams unlike the more complex BLDC current waveforms. The equations derived are therefore not directly applicable to BLDC control, but the general trends observed for BLAC control are still valid.

The maximum torque curve produced by a motor, driven by an inverter with a fixed DC link voltage, can be classified into one of three forms depending on the ratios of the phase inductance, the phase back EMF constant and the maximum phase current. For the purposes of this thesis, the arbitrary decision has been made to use the phase inductance, L_{ph}, relative to $k/I_{ph,max}$ as the determining characteristic. However, a similar discussion could use k or $I_{ph,max}$ relative to the other parameters. Motors will therefore be classified as having a low, critical, or high inductance.

4.4.1 Low Inductance Machines

Low inductance machines will be considered first, where:

$$L_{ph} < \frac{k}{I_{ph,max}} \tag{4.13}$$

Permanent magnet synchronous machines are characterised by a constant torque region up to the base speed. In this region, the motor is capable of producing the rated torque as the inverter is able to supply full current to the motor for torque generation. As the motor speed increases, so must the voltage supplied by the inverter. Eventually, the motor speed will reach the point where the maximum available phase voltage is required to meet the inverter current limit (the base speed), as shown in Figure 4.7.

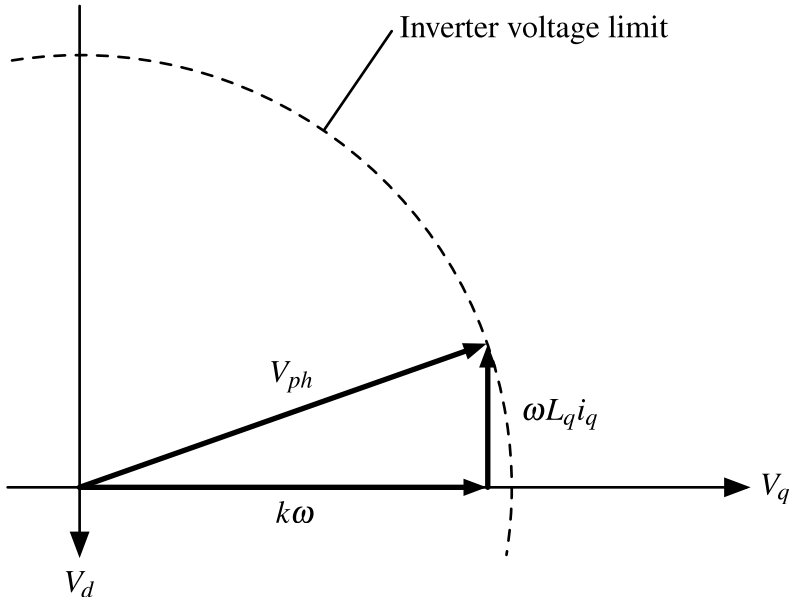

Figure 4.7: Motor voltage vectors at base speed for a low inductance machine.

The phase resistance has been neglected as the resulting voltage drop is typically small in comparison to the phase back EMF and inductive terms. For the 500 N m YASA motor at base speed (1693 rpm for a 400 V DC link voltage and a 300 A amplitude phase current), the resistive term is only 8.1 V whereas the inductive, back EMF, and applied phase voltages are 122.9 V, 195.6 V, and 230.9 V respectively. The maximum line-to-line voltage that can be applied to the motor by the inverter using space vector modulation is equal to the DC link voltage. Therefore, the maximum phase voltage is given by:

$$V_{ph,max} = \frac{V_{dc}}{\sqrt{3}} \tag{4.14}$$

The base speed can be calculated from the phasor diagram as:

$$\omega_b = \frac{V_{ph,max}}{\sqrt{k^2 + L_q^2 I_{ph,max}^2}} \tag{4.15}$$

Any further increase in speed will require a field weakening current to maximise the torque output. As the inverter is already current limited, it is necessary to reduce the quadrature axis current to stay within the inverter limits as shown in Figure 4.8 where:

$$i_q = \sqrt{I_{ph,max}^2 - i_d^2} \tag{4.16}$$

Resolving the voltage vectors in Figure 4.8 yields the following equations:

$$V_d = -\omega L_q i_q \tag{4.17}$$

$$V_q = k\omega + \omega L_d i_d \tag{4.18}$$

$$V_d^2 + V_q^2 = V_{ph,max}^2 \tag{4.19}$$

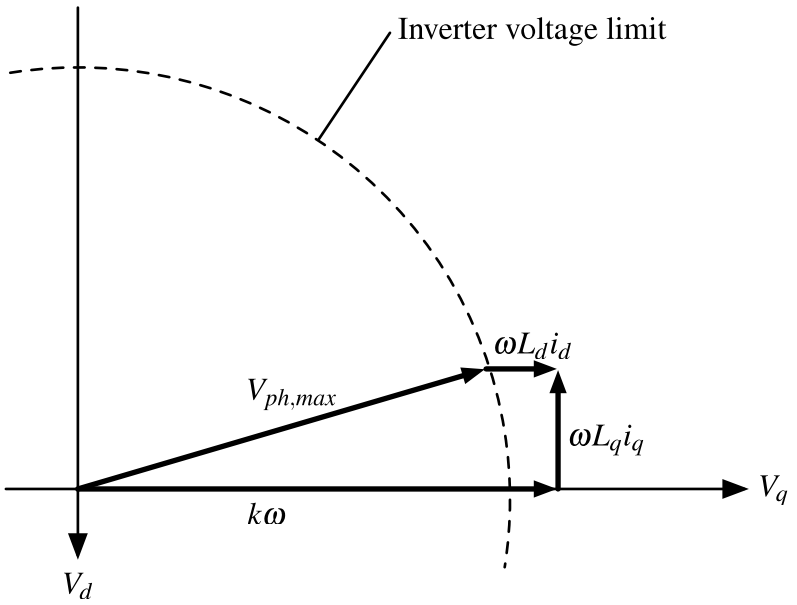

Figure 4.8: Motor voltage vectors beyond base speed for a low inductance machine.

For surface mounted permanent magnet machines, such as the YASA motor used in this thesis, the direct and quadrature inductances are approximately equal:

$$L_d \approx L_q \approx L_{ph} \tag{4.20}$$

Solving Equations 4.19 and 4.16 for i_q above the base speed gives:

$$i_q = \frac{1}{2}\sqrt{-\frac{k^4\omega^4 + (V_{ph,max}^2 - \omega^2 L_{ph}^2 I_{ph,max}^2)^2 - 2k^2\omega^2(V_{ph,max}^2 + \omega^2 L_{ph}^2 I_{ph,max}^2)}{\omega^4 k^2 L_{ph}^2}} \tag{4.21}$$

The motor torque and power are directly proportional to the quadrature current and are given by:

$$T = \frac{3}{2} n_{pp} k i_q \tag{4.22}$$

$$P = \frac{3}{2} k i_q \omega \tag{4.23}$$

The quadrature current, and hence the motor torque, does not vary linearly with the motor speed when maintaining the maximum phase voltage and phase current to maximise the output torque. The speed at which peak power occurs can be found by differentiating the motor power with respect to speed:

$$\omega_p = \frac{V_{ph,max}}{\sqrt{k^2 - L_{ph}^2 I_{ph,max}^2}} \tag{4.24}$$

By substituting Equation 4.24 into Equation 4.23, the maximum motor power can be determined. Interestingly, the theoretical maximum power (given by Equation 4.25) is independent of the motor parameters and is therefore limited entirely by the inverter. However, the analysis neglects the losses in the system which will reduce the power output for a real machine.

$$P_{max} = \frac{3}{2} V_{max} I_{ph,max} \tag{4.25}$$

As the speed increases, the field weakening current will become increasingly negative until all of the available inverter current is used for field weakening. At this point no current is available for torque production (positive or negative). This maximum speed is given by:

$$\omega_{max} = \frac{V_{ph,max}}{k - L_{ph} I_{ph,max}} \tag{4.26}$$

At this point, the applied quadrature voltage is equal to the maximum phase voltage and the direct voltage is equal to zero, as shown in Figure 4.9. A further increase in speed would result in a loss of regulation over the motor phase currents and the inverter current limit being exceeded, potentially causing damage to the motor and inverter.

The resulting general torque and power curves for low inductance machines are shown in Figures 4.10 and 4.11. The maximum torque can be seen to decrease beyond the base speed where the inverter output voltage is limited. However, the maximum output power continues to rise with motor speed until the peak power, limited by the inverter, is reached.

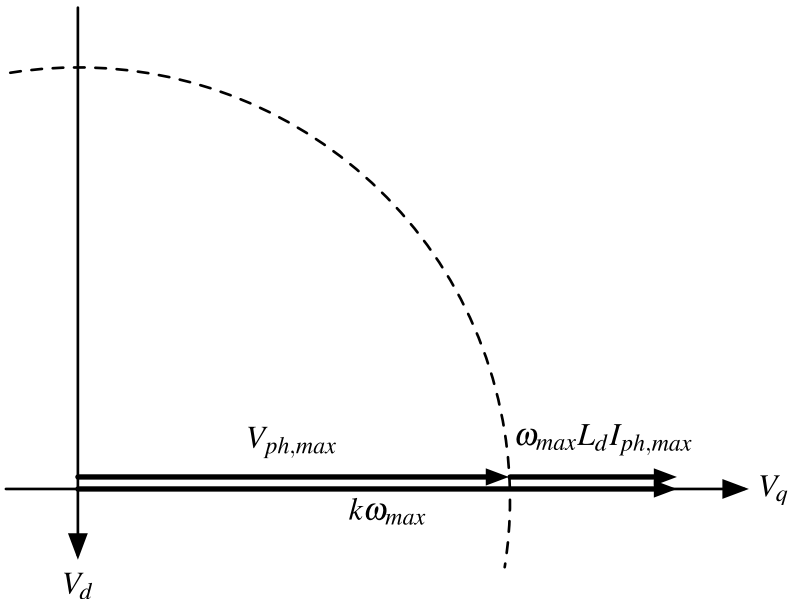

Figure 4.9: Motor voltage vectors at the maximum controllable speed for a low inductance machine.

Further increases in speed result in the maximum torque decreasing until the speed is reached where all of the available inverter current is being used for field weakening. At this point, the torque output has decreased to zero and the motor cannot be driven to a higher speed by the inverter. The same trend is seen for both positive and negative torques.

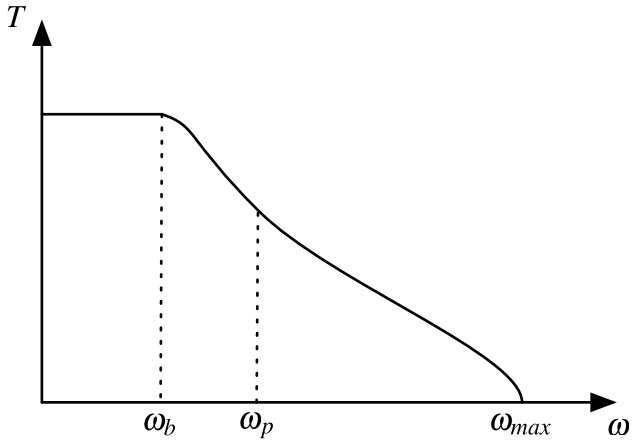

Figure 4.10: Motor torque curve for a low inductance machine.

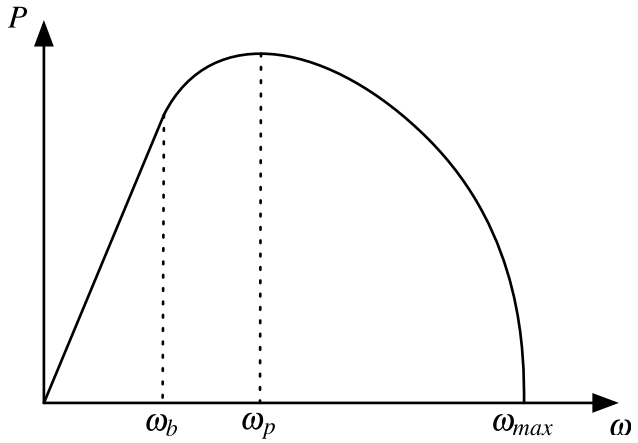

Figure 4.11: Motor power curve for a low inductance machine.

4.4.2 Critical Inductance Machines

The following section examines the performance of critical inductance machines where:

$$L_{ph} = \frac{k}{I_{ph,max}} \tag{4.27}$$

As with low inductance machines, full motor torque is available until the base speed (Equation 4.15) where the inverter voltage and current limits are simultaneously reached. Beyond the base speed the motor torque begins to decrease as more field weakening is required. The motor power asymptotically approaches the peak power value (given by Equation 4.25) as the speed increases, while V_d and V_q approach $-V_{ph,max}$ and 0 respectively, as shown in Figures 4.12 to 4.14.

Unlike for low inductance machines, the quadrature current never reduces to zero and the direct current never reaches $-I_{ph,max}$. This gives a theoretically infinite speed range for the machine [114]. However, this does not take into account the system losses and mechanical limitations which would give a finite speed limit for a real motor.

4.4.3 High Inductance Machines

Finally, the performance of high inductance machines will be examined where:

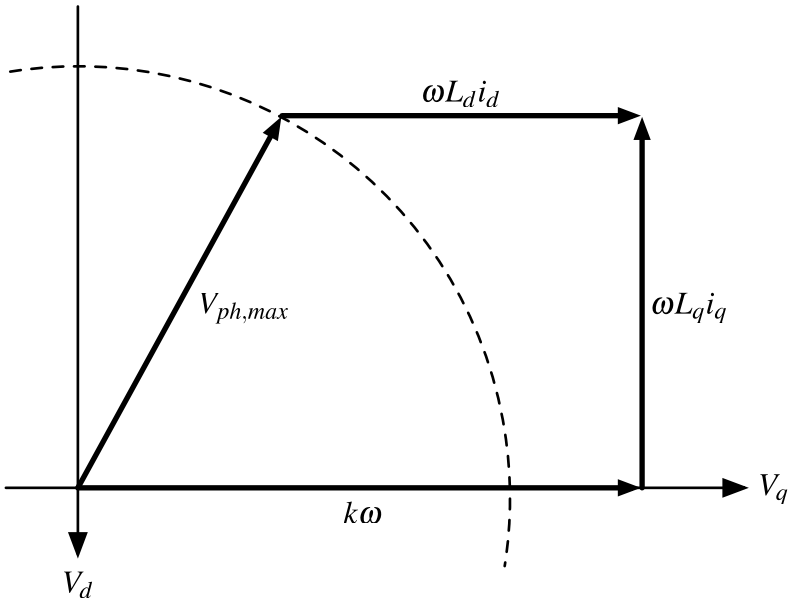

Figure 4.12: Motor voltage vectors beyond base speed for a critical inductance machine.

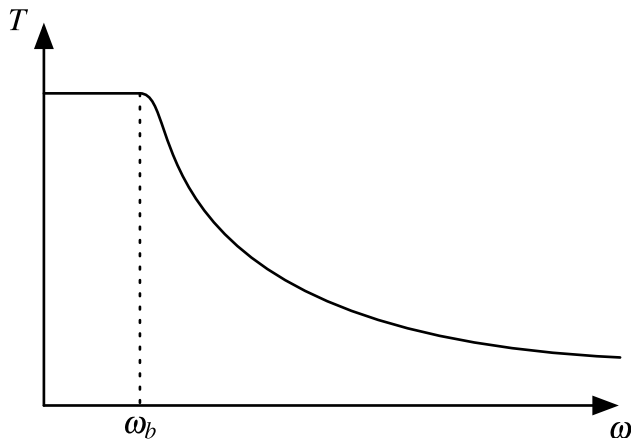

Figure 4.13: Motor torque curve for a critical inductance machine.

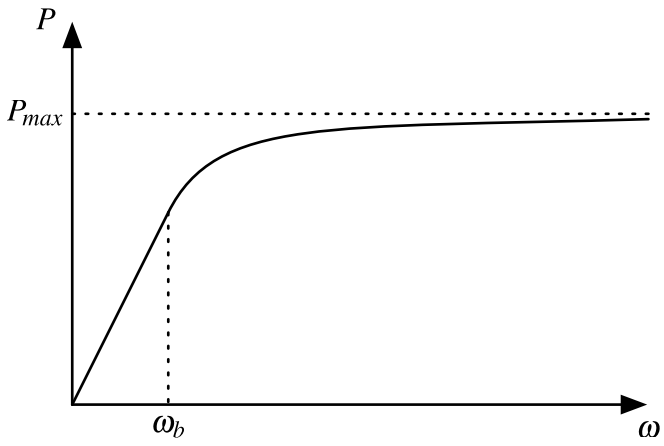

Figure 4.14: Motor power curve for a critical inductance machine.

$$L_{ph} > \frac{k}{I_{ph,max}} \tag{4.28}$$

Again, full torque is available until the base speed (given by Equation 4.15) is reached, at which point the inverter becomes current and voltage limited. Beyond the base speed, the motor power continues to rise until V_q has reduced to zero and V_d has reached $V_{ph,max}$, as shown in Figure 4.15. The speed at which this occurs is given by:

$$\omega_p = \frac{V_{ph,max}}{\sqrt{L_{ph}^2 I_{ph,max}^2 - k^2}} \tag{4.29}$$

Once the peak power has been reached, the total phase current must be reduced in order to maximise the torque output. Otherwise, the direct current component would be increased unnecessarily to maintain control over the phase currents. This would further reduce the available quadrature current and hence the torque output. The direct and quadrature currents once peak power has been reached are given by Equations 4.30 and 4.31. The direct current component remains constant with increasing speed to balance the increasing back EMF vector. The quadrature current decreases to maintain a fixed direct voltage component balancing the phase voltage applied by the inverter. This results in the torque being inversely proportional to the motor speed, but constant power output given by

Equation 4.32 and shown in Figures 4.16 and 4.17.

$$i_d = -\frac{k}{L_{ph}} \tag{4.30}$$

$$i_q = \frac{V_{ph,max}}{\omega L_{ph}} \tag{4.31}$$

$$P_{max} = \frac{3}{2} k i_q \omega = \frac{3kV_{ph,max}}{2L_{ph}} \tag{4.32}$$

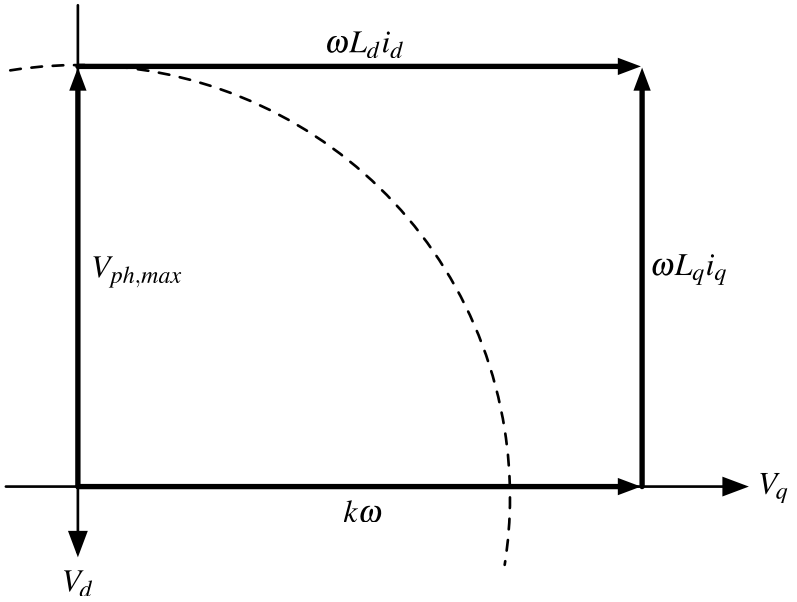

Figure 4.15: Motor voltage vectors in the constant power region for a high inductance machine.

Unlike the case for low inductance machines, Equation 4.32 shows the maximum power output for high inductance machines is highly dependent on the motor characteristics rather than just the inverter limits. A machine design with an inductance much greater than the critical value would result in a greatly reduced power output. However, the speed at which constant power is reached will be lower with an increased inductance value (although at a lower power value) giving a greater constant power speed range, which could be desirable for some applications.

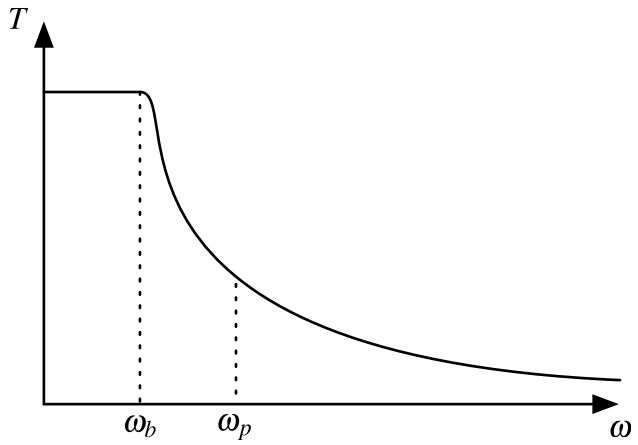

Figure 4.16: Motor torque curve for a high inductance machine.

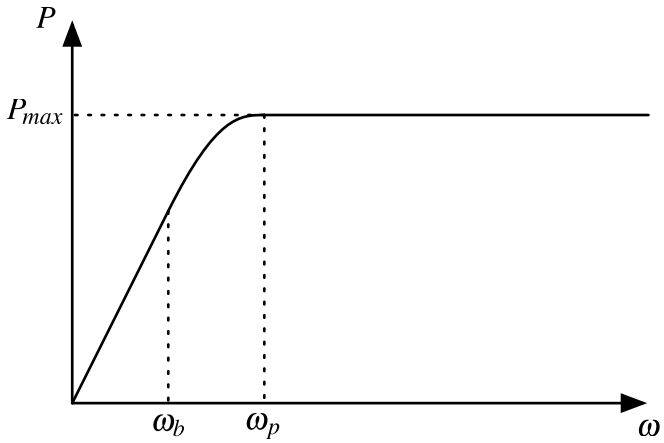

Figure 4.17: Motor power curve for a high inductance machine.

In practice, the phase inductance and back EMF are interrelated through the geometry and material properties of the motor. This limits control over the two parameters and the ability to design a machine to give a particular shape torque or power curve. However, the performance which results from these parameters must be considered when designing or selecting a motor for a particular application.

4.4.4 Comparison of Machine Performance

To compare the performance of low, critical, and high inductance machines, the torque and power curves for an example machine (taking the parameters of the 500 N m YASA motor from Table 1.3, except for the phase inductance) are given in Figure 4.18 for a DC link voltage of 400 V and a maximum phase current of 300 A. The Figure shows the effect of varying the phase inductance while keeping all other parameters constant where $L_{ph,0}$ is the critical inductance value of 367 µH. While it is unlikely to be possible to change the inductance for a real motor design without changing the other motor parameters, the example illustrates the effect of the inductance on the motor performance.

As the inductance is increased from a low inductance value of $0.7L_{ph,0}$ to a high inductance value of $1.3L_{ph,0}$, the base speed is reduced from 1646 rpm to 1224 rpm, with a base speed of 1420 rpm at the critical inductance value. This is because the direct voltage component for a given speed and phase current increases with the inductance value. Consequently, the inverter phase voltage limit will be reached for a lower back EMF voltage, and therefore at a lower speed.

As the inductance value approaches the critical value from $0.7L_{ph,0}$, the maximum speed and the speed at which peak power is reached increase from 6667 rpm and 2801 rpm respectively and both tend to infinity. This is because with a higher phase inductance, the size of the back EMF voltage vector does not increase relative to the field weakening voltage vector ($\omega L_d i_d$) as fast with increasing motor speed. This allows higher speeds to be reached before the inverter becomes voltage and current limited. The peak power

remains constant at 103.9 kW, as given by Equation 4.25, which is independent of the motor characteristics.

For inductance values above the critical value, the peak power output is reduced, and has fallen to 79.9 kW for $1.3L_{ph,0}$. This is because the maximum direct voltage component (given by Equation 4.17) that can be applied to the motor is limited by the the DC link voltage, and hence maximum inverter phase voltage. If the inductance increases, this voltage limit will be reached at a lower speed for a given quadrature current. The current (and therefore the torque) at which the voltage limit is first reached will remain constant as the inverter current limit has not changed. However, as the speed at which the voltage limit is first reached will reduce with an increased inductance, the peak power output will also reduce.

While the lowest inductance machine in the example offers the highest torque output at the start of the extended speed range (464 N m at 2000 rpm compared to 429 N m for $1.0L_{ph,0}$ and 377 N m for $1.3L_{ph,0}$), the torque output decays more quickly than for the higher inductance configurations. By 6000 rpm, the maximum torque output of the low inductance machine has fallen to 85 N m, whereas the critical and high inductance machines can still produce 163 N m and 127 N m respectively.

The ideal inductance value for a machine is application specific. The phase inductance value must be high enough to ensure the required top speed can be achieved. The inductance should also be as low as possible to ensure peak power and torque output are maximised. For the example above, if the application required a top speed of 3000 rpm, the $0.7L_{ph,0}$ configuration would offer a better torque and power output than the $1.0L_{ph,0}$ configuration. The opposite would be true if the application required a top speed of 6000 rpm. However, the phase current ripple will increase if the inductance is reduced and implications for system efficiency would also need to be considered.

If the machine output power is limited by the power supply, rather than by the characteristics of the motor, it is desirable to increase the machine inductance so that the

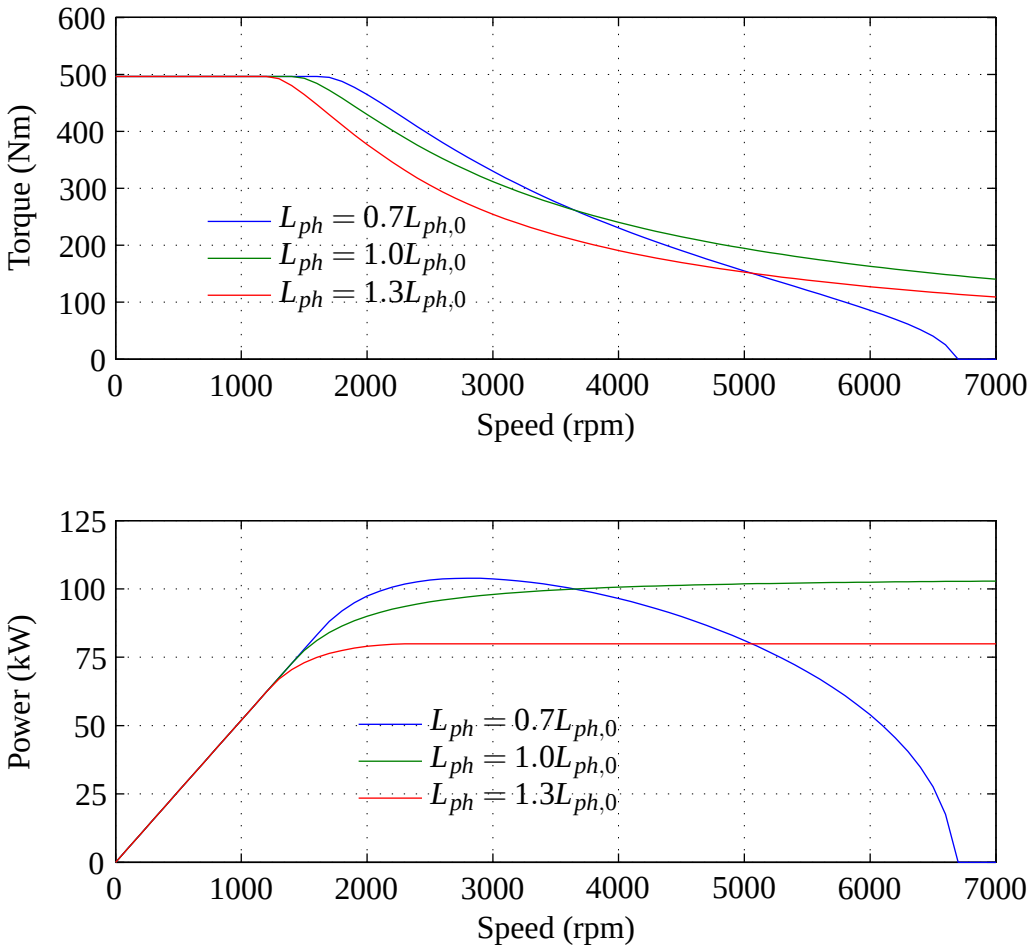

Figure 4.18: Motor torque and power output for varying machine inductance values.

machine and power supply limits coincide. This will ensure the highest motor efficiency as a lower direct current will be required for most of the extended speed range. This is shown in Figure 4.19 for the same motor configurations described above. The direct and quadrature currents for the $0.7L_{ph,0}$ configuration do not extend beyond 6667 rpm as this is the limit for controllable operation.

At 6000 rpm, the amplitude of the direct current component for the $1.3L_{ph,0}$ is -171 A, while -294 A is required for the $0.7L_{ph,0}$ configuration. The quadrature current component is the same for the two configurations at 48 A, but the phase current amplitude would be 68 % higher for the $0.7L_{ph,0}$ configuration, and the resulting winding losses would be 181 % higher.

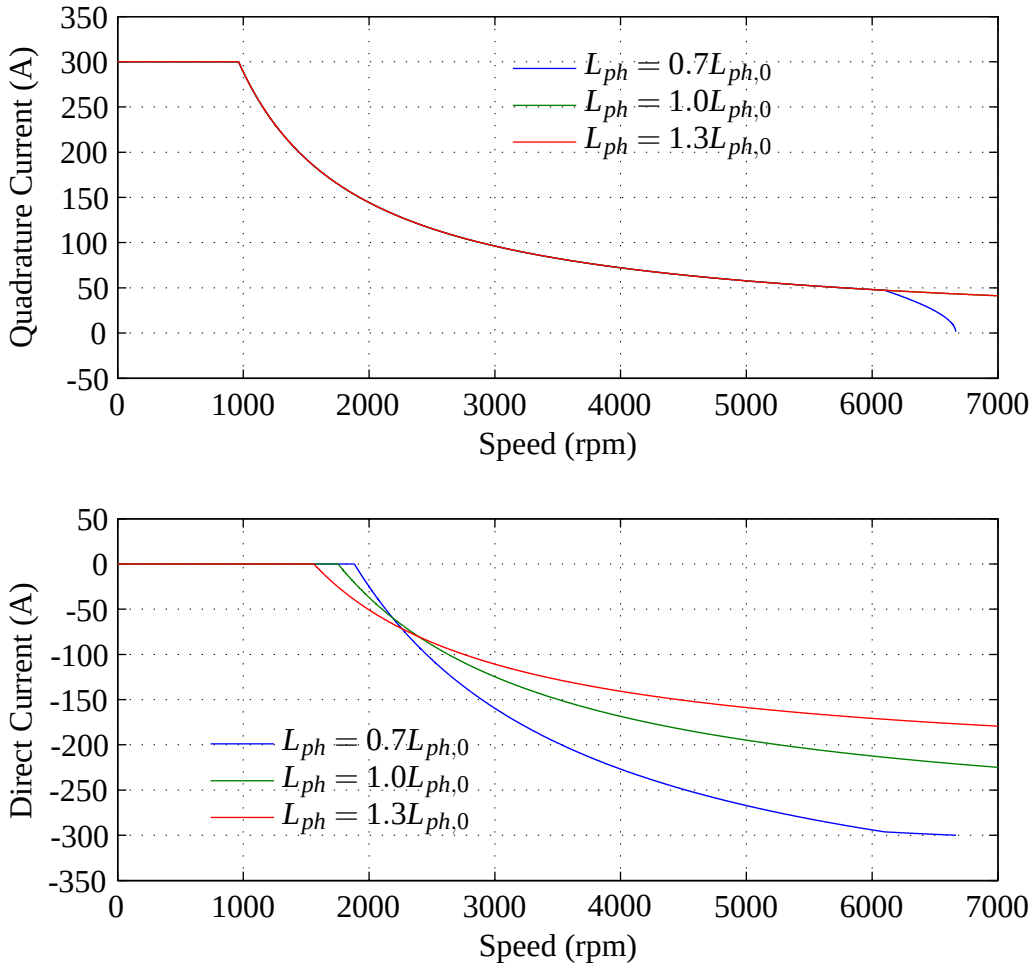

Figure 4.19: Direct and quadrature currents for varying machine inductance values with a 50 kW power supply limit.

4.5 A Comparison of Maximum Torque and Power Outputs for the Example System Under Different Control Modes

The performance of BLDC-120 and BLDC-180 control modes cannot be analysed as easily as the BLAC control mode because of the non-sinusoidal current waveforms shapes which change with motor speed and load. Therefore, a simulation of the system given in Tables 1.3 and 1.4 will be used to determine the output torque and power for the 500 N m YASA motor and is shown in Figure 4.20.

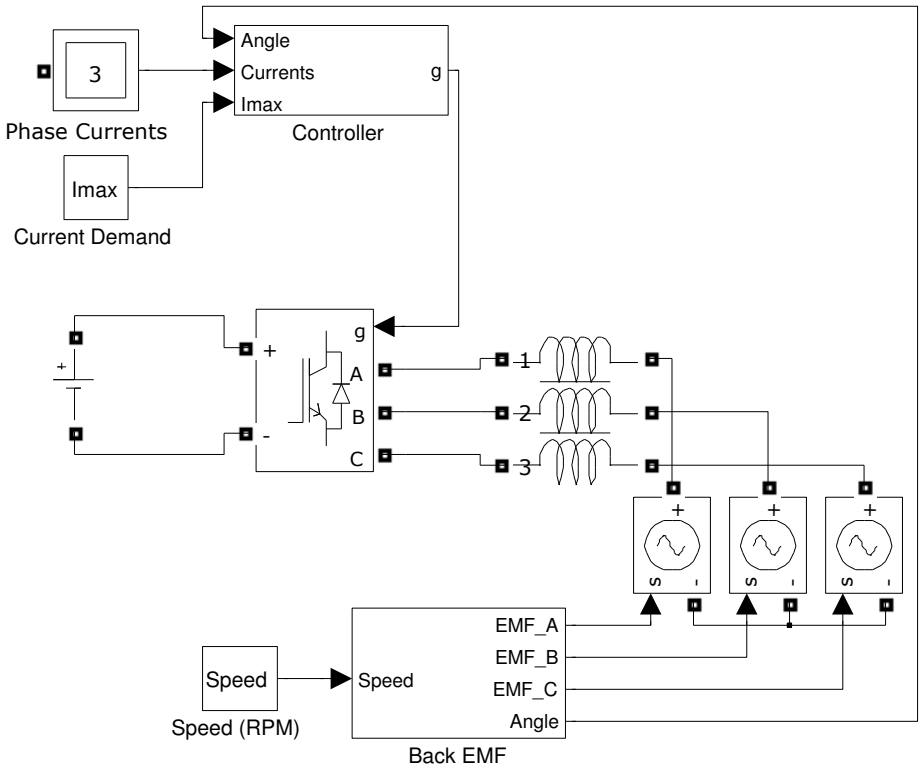

Figure 4.20: Motor and inverter Simulink model used to determine the motor phase currents for the three control modes.

The motor model consists of a three-phase series resistance and inductance to represent the winding impedance and three voltage sources with a star connection to represent the back EMFs. The mutual inductance is very low in comparison to the phase self-inductance

for fractional-slot machines with concentrated windings [123], such as the 500 N m YASA motor, and has therefore been neglected in the model.

The motor speed and current demand (proportional to the required motor torque) are inputs to the model and are used to set the desired operating point for the simulation. The motor speed is passed to back EMF block and is integrated to give the motor angle. The angle and speed are used to calculate the back EMF voltage amplitudes for each of the three phases. The measured no-load line-to-line back EMF for the 500 N m YASA motor is highly sinusoidal, as shown in Figure 4.21. The back EMFs are modelled as purely sinusoidal, which gives a maximum error of 2.1 % compared to the measured back EMF of the real motor.

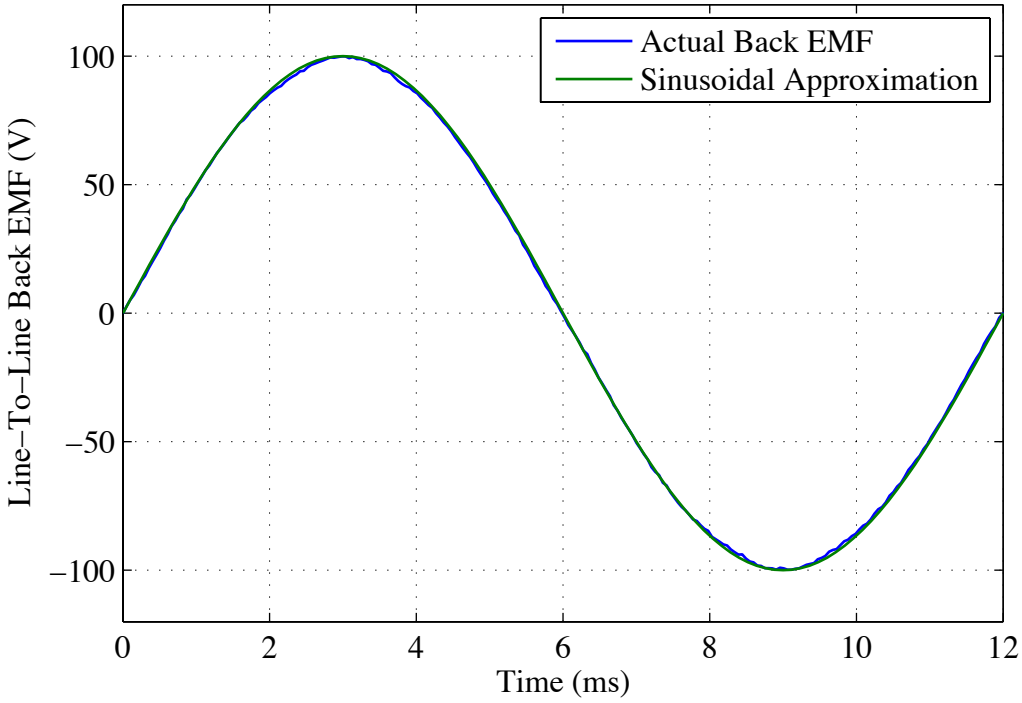

Figure 4.21: The measured line-to-line back EMF at 500 rpm for the 500 N m YASA motor.

The model does not take into account any saturation effects on the machine's back EMF or inductance as experimental results have shown the motor torque to be highly linear with current amplitude in the range of 0 N m to 500 N m, as shown in Figure 4.22. A least squares linear approximation has been fitted to the torque measurements and all

data points are within 4 N m of the best fit line. This is also within the 5 N m measurement tolerance of the torque sensor used. Therefore, the linear torque approximation used in the model will not result in significant error over the range of interest. However, it would be necessary to model the non-linearity for higher torque limits if saturation effects were observed. Measurements for both the motor torque and back EMF have been taken using the experimental test rig described in Chapter 5.

Changes to the motor characteristics with temperature have not been modelled as there is currently insufficient data to characterise the relationship between motor losses and component and coolant temperatures. The duration of the simulation is also assumed to be so short that temperature rises will be negligible and the motor parameters will be assumed to be constant. For the real motor, the temperature of the windings and hence the phase resistance will increase while the motor is under load. Iron losses in the rotor will also increase the magnet temperature causing the motor torque constant to decrease [124]. The motor model will therefore overestimate the real torque output of the motor by assuming a constant motor temperature of 60 °C.

The motor angle is also used by a controller block which determines the required switching signals for the inverter. The block implements the chosen control strategy (BLDC-120, BLDC-180 or BLAC) using the six-step commutation or FOC strategies described in Chapter 3 with the motor phase currents used for feedback. The required maximum phase current is input and 10 kHz three-phase PWM signals are output. PWM frequencies are typically chosen to be at least ten times the maximum electrical frequency of the motor [52]. Therefore, a 10 kHz PWM will be suitable for the theoretical maximum speed of 5291 rpm (881 Hz maximum electrical frequency) for the YASA motor predicted by Equation 4.26. The PWM duty cycles are updated at PWM frequency (100 µs intervals).

A standard three leg model with six IGBTs and six inverse diodes has been used for the inverter. The power electronic devices are modelled as ideal switches with the on-state voltage drops and resistances taken from the device datasheets (given in Table 1.4). A fixed

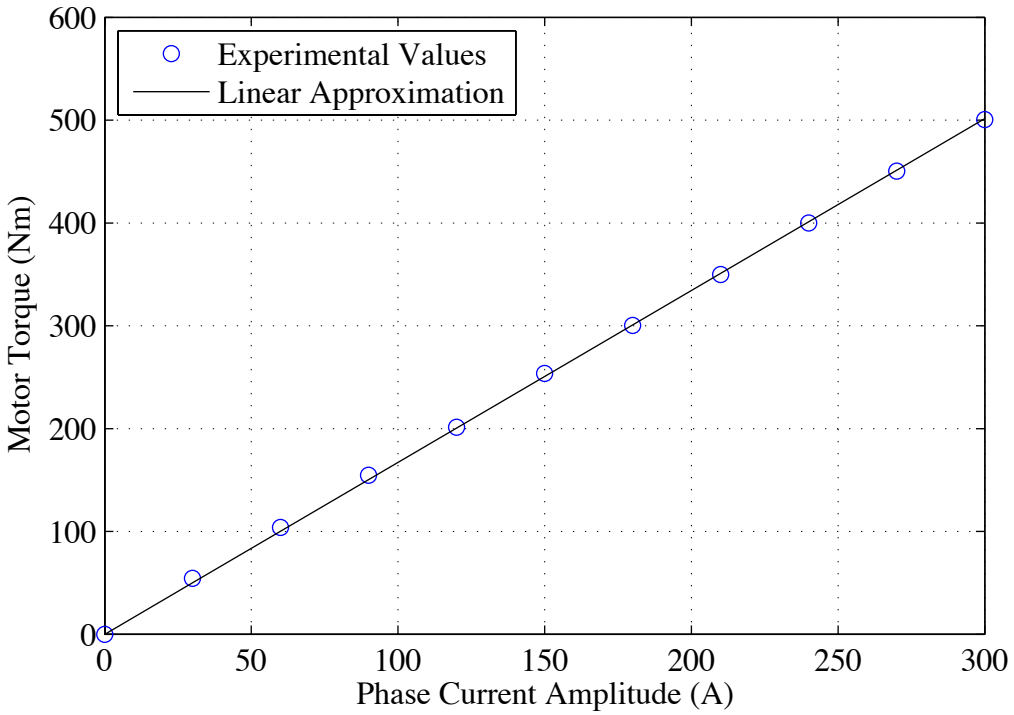

Figure 4.22: Experimental locked rotor torque output under BLDC-120 control for the 500 N m YASA motor.

400 V source is connected to the inverter, which is in the typical range for hybrid vehicles [54]. The model does not consider the effects of transient currents on the bus voltage as would be observed for real power supplies. The exact behaviour of the supply would depend on the type of power source being used and is beyond the scope of this thesis.

The system is simulated with fixed time steps of 1 µs for a total simulation time of 0.4 s. This time is sufficiently long for the model to reach a steady state for all achievable operating points for the three control modes. The instantaneous motor torque is calculated from the phase currents and back EMFs using Equation 3.1. The average torque over the last 0.1 s of the simulation is taken as the steady state value for the simulated motor speed and current demand.

Figure 4.23 shows a comparison of the predicted motor torque for the Simulink model under BLAC control and analytical Equations 4.21 and 4.22 using the same motor characteristics. The analytical equations overestimate the simulated torque by only 3.7 N m

(0.7 % of the maximum torque) at worst case. The small discrepancy is due to the phase resistance, phase current ripple from the PWM operation, and inverter characteristics not being taken into account by the analytical equations. The simulation is therefore in close agreement with the torque output that would be expected from the analytical equations. The simulation can now be used to determine the maximum motor operating range for the three control modes.

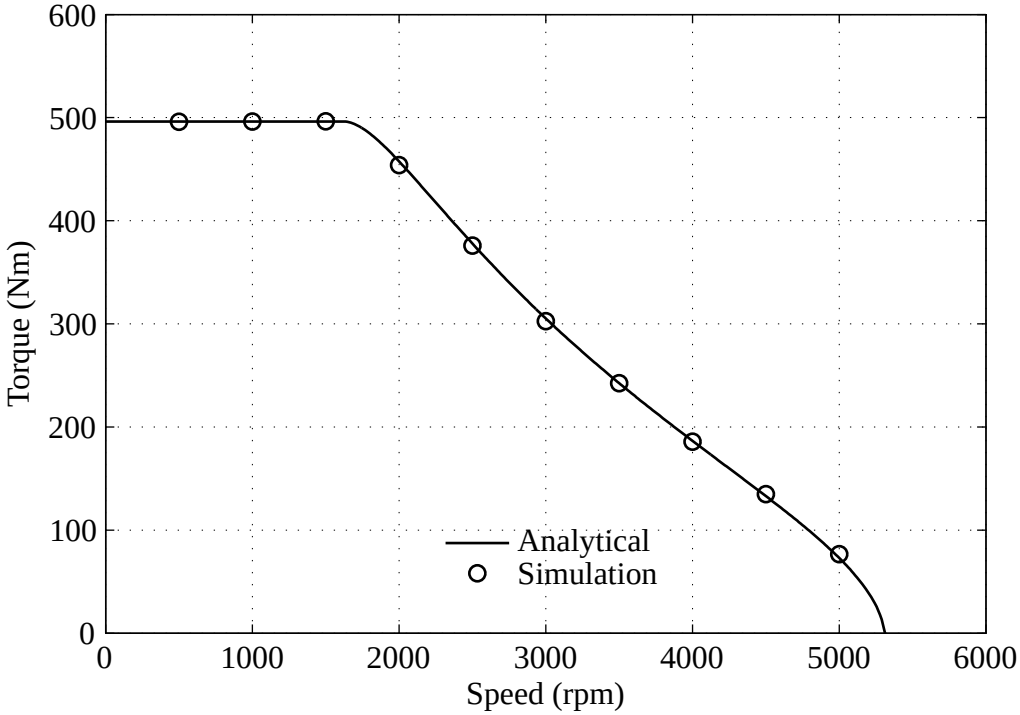

Figure 4.23: Comparison of analytical and simulated torque curves for a 300 A peak phase current and 400 V DC link voltage.

4.5.1 Simulated Performance with the Same Peak Phase Currents

Figures 4.24 and 4.25 compare the torque and power output for an identical machine under BLDC-120, BLDC-180 and BLAC control with a peak phase current of 300 A. BLDC-120 offers the highest torque output below base speed (507 N m) while BLDC-180 offers the lowest (474 N m). The additional harmonic content of the phase currents for BLDC-120 gives a higher torque output than BLAC (492 N m). However, the torque output is reduced

for BLDC-180 because of the current waveform shapes, as shown in Figure 4.26. For all three control modes, the phase currents peak close to the phase back EMF peak. However, the BLDC-180 currents fall most sharply either side of the peak. This reduces the average torque produced and is therefore the lowest of the three control modes.

Above base speed, the situation is reversed with the torque output for BLDC-120 dropping the fastest and BLDC-180 consistently the highest. At 3000 rpm, the maximum torque outputs for BLDC-120, BLDC-180 and BLAC have fallen to 237 N m, 344 N m and 299 N m respectively. The torque output is highest for BLDC-180 in this region as BLDC-180 gives the best utilisation of the available DC-link voltage. For BLDC-120, the motor inductance begins to have a significant effect on the phase currents (shown in Figure 4.27) and the current waveform harmonics become increasingly suppressed by the winding reactance as the speed increases [40]. The BLDC-120 current waveform requires the greatest phase advance with respect to the back EMF to achieve the required peak phase current and hence has the lowest torque output. Consequently, the BLDC-120 control mode has the lowest peak power output.

4.5.2 Simulated Performance with the Same RMS Phase Currents

Figures 4.28 and 4.29 compare the torque and power outputs of the different control modes for the same RMS phase current of 212 A. Figure 4.28 shows an almost identical torque output for the BLAC and BLDC-180 control modes below base speed (peak torques of 496 N m and 493 N m respectively). However, the base speed for the BLDC-180 control mode (1800 rpm[1]) is higher than for BLAC control (1600 rpm[1]) and BLDC-120 control (1400 rpm[1]) because of the better DC link voltage utilisation. The better DC link voltage utilisation also gives the BLDC-180 control mode the highest torque output across the majority of the extended speed range, and hence the highest peak power output of 108 kW.

[1]The base speed values are approximate as simulations have only been performed at 200 rpm steps to minimise computation time.

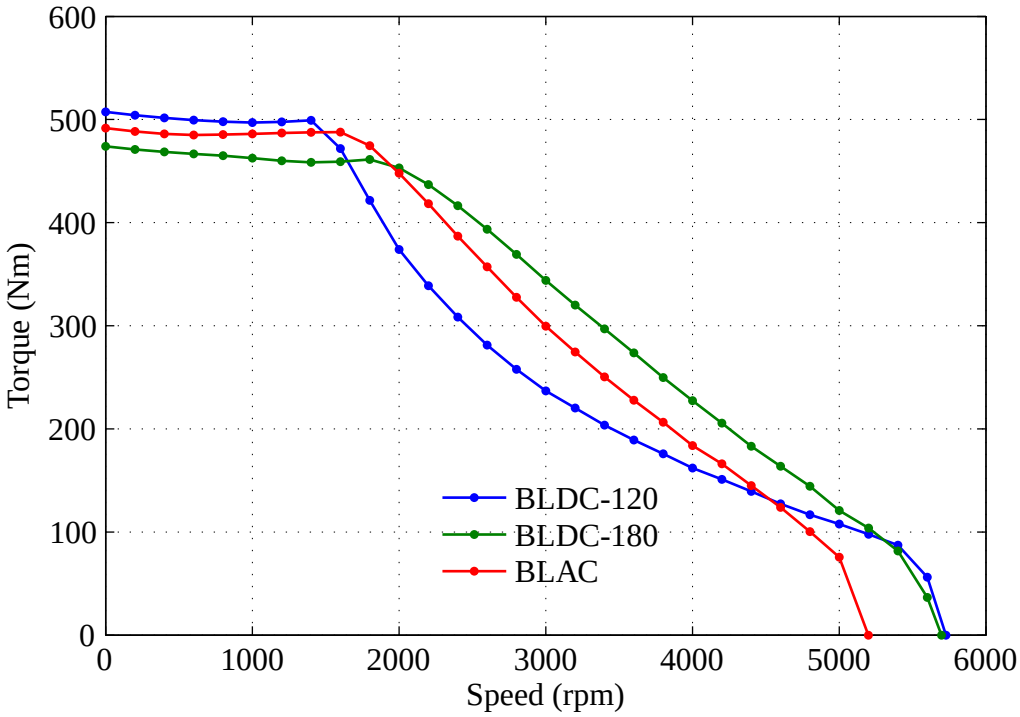

Figure 4.24: Maximum torque curves for a 300 A peak phase current and 400 V DC link voltage.

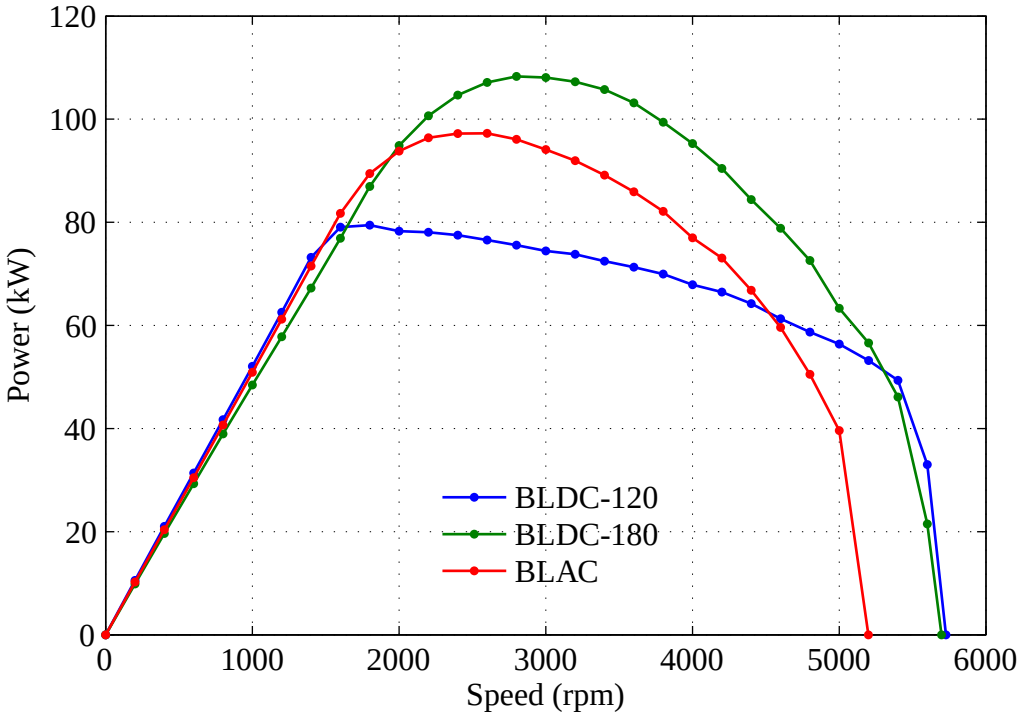

Figure 4.25: Maximum power curves for a 300 A peak phase current and 400 V DC link voltage.

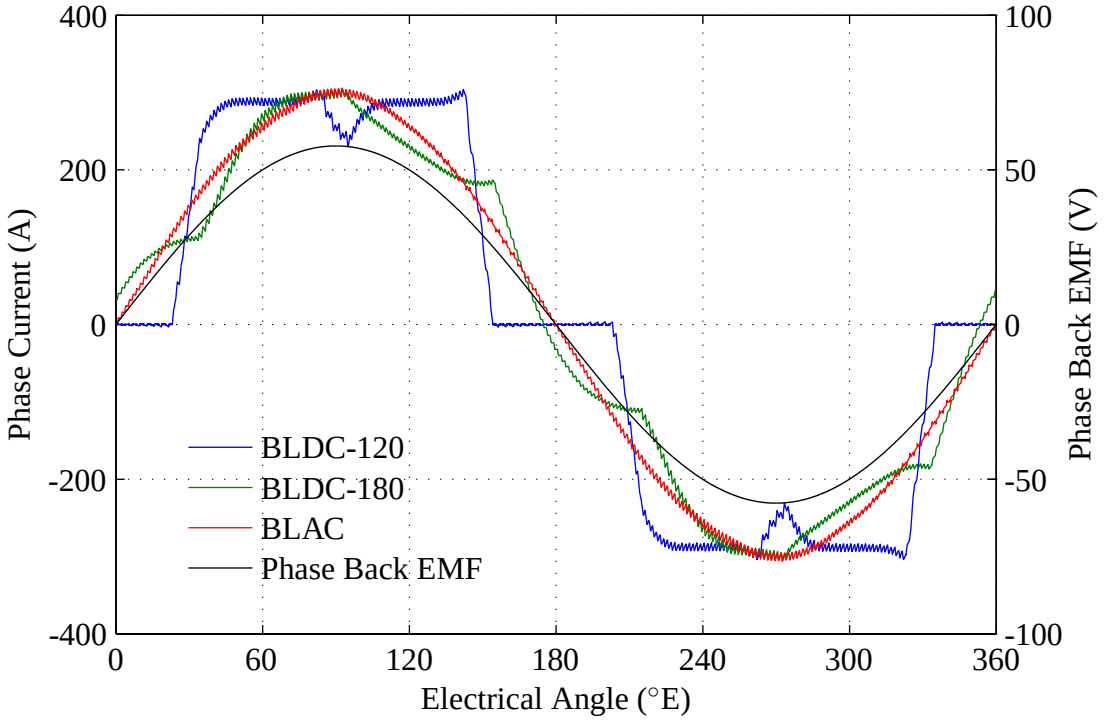

Figure 4.26: Phase currents and back EMF at 500 rpm for a 300 A peak current and 400 V DC link voltage.

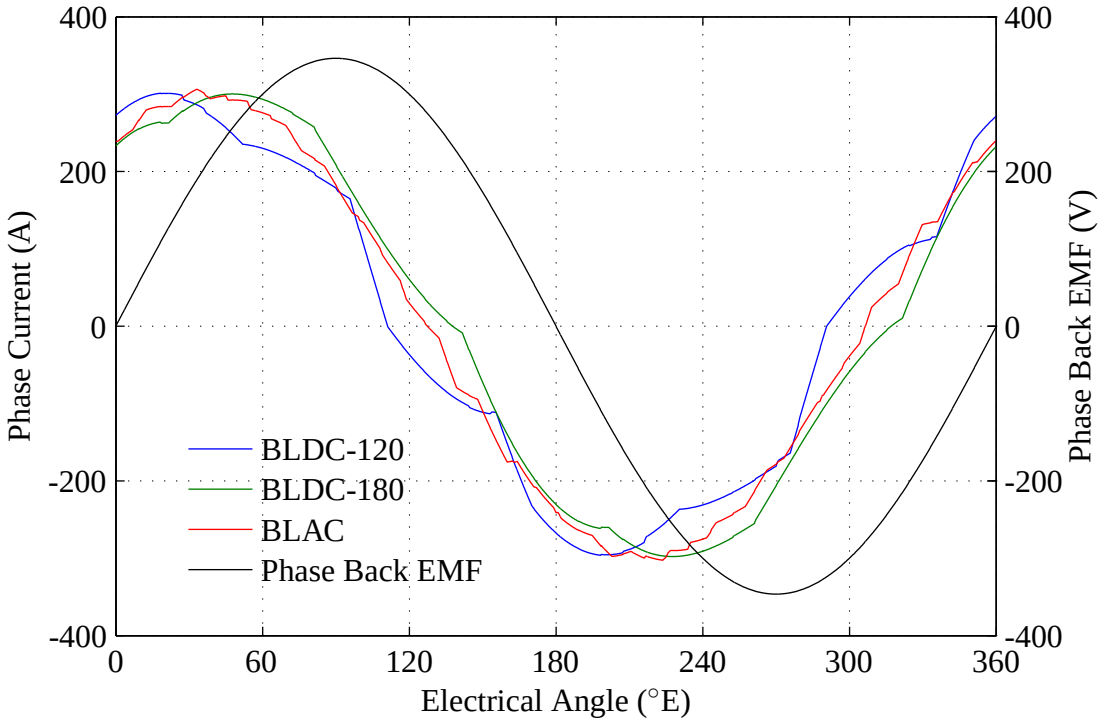

Figure 4.27: Phase currents and back EMF at 3000 rpm for a 300 A peak current and 400 V DC link voltage.

Figure 4.30 shows the phase currents for the three control modes below base speed. The rectangular shape of the BLDC-120 current waveforms gives the lowest peak current value of 281 A for the RMS current limit, compared to 311 A and 302 A for BLDC-180 and BLAC control respectively. The BLDC-120 control mode produces the lowest torque output below base speed as a result, peaking at 485 N m. Figure 4.31 shows the phase currents for the three control modes above base speed. It can be seen that the BLDC-120 control mode requires the greatest phase advance of the currents with respect to the back EMF to achieve the RMS phase current limit. This results in the BLDC-120 control mode having the lowest torque output across the majority of the extended speed region.

The BLDC-120 control mode is shown to produce a higher torque output than the BLDC-180 control mode above 5400 rpm in Figure 4.28. At 5600 rpm, 36.9 N m of torque is available in the BLDC-180 mode compared to 57.6 N m in the BLDC-120 mode. As each phase of the inverter is not switched for 120 °E of the electrical cycle in the BLDC-120 mode, the freewheeling diode conduct for a larger proportion of the cycle time than in the BLDC-180 mode. This improves the DC link voltage utilisation for large phase advance angles, resulting in a higher torque output for the BLDC-120 mode.

4.6 Summary

In this chapter, the torque output available from a permanent magnet synchronous motor has been investigated for the three control modes. This allows the maximum range of torque and speed operation to be determined, over which the system efficiency for the three control modes should be compared. The need for an extended speed range has been discussed with a description of techniques for BLDC and BLAC control modes to achieve this.

The effect of the machine characteristics on the performance of SMPMSMs were discussed, and analytical equations for predicting the performance were derived for BLAC control. It was shown that a critical value for the machine inductance exists (relative to

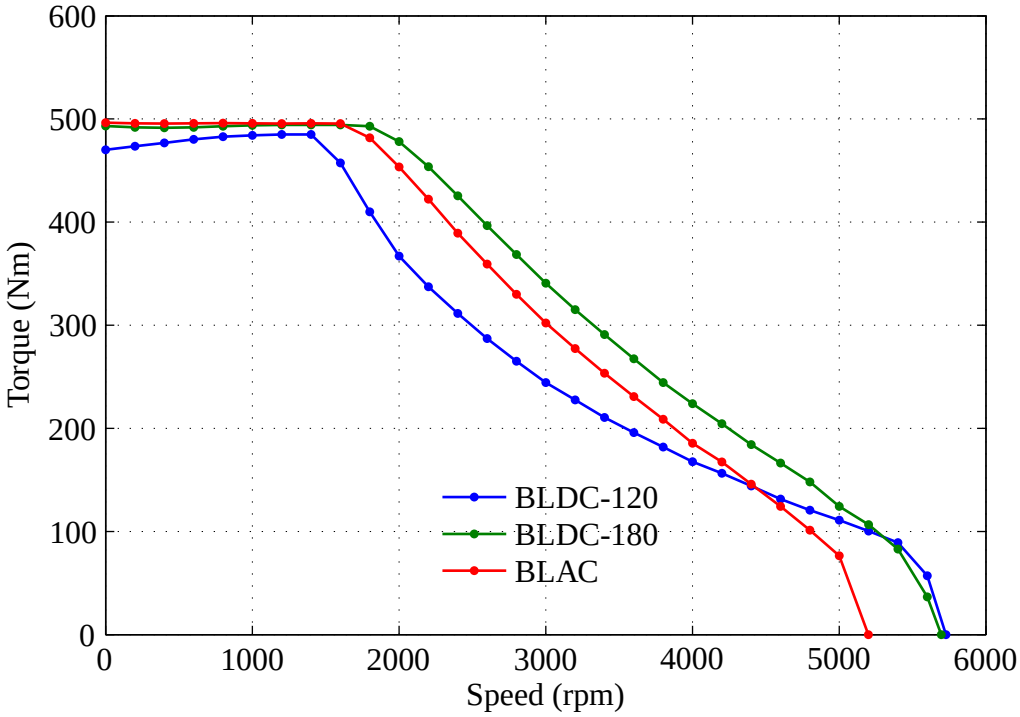

Figure 4.28: Maximum torque curves for a 212 A RMS phase current and 400 V DC link voltage.

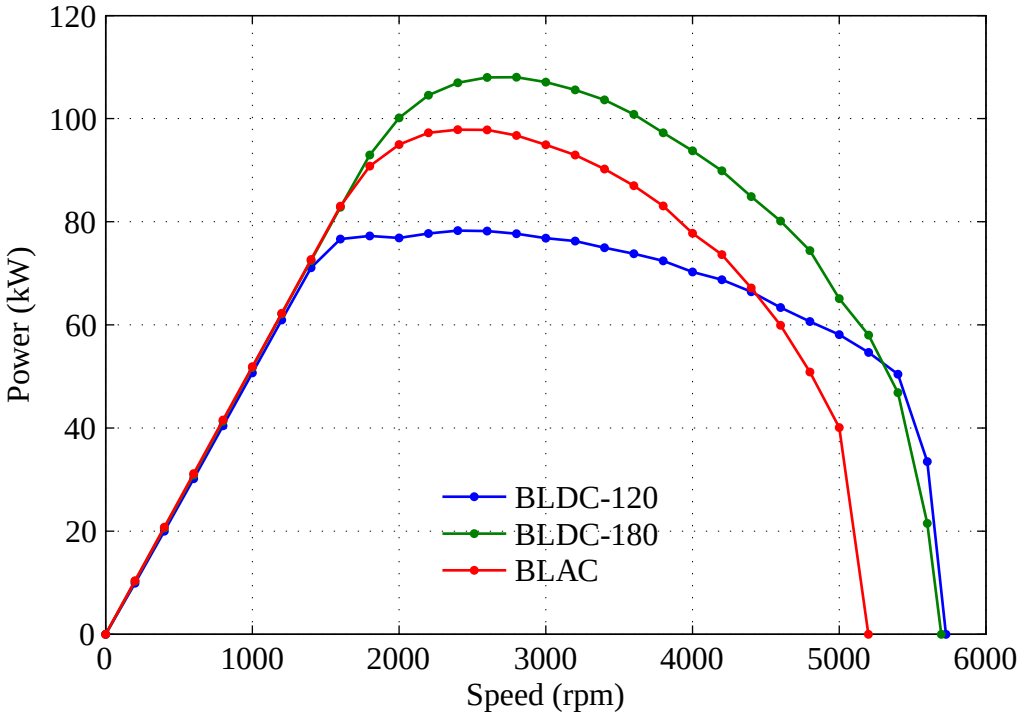

Figure 4.29: Maximum power curves for a 212 A RMS phase current and 400 V DC link voltage.

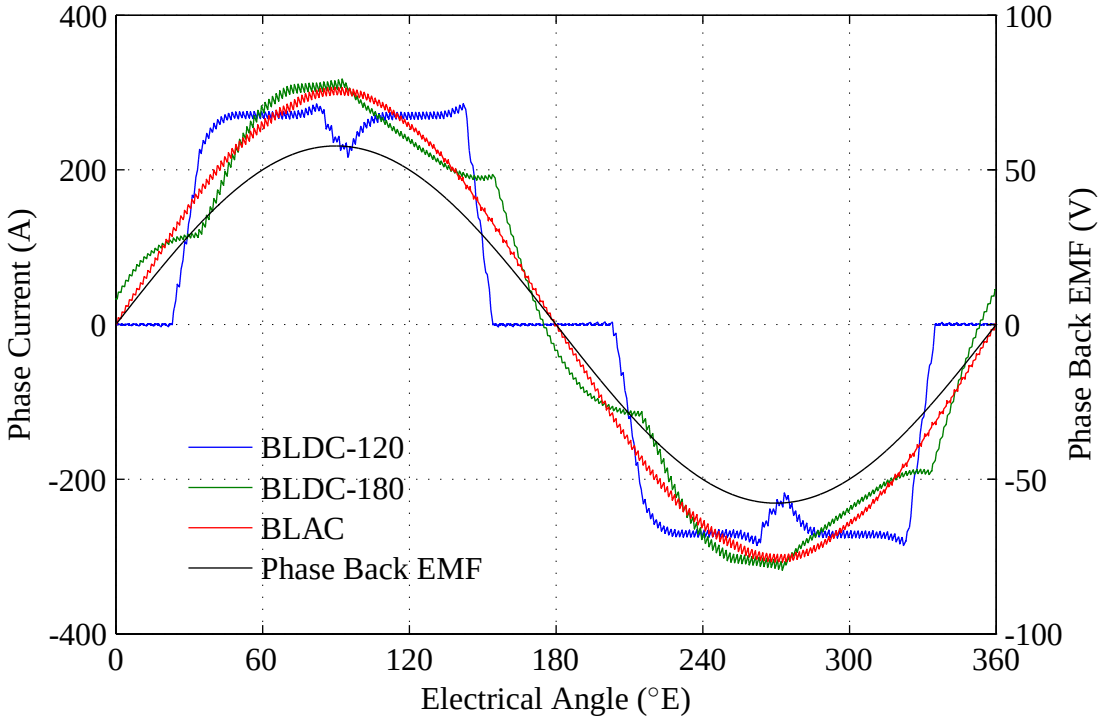

Figure 4.30: Phase currents and back EMF at 500 rpm for a 212 A RMS current and 400 V DC link voltage.

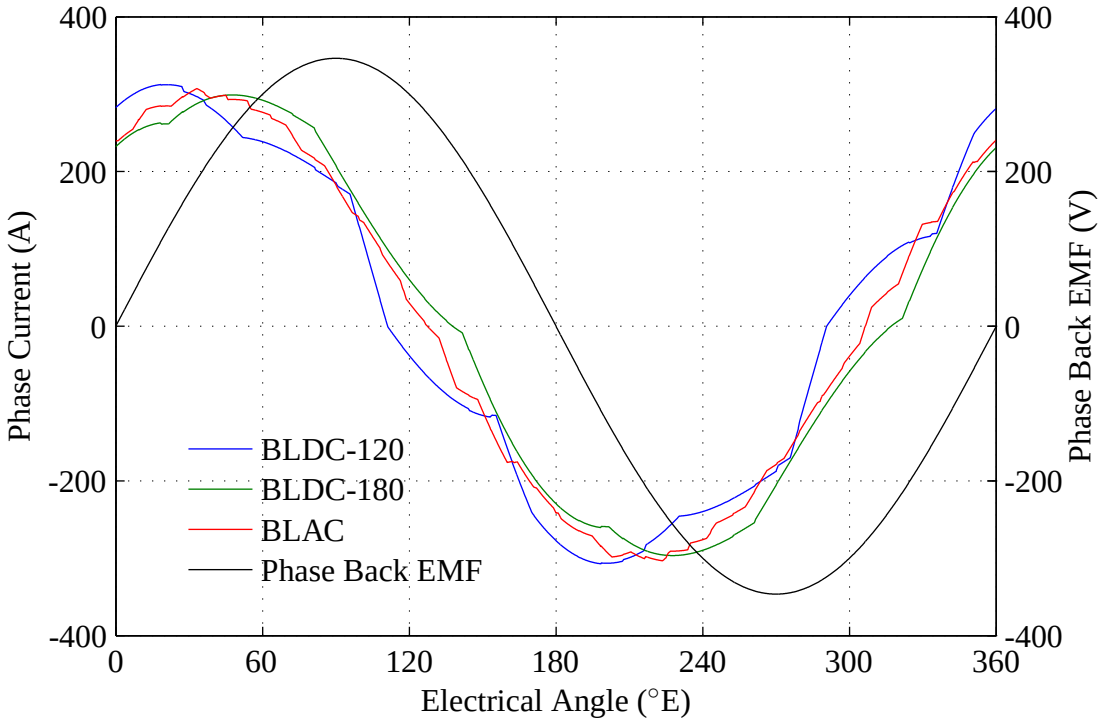

Figure 4.31: Phase currents and back EMF at 3000 rpm for a 212 A RMS current and 400 V DC link voltage.

the maximum phase current and torque constant), below which an infinite constant power speed range is not possible. Increasing the inductance above the critical value has the undesirable effect of reducing the maximum possible power output from the motor.

Finally a comparison of the maximum motor torque and power outputs was given for the three control modes for the 500 N m YASA motor. A Simulink simulation of the example motor system was used to determine the maximum torque achievable across the operating speed range limited by a DC link voltage of 400 V and a maximum RMS phase current of 212 A. It was shown that below the base speed, the BLAC control mode gave the highest torque output, peaking at 496 N m, whereas above base speed the BLDC-180 control mode gave the highest power output, peaking at 108 kW. To maximise the torque output as the motor speed changes, it is therefore necessary to change control modes as a function of the motor speed.

5

Analysis of Losses in PM Motor Systems

5.1 Introduction

The one of the most important considerations when selecting a motor system for a vehicle application is the system efficiency [35]. In order to compare the efficiency of the three control modes (BLDC-120, BLDC-180 and BLAC), the efficiency maps for each mode must be determined over the required operating range. This chapter first determines each of the loss components for the example motor and the inverter using a combinations of methods. A Simulink model of the system (described in Chapter 4) is used to determine the motor currents for each of the control modes over the theoretical maximum operating range determined in the previous chapter. From this, the inverter losses and motor winding losses can be estimated. The simulated phase current waveforms are then used in a magnetic finite element analysis of the motor to estimate the hysteresis and eddy current losses. Once all of the loss components have been determined, an estimated efficiency map can be calculated for each operating mode for comparison.

The loss component maps in this chapter are shown and described predominantly for the BLDC-120 control mode. Loss maps for the BLDC-180 and BLAC control modes are given in Appendix A. However, the trends in losses with motor speed and torque apply to all control modes.

5.2 Simulink System Model

A Simulink model of the motor and inverter has been used to determine the steady state performance of the system for each control mode as in Chapter 4. For the purposes of determining the system losses, the motor phase currents and inverter phase PWM duties are also required in addition to the motor torque output.

The model has been used to determine the steady state phase currents and PWM duty cycle waveforms over an electrical cycle for an array of operating points. The operating range being considered is limited by an RMS inverter phase current of 212 A (the rated current limit of the motor), corresponding to a peak current of 300 A for the BLAC mode. The operating range is also limited by a DC-link voltage of 400 V. This voltage is typical for electric and hybrid vehicles [54].

Motor speed steps of 200 rpm and current demand steps of 20 A have been used to generate a grid of results over the operating range. The inverter has been modelled with a fixed switching frequency of 10 kHz. This switching frequency is below the specified maximum for the Semikron inverter but sufficiently high for the maximum electrical frequency of the motor, as discussed in Chapter 4.

The current waveforms used for calculation of losses are taken from the last 0.1 s of the simulation when they have reached a steady state and are averaged over multiple electrical cycles to give the current waveforms at 5 °E intervals.

5.2.1 Winding Losses

The simplest system loss component to estimate is the motor winding resistive loss. The motor has 24 pole pieces, each wound with 45 turns of square copper wire, which are connected into four parallel groups of three star-connected phases. The wire used has a 3.0 mm^2 cross-section and approximately 7 m is required for each coil. The total measured DC phase resistance (including the phase cables connecting the motor to the inverter) is 27 mΩ at 60 °C.

A constant stator temperature of 60 °C will be assumed when determining the motor efficiency map as this is the specified continuous operating temperature of the motor. When operating on a real vehicle, the precise winding temperature, and therefore the winding losses, will depend on the motor usage prior to the point of interest.

At 5000 rpm, the fundamental electrical frequency of the 500 N m YASA motor will be 833 Hz giving a skin depth of 2.43 mm for the copper windings. Equation 2.6 predicts a 0.035 % increase in the winding resistance from the skin effect at this frequency and is sufficiently small to be neglected. However, Equation 2.7 predicts a 19.6 % increase in resistance from the proximity effect for the 3 layer winding (neglecting the current harmonics for a first order approximation). This will give 19.6 % higher copper loss for a given RMS motor phase current at 5000 rpm than for the same current when stationary.

If the stator temperature was not assumed to be constant, an increase in temperature would cause the copper winding resistivity, and hence the skin depth, to increase as shown by Equations 2.3 and 2.4. An increase in the skin depth would reduce the DC resistance correction factors for the skin effect and proximity effect, estimated by Equations 2.6 and 2.7. For example, a winding temperature rise from 60 °C to 100 °C at 5000 rpm would cause to skin effect and proximity effect correction factors to fall to 0.027 % and 15.3 % respectively. However, the total AC resistance, and therefore the winding losses, would still increase by 9.3 % as a result of the change in the dominant DC resistance.

Having determined the RMS motor phase currents over a steady state electrical cycle,

the winding losses can be calculated using Equation 2.8 for each of the simulated operating points. Figure 5.1 shows the winding losses for the BLDC-120 control mode over the operating range. The winding losses can be seen to increase with motor torque but do not change significantly with motor speed below the base speed as the motor torque is directly proportional to the quadrature current component and no field weakening is required. For the BLDC-120 mode at 1000 rpm, the winding losses increase from 0.88 kW at 200 N m to 3.45 kW at 400 N m.

Beyond the base speed, field weakening currents are required to maintain torque output and the magnitude of the field weakening current increases with motor speed. Therefore the losses for a given torque increase significantly with the motor speed once the base speed is exceeded. At 200 N m, the winding losses have risen to 3.52 kW at 3000 rpm.

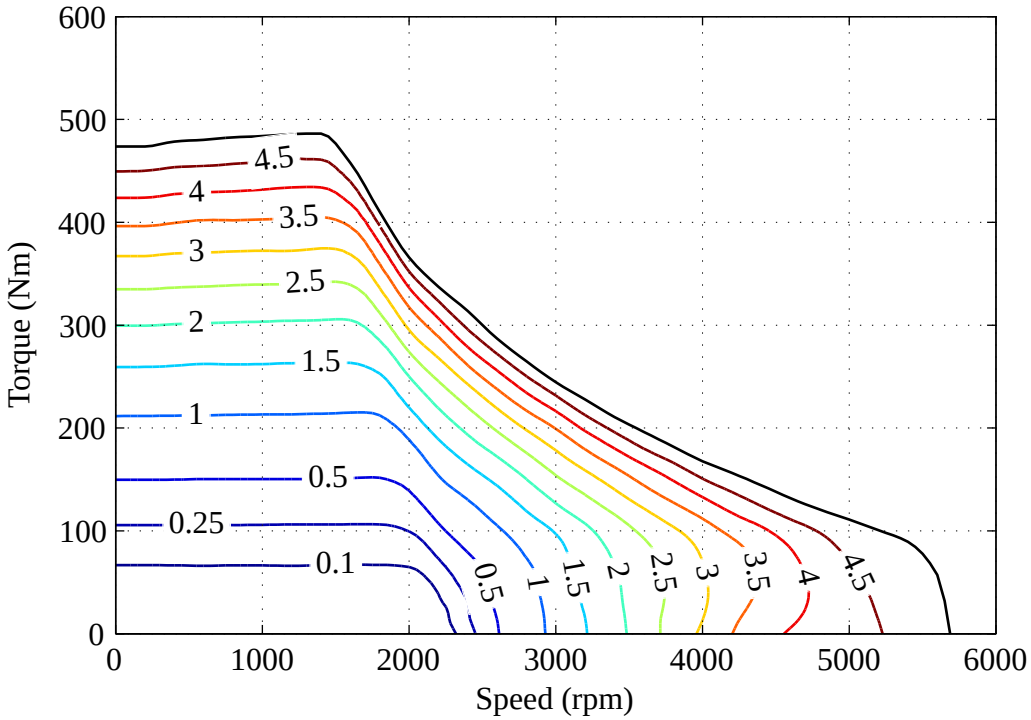

Figure 5.1: BLDC-120 winding loss map (contour values in kW).

5.2.2 Inverter Losses

The inverter losses can be split into two components as discussed in Chapter 2; switching losses and conduction losses.

The switching losses are the simpler of the two components to determine. For each simulated operating point, the switching losses for each device are first determined for each point of the phase current waveform over the electrical cycle using Equations 2.16 and 2.17. The losses are then averaged over an electrical cycle for use in determining the efficiency map. The switching losses for the BLDC-120 control mode are shown in Figure 5.2.

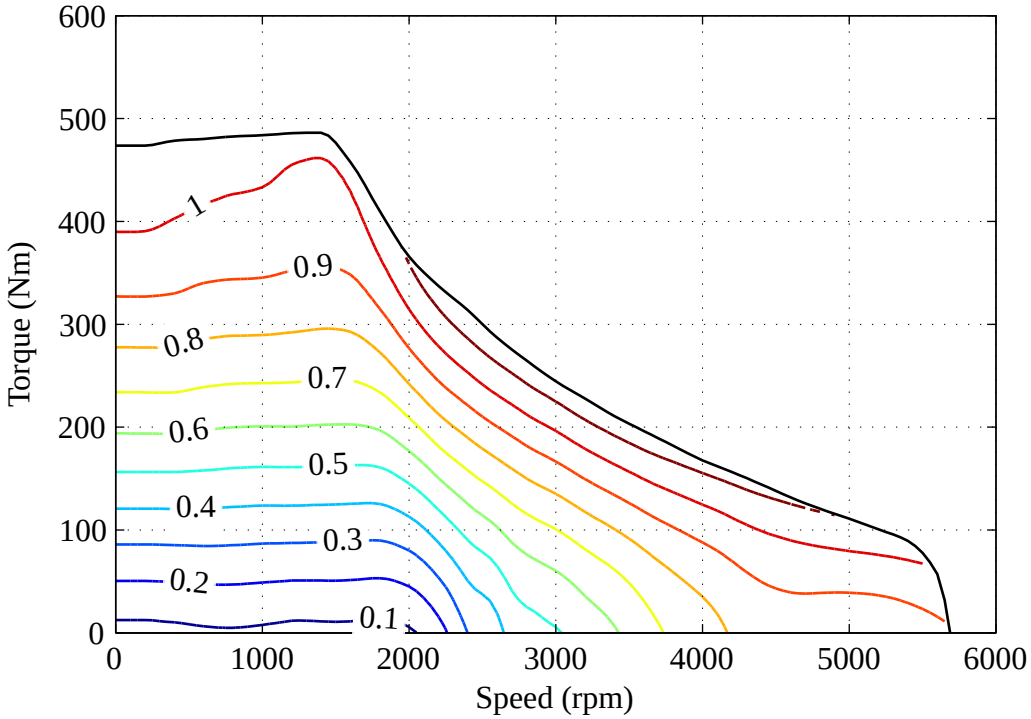

Figure 5.2: BLDC-120 inverter switching loss map (contour values in kW).

At high torques below base speed, the switching losses can be seen to decrease with increasing motor speed. For example, the switching losses at 400 N m decrease from 1.01 kW at 100 rpm to 0.94 kW at 1400 rpm. This is because as the motor speed, and hence the impedance of the motor windings increases, the motor phase currents become more sinusoidal. The reduction of the phase current amplitude towards the end of the conduction

period is reduced giving lower switching losses. In comparison, the switching losses for BLDC-180 and BLAC control below base speed are almost constant with speed, as shown in Figures A.2 and A.9 in Appendix A.

When determining the conduction losses for the inverter, it is also necessary to take into account the PWM duty cycle waveforms in relation to the motor phase currents. This allows the balance of the phase current conduction between the IGBTs and diodes to be determined.

For each point through the electrical cycle, the conduction loss is given by the sum of the IGBT and diode losses calculated using Equations 2.13 and 2.14. From the PWM duty cycle and phase current direction, it is possible to determine the duty ratio for the IGBTs and diodes to give the conduction loss at that point in the electrical cycle. The losses can then be averaged over an electrical cycle to estimate the conduction losses at the chosen motor operating point. The conduction losses for the BLDC-120 control mode are shown in Figure 5.3. The conduction losses are highly dependent on the on-state resistance of the IGBTs and diodes, in addition to the forward voltage drops, and hence follow a similar pattern to the winding losses.

It can be seen for all three control modes that the inverter losses are dominated by the switching losses for a switching frequency of 10 kHz. For BLDC-120 control, the switching losses peak at 1.17 kW whereas the highest conduction loss is 0.89 kW. Therefore, a reduction in switching frequency would have a significant impact on the inverter efficiency. If the switching frequency were halved, Equations 2.16 and 2.17 suggest the switching losses would decrease to 0.58 kW reducing the peak inverter losses by 28 %. However, the increased phase current ripple would also have to be taken into account and the true improvement would be lower.

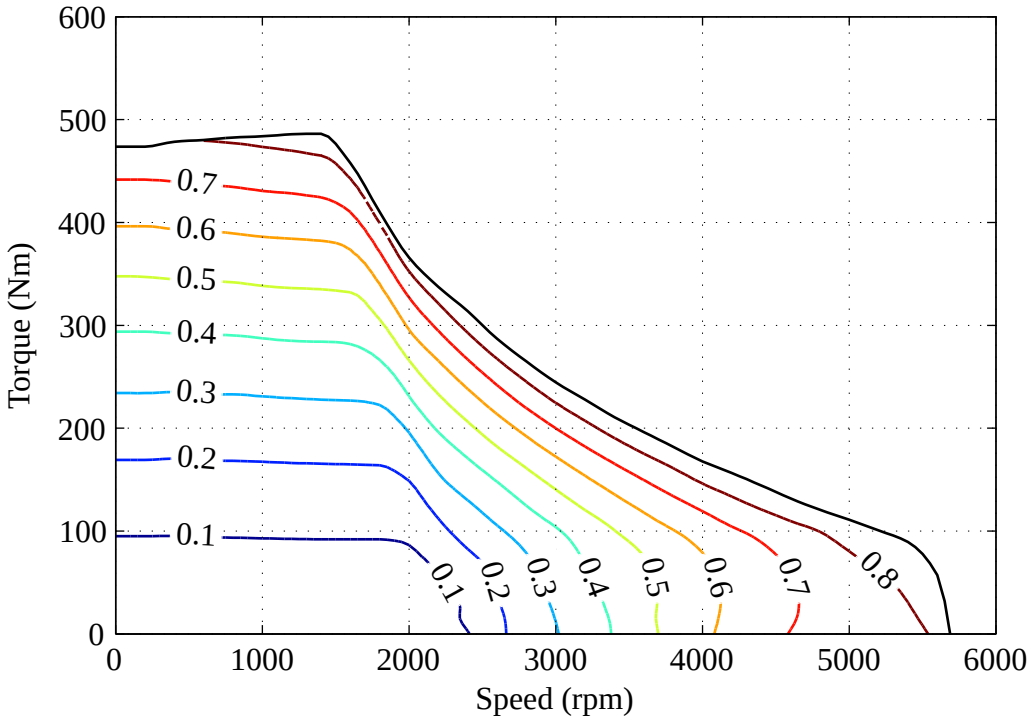

Figure 5.3: BLDC-120 inverter conduction loss map (contour values in kW).

5.3 Finite Element Analysis

A three-dimensional model of the motor has been created using the Opera Vector Fields magnetic FEA software and is shown in Figure 1.3. The model accurately reflects the geometry of the motor's active materials but also allows the non-linear material properties of the components to be specified. The material properties used for the FEA can be found in Appendix B. The finite element analysis will allow the motor iron losses to be determined for each of the control modes. A constant motor temperature of 60 °C has been assumed with material property values taken at this temperature.

In Chapter 4, it was noted that large field weakening currents could result in permanent demagnetisation of the magnets in a PMSM. Figure 5.4 shows the FEA results for the worst case field weakening in the 500 N m YASA motor. The component colours indicate the magnetic flux density, while the arrows show the direction of the magnetic flux. With the 300 A rated current applied entirely to the direct axis, the magnet flux density is reduced to a minimum of 0.44 T, from 0.87 T at no load. The datasheet for the permanent

magnet material [122] shows that at 100 °C, the magnets are not at risk of permanent demagnetisation for this level of field weakening. However, at 140 °C the magnet flux density can only be reduced to 0.65 T before permanent demagnetisation would occur. Therefore, the full operating range predicted for the YASA motor in Chapter 4 is achievable if the rotor can be cooled sufficiently. Design of the motor cooling system is beyond the scope of this thesis.

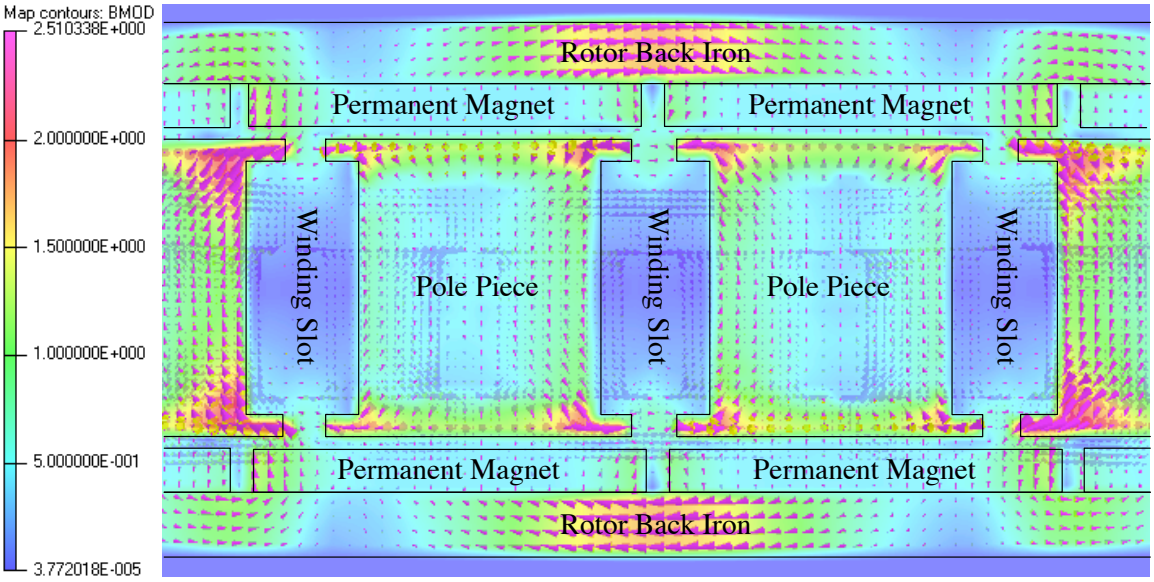

Figure 5.4: Flux paths in the 500 N m YASA motor for a 300 A direct axis current and 0 A quadrature axis current at 0 rpm (BMOD in T).

To determine the hysteresis and eddy current losses, it is necessary to analyse the motor at a sufficient number of time steps to estimate the average loss over an electrical cycle. At each time step, the motor phase currents (determined using the Simulink model) were input for the operating speed, torque and control mode being simulated. An iterative solver was used to determine the magnetic fields in the machine at each time step.

For each motor speed and torque operating point analysed, the losses were determined for thirty six time steps. Each time step corresponded to a 5 °E change in the motor position. It was found that simulated eddy currents had typically reached a steady state with a periodic variation by the tenth step of the simulation. The total machine losses cycle six times per electrical cycle, owing to the 120° phase rotation. Therefore, the average losses

over the last twenty four time steps were taken as the losses for the simulated operating point.

Each FEA took approximately eighteen hours to simulate thirty six time steps for the 474,894 element model on a desktop computer with a 2.0 GHz processor and 2.0 GB of memory. The processing time required makes it unfeasible to simulate the same number of operating points across the theoretical motor operating range as for the Simulink model. Therefore, a small subset of operating points has been used and the estimated losses have been interpolated for the remaining operating points. For each operating point analysed, the phase current waveforms used for the analysis were determined using the Simulink model to more accurately determine the effect of the motor current on the magnetic losses. The winding currents were specified in the form of a look-up table at 5 °E intervals.

5.3.1 Eddy Current Losses

In order to determine the eddy current losses, the rotating magnetic FEA for the motor is used to examine the rate of change of the magnetic field through the machine's active materials. The FEA software calculates the resulting eddy currents for the machine using the specified material conductivities. The eddy current losses are then integrated across the volume of the machine to give a total loss value for each time step. The electrical and magnetic properties for the motor components can be found in Appendix B.

Figures 5.5 to 5.7 show the eddy current densities present in the rotor back iron, magnets and pole pieces for the BLDC-120 control mode with an RMS phase current of 212 A at 500 rpm. The eddy currents are more concentrated spatially across the machine for the BLDC-120 control mode than for the BLDC-180 or BLAC control modes as only two thirds of the windings are conducting at any time.

The high rate of change of phase currents resulting from the BLDC-120 six-step commutation gives rise to the highest eddy current losses, as shown in Figure 5.8. The eddy current losses increase significantly each time the motor is commutated, but decays

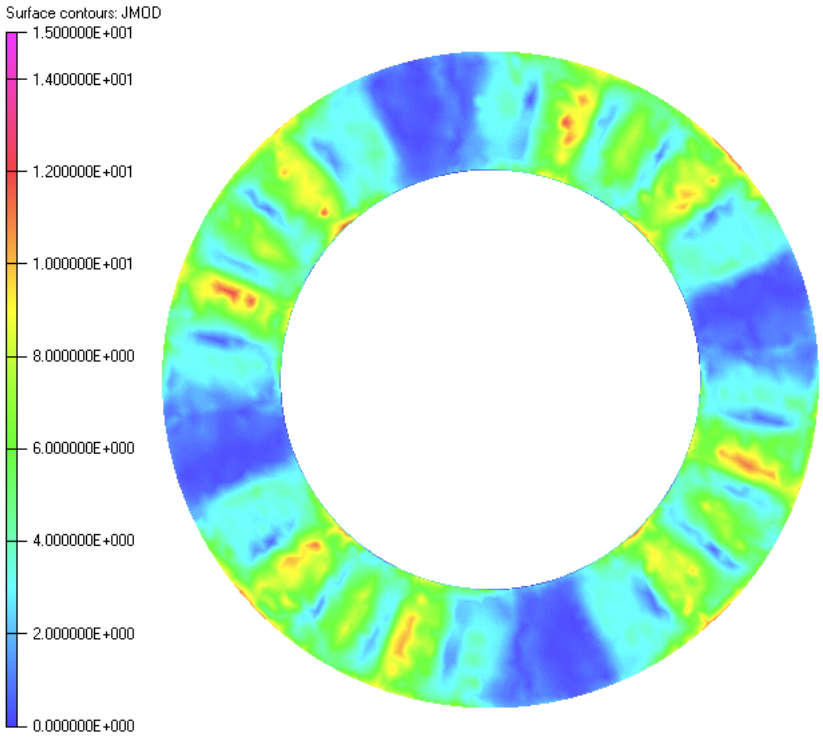

Figure 5.5: Back iron eddy current density for BLDC-120 control with a 212 A RMS phase current at 500 rpm (JMOD in A/mm^2).

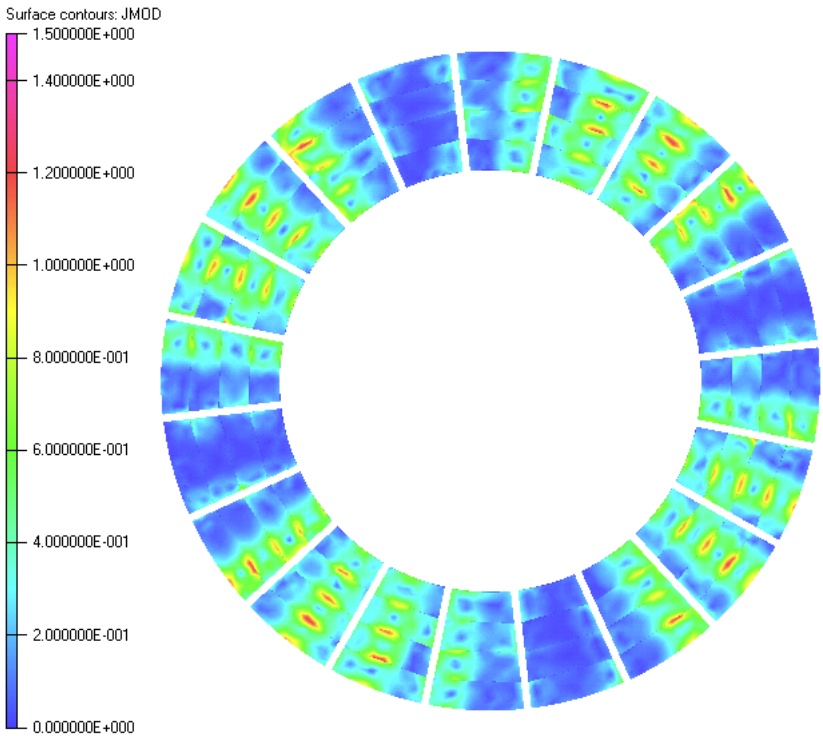

Figure 5.6: Magnet eddy current density for BLDC-120 control with a 212 A RMS phase current at 500 rpm (JMOD in A/mm^2).

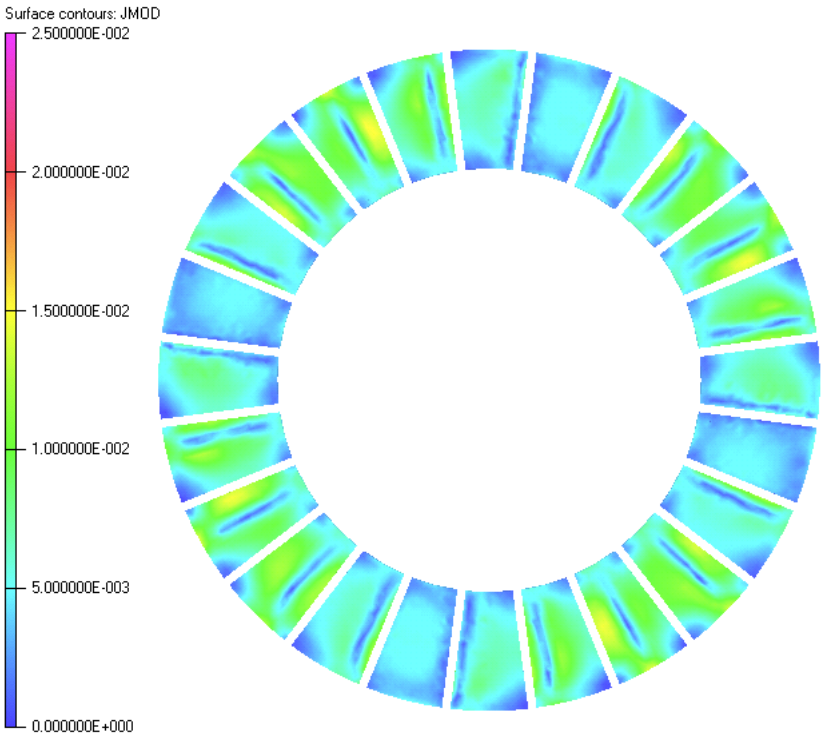

Figure 5.7: Stator eddy current density for BLDC-120 control with a 212 A RMS phase current at 500 rpm (JMOD in A/mm^2).

away through the commutation period to only 10.3 % of the peak value.

The same pattern is observed for the BLDC-180 control mode, but with a significantly reduced peak eddy current loss at only 2.3 times the steady state loss. The BLAC eddy current losses are almost constant throughout the electrical cycle, with only a 15 % variation from maximum to minimum value. Figures 5.9 and 5.10 show the difference in the magnetic flux density through one of the stator pole pieces and one of the rotor magnets for each of the control modes over an electrical cycle. It can be seen that under BLDC-120 control, the motor components are exposed to the highest rates of change of magnetic flux density, resulting in the highest eddy current losses. The BLAC flux density has the lowest harmonic content for a 212 A RMS phase current at 500 rpm, and therefore the lowest rate of change of magnetic flux density. This gives in the lowest cycle average eddy current loss of 1.05 kW. The BLDC-120 flux density has significantly more harmonic components resulting in the highest average eddy current loss at 2.13 kW. The BLDC-180 average eddy

current losses are only slightly greater than for BLAC control at 1.23 kW.

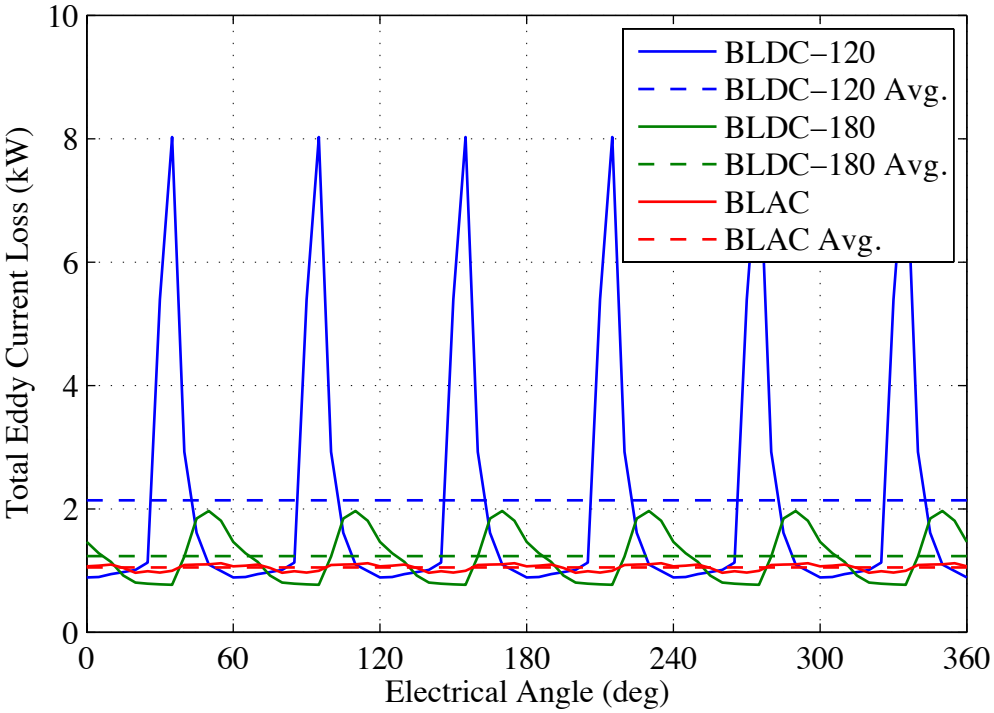

Figure 5.8: A comparison of the total eddy current losses for different control strategies at 500 rpm with an RMS phase current of 212 A.

In order to minimise the number of FEAs required to estimate the eddy current losses over the required operating range, the following procedure was used to determine the losses for each motor control mode. Firstly, the eddy current losses were determined at six speeds, including the base speed and the theoretical maximum speed, for RMS phase currents of 71 A, 141 A and 212 A (33 %, 66 % and 100 % of the rated maximum RMS motor phase current). The no load eddy current losses were also determined at 2000 rpm, 4000 rpm and 6000 rpm.

The trend shown by the FEA results has been approximated by Equation 5.1, where ω_b is the base speed, and has been fitted to the FEA results using a least squares method. The form of this equation has been chosen to fit the exponential dependence of the loss component on both the motor speed and RMS phase current. It also allows for the discontinuity in the losses above base speed where a field weakening current is required.

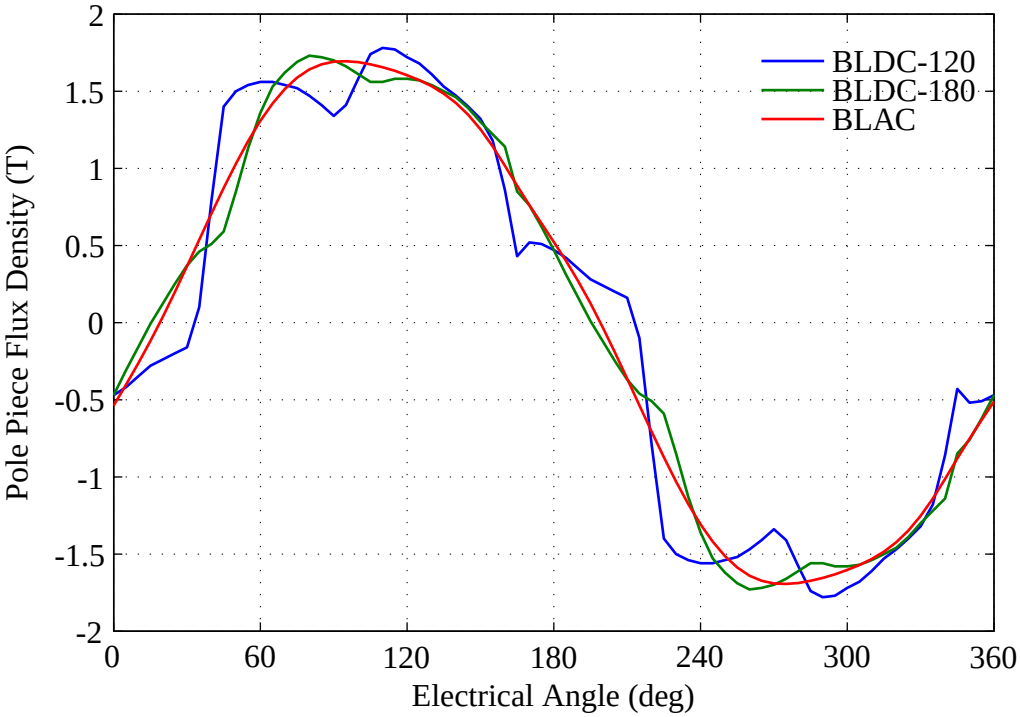

Figure 5.9: The pole piece flux density for different control modes at 500 rpm with an RMS phase current of 212 A.

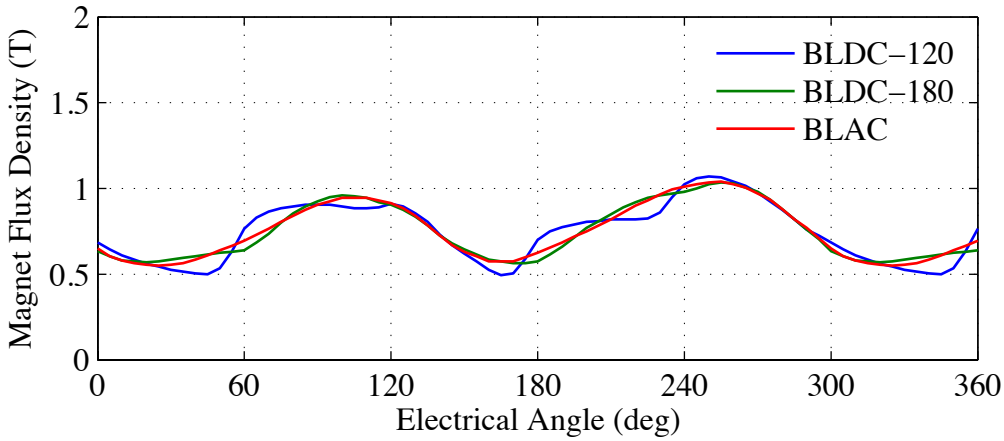

Figure 5.10: The magnet flux density for different control modes at 500 rpm with an RMS phase current of 212 A.

The first term of the equation describes the no load losses, which increase exponentially with speed and are independent of the phase current. The second term describes the increase in losses over the no-load losses as a result of the phase current. This term increases with both motor speed and the phase current amplitude. At the base speed, which changes as a function of the motor phase current, there is a discontinuity in the shape of the loss curve, resulting from the field weakening current. A third term is added to the loss equation to describe the different rate of increase in losses with motor speed and the RMS phase current above base speed. The same equation (with different coefficient values) has also been used to interpolate the hysteresis loss data in the following section.

$$P_{eddy}(\omega, I_{ph,RMS}) = \begin{cases} a_1 \omega^{a_2} + b_1 \omega^{b_2} I_{ph,RMS}^{b_3} & \text{for } \omega \leq \omega_b \\ a_1 \omega^{a_2} + b_1 \omega_b^{b_2} I_{ph,RMS}^{b_3} & \\ \quad + c_1 (\omega - \omega_b)^{c_2} I_{ph,RMS}^{c_3} & \text{for } \omega > \omega_b \end{cases} \tag{5.1}$$

Figure 5.11 shows the eddy current losses for the BLDC-120 control mode with the approximated loss curves closely fitting the FEA results. The coefficients calculated for each control mode using a least squares data fitting method are given in Table 5.1 and give a worst case error of 0.34 kW between the FEA and approximated data (1.03 % of the maximum loss). The motor output torque at each selected phase current and speed have been determined using the Simulink model. The eddy current losses at each point can then be determined from Equation 5.1 for use in the system efficiency map and are shown in Figure 5.12.

The eddy current losses can be seen to increase exponentially with both speed and torque below the base speed, as a result of the increasing magnetic field applied by the stator and the increased rate of change of flux with speed. Beyond the base speed, the eddy current losses increase more linearly with speed as the field weakening current component

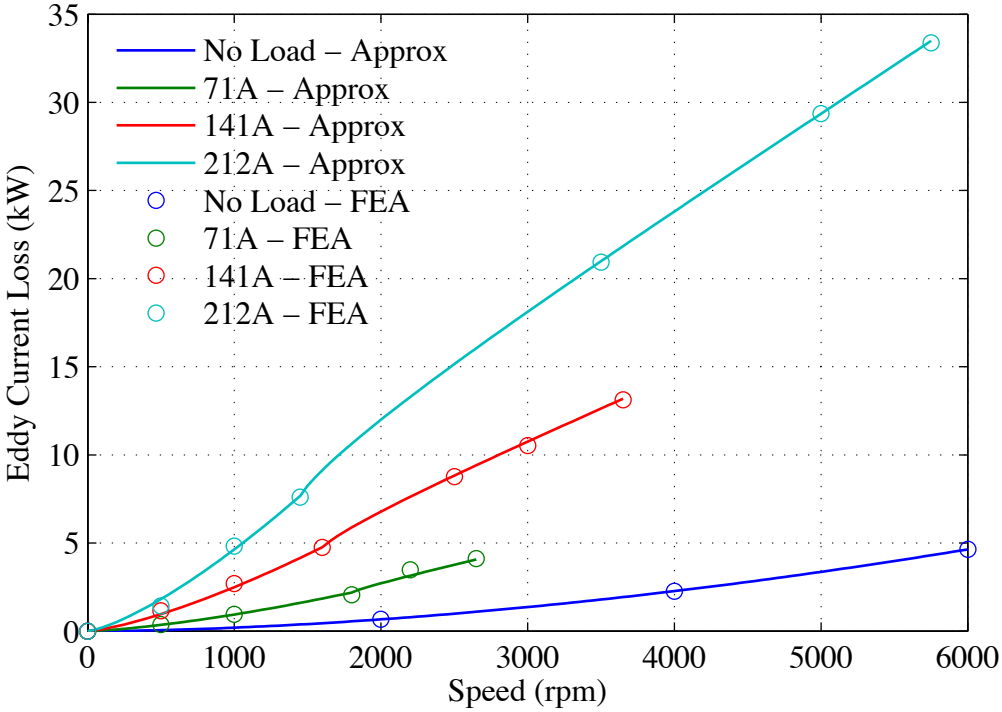

Figure 5.11: BLDC-120 eddy current loss approximation fitted to FEA data.

Table 5.1: Eddy current loss approximation coefficients

Coefficient	BLDC-120	BLDC-180	BLAC
a_1	1.021×10^{-3}	1.021×10^{-3}	1.021×10^{-3}
a_2	1.762	1.762	1.762
b_1	7.315×10^{-5}	1.284×10^{-5}	2.089×10^{-6}
b_2	1.336	1.451	1.563
b_3	1.623	1.751	1.925
c_1	1.794×10^{-2}	5.452×10^{-2}	5.138×10^{-2}
c_2	0.823	0.865	0.873
c_3	1.331	1.076	1.079

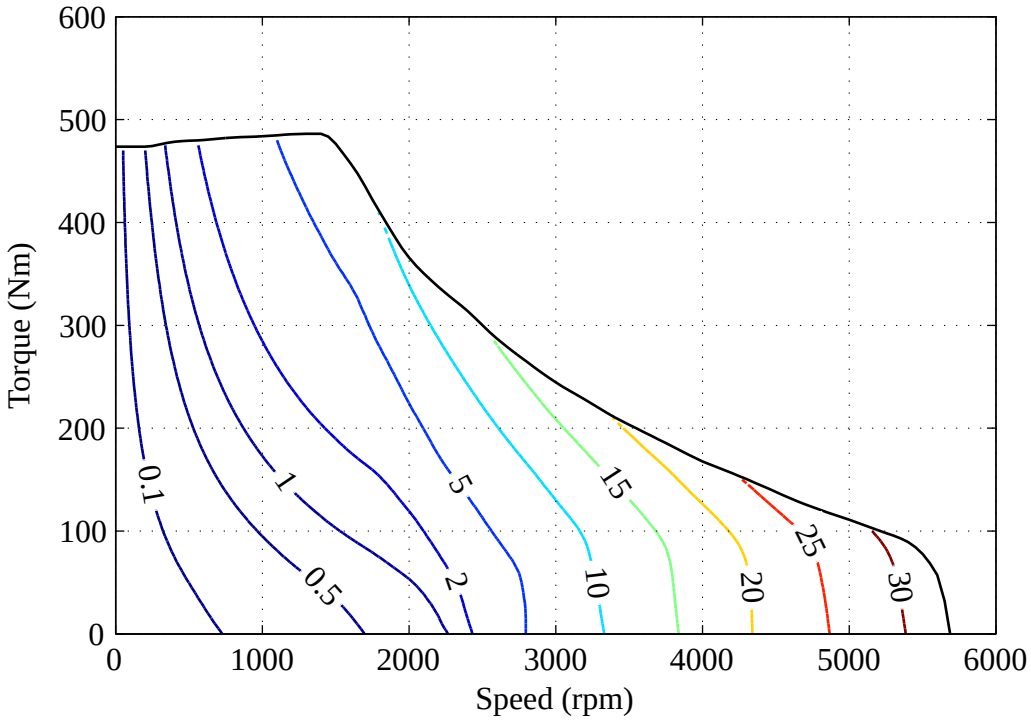

Figure 5.12: BLDC-120 eddy current loss map (contour values in kW).

opposes the magnetic field produced by the permanent magnets. This reduces the amplitude of the magnetic field seen by the stator.

5.3.2 Hysteresis Losses

The rotating FEA also allows calculation of the stator hysteresis losses from the pole piece flux density variations. The flux patterns for the pole pieces have been determined for different motor speeds and torques by looking at the flux densities through their centres over one electrical cycle using finite element modelling. This method does not take into account the higher flux densities around the teeth of the pole pieces which will experience greater hysteresis losses. However, it allows an estimation of the hysteresis losses in the bulk of the material where the majority of losses will occur. By performing a Fourier transform of the flux density curves, the losses can be determined for each of the harmonic components using Equation 2.10.

In Chapter 2, it was noted that the iron losses in the rotors of PMSMs are often neglected

in loss calculations as the flux density variation is small compared to that of the stator. Figure 5.10 shows the flux density variation through the centre of one the permanent magnets in the YASA motor for each of the control modes. The flux density is not constant in any of the control modes and the magnets will therefore suffer from hysteresis losses, as will the rotor back irons which exhibit a similarly low flux variation. However, the amplitude of the flux variation for the magnets is only 15.8 % of the amplitude for the pole pieces in the BLDC-120 control mode at 500 rpm and 212 A RMS phase current. The rotor hysteresis loss will therefore be small in comparison to the stator and will be neglected in the absence of accurate hysteresis loss data for the magnetic materials. The hysteresis losses will therefore be underestimated in the following analysis.

The high harmonic content of the BLDC-120 flux density shown in Figure 5.9 causes higher hysteresis losses in the stator than for BLDC-180 or BLAC control modes. Figure 5.13 shows the relative amplitudes of the flux density harmonics and Figure 5.14 shows the contribution of each harmonic to the total hysteresis losses for RMS phase currents of 212 A at 500 rpm.

The amplitudes of the fundamental frequency components for each control mode are very similar at this operating point, but the fifth harmonic for the BLDC-120 mode at 0.298 T is 2.3 times greater than for BLDC-180 at 0.128 T and 8.3 times greater than for BLAC at 0.036 T. The total hysteresis losses for BLDC-120, BLDC-180, and BLAC are 234.8 W, 160.3 W and 149.0 W respectively.

As was the case for calculating eddy current losses, it is impractical to determine FEA results for every speed and torque point on the efficiency map from which the hysteresis losses can be determined. Again, a limited number of results have been used to approximate the loss trend as a function of motor speed and peak phase current. Figure 5.15 shows the hysteresis losses for the BLDC-120 control mode. The coefficients calculated for each control mode using a least squares data fitting method are given in Table 5.2 and give a worst case error of 0.03 kW between the FEA and approximated results (1.22 %

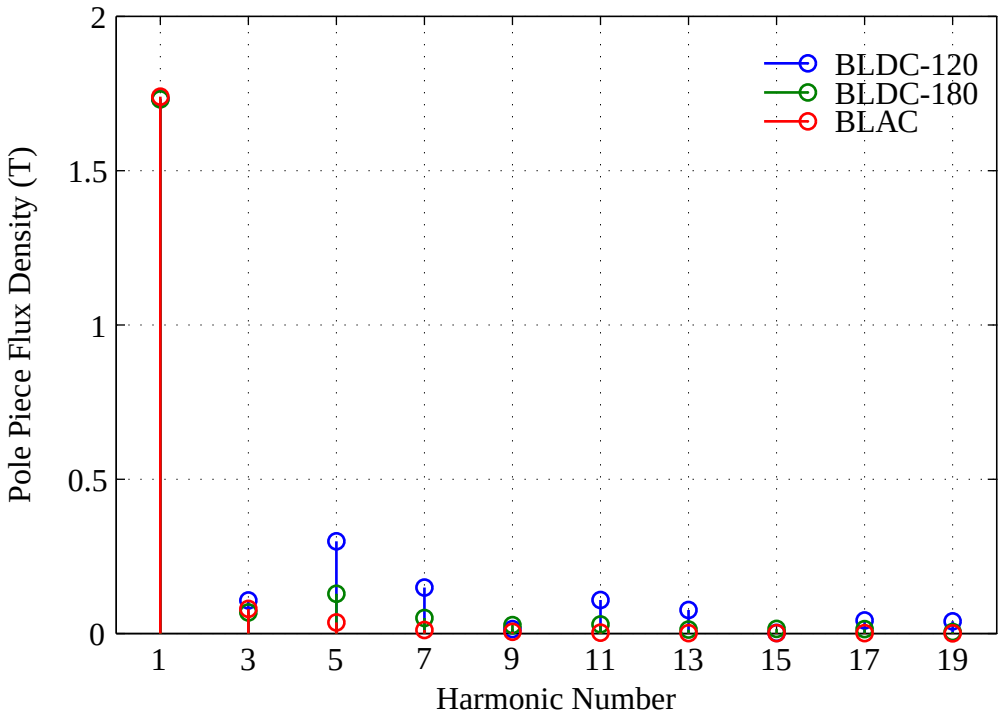

Figure 5.13: The pole piece flux density harmonics for different control strategies at 500 rpm with RMS phase currents of 212 A.

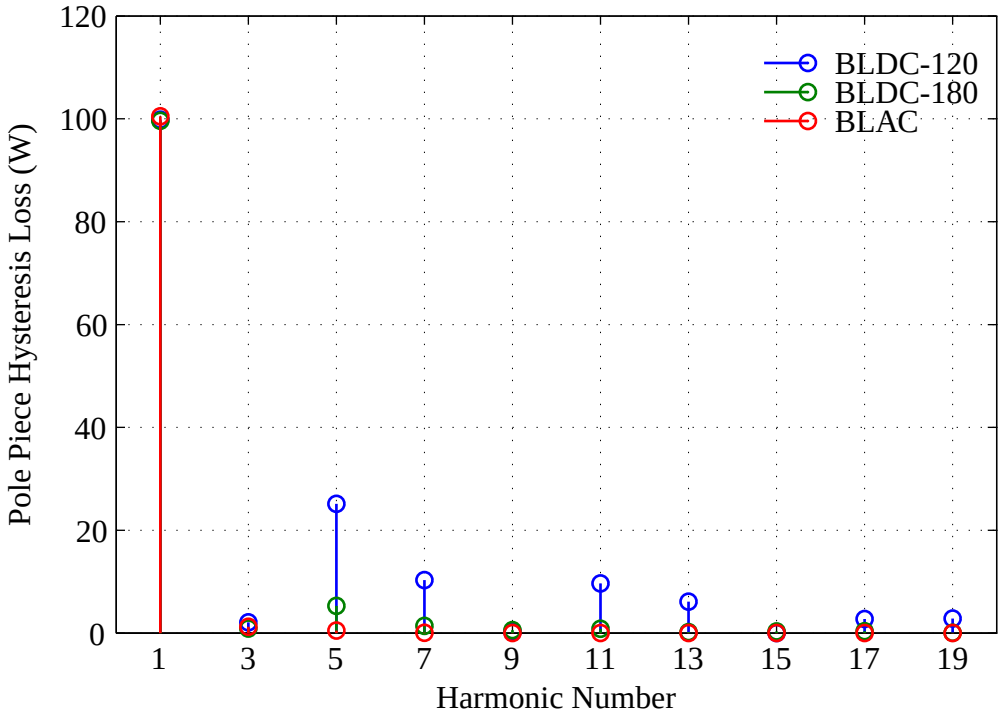

Figure 5.14: The pole piece hysteresis loss components for different control strategies at 500 rpm with RMS phase currents of 212 A.

of the highest loss). The hysteresis losses at each point on the efficiency map have been determined from Equation 5.1 and are shown in Figure 5.16.

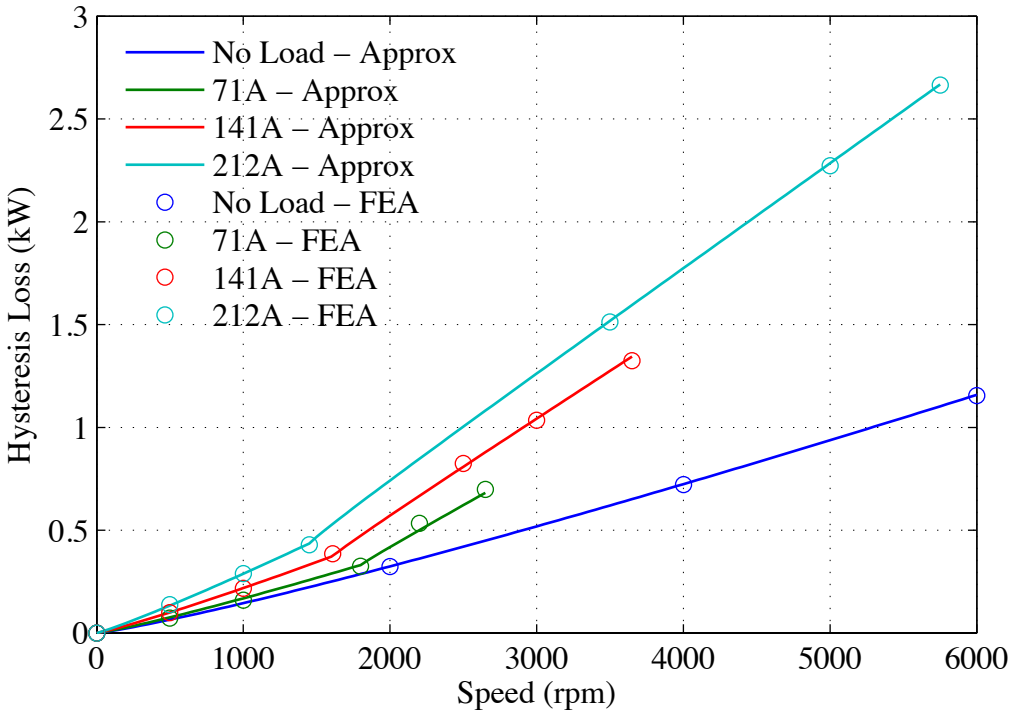

Figure 5.15: BLDC-120 hysteresis loss approximation fitted to FEA data.

The hysteresis losses can be seen to increase almost linearly with speed for a given RMS phase current, but with a higher rate of increase above the base speed. As the phase difference between the back EMF and phase currents increases beyond base speed, the amplitude of the flux density waveform for the pole pieces also increases giving higher hysteresis losses.

5.4 Simulated Efficiency Maps

Having determined the motor and inverter loss components for the three control modes, it is possible to estimate the motor and inverter efficiencies over the system operating range. The mechanical losses for the motor have not been estimated in the previous sections as the mechanical loss coefficient required for Equation 2.12 is not known. It has also not

Table 5.2: Hysteresis loss approximation coefficients

Coefficient	BLDC-120	BLDC-180	BLAC
a_1	4.834×10^{-2}	4.834×10^{-2}	4.834×10^{-2}
a_2	1.159	1.159	1.159
b_1	1.401×10^{-5}	1.300×10^{-5}	1.286×10^{-7}
b_2	1.060	1.034	1.203
b_3	1.647	1.613	2.235
c_1	5.998×10^{-2}	2.547	0.253
c_2	0.917	0.486	0.888
c_3	0.438	0.482	0.229

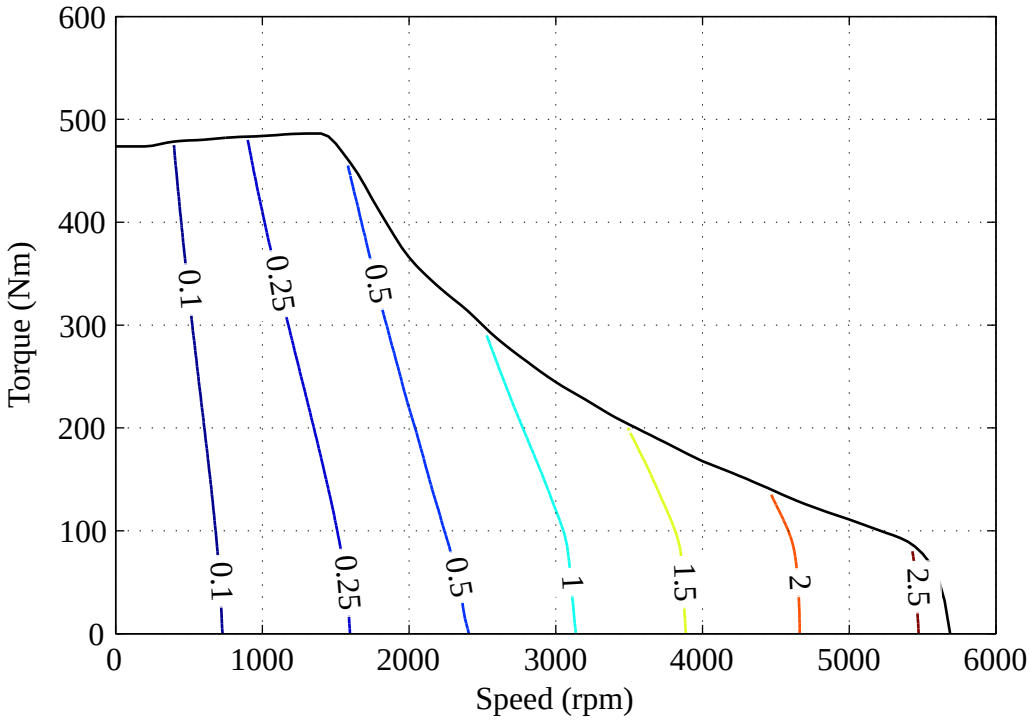

Figure 5.16: BLDC hysteresis loss map (contour values in kW).

been possible to measure this coefficient using the experimental setup in Section 5.5.1. This is because the mechanical losses are too small to accurately measure and separate out from the other loss components using the available equipment. Equation 2.12 shows that the mechanical losses depend only on the motor speed and not the control mode used. Therefore, neglecting this component will not have a significant impact on a comparison of the total losses for the three control modes.

The motor efficiency is calculated using Equations 5.2 and 5.3 and the motor efficiency map is shown for the BLDC-120 mode in Figure 5.17. The motor efficiency peaks at 92 % in the region of 80 N m and 900 rpm. The efficiency decreases sharply beyond the base speed as the required field weakening current increases.

$$\eta_{motor}(T,\omega) = \frac{P_{motor,out}(T,\omega)}{P_{motor,out}(T,\omega) + \sum P_{loss,motor}(T,\omega)} \tag{5.2}$$

$$P_{motor,out}(T,\omega) = T\omega_{motor} \tag{5.3}$$

The efficiency of the inverter can also be calculated from the required motor input power and the inverter loss components using Equations 5.4 and 5.5. The resulting inverter efficiency map for the BLDC-120 control mode is shown in Figure 5.18. The inverter efficiency peaks at 97.5 % in the region of 200 N m and 2000 rpm. Below the base speed, the inverter efficiency increases with the motor speed. This is because the inverter loss do not increase significantly with speed, as shown in Figures 5.2 and 5.3. The motor output power therefore increases relative to the losses. The total inverter losses increase almost linearly with torque below the base speed. This gives little variation in the efficiency as the torque increases over most of the torque range. However, the efficiency drops off sharply above the base speed as a result of the field weakening current. Both the switching and conduction losses are highly dependent on the motor phase currents and so the losses increase with the amount of field weakening required, while the motor output power decreases for a given

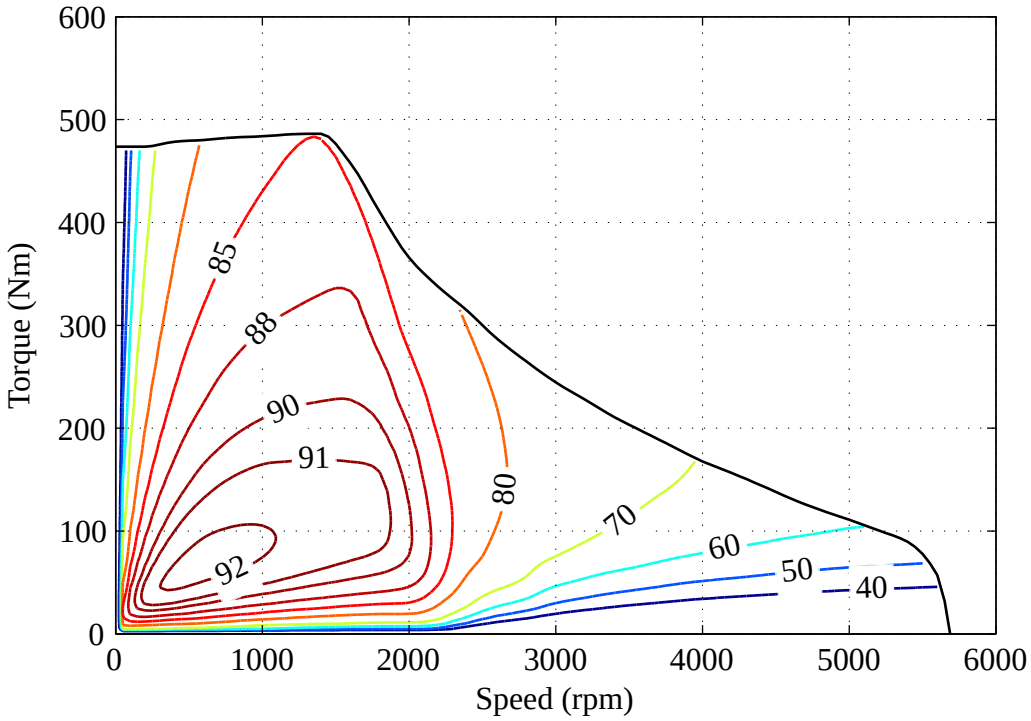

Figure 5.17: BLDC-120 motor efficiency map (contour values in %).

RMS phase current limit.

$$\eta_{inverter}(T,\omega) = \frac{P_{motor,in}(T,\omega)}{P_{motor,in}(T,\omega) + \sum P_{loss,inverter}(T,\omega)} \tag{5.4}$$

$$P_{motor,in} = \eta_{motor} P_{motor,out} \tag{5.5}$$

The overall system efficiency is given by the product of the motor and inverter efficiencies. The combined motor and inverter efficiency map for BLDC-120 operation is shown in Figure 5.19 with the peak efficiency falling to 89.2 % and shifting to 150 N m and 1600 rpm.

Using an identical method to that described above, the BLDC-180 and BLAC control mode efficiency maps have also been determined and are shown in Figures 5.20 and 5.21. It can be seen that the BLAC mode gives the highest estimated peak efficiency at 90.7 % compared to 89.7 % for the BLDC-180 mode and 89.2 % for the BLDC-120 mode.

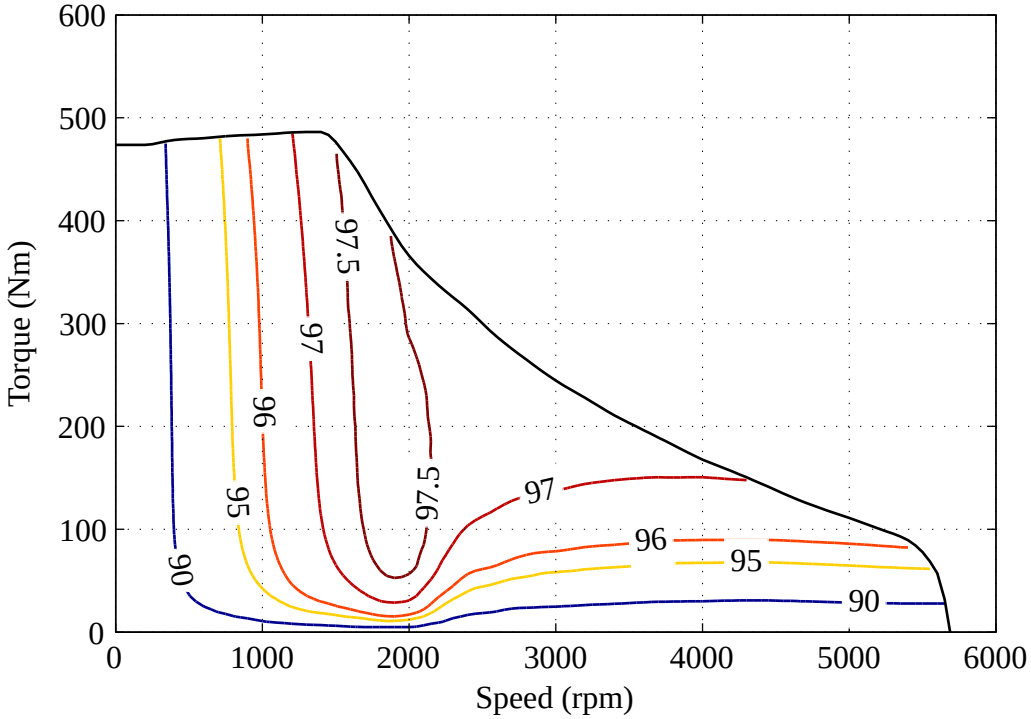

Figure 5.18: BLDC-120 inverter efficiency map (contour values in %).

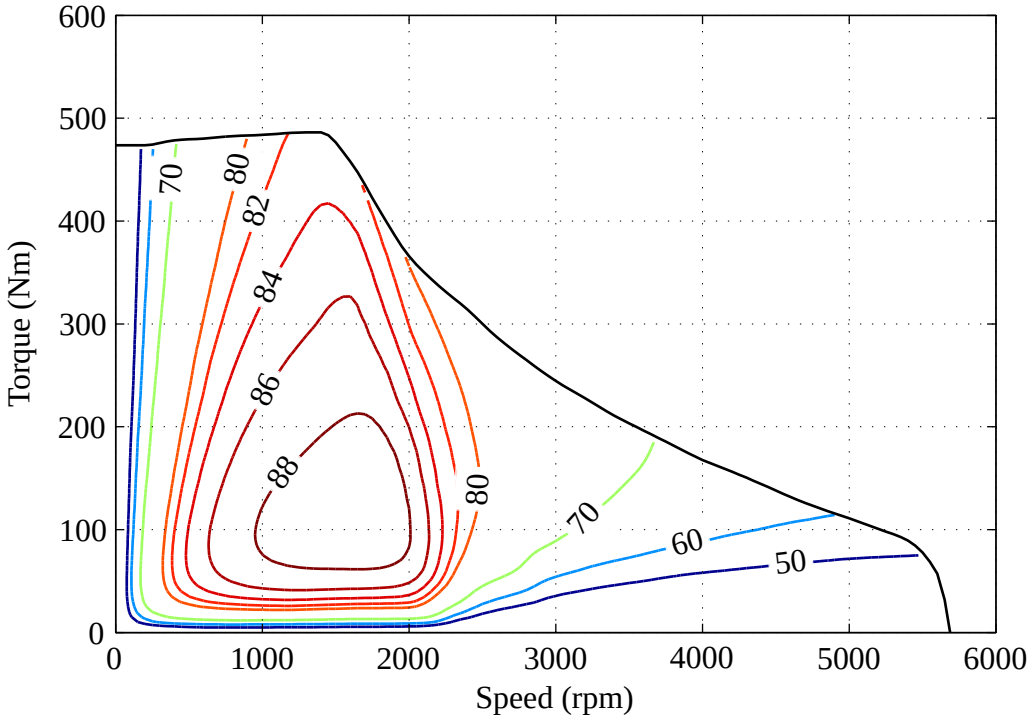

Figure 5.19: BLDC-120 combined motor and inverter efficiency map (contour values in %).

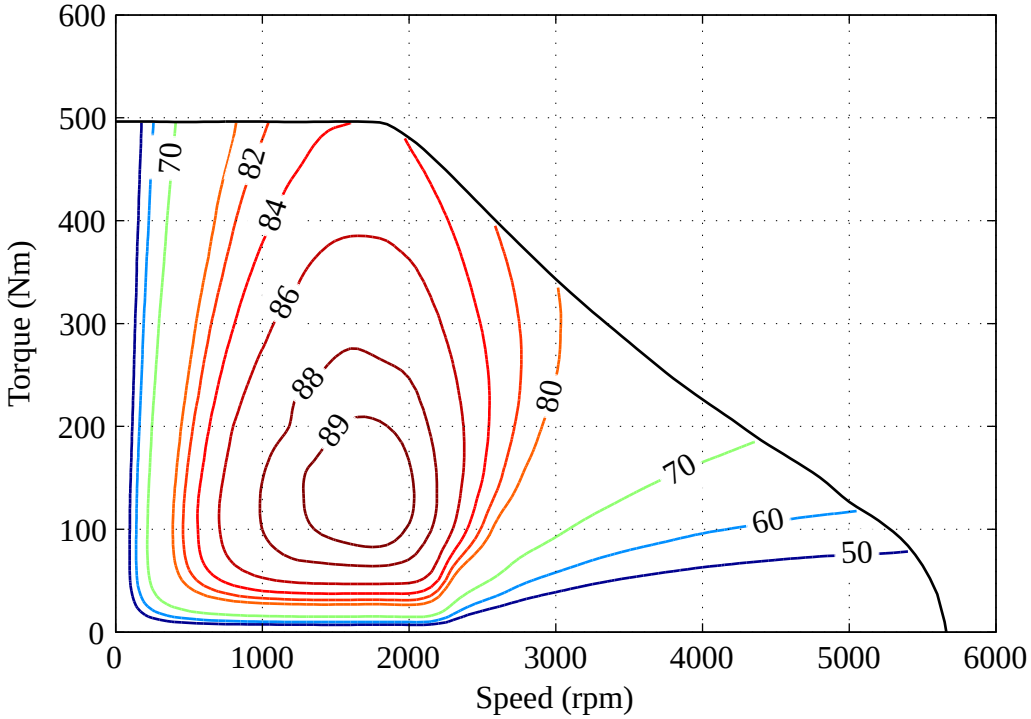

Figure 5.20: BLDC-180 combined motor and inverter efficiency map (contour values in %).

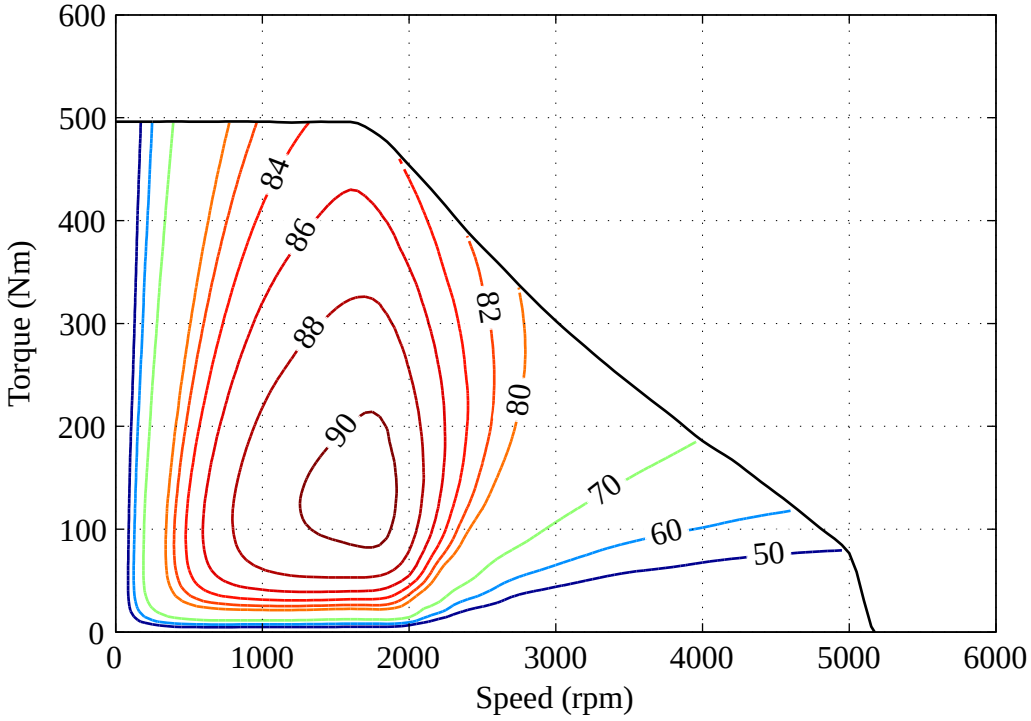

Figure 5.21: BLAC combined motor and inverter efficiency map (contour values in %).

5.5 Experimental Efficiency

To verify the method used to estimate the motor and inverter efficiencies, the calculated values must be compared to experimental results. A motor experimental test rig has been used to collect results for BLDC-120 and BLAC operation and is described in the following sections.

5.5.1 Experimental Method

The motor and inverter losses have been measured experimentally using a back-to-back test rig shown in Figure 5.22 and schematically in Figure 5.23. Two 500 N m YASA motors have been coupled in a back-to-back configuration with a torque sensor to measure the output torque and speed. Each machine is controlled by a Semikron SKAI inverter. The machines both use a low resolution optical position sensor to determine the rotor position with an output change every 60 °E.

The inverters and control systems allow each machine to operate for both motoring and regenerative braking. When the machine under test is motoring, the load motor is generating and vice versa. The DC terminals of the two inverters are connected in parallel so that power produced by the generating machine can be recirculated to the motoring machine. This reduces the input power requirement of the DC supply. The DC supply is then only required to supply the system losses. Each inverter contains a 1 mF DC link capacitor to help stabilise the DC link voltage. No other energy storage systems are used.

The test motor is operated under torque control as would be the case for a vehicle application. The load motor is operated under speed control so that the desired operating load and speed of the test motor can be maintained. To measure the system efficiency, the input and output powers are measured for speed and torque intervals over the operating range of interest. The input DC link voltage and current of the inverter of the test motor is measured so the input power to the system can be calculated. The test motor speed and

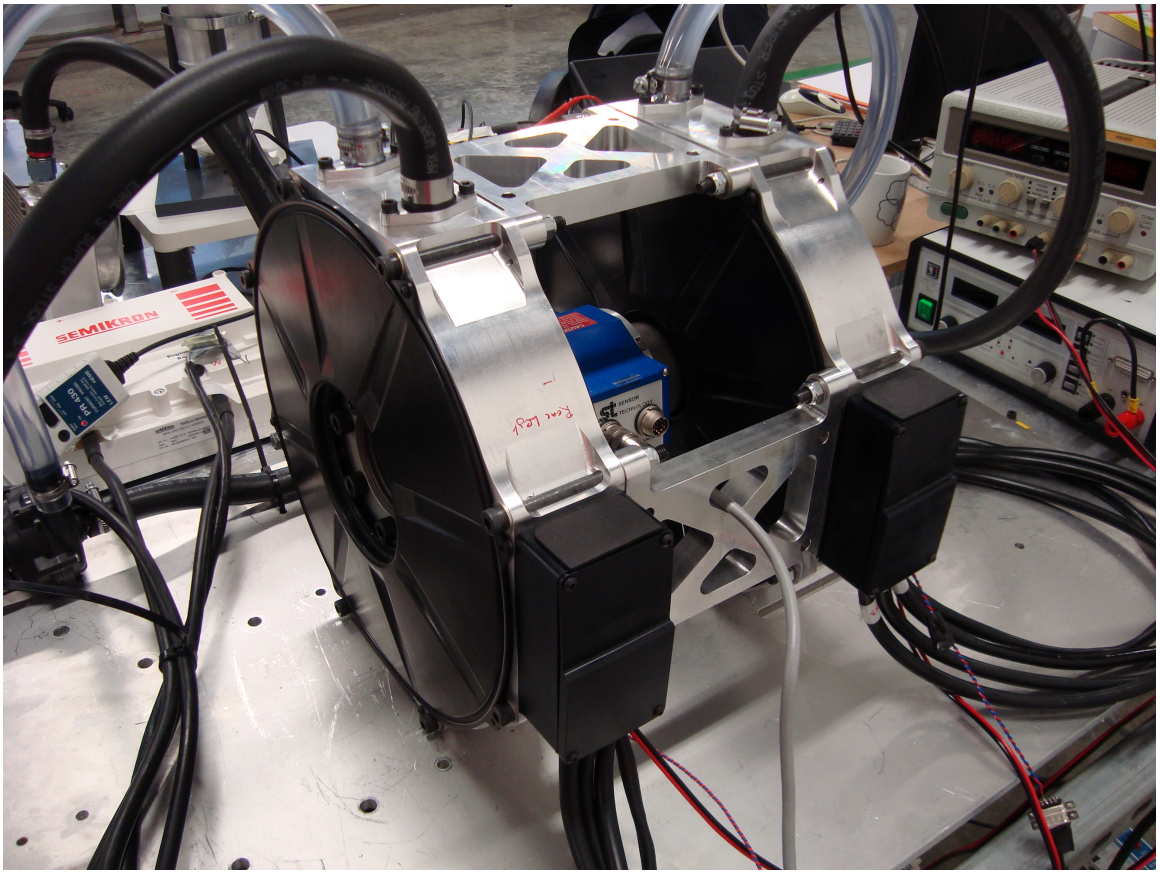

Figure 5.22: The experimental back to back motor test rig consisting of two 500 N m YASA motors connected with a torque sensor.

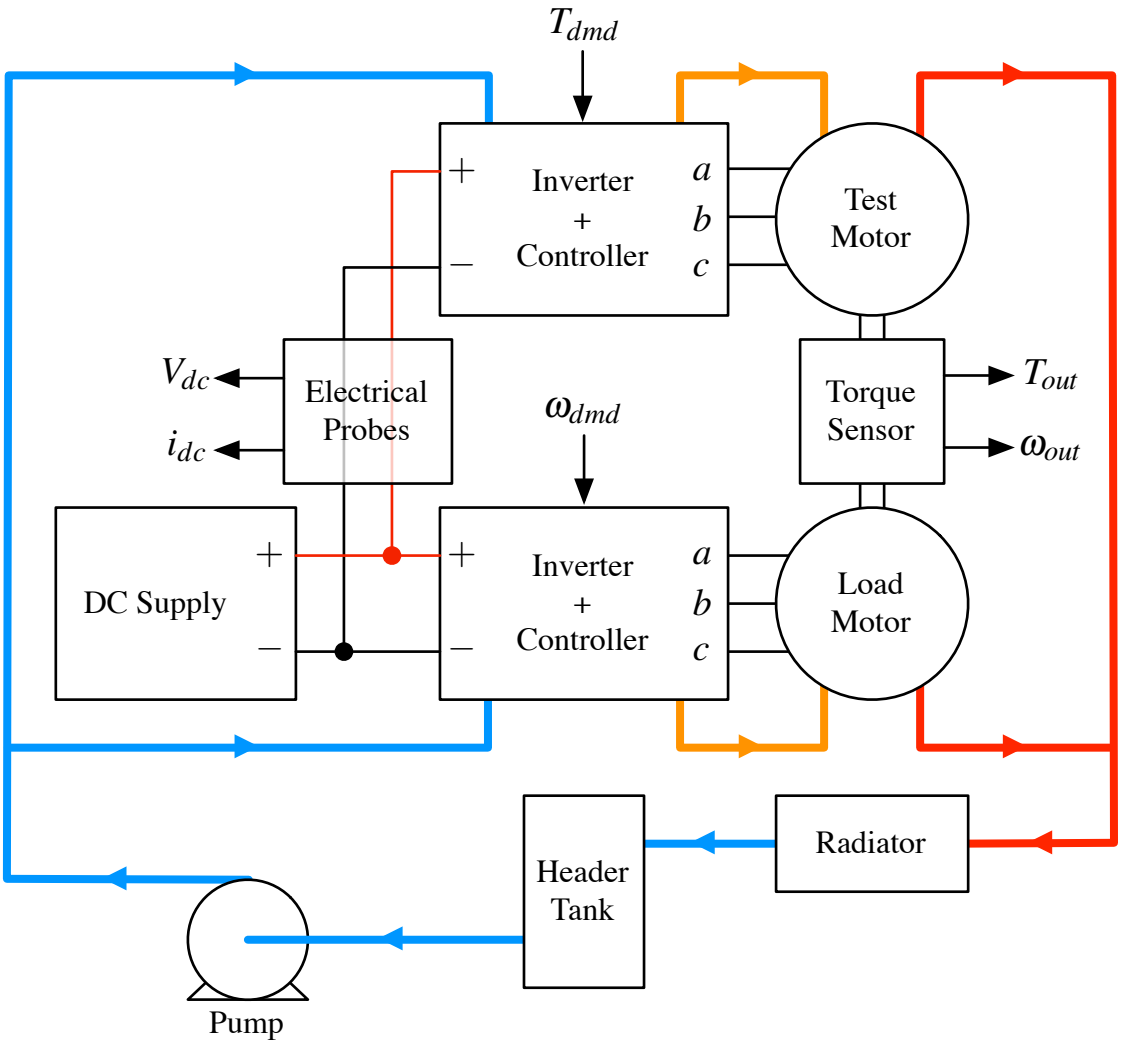

Figure 5.23: Schematic of the experimental motor test rig.

output torque measured by the torque sensor are used to calculate the output power. The efficiency can then be calculated using Equation 5.6.

$$\eta_{system} = \frac{T_{out}\omega_{out}}{V_{dc}i_{dc}} \tag{5.6}$$

The experimental setup only allows the overall system efficiency to be measured. It is not possible to directly determine the motor and inverter efficiency maps or individual loss components. However, it will allow the experimentally measured efficiencies to be compared to the values determined through simulation. For each sample point, the system is allowed to reach a steady state before measurements are taken. The input and output powers are averaged over a one second period to allow for small fluctuations in speed and torque.

The two motors and inverters used on the test rig are liquid cooled by a common cooling circuit, as shown in Figure 5.23. Cooling fluid is pumped from a header tank, through both inverters and motors in parallel, before returning to the header tank through a radiator. The temperature of the test motor is controlled by manually adjusting the pump and radiator fan speeds. The motor winding and rotor temperatures are monitored using the embedded temperature sensors. Before taking the measurements for each experimental test point, the motor was allowed to reach a temperature of approximately 60 °C, the temperature used for the calculation of the simulated motor efficiency maps.

The torque and speed of the experimental rig is limited to 400 N m and 1000 rpm by the torque transducer capabilities. Below 50 N m, the accuracy of the torque measurements is too low to take meaningful efficiency measurements. The load motor is also unable to accurately control the motor speed below 200 rpm. Therefore, the comparison of experimental and simulated motor efficiencies must be limited to the range of 50 N m to 400 N m and 200 rpm to 1000 rpm.

Table 5.3: Accuracy of sensors used to take experimental motor efficiency measurements [21–23].

Sensor	Sensor Range	Accuracy
DC link current	±400 A	1 %
DC link voltage	±700 V	2 %
Motor torque	±400 N m	1 %
Motor speed	±1000 rpm	0.1 rpm

5.5.2 Experimental Efficiency Maps

Electrical input and mechanical output power measurements have been taken for the test motor and inverter under both BLDC-120 and BLAC control over the operating range of 50 N m to 400 N m and 200 rpm to 1000 rpm. Sample point steps of approximately 50 N m and 100 rpm have been used. The system efficiency at each step was then calculated. An efficiency map over the torque and speed range has been produced by fitting a surface to the experimental data using the Gridfit interpolation tool [125] with a smoothness factor of one. The time limited availability of the experimental equipment prevented efficiency measurements being taken for the BLDC-180 mode. Table 5.3 gives the measurement accuracies of the sensors used when collecting experimental efficiency measurements. This gives an overall estimate of 2.5 % accuracy for efficiency measurements at 400 N m and 1000 rpm.

Figures 5.24(a) and 5.25(a) show the experimental efficiency maps for the BLDC-120 and BLAC control modes respectively. The efficiency maps both peak at over 88 % in the region of 150 N m and 1000 rpm. However, the BLDC-120 efficiency decreases more quickly than the BLAC efficiency as the motor torque increases, falling to 84 % at 300 N m and 1000 rpm whereas the BLAC efficiency has only dropped to 87 %. This is a result of the additional harmonic content of the BLDC current waveforms giving rise to additional losses.

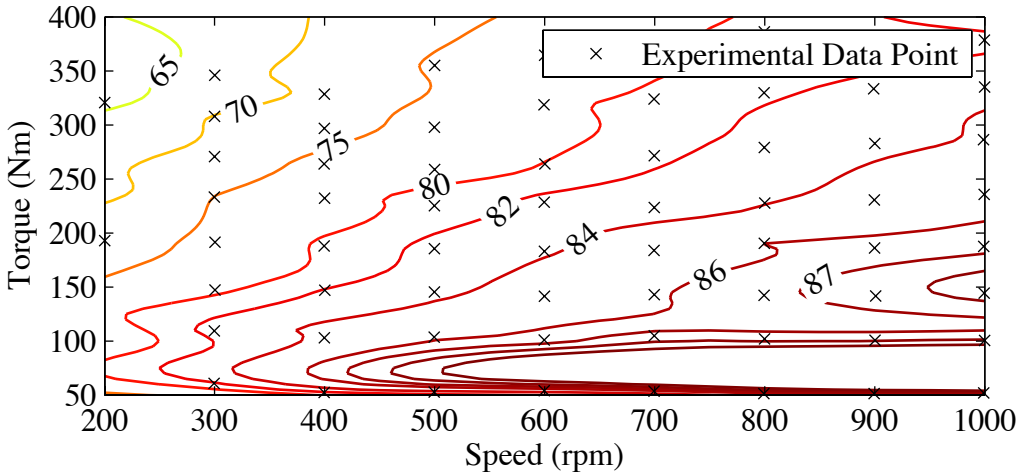

(a) Experimentally determined efficiency

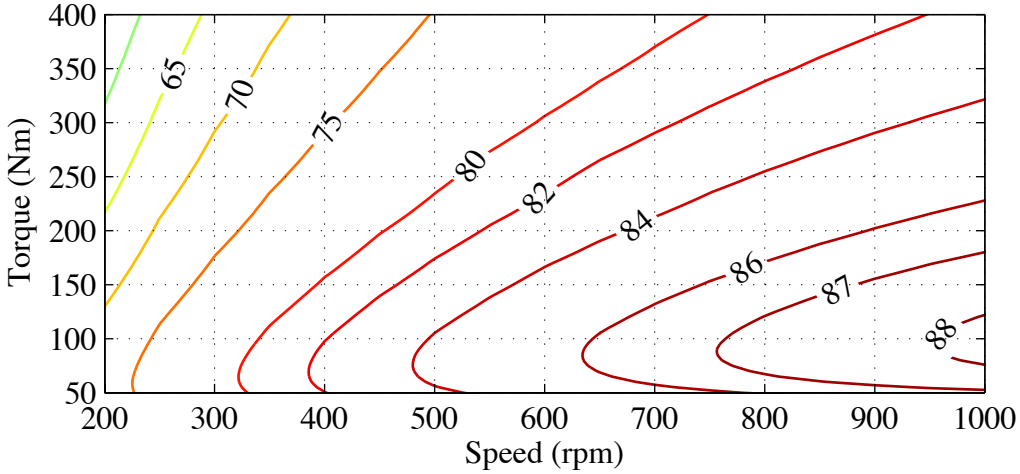

(b) Simulated efficiency over the experimental range

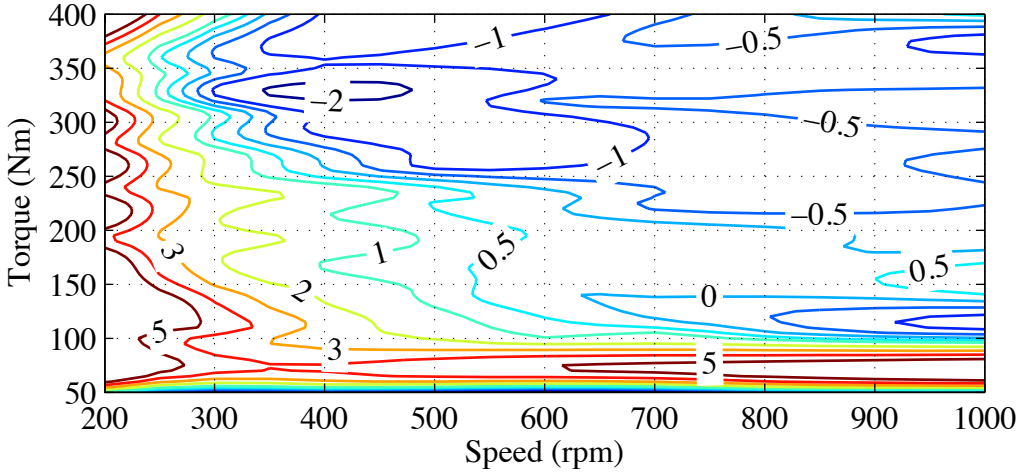

(c) Discrepancy between simulated and experimental efficiency

Figure 5.24: A comparison of experimental and simulated system efficiency maps for BLDC-120 operation (contour values in %).

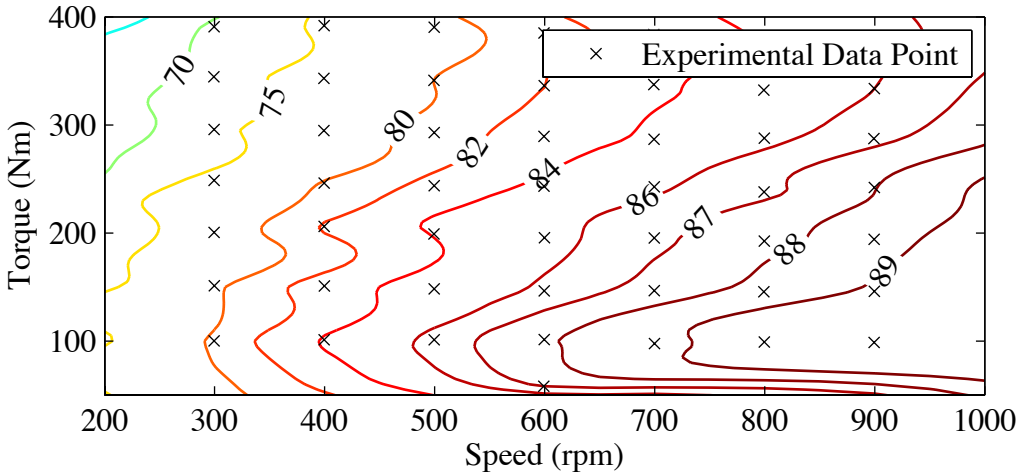

(a) Experimentally determined efficiency

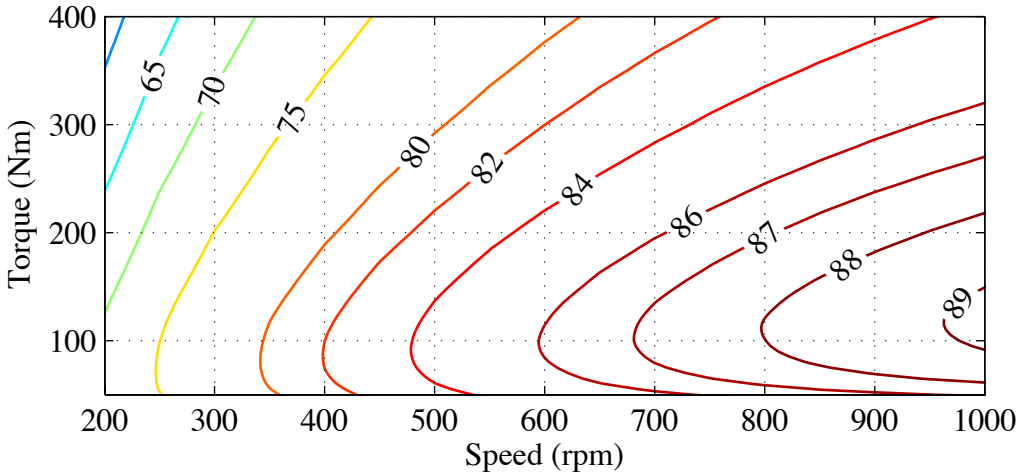

(b) Simulated efficiency over the experimental range

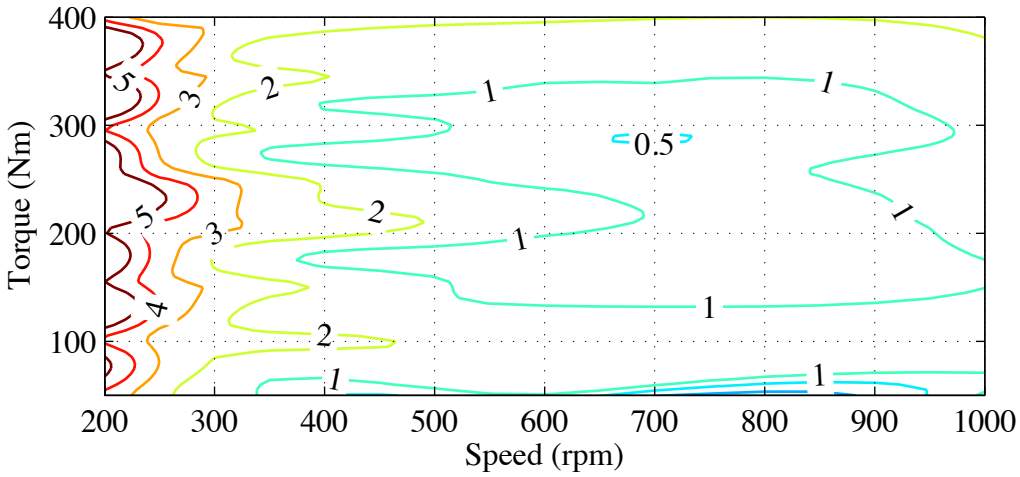

(c) Discrepancy between simulated and experimental efficiency

Figure 5.25: A comparison of experimental and simulated system efficiency maps for BLAC operation (contour values in %).

5.5.3 Verification of the Estimated Efficiency Maps

Having experimentally determined the combined motor and inverter efficiencies for the BLDC-120 and BLAC control modes, the results can be compared to the predicted efficiencies. The limitations of the experimental setup described in Section 5.5.1 allows only a limited range of the predicted efficiency maps to be compared. While this does not provide sufficient results to show the validity of the predicted efficiency map over the entire theoretical operating range, it does provide an indication to the accuracy of the method. The simulated efficiency maps have been plotted over the experimental data range in Figures 5.24(b) and 5.25(b) for easier comparison to the experimental data.

Figures 5.24(c) and 5.25(c) show the efficiency percentage discrepancy between the experimental and simulated results for BLDC-120 and BLAC control modes respectively. A positive efficiency error shows the simulation underestimating the measured system efficiency. 70.0 % of the BLDC-120 simulated efficiency map and 81.3 % of the BLAC simulated efficiency map is within the estimated 2.5 % measurement accuracy of the equivalent experimental efficiency. The mean absolute efficiency errors over the experimental range are 4.4 % for the BLDC-120 map and 2.3 % for the BLAC map.

The simulated efficiency maps have not taken into account the hysteresis losses in the rotors of the machine, or the resistance of the motor phase or DC link cables. Furthermore, the mechanical bearing and windage losses have not been included. Despite neglecting these loss components, the simulated efficiency maps are in close agreement with the experimental results. However, if these additional loss components had been included in the loss simulation, the total simulated losses would exceed the experimental results, giving an underestimate of the true system efficiency. Therefore, the loss components which have been simulated must be an overestimate of the true values. The simulated loss component values would need to be lower to maintain close agreement between the experimental and simulated total system losses if all loss components were accounted for. However, the simulation method used still allows a comparison to be made between the

relative performance of the three control modes.

For the example motor system comprising of a 500 N m YASA motor and a Semikron SKAI inverter, the proposed method for estimating the efficiency of the system provides a close match to experimental results in the region of 50 N m to 400 N m and 200 rpm to 1000 rpm. However, further experimental results are needed to verify the simulation method beyond this range.

5.6 Comparison of Control Mode Efficiencies

The efficiency maps for the example system have been estimated for the BLDC-120, BLDC-180 and BLAC control modes over the operating range limited by a DC link voltage of 400 V and a maximum RMS phase current of 212 A. The efficiency estimations have been compared with limited available experimental results and found to match closely. Each of the control modes can now be compared to determine the optimal mode utilisation for the system.

Figures 5.19 to 5.21 show the efficiency maps for the three control modes. The BLAC mode gives the highest peak efficiency at 90.7 %, and BLDC-120 the lowest at 89.2 %. More significant is the variation of efficiencies over the operating range. Figures 5.26 to 5.28 show the regions of the motor operating range in which a particular control mode is most efficient for the motor, inverter and combined system respectively.

The optimal motor efficiency map shows three distinct regions, each with a different control modes giving the highest efficiency. Below approximately 2000 rpm (below the base speed), the low harmonic content of the BLAC phase current waveforms gives the lowest motor losses and hence the highest efficiency. For the operating range above base speed and above approximately 100 N m, the BLDC-180 mode gives the highest efficiency. In this region, the superior DC link voltage utilisation of the BLDC-180 control mode means less field weakening is needed and lower phase currents are required than

for the other control modes. Above base speed but below approximately 100 N m, the BLDC-120 mode gives the highest motor efficiency. In this region, the BLDC-120 mode gives the highest torque output for a given RMS phase current and hence the lowest losses. For example, at 4000 rpm and 50 N m the RMS phase current for the BLDC-120 mode is 135.9 A compared to 161.1 A and 178.8 A for the BLDC-180 and BLAC modes respectively.

The inverter efficiency is maximised over the majority of the operating range with the BLDC-120 mode. This is a result of having only two active phases at any time, giving lower switching and conduction losses. For the operating range above approximately 2000 rpm and 150 N m, the BLDC-180 mode gives the highest efficiency. As with the motor efficiency map, the superior DC link voltage utilisation and lower field weakening currents give the highest efficiency. Figure 5.27 also shows two small regions where the BLAC mode offers the highest inverter efficiency. The region around 500 N m is beyond the torque capability of the BLDC-120 mode and the region around 0 N m offers a negligible improvement over the BLDC-120 mode.

The optimal control mode utilisation to maximise the combined system efficiency is very similar to that which maximises the motor efficiency. This is because the high efficiency of the inverter has only a small effect on the system efficiency in comparison to the motor.

By analysing which region of the operating range a motor system for a particular application is expected to operate in for the majority of its running time, it is possible to choose a single control mode to maximise efficiency. However, as different control modes offer the highest system efficiency at different operating points, it raises the possibility of changing between control modes while running to maximise the efficiency at all speed and torques. This concept will be explored further in the following chapter.

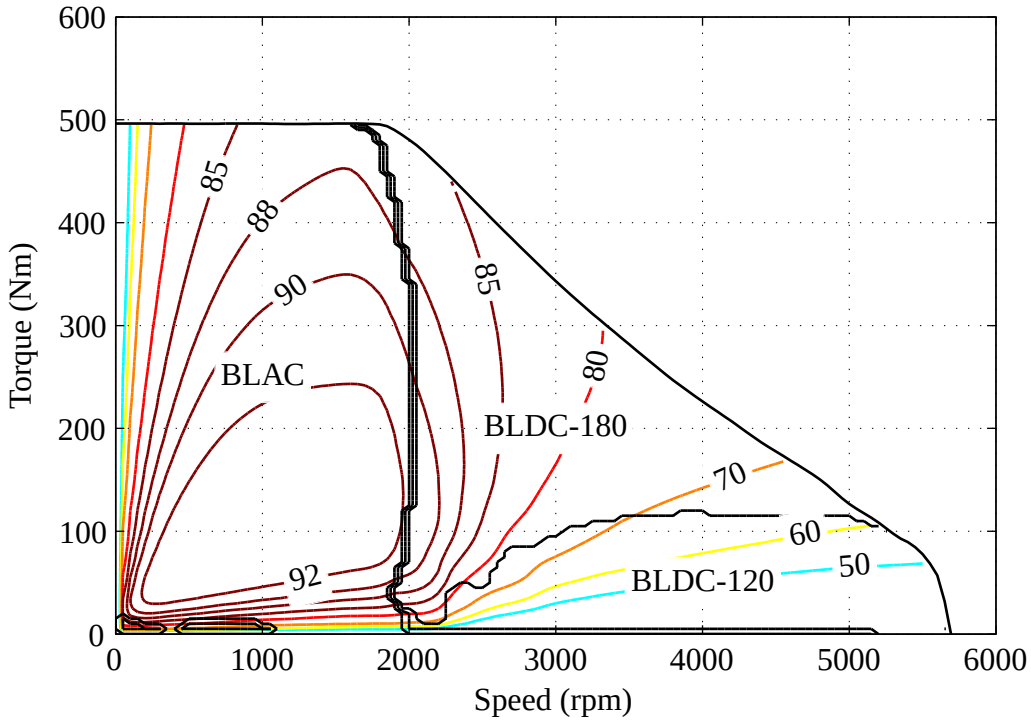

Figure 5.26: Control mode utilisation to maximise motor efficiency (contour values in %).

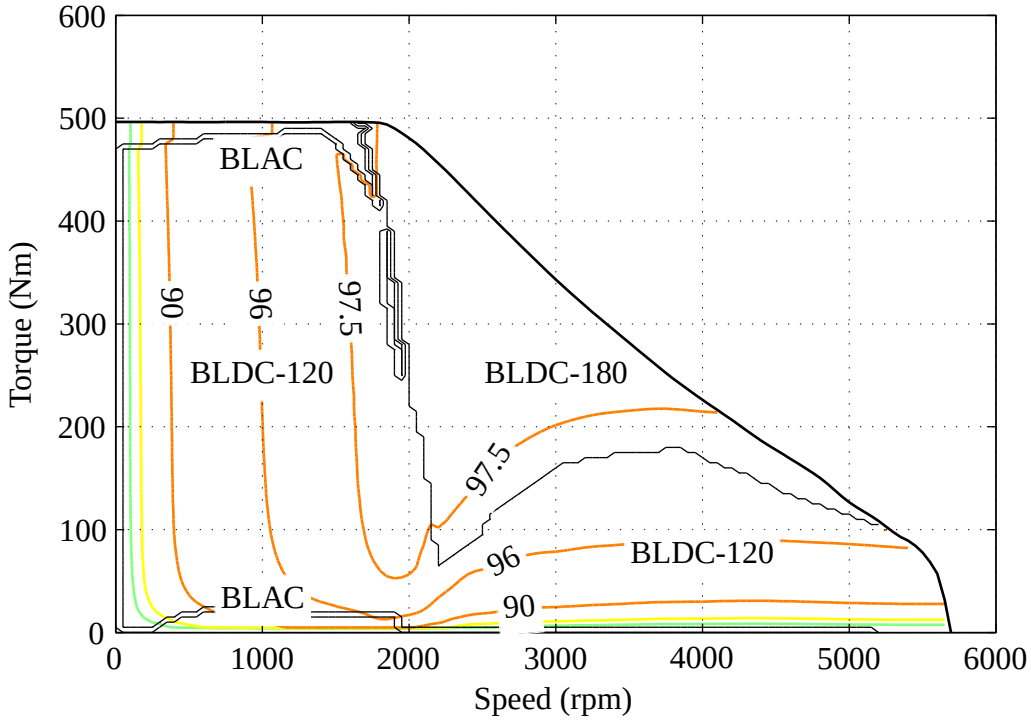

Figure 5.27: Control mode utilisation to maximise inverter efficiency (contour values in %).

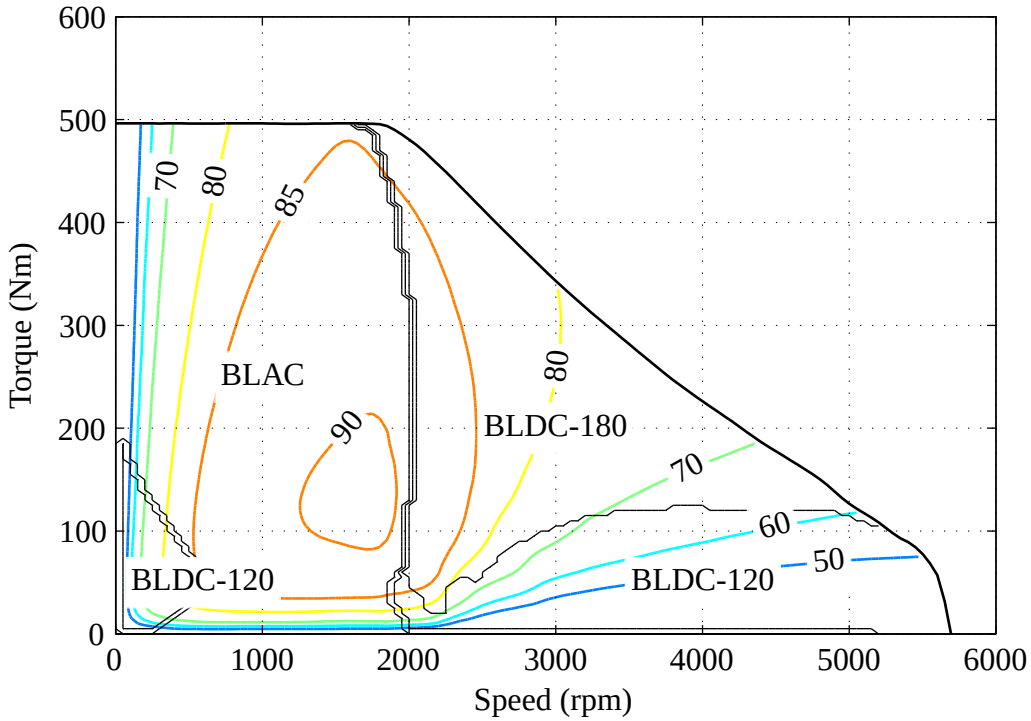

Figure 5.28: Control mode utilisation to maximise system efficiency (contour values in %).

5.7 Summary

In this chapter, the loss components for the example vehicle motor system consisting of a 500 N m YASA motor and a Semikron SKAI inverter have been determined. A Simulink model of the motor system was first used to simulate the motor phase currents for each of the control modes. The operating range considered was limited by a DC link voltage of 400 V and a maximum RMS phase current of 212 A. From the motor phase currents, the motor winding losses and inverter losses were calculated. The BLDC-120 mode was found to have the lowest switching and conduction losses, peaking at 1.18 kW and 0.89 kW respectively. The BLAC mode gave the lowest winding losses with a maximum value of 5.03 kW over the operating range.

A finite element analysis was then used to estimate the magnetic losses in the motor. The motor phase currents determined from the Simulink system were input into a FEA model of the motor. This provided a more accurate simulation of the motor losses resulting from the harmonic content of non-sinusoidal currents. The FEA results showed that the

peak eddy current losses for the BLDC-120 mode were 6.7 times greater than for the BLAC mode at 500 rpm and 212 A RMS phase current.

A harmonic analysis of the magnetic flux density variation through the stator pole pieces of the motor was carried out to estimate the hysteresis losses. While all three control modes had very similar fundamental harmonic amplitudes, the BLDC-120 mode was shown to have significantly greater 5th and 7th order harmonic flux components than both the BLDC-180 and BLAC modes. At 500 rpm and 212 A RMS phase current, the BLDC-120 5th harmonic is 2.7 times greater than for the BLDC-180 mode, and 8.0 times greater than for the BLAC mode.

The loss components were used to calculate a system efficiency map for each of the control modes. Peak efficiencies of 89.2 %, 89.7 % and 90.7 % were predicted for the BLDC-120, BLDC-180 and BLAC control modes respectively. The efficiency maps were then compared to limited available experimental data. 70.0 % of the BLDC-120 simulated efficiency map and 81.3 % of the BLAC simulated efficiency map was found to be within the estimated 2.5 % accuracy of the experimental efficiency data. The simulated efficiency maps therefore give a good estimate of the true efficiency over the experimental range.

Finally, a comparison of the simulated efficiency maps was made and it was shown that the control mode that gives the highest system efficiency changes with motor speed and torque. It was therefore demonstrated that in order to maximise the system efficiency, it is necessary to change between control modes as the motor operating point changes.

6

Combining the Benefits of BLDC and BLAC Control Modes

6.1 Introduction

Chapter 4 compared the the motor torque performance that can be achieved for each of the BLDC-120, BLDC-180 and BLAC control modes. It was shown that for permanent magnet synchronous motors, the peak torque curve for a given DC link voltage and maximum RMS phase current is not the same for all control modes. In order to maximise the motor torque across the entire speed range, it would be necessary to change between control modes as the motor speed varies.

In Chapter 5, efficiency maps for each of the control modes were compared. It was shown that the efficiency of both the motor and inverter varies as a function of the motor speed and torque. Furthermore, no single control mode was found to give the highest

efficiency over the entire motor operating range. The system efficiency for a motor and inverter system could therefore be improved by changing between control modes as the motor speed and torque output varies.

A control system for changing between control modes for a motor using using Hall effect sensors for position feedback has been proposed in [43] and [115]. The sensors give the rotor position in 60°E steps, allowing the motor to be started with full torque under BLDC-120 control. At higher speeds, a more accurate position estimation can be made, and the controller can switch over to BLAC control without interrupting the motor torque. However, separate controllers are proposed for each control mode and they must be synchronised to ensure a smooth control mode transition. In [115], the transition between control modes is limited to occurring at the boundary of a SVM sector. In both cases, the proposed techniques are designed to allow a motor to be run with BLAC control, but started with BLDC-120 control to allow low resolution position sensors to be used. The mode transitions are also made at a single speed threshold. The benefits of changing modes to maximise motor torque or system efficiency have not been considered.

In this chapter, a control strategy is proposed which allows a brushless motor to change between BLDC-120, BLDC-180 and BLAC control modes while the motor is running and with mode transitions between any of the three modes. The control system described provides several improvements over existing techniques. The control mode transitions can take place at any rotor position rather than limited to the edge of space vector modulation sectors. A single controller is proposed to drive a motor in all three control modes with mode transitions possible at any speed and torque. The controller also allows the motor to switch between control modes without interruption of the output torque.

6.2 Switching Between Control Modes

In order to change between BLDC-120, BLDC-180 and BLAC control modes while the motor is running, a motor control strategy is needed which is capable of controlling the motor in all three modes. It is also desirable to be able to change between the modes without interruption in the motor's output torque for vehicle applications so power can be delivered continuously to the wheels.

BLAC motors are often controlled using space vector modulation (SVM) [99] to produce a three-phase sinusoidal output voltage where all three inverter legs are active simultaneously. The eight switching vectors are shown schematically in Figure 6.1(a) where the vectors represent the switching states of each inverter leg. The state where the high side switch is on and the low side switch is off is indicated by a '1', and a '0' indicates the opposite. The two zero voltage vectors (V_0 and V_7) represent the condition when all three inverter phase outputs are at the same voltage and so no net voltage is applied to the motor.

In comparison, BLDC motors are typically controlled using six-step commutation, where only two of the three inverter legs are active at any time. This creates a different set of switching vectors for BLDC-120 control, as shown in Figure 6.1(b) where 'X' indicates that both the high side and low side switches for a phase are off. This set of switching vectors is 30°E out of phase with the BLAC set. Each BLDC-120 space vector is placed mid-way between two BLAC vectors, which differ by the switching state of one inverter leg. The BLDC-120 zero voltage vectors are as for BLAC operation but with one phase inactive depending on the motor position. The resulting voltage vectors are also smaller in amplitude than for BLAC by a factor of $\sqrt{3}$ as a result of the inactive phase. BLAC control is therefore able to apply higher voltages to the motor giving a higher base speed, as seen in Chapter 4.

BLDC-180 control uses the same switching vectors as for BLAC. However, only one non-zero voltage vector is used during each switching period. BLDC-180 control

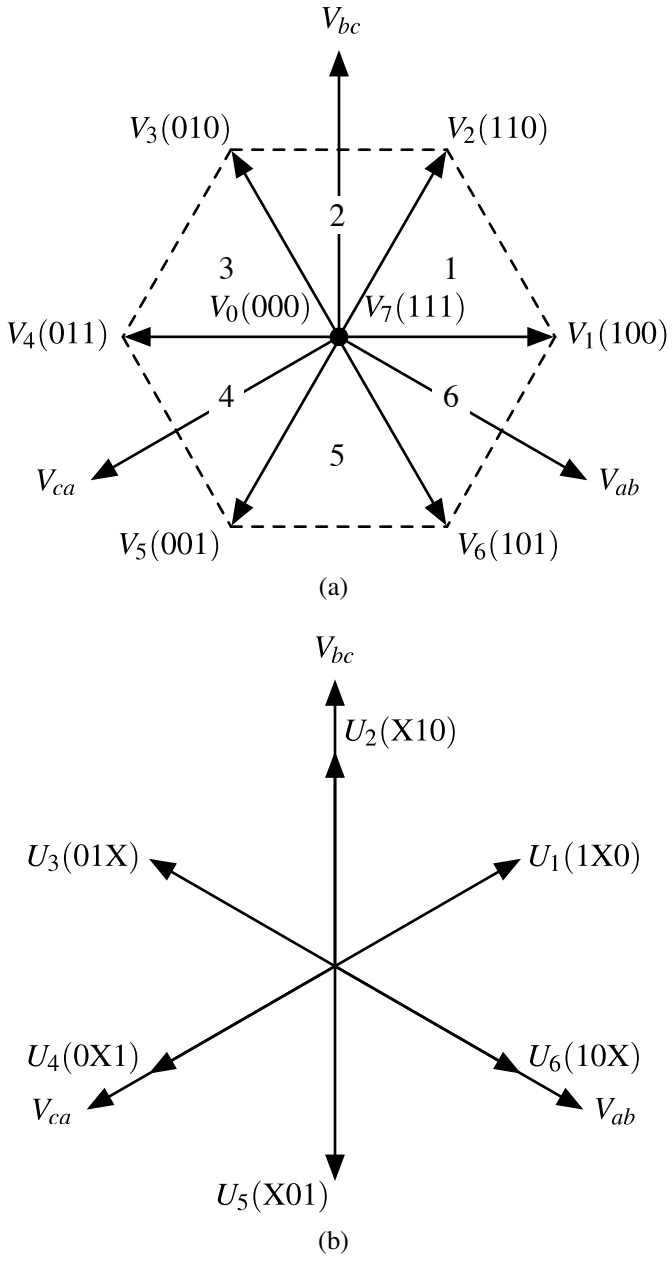

Figure 6.1: 3-phase space vectors in the α,β-plane for (a) BLAC and (b) BLDC-120 control. The possible switching states for each inverter leg are: '1' for top switch on and bottom switch off, '0' for top switch off and bottom switch on, and 'X' for both switches off [126].

is therefore a special case of the BLAC mode. Transition from BLAC to BLDC-180 control is simple to achieve by limiting the use of non-zero space vectors to one in any 60°E period rather than two for BLAC [99]. This mode transition will therefore not be considered further. The remainder of this chapter will focus on the more complicated transition between BLDC-120 and BLAC control modes.

To simplify the design of a control system for use with all control modes, it is desirable to use a single modulation scheme. Space vector modulation is not normally used for BLDC-120 control, as it cannot produce the six-step commutation pattern in its standard form. However, six-step commutation can be achieved using space vector modulation, if one of the inverter legs is disabled as a function of the rotor angle. Such a change is easily implemented on an embedded controller, but has the benefit of leaving the rest of the control loop unchanged.

The proposed control system is based around conventional SVM with field oriented control (FOC), as shown in Figure 6.2. The motor phase currents ($i_{a,b,c}$) are measured and Clarke and Park transforms are applied to give the direct (i_d) and quadrature (i_q) current components (Equations 6.1 and 6.2) with respect to the rotor reference frame (θ_e). These currents are compared to the set-point values and two PI controllers are used to control the current errors to zero. The PI controller outputs adjust the magnitudes of the direct (V_d) and quadrature (V_q) voltage components. These two components are then space vector modulated to produce a 3-phase voltage output, which is applied to the motor.

$$i_d = \frac{2}{3}\left(i_a \sin(\theta_e) + i_b \sin\left(\theta_e - \frac{2\pi}{3}\right) + i_c \sin\left(\theta_e + \frac{2\pi}{3}\right)\right) \tag{6.1}$$

$$i_q = \frac{2}{3}\left(i_a \cos(\theta_e) + i_b \cos\left(\theta_e - \frac{2\pi}{3}\right) + i_c \cos\left(\theta_e + \frac{2\pi}{3}\right)\right) \tag{6.2}$$

Unlike conventional field oriented control, the modulation scheme used allows for the transition between control modes by selectively blocking switching signals to an inverter

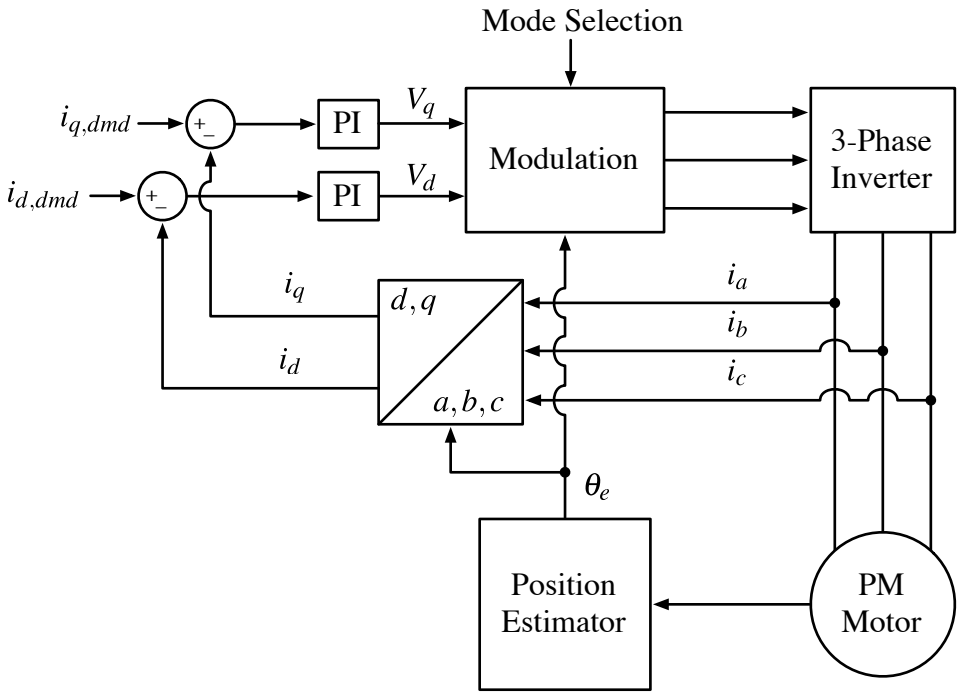

Figure 6.2: The proposed Field Oriented Control based system.

phase. This allows BLDC-120 switching signals to be produced. Figure 6.3 shows how the signals are routed to and from the a standard space vector modulation (SVM) block. When running in BLAC mode, the space vector PWM switching signals, calculated for the demanded direct and quadrature voltage components, are passed unchanged to the inverter. When running in BLDC-120 mode, a look-up table (Table 6.1) is used to control which SVM output signal pairs ($S_{n,m}$) are passed to the inverter gate driver inputs ($G_{n,m}$) as a function of the electrical angle.

Table 6.1: Switching signals passed to the inverter in BLDC-120 mode.

θ_e	$G_{1,2}$	$G_{3,4}$	$G_{5,6}$
0° - 60°	$S_{1,2}$	$S_{3,4}$	0
60° - 120°	$S_{1,2}$	0	$S_{5,6}$
120° - 180°	0	$S_{3,4}$	$S_{5,6}$
180° - 240°	$S_{1,2}$	$S_{3,4}$	0
240° - 300°	$S_{1,2}$	0	$S_{5,6}$
300° - 360°	0	$S_{3,4}$	$S_{5,6}$

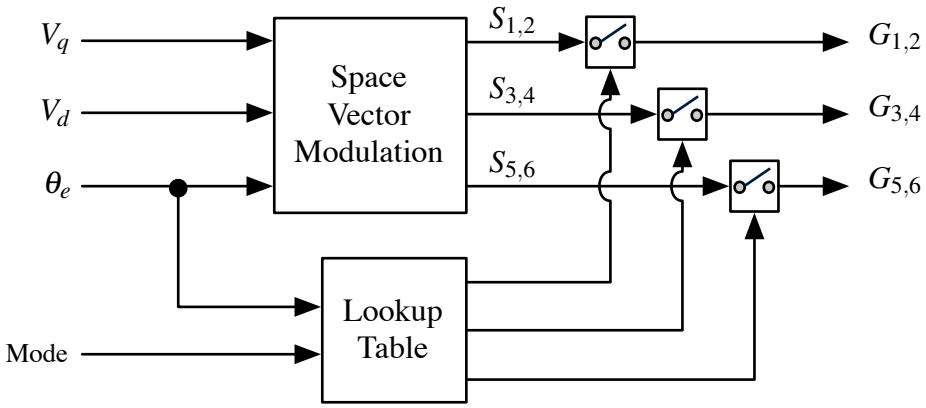

Figure 6.3: Signal routing for the modulation block.

In the BLDC-120 mode, the Clarke and Park transforms of the motor currents produce a quadrature current component proportional to the motor torque and with the same motor torque constant as for the BLAC mode. While there is more current ripple on the direct and quadrature components of the motor phase currents for the BLDC modes (shown in Figure 6.4), they are still adequate for controlling the motor. Using the same quadrature current reference to control the motor torque allows a single control system to be used for all control modes.

When the controller changes from BLDC-120 to BLAC mode all three legs of the inverter are enabled allowing a full sinusoidal output. Unlike the method in [115], the controller does not need to wait until the motor reaches the edge of a SVM sector to switch to BLAC mode; it can change modes at any angle. When operating above base speed, it is necessary to advance the commutation points for the BLDC control modes to achieve field weakening, as described in Section 4.3.1.

The control system has been simulated on a Simulink model of a permanent magnet motor to evaluate the performance of the control technique during mode transitions. The motor characteristics given in Table 1.3 have been used although the technique is equally applicable to other permanent magnet synchronous motors.

Figure 6.5 shows the direct and quadrature current component control loop model used to determine the gains of the motor PI controllers. The controller transfer function, $C(s)$,

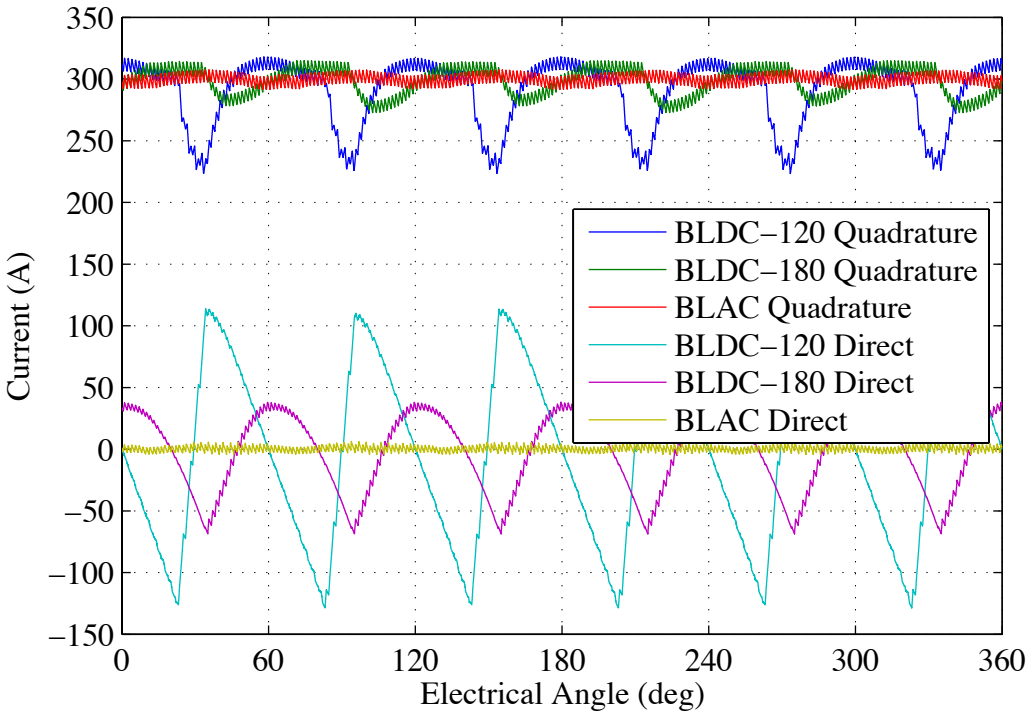

Figure 6.4: Simulated direct and quadrature currents for the three control modes at 500 rpm and an RMS phase current of 212 A.

is given by Equation 6.3. K_p and K_i are the PI controller proportional and integral gains respectively, and L and R are the motor phase inductance and phase resistance.

$$C(s) = \frac{K_p s + K_i}{s} = \frac{K(Ls+R)}{s} \tag{6.3}$$

A delay of T_s has been added to model the delay between when the phase current measurements are taken and when the new voltage output is updated, which occurs once every cycle of the 10 kHz Space Vector Modulation. The delay will reduce the phase margin of the PI controllers and must be considered, otherwise the calculated controller gains may be too high for stable operation.

Figure 6.5 also shows the cross-coupling terms from Equations 4.17 and 4.18 which act as a disturbance on the PI controller outputs. While the direct current component does not contribute to torque production, it still affects the quadrature current control loop and therefore the dynamics of the motor [6]. The disturbance to the controller from

cross coupling can be reduced through feed-forward compensation [127]. However, the motor controller response was found to be adequate without such measures as will be demonstrated in the remainder of this chapter.

The PI controllers have been tuned by making the numerator of the PI controller transfer function cancel the denominator of the motor transfer function to give an approximately first order current response. The value for the overall controller gain (K) has then been calculated to give a phase margin of 60°. Using the phase resistance and inductance values from Table 1.3 and a controller delay of 100 µs gives a value of 5230 for K.

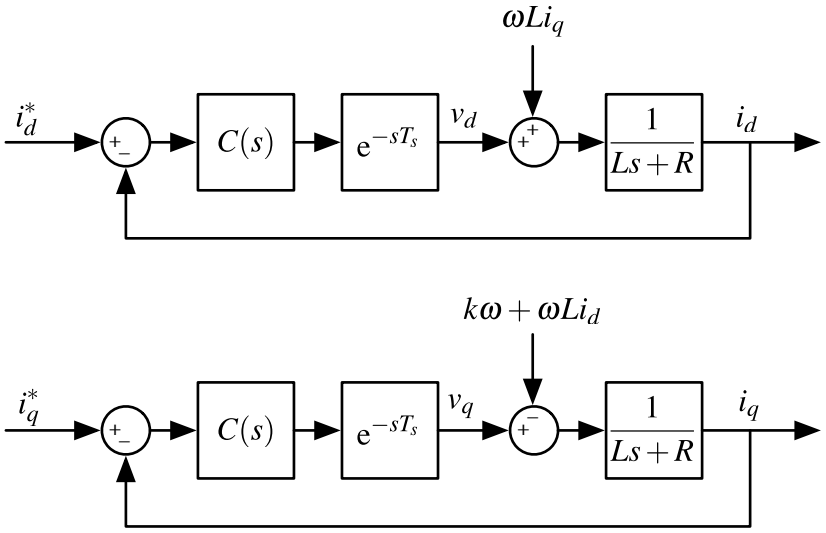

Figure 6.5: The direct and quadrature current component control loops [6].

The simulation was set to run the motor at a constant speed of 200 rpm in the BLDC-120 mode with a constant torque demand of 50 N m corresponding to a quadrature current demand of 30 A. When the motor currents have reached a steady state, the motor controller is switched into BLAC mode to see how quickly the system returns to a steady state. The simulation shows that during the transition (presented in Figure 6.6), the motor currents change shape to that of the new control mode within 2 ms. Furthermore, motor output torque is produced throughout the transition, but takes approximately 8 ms to reach steady state for the BLAC mode. The motor torque during the transitions falls to 3 N m below the steady state average torque for the BLAC mode. However, this is small compared to

the 28 N m of torque ripple in the BLDC-120 control mode. The mean torque is 49.69 N m before the transition, and 49.76 N m after. A similarly small transient torque is observed when changing back to the BLDC-120 mode. The change in torque and duration of a mode transition is therefore too small to be noticed by the driver of a vehicle using such a system.

6.3 Experimental Results

The control system has been implemented and tested on real hardware to validate the proposed control strategy and simulation results. The experimental setup described in Chapter 5 has been used with the position estimation technique discussed in Section 3.5.4. The low resolution motor position sensor gives an output change every 60 °E and is aligned for BLDC-120 control. On start-up, this provides the rotor position with an accuracy of ±30 °E and is sufficient to determine the correct commutation step for BLDC-120 control.

Once the motor is running, the motor speed can be measured from the rate of change of the position sensor output (Equation 6.4). A more accurate position estimation (θ_e) can then be made using the zeroth-order algorithm described in [128] and the controller can switch into BLAC or BLDC-180 control. The position estimation algorithm (Equation 6.5) assumes constant speed across a 60 °E SVM sector. The last speed measurement (ω_k) is integrated over the time since the last change of position sensor output (θ_k at time t_k). When the motor speed is too low to make a more accurate position estimate (less than 50 rpm), the control system reverts back to BLDC-120 control and the last position sensor output (θ_k) is used as the rotor angle.

The control system could be equally well applied to a motor with a high resolution position sensor such as an encoder or resolver. This would further increase the controller flexibility by allowing the motor to operate from zero speed in BLAC mode in addition to either BLDC modes.

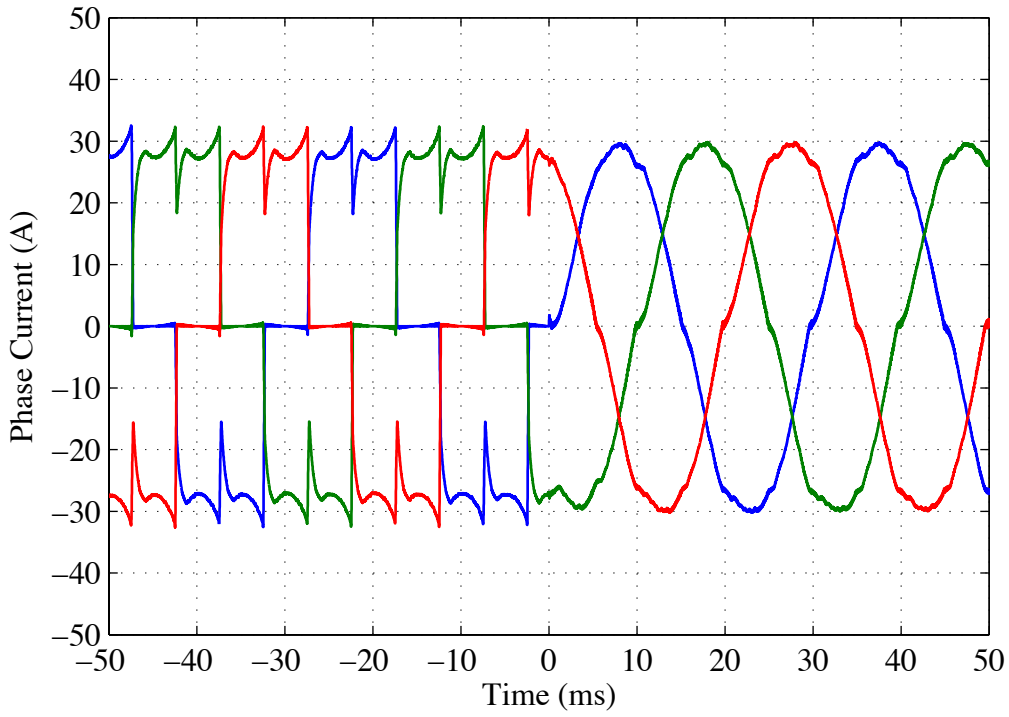

(a)

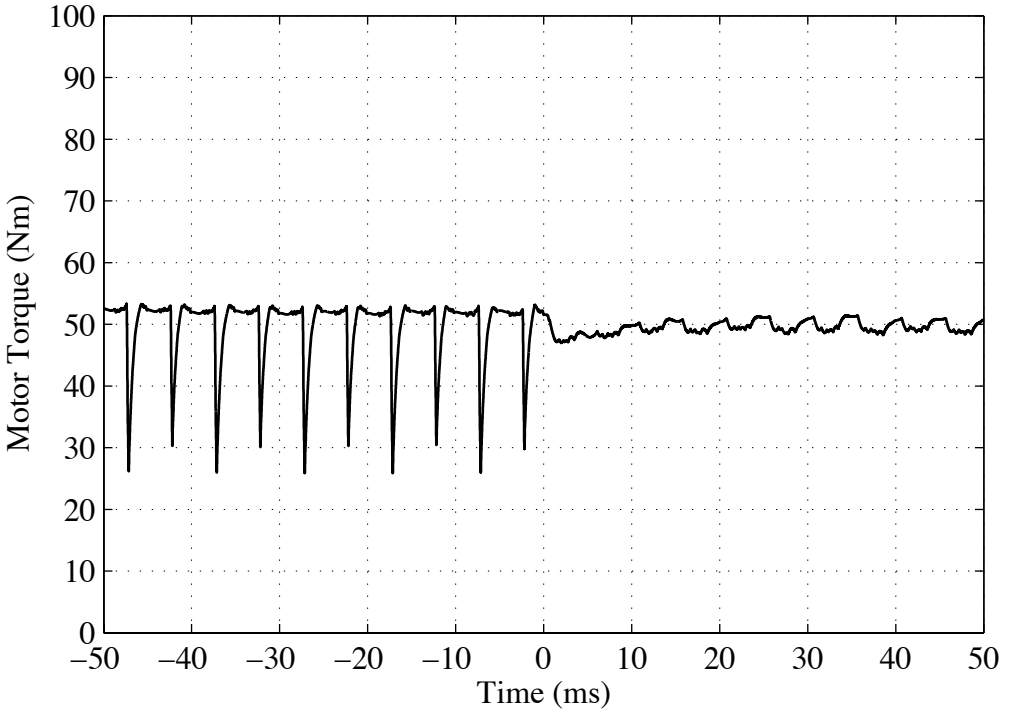

(b)

Figure 6.6: Simulated (a) motor phase currents and (b) motor torque for a BLDC-120 to BLAC mode transition at 200 rpm and 50 N m at t = 0 s.

$$\omega_k = \frac{\frac{\pi}{3}}{t_k - t_{k-1}} \tag{6.4}$$

$$\theta_e(t) \approx \theta_k + \omega_k(t - t_k) \tag{6.5}$$

To test the performance of the control strategy during a mode transitions, the load motor was set to maintain a constant speed of 200 rpm, while the machine under test was given a constant torque demand of 50 N m. Starting with the test machine in BLDC-120 mode, the system was brought up to the operating set-point with a supply voltage of 50 V for initial tests. Once the system had settled to a steady state, a command was sent to the test machine to change control mode to BLAC and subsequently back to BLDC-120 while the test motor phase currents and motor shaft torque were recorded. The load motor was kept in the BLAC mode throughout the test to minimise any torque ripple on the test motor.

Figures 6.7 and 6.8 show the motor phase currents and measured shaft torque during a transition from BLDC-120 to BLAC and BLDC-120 to BLAC respectively. The phase currents change smoothly for control mode transitions in both directions and settle within 2 ms. This matches the expected duration from the simulation mode transition. The torque sensor output (sampled at 1.62 kHz, although internally filtered with a sixteen sample moving average) shows no transient machine torque during the mode transitions. This was also the case when the test was repeated at different speeds, torques and higher DC link voltages, regardless of where in the electrical cycle the transition was made. The controller remains stable and there is no significant deviation from the demanded torque output when the control mode is changed. However, the amount of audible noise produced by the motor decreases significantly when the control mode changes from BLDC-120 to BLAC. This is a result of the reduced harmonic content of the motor phase currents and hence a lower motor torque ripple. Figure 6.9 shows the sound amplitude recorded with a microphone in close proximity to the test motor during a BLDC-120 to BLAC transition. The peak

sound amplitude is approximately 5 times greater in BLDC-120 mode than in BLAC mode at 50 N m and 200 rpm.

6.4 Maximising the System Efficiency

When a brushless machine is controlled in BLAC mode rather than a BLDC mode, the reduced harmonic content in the motor phase currents result in reduced torque ripple and quieter operation. This also improves the efficiency of the motor below base speed from the decreased eddy current and hysteresis losses, as shown in Chapter 5. However, the BLAC and BLDC-180 modes use all three legs of a three phase inverter simultaneously, which gives rise to additional switching and conduction losses compared to the BLDC-120 mode. To determine which control mode is most efficient at a given motor speed and torque output, an analysis of the combined motor and inverter system loss is needed for the particular system being used for each control mode. In the previous chapter, this was performed for the case of a 500 N m YASA motor driven by a Semikron SKAI inverter.

The results show for the case of the chosen system, that no single control mode is most efficient over the entire operating range. To maximise the combined motor and inverter efficiency, it is necessary to switch control modes as the motor speed or torque changes, as demonstrated by Figures 6.10 and 6.11. The optimal mode utilisation to maximise the system efficiency is shown in Figure 5.28.

The highest system efficiency can generally be achieved in BLAC mode below base speed where the difference in motor efficiency is greatest. However, there are small regions where other control modes are more efficient. For example, at 400 rpm and 70 N m, the BLDC-120 mode gives the highest efficiency at 82.4 %. At the same operating point, the BLAC mode efficiency is 81.9 % and the BLDC-180 mode is only 79.9 % efficient.

Above base speed, BLDC-120 gives the highest efficiency at low torques and BLDC-180 at high torques. Therefore, by changing between the different control modes as

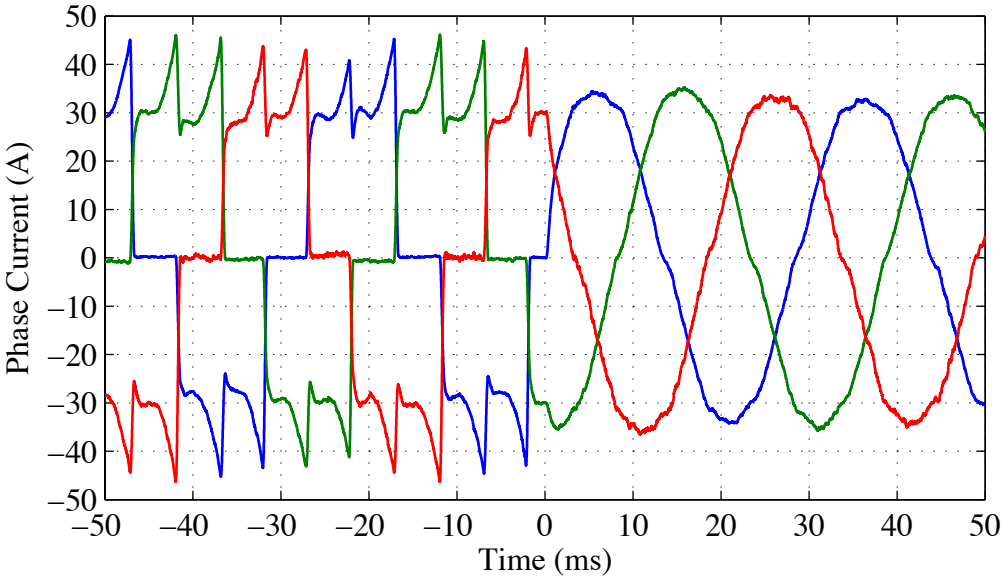

(a)

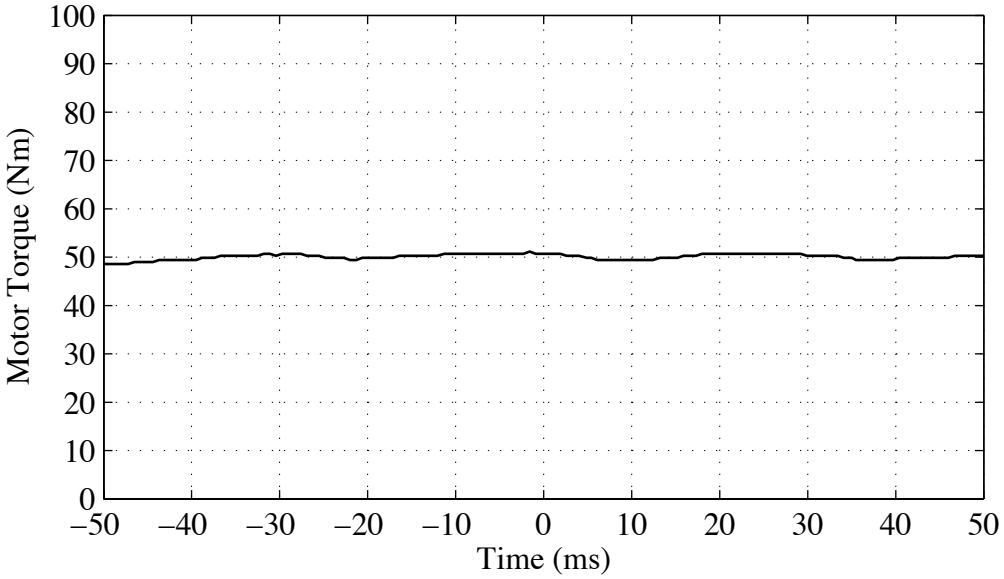

(b)

Figure 6.7: Experimental control mode transitions at t = 0 s at 200 rpm and 50 N m for (a) BLDC-120 to BLAC phase currents and (b) BLDC-120 to BLAC torque.

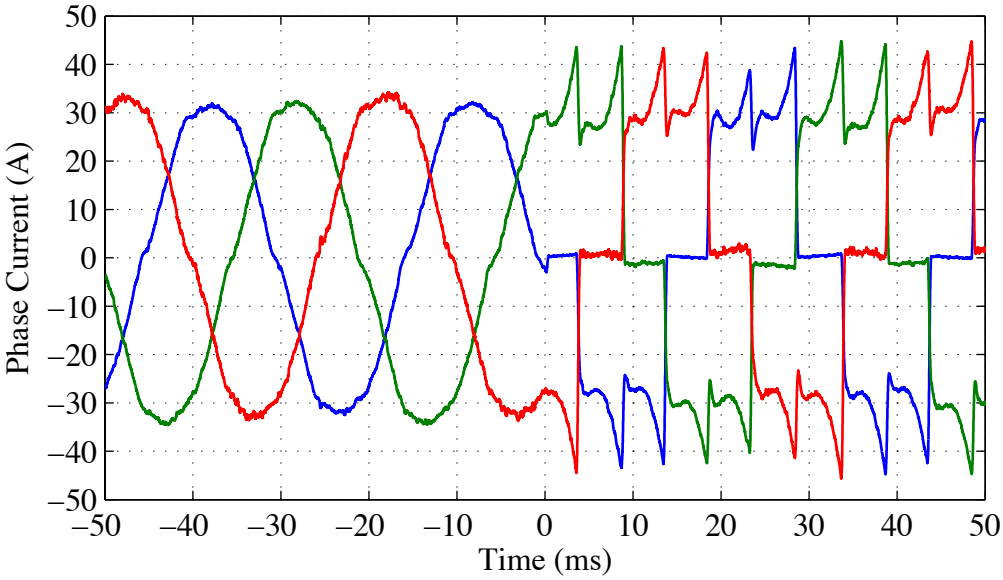

(a)

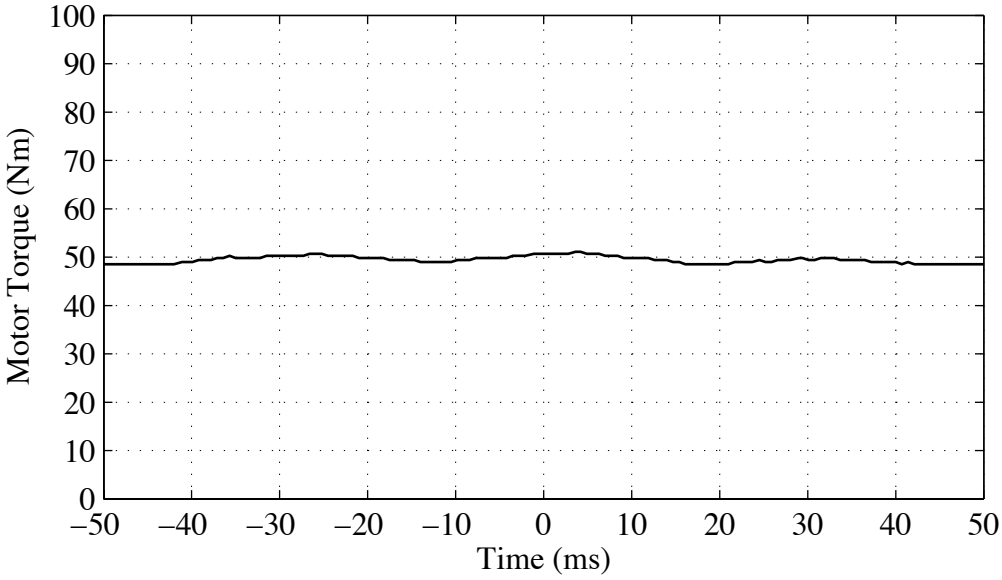

(b)

Figure 6.8: Experimental control mode transitions at t = 0 s at 200 rpm and 50 N m for (a) BLAC to BLDC-120 phase currents and (b) BLAC to BLDC-120 torque.

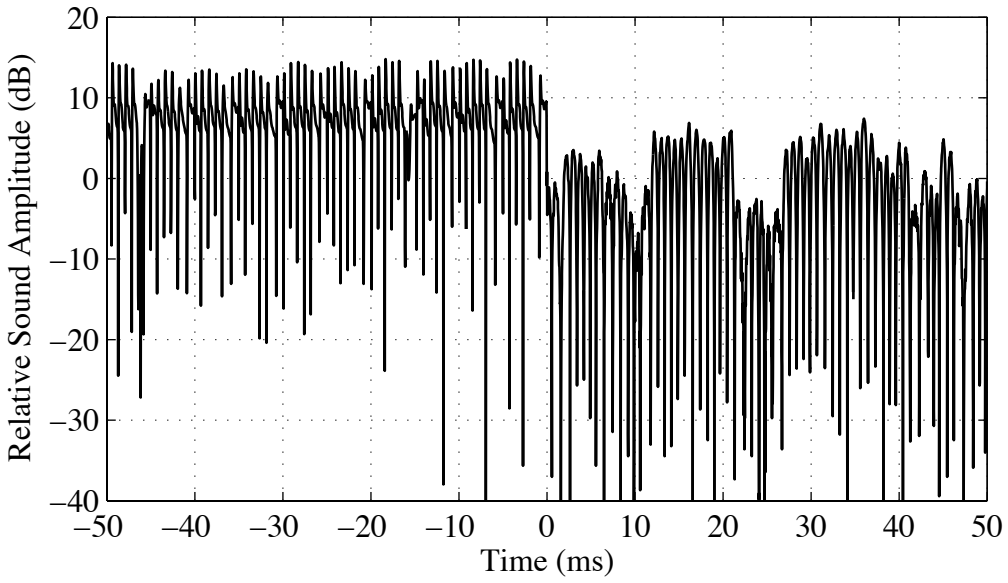

Figure 6.9: The change in the audible sound level for a BLDC-120 to BLAC mode transition at t = 0 s at 200 rpm and 50 N m relative to BLAC control.

the torque demand and motor speed change, the system efficiency can be improved. Figure 6.11 shows at 2500 rpm and 300 N m, changing from the BLDC-120 to the BLDC-180 control mode would result in the efficiency improving from 76.9 % to 83.9 %. Significant improvements to the maximum torque output can also be achieved by changing control modes. The BLDC-180 mode is capable of producing 110 N m more torque than the BLDC-120 mode at 2500 rpm. For vehicle applications where the required torque is constantly changing, this suggests that it would be advantageous to change between control modes.

Drive cycles, such as The Unified Cycle Driving Schedule (UCDS) [7] shown in Figure 6.12(a), are used to assess vehicle performance over a speed profile representative of real world driving conditions. A simulation of the longitudinal dynamics of an example electric vehicle, shown in Figure 6.13, has been performed to assess the drive cycle energy requirements for the different control modes. The vehicle's front axle is driven by the example 500 N m motor system described above via a fixed 3.0:1 reduction gearbox. The vehicle parameters are given in Table 6.2.

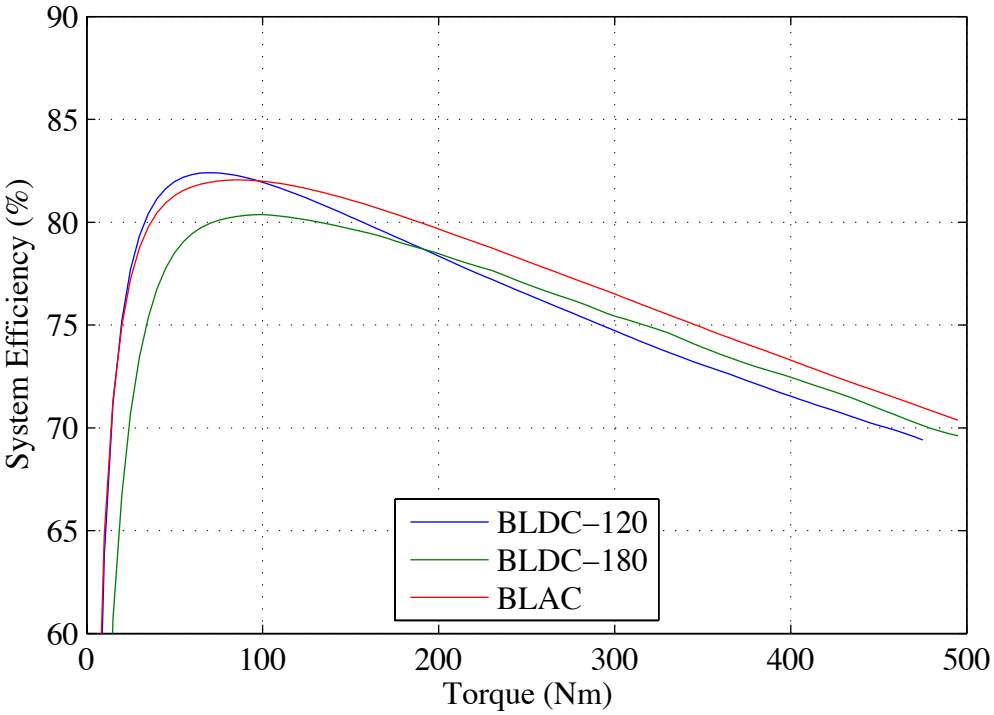

Figure 6.10: Combined motor and inverter efficiencies for the three control modes with a 400 V DC supply at 400 rpm.

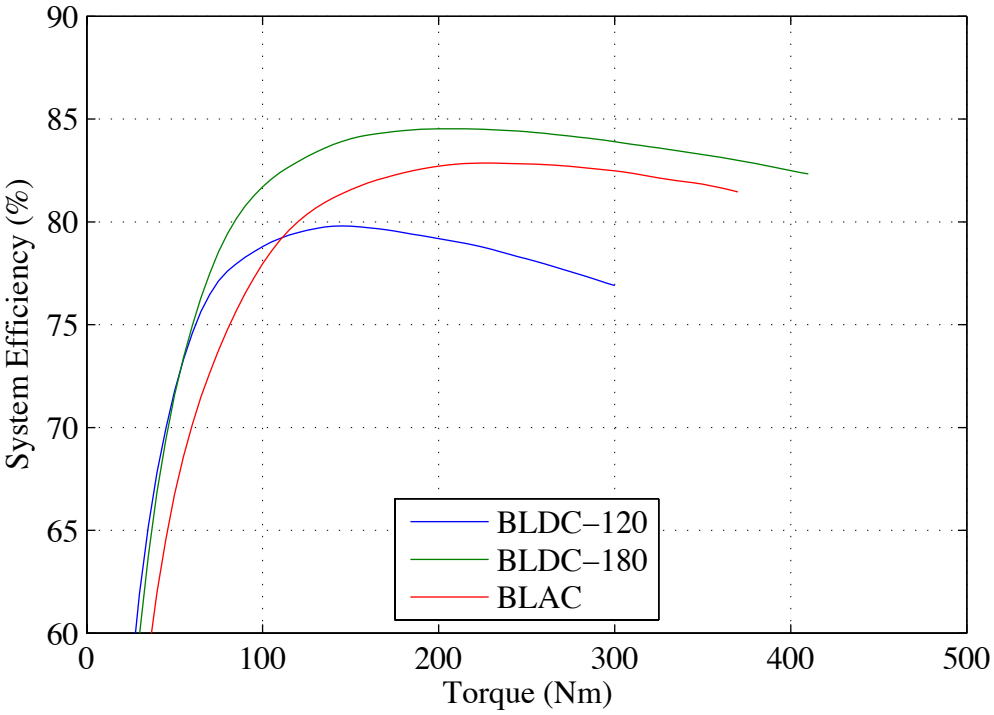

Figure 6.11: Combined motor and inverter efficiencies for the three control modes with a 400 V DC supply at 2500 rpm.

Table 6.2: Example electric vehicle characteristics used for the UCDS cycle simulation.

Mass (m)	1500 kg
Drag coefficient (C_D)	0.3
Frontal area (A)	2.0 m^2
Rolling radius (r_{wheel})	0.3 m
Rolling resistance (F_{rr})	150 N
Motor gear ratio (G)	3.0:1

The motor torque required for the vehicle to complete the cycle is shown in Figure 6.12(b) and was calculated by solving Equation 6.6 for each time step of the drive cycle. The equation assumes that there is no change in the vehicle altitude during the drive cycle. The gear ratio has been selected to allow a single motor to meet the vehicle acceleration torque requirement while minimising the peak motor speed. A higher gear ratio would result in the motor running to higher speeds where the efficiency decreases rapidly (as shown in Figures 5.19 to 5.21) and the motor torque capability being under utilised. If a lower gear ratio were used, the motor torques required by the drive cycle would exceed the motor capability.

In addition to providing all of the accelerating torque for the example vehicle, the motor will also allow regenerative braking to decelerate the vehicle and recover energy. It has been assumed that only 60 % of the total required vehicle braking torque can be met by the motor through the front axle. To maintain vehicle stability during braking, it is necessary to limit the front axle braking torque [129]. The balance of the required braking torque must be met by conventional friction brakes on the rear axle of the vehicle. The limiting axle braking torque balance for a real vehicle will depend on the static weight distribution, as shown in [129].

$$m\frac{dv}{dt} = \frac{T_{motor}G}{r_{wheel}} - \frac{1}{2}\rho C_D A v^2 - F_{rr} \tag{6.6}$$

The total vehicle output energy, required to complete the drive cycle, has been

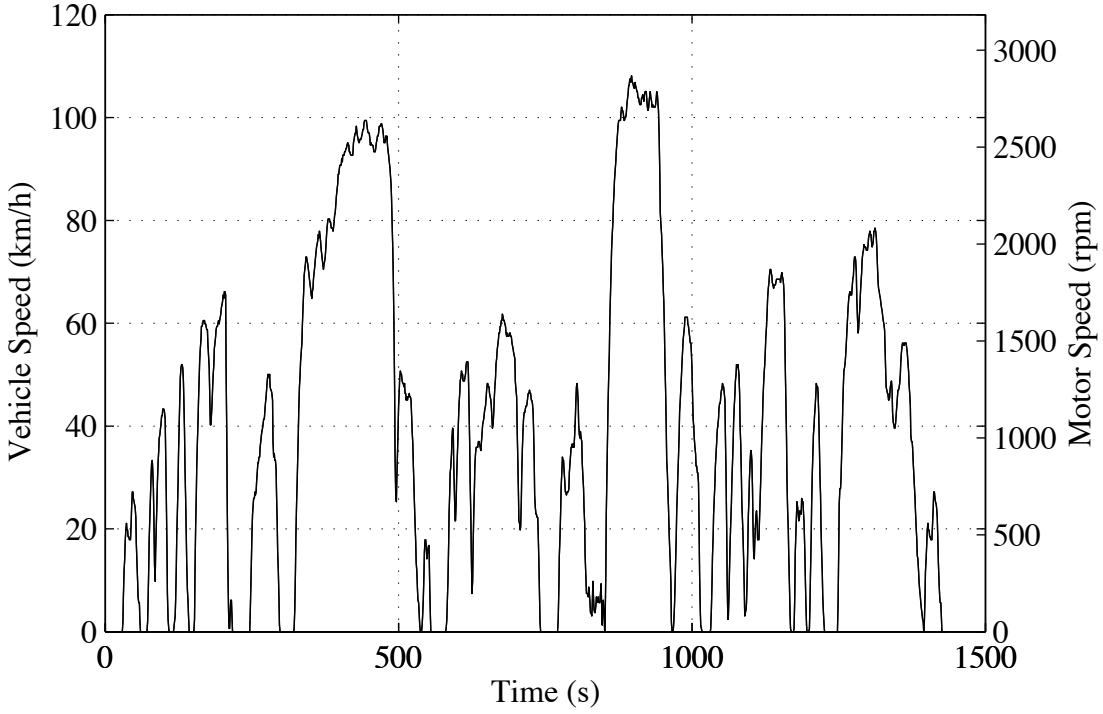

(a)

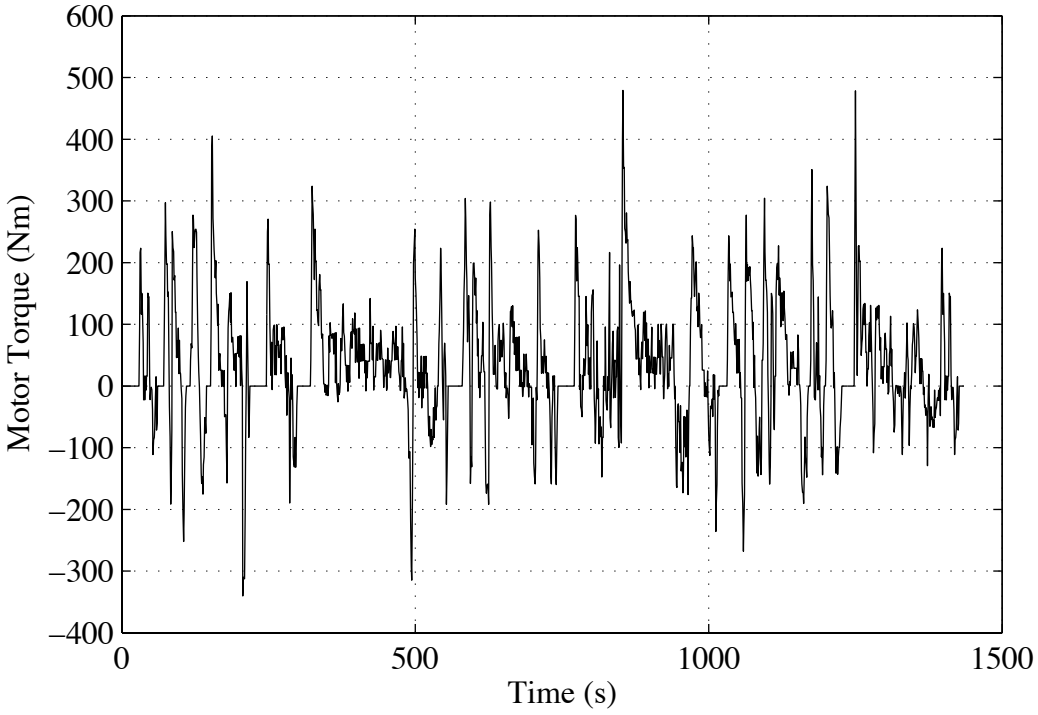

(b)

Figure 6.12: (a) Speed profile and (b) required motor torque for the Unified Cycle Driving Schedule [7].

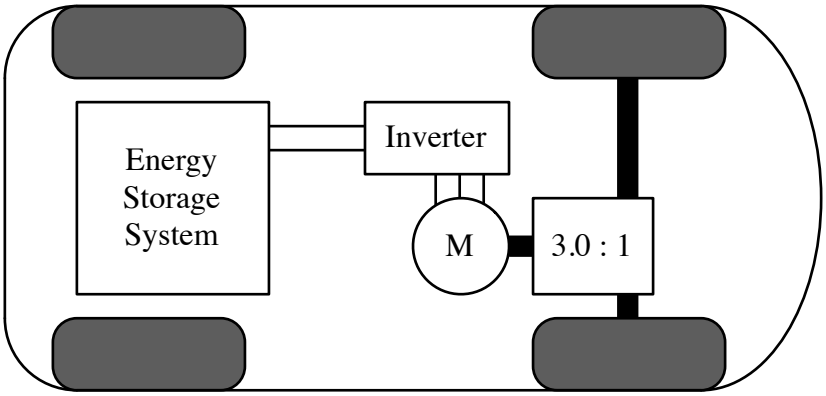

Figure 6.13: Example front wheel drive electric vehicle driven by a single motor through a 3.0:1 reduction gearbox and differential.

Table 6.3: Energy required to complete the UCDS.

Control mode	Cycle energy	Average efficiency
BLDC-120 only	8.32 MJ	63.9 %
BLDC-180 only	8.36 MJ	63.6 %
BLAC only	8.45 MJ	62.9 %
Optimal mode strategy	8.13 MJ	65.4 %

calculated for each control mode when used exclusively and then for the optimal mode strategy. The motor and inverter efficiency maps determined through simulation in Chapter 5 have been used. The results of the simulations are given in Table 6.3. The optimal mode strategy reduces the vehicle losses by 6.7 %, 7.7 % and 10.3 % compared to the losses the for the BLDC-120, BLDC-180 and BLAC modes respectively, when used in isolation.

For this particular drive cycle when using the optimal mode strategy, 21.2 % of the example vehicle's non-stationary time is spent in the BLDC-120 mode, 7.7 % in the BLDC-180 mode and 71.1 % in the BLAC mode. Therefore, the BLAC mode is used extensively despite giving the worst cycle energy requirement if used on its own. This is because a large proportion of the cycle time is spend in the operating region where the BLAC mode is most efficient. However, savings to the system losses can be made by changing modes above base speed where the BLAC mode is less efficient than the BLDC modes.

The reduction in system losses is significant, as the performance of electric drivetrains is often constrained by the maximum operating temperatures and the ability to remove the heat generated through loss mechanisms. The reduction in losses could allow the peak system output power to be increased or the size of the cooling system to be reduced without the system overheating. The duration for which full torque can be sustained during acceleration or braking before the system reaches a thermal limit could also be increased. Furthermore, use of such a control strategy in electric vehicles could increase the maximum range by improving the utilisation of the vehicle's stored energy.

6.5 Gradual Transitions Between Control Modes

The previous sections of this chapter have shown that it is possible to make an almost instantaneous switch between the different control modes without interruption of the motor torque. In this section an extension to the control scheme will be described, which allows multiple mode switches to be made in a single electrical cycle. It also allows a gradual transition to be made between two distinct control modes.

Figure 6.14 illustrates a modulation scheme where a transition is made twice in each space vector modulation sector between BLDC-120 and BLAC control modes. The proportion of time spent in each mode can be modulated to gradually blend between the full BLDC-120 and BLAC modes over many electrical cycles. The controller operates in BLDC-120 mode around the locations of the BLDC-120 space vectors and the span of the BLDC-120 mode (θ_s), in electrical degrees, can be decreased from 60°E (100% BLDC-120) to 0°E (100% BLAC).

Modulation of the control mode has been implemented on the back-to-back test rig to experimentally validate the technique described above. With the motor running at a constant speed of 200 rpm, a DC link voltage of 400 V and a constant torque demand of 50 N m, the mode span was changed from 0% BLAC (100% BLDC) to 100% BLAC (0%

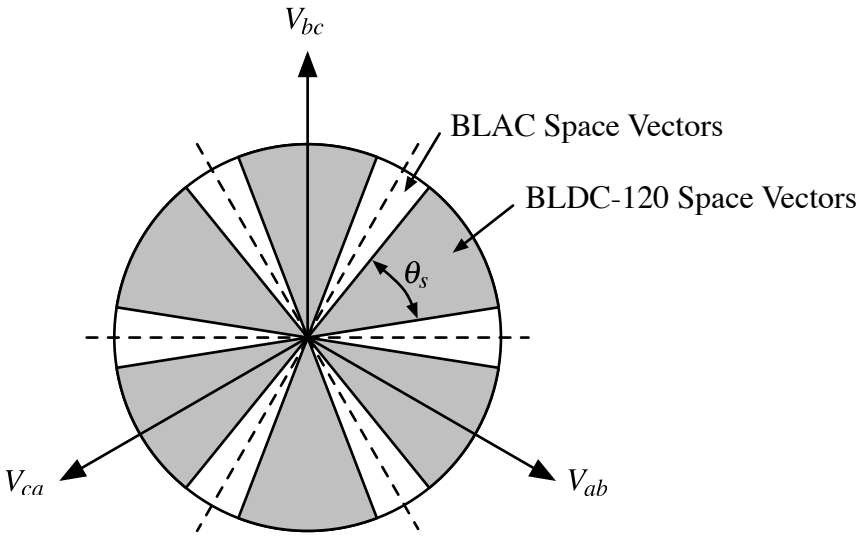

Figure 6.14: Space vectors used for a gradual mode transition between BLDC-120 and BLAC modes.

BLDC) in 25 % steps, as shown in Figure 6.15. The motor phase currents can be seen to gradually change from the characteristic rectangular BLDC-120 shape to a sinusoidal BLAC shape, while the motor torque remains constant. Although not discussed further in this section, a similar gradual mode transition between BLDC-120 and BLDC-180 or BLAC and BLDC-180 control modes could also be made.

The lack of audible noise produced by electric vehicles has raised concerns over the safety of pedestrians who may be unaware of their presence [130]. The sound produced by vehicles is also important for driver feedback and artificial sound generators have been suggested as a means of addressing these issues for electric vehicles [131]. However, one possible application of modulating between control modes is to control the intensity of the sound produced by the motor.

The amount of audible noise produced by the vehicle motor tested can be heard to increase as the motor control mode is modulated from BLAC to BLDC-120. Measurements of the motor sound intensity show a linear increase with the BLDC-120 mode span (Figure 6.16) to over five times that for 100 % BLAC mode. As the motor torque does not

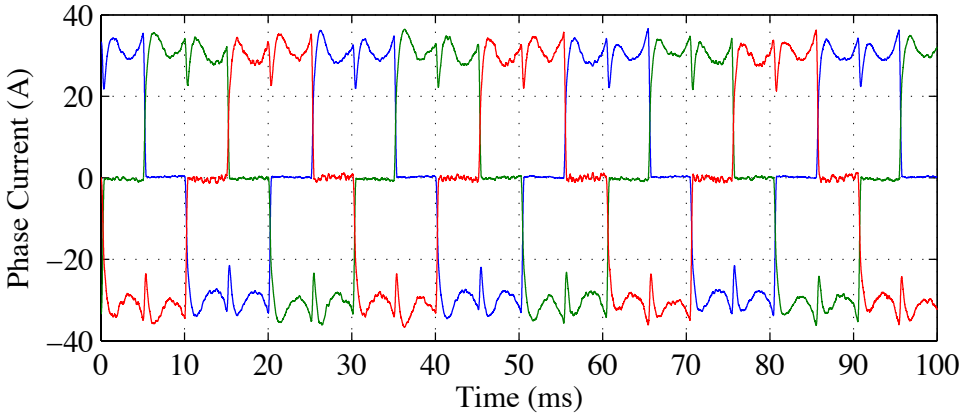

(a)

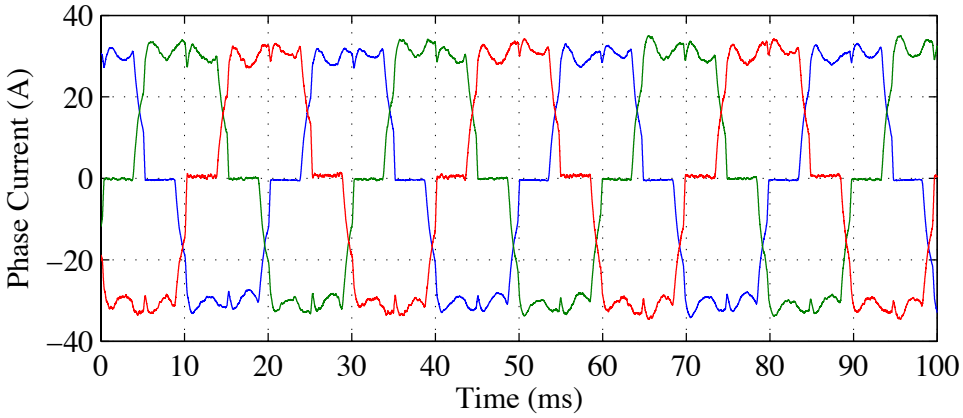

(b)

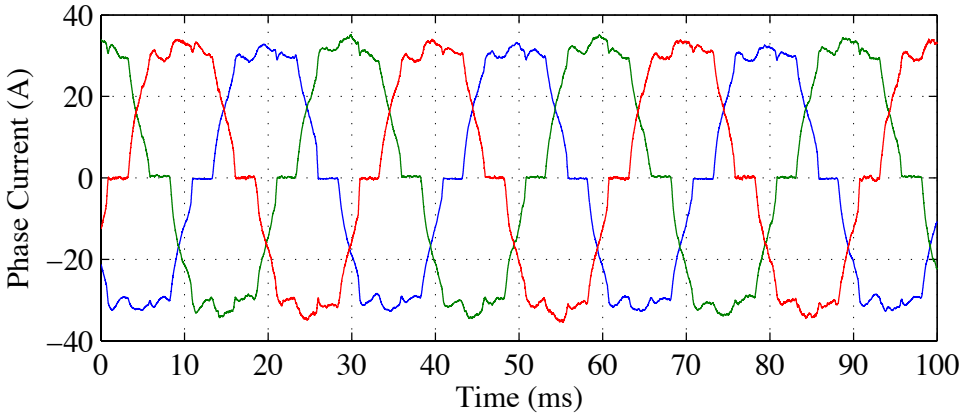

(c)

Figure 6.15: Gradual mode transition from BLDC-120 to BLAC at 200 rpm and 50 N m for (a) 0 %, (b) 25 %, (c) 50 %, (d) 75 %, and (e) 100 % BLAC.

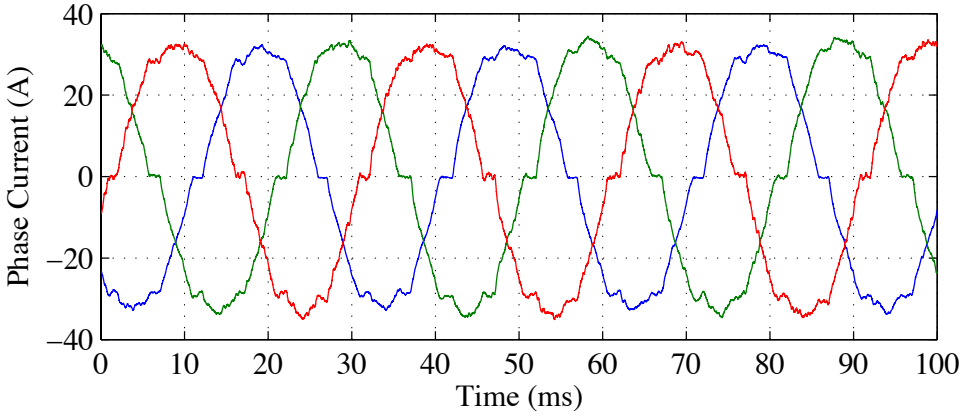

(d)

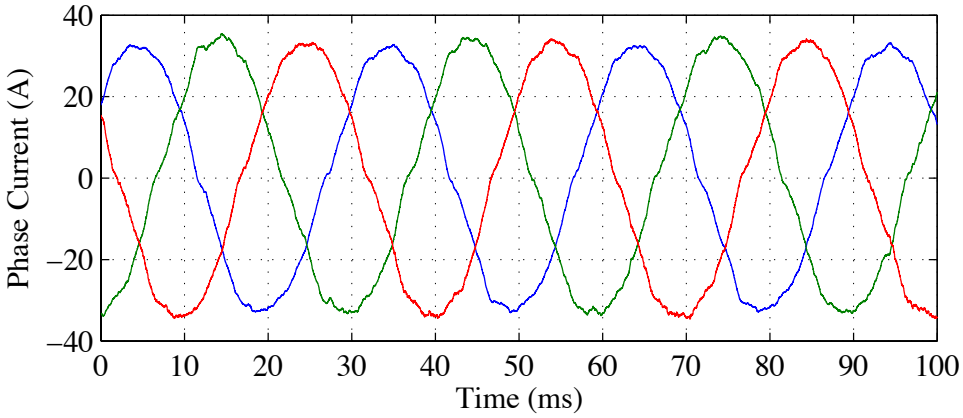

(e)

Figure 6.15: Gradual mode transition from BLDC-120 to BLAC at 200 rpm and 50 N m for (a) 0 %, (b) 25 %, (c) 50 %, (d) 75 %, and (e) 100 % BLAC.

change with the amount of modulation, the motor sound level can be tuned as a function of speed and torque to meet the expectations of pedestrians and drivers. However, an increase in the audible noise from the motor could be indicative of increased stresses on the motor components and a reduction in component times to failure. The impact on the fatigue life of the motor should therefore be carefully considered.

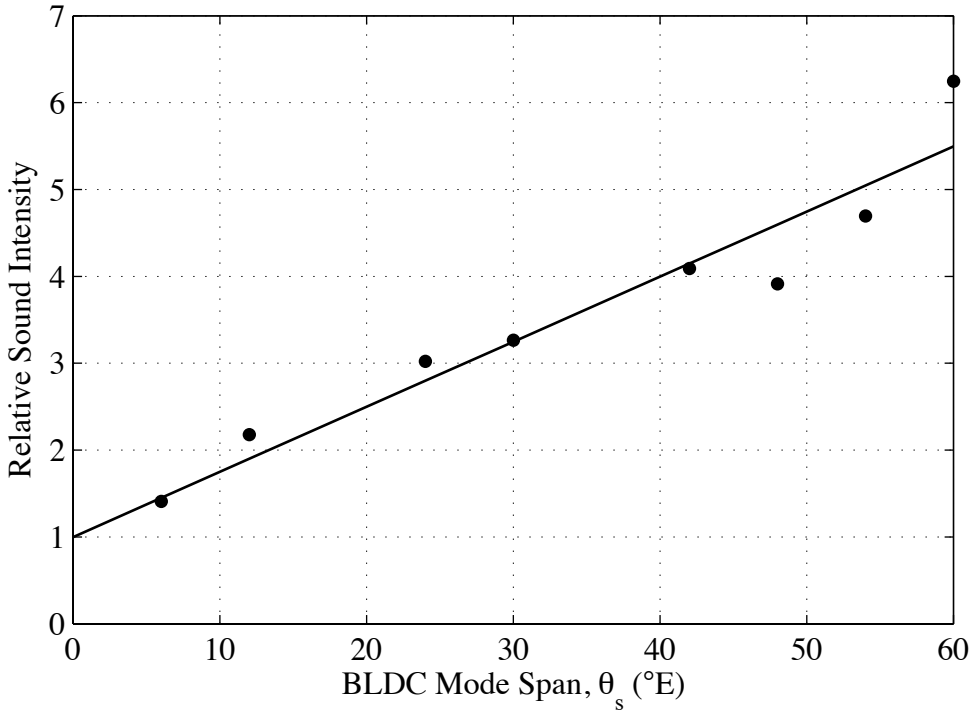

Figure 6.16: The change in the motor sound intensity for gradual mode transitions between BLAC and BLDC-120 control modes.

6.6 Summary

This chapter has presented a control strategy allowing a brushless motor with a sinusoidal back EMF to be switched between different control modes while running and without interruption of the output torque. The proposed single controller can drive a motor in BLDC-120, BLDC-180 and BLAC control modes and can change between the modes at any time.

The proposed technique based on space vector modulation with field oriented control has been described and demonstrated with simulated results. The controller has also been implemented and tested on real hardware using a vehicle motor to verify the simulation. The measured motor phase current waveforms show the transition between BLDC-120 and BLAC modes takes less than 2 ms and give a negligible change in the average motor torque output.

Benefits of the technique have also been discussed. A strategy utilising all three control modes to maximise the system efficiency has been proposed. The performance of the strategy has been simulated for an example electric vehicle over the UCDS drive cycle and has been shown to reduce the cycle energy requirement by 312 kJ compared to using the BLAC mode in isolation.

The mode switching technique has also been extended to allow modulation between BLDC-120 and BLAC modes with an experimental demonstration. The sound intensity of the motor was shown to increase linearly as the control mode was modulated from BLAC to BLDC-120. A proposed application for this control technique is to address electric vehicle sound safety issues.

7

Conclusions and Further Work

7.1 Conclusions

This thesis has presented a new control strategy to improve the efficiency of permanent magnet synchronous motors for use in hybrid and electric vehicles.

In Chapter 2, the loss mechanisms affecting permanent magnet motors and inverters were identified and a review of methods for determining losses was given. Analytical equations were chosen for determining the motor winding and inverter losses of the example system, as they can be applied to simulated motor phase currents using the characteristics from component datasheets. The use of simulated phase current waveforms instead of a sinusoidal approximation also allows the behaviour of different control modes to be taken into account. Finite element analysis was chosen to determine eddy current and hysteresis losses for the motor, as it allows the three-dimensional geometry of the machine to be modelled and does not require invasive measurements to be taken from the motor.

Chapter 3 provided a review of control techniques for permanent magnet synchronous

motors. The BLAC method was shown in the literature to give the lowest motor torque ripple as a result of the low harmonic content of the motor phase current waveforms. However, additional computation is required over BLDC control to implement the reference frame transformations and space vector modulation. A review of the literature found few quantified comparisons of motor and inverter efficiencies for each of the three control modes. This was identified as an important prerequisite to developing an improved control strategy that meets the thesis objective of improving system efficiency.

Motor position sensing techniques were discussed and an angle tracking algorithm was proposed for use with the experimental YASA motor. The algorithm is shown to track the true motor position to within 1 °E under steady state operation and to within 10 °E when subjected to a 1200 rpm/s acceleration. Therefore, **the position resolution required for BLAC control can be achieved using inexpensive low resolution position sensors when combined with the proposed software based extrapolation technique.** This allows the 500 N m YASA motor to be controlled in BLAC mode without modification, as required under the experimental constraints in Section 1.5.

In Chapter 4, the motor torque and power output for each of the three control modes were compared. Analytical equations for predicting the performance of the BLAC mode were derived to show how the maximum motor torque can be predicted for known motor parameters. It was also shown that a critical value for the motor winding inductance, $k/I_{ph,max}$, is needed to achieve a theoretically infinite constant power speed range. For the example system given, reducing the inductance to 70 % of the critical value increased the base speed from 1429 rpm to 1654 rpm before the inverter output voltage limitation was reached. The speed at which peak power is achieved fell to 2801 rpm from a theoretically infinite speed for the critical inductance machine. The maximum speed also fell to 6667 rpm as more field weakening current is required from a lower speed, reducing the current available for torque production.

The peak torque output across the theoretical motor speed operating range was assessed

using a Simulink model of the example YASA motor system. The BLDC-180 mode was found to give the highest peak power output of 108 kW at 2600 rpm as a result of the highest DC link voltage utilisation at this speed. However, the maximum torque output is higher for the BLAC mode below 1600 rpm by up to 4.2 N m as a result of the more optimally shaped phase current waveforms. Above 5400 rpm, the DC link voltage utilisation for the BLDC-120 mode is superior and the maximum torque output is higher than for the BLDC-180 mode by up to 20.5 N m. Therefore, **to maximise the available motor torque output, it is necessary to change the control mode as the motor speed changes.** The maximisation of the motor torque was identified as a key objective of the new control strategy in Section 1.5.

The motor and inverter losses for the example system were determined across the operating range in Chapter 5. The simulated efficiency results were compared to available experimental data over a limited operating range and were found to differ by less than 6 %. The BLAC mode gives the highest efficiency for the example system of 90.7 % at 1750 rpm and 140 N m. Below base speed of approximately 2000 rpm, the BLAC mode phase currents have the lowest harmonic content and give the lowest system losses. Beyond the base speed, the BLDC modes become more efficient as a result of better DC link voltage utilisation and reduced field weakening currents. At 2500 rpm and 130 N m, the system efficiency is 2.71 % lower for the BLAC mode than the BLDC-180 mode, giving in a 20.2 % increase in losses. Therefore, **to maximise the efficiency of the system, it is necessary to change the control mode as the motor speed and torque changes.**

In Chapter 6, a new control strategy was presented which allows the motor control mode to be changed while the motor is running and without interruption of the torque output. **The proposed technique allows the system efficiency to be improved, by changing to the control mode that will give the highest efficiency for the instantaneous speed and torque.** The total system losses over a simulated drive cycle for an example electric vehicle were reduced by 10.3 % using the new strategy compared to using the BLAC control mode in isolation. Use of the new control strategy therefore meets the thesis objective of

improving system efficiency. It also offers the potential for improved fuel economy and range for hybrid and electric vehicles.

Finally, a method to allow a continuous transition between modes by making two control mode changes in each 60°E sector was demonstrated. The relative sound intensity of the motor was found to increase in the BLDC-120 mode to 5.5 times the level for the BLAC mode as a result of the increased phase current harmonics and torque ripple. Therefore, **the sound level produced by the motor can be controlled by blending between control modes.** Sound generation as a means of improving electric vehicle safety has been identified as a potential application for this technique.

7.2 Specific Contributions of this Thesis

This thesis has made the following contributions to academic literature:

1. A position tracking algorithm has been developed, which allows motors with inexpensive low resolution position sensors to be controlled in the BLAC mode.

2. A detailed analysis of the loss components for a new permanent magnet motor topology, the YASA topology, has been presented.

3. A method of fitting limited simulated losses to a loss map has been shown. This minimises the number of FEA results required to produce an estimated motor efficiency map.

4. The torque of the YASA motor topology and the system efficiency when controlled in BLDC-120, BLDC-180 and BLAC modes has been determined and compared.

5. A motor control strategy that switches between motor control modes has been developed to maximise system efficiency and motor torque output.

6. A method for gradual transitions between control modes has been found, allowing control over the motor sound intensity independent from the motor torque output.

7.3 Further Work

While the method for switching between control modes has been demonstrated experimentally, further experimental results are needed to validate the simulated efficiency model over the entire operating range. The motor and inverter losses have also not been characterised for the example system between control modes. Further investigation into the losses under these operating conditions may yield further improvements to the system efficiency.

The efficiency analysis presented in this thesis has looked at the motor phase current waveforms resulting from three specific control modes. A study into phase current waveform shapes should be conducted to determine the current waveform that will maximise the system efficiency.

The choice of control mode has been shown to influence the torque ripple and audible noise produced by the motor. A mechanical stress analysis of the motor should be undertaken to determine if the use of different control modes will impact on the fatigue life of the motor components. This could also affect the design of the drive shafts and motor mountings for the vehicle to which the motor is connected.

A useful development of the motor control strategy would be to change control modes as the component temperatures approach their operating limits. This would allow the losses of specific components to be reduced and the system output power to be sustained for longer before the system must be derated. An investigation into the thermal performance of the example system should be undertaken to determine the maximum safe operating time at a given torque and speed, before component thermal limits are reached. Once established for the motor and inverter in each control mode, a thermal mode utilisation strategy could be determined.

Finally, the control system developed in this thesis should be applied to a real electric vehicle. This would allow collection of data to validate the performance of the control strategy and measure the improvement in vehicle range for real world driving conditions.

A

Loss Maps for BLDC-180 and BLAC Control Modes

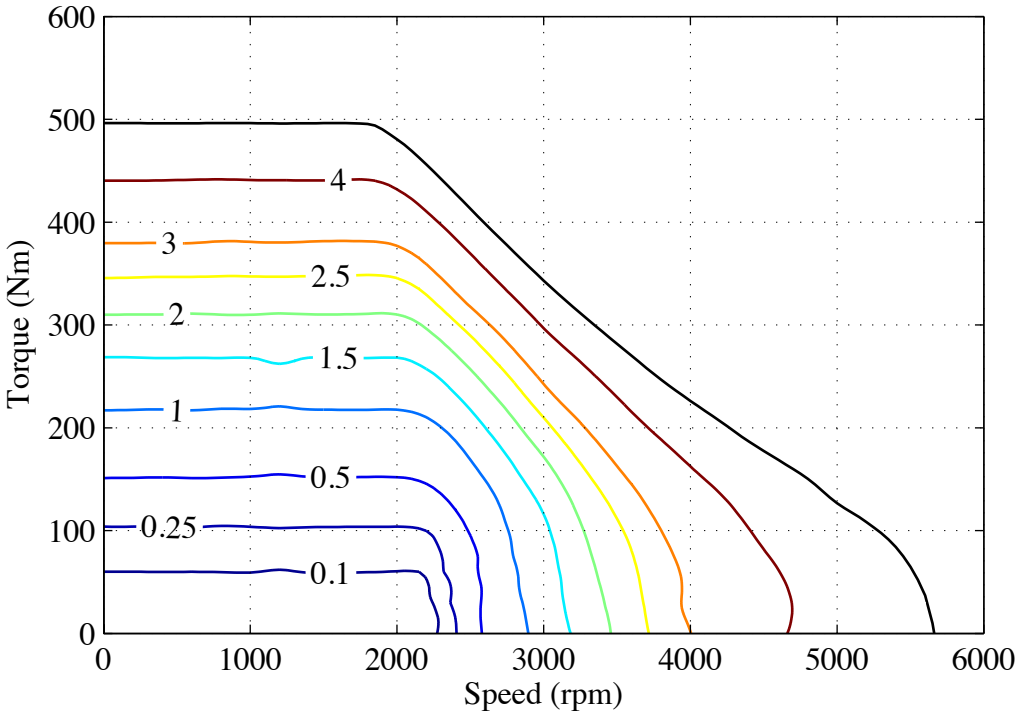

Figure A.1: BLDC-180 winding loss map (contour values in kW).

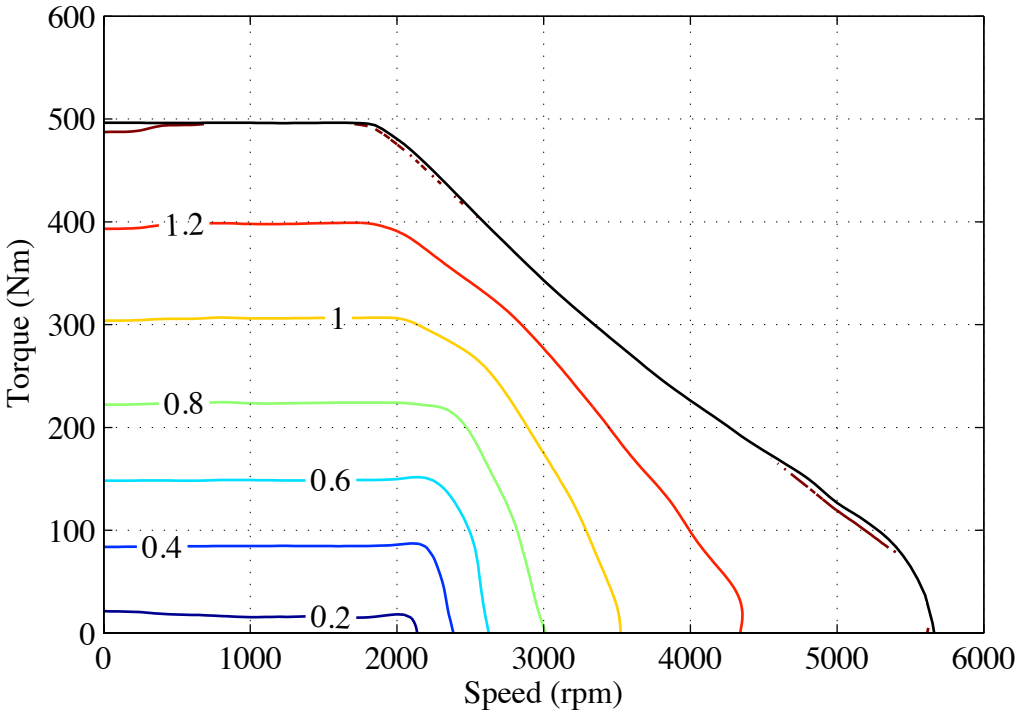

Figure A.2: BLDC-180 inverter switching loss map (contour values in kW).

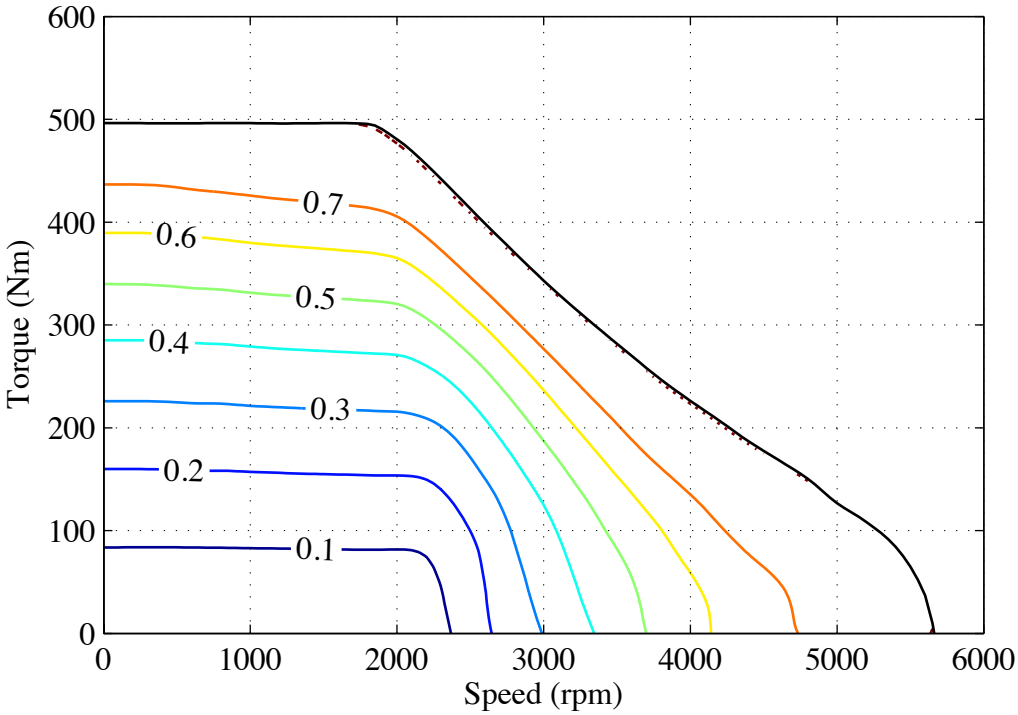

Figure A.3: BLDC-180 inverter conduction loss map (contour values in kW).

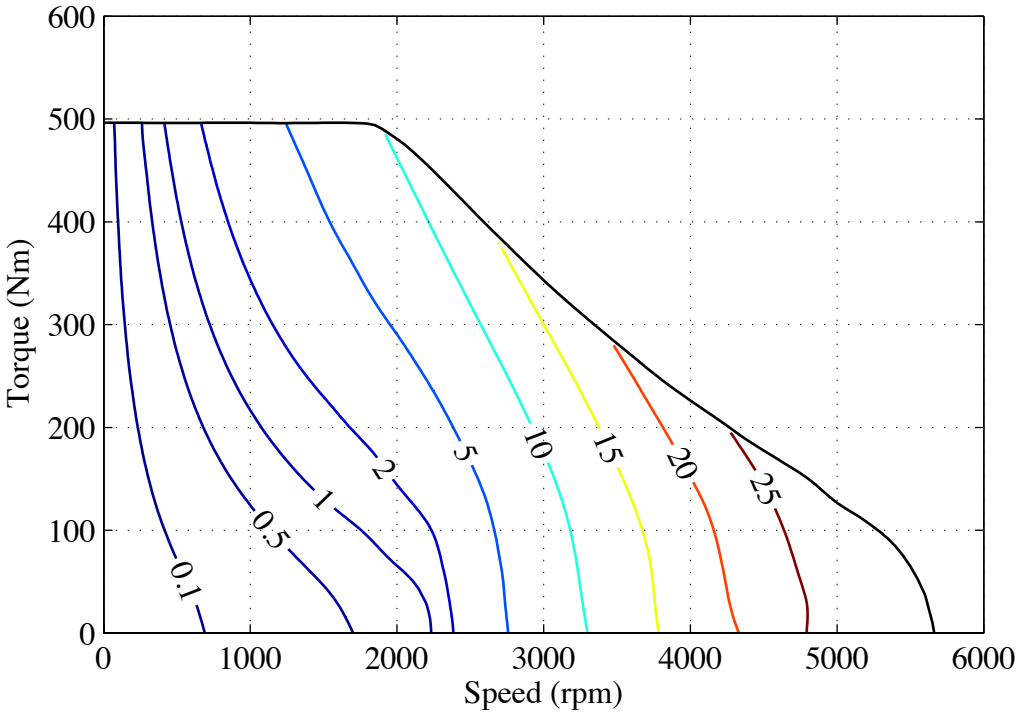

Figure A.4: BLDC-180 eddy current loss map (contour values in kW).

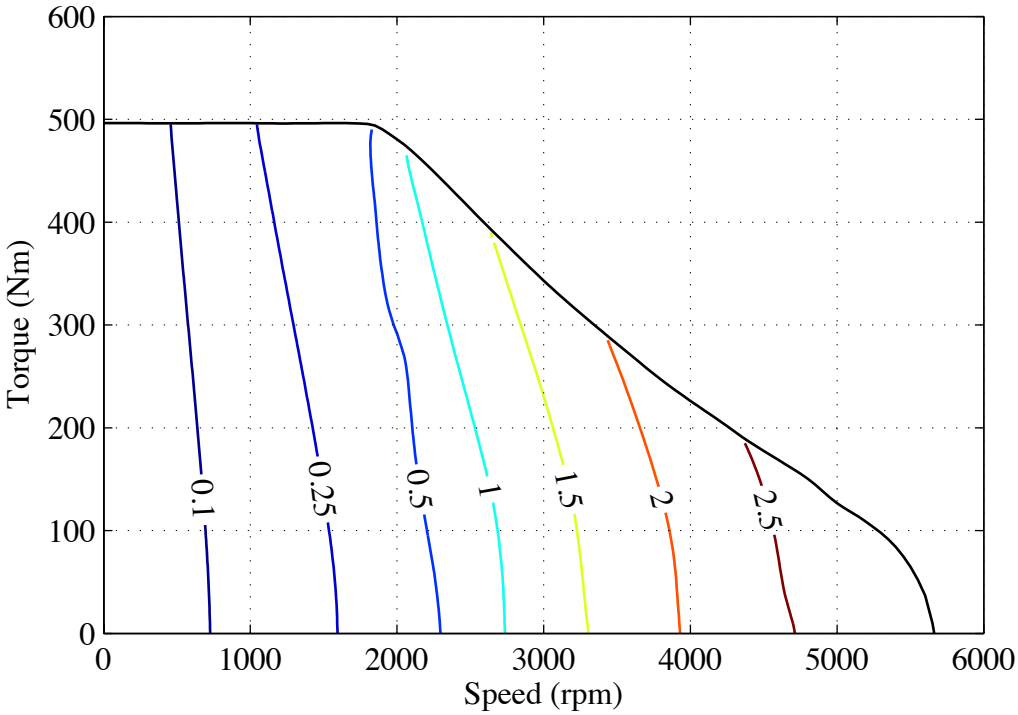

Figure A.5: BLDC-180 hysteresis loss map (contour values in kW).

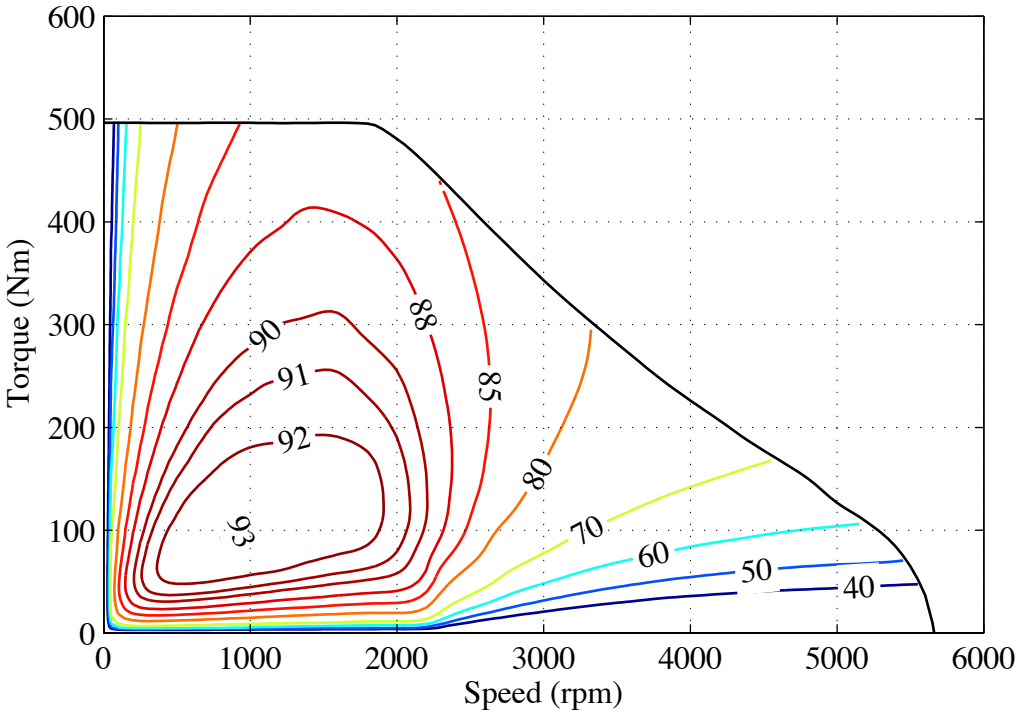

Figure A.6: BLDC-180 motor efficiency map (contour values in %).

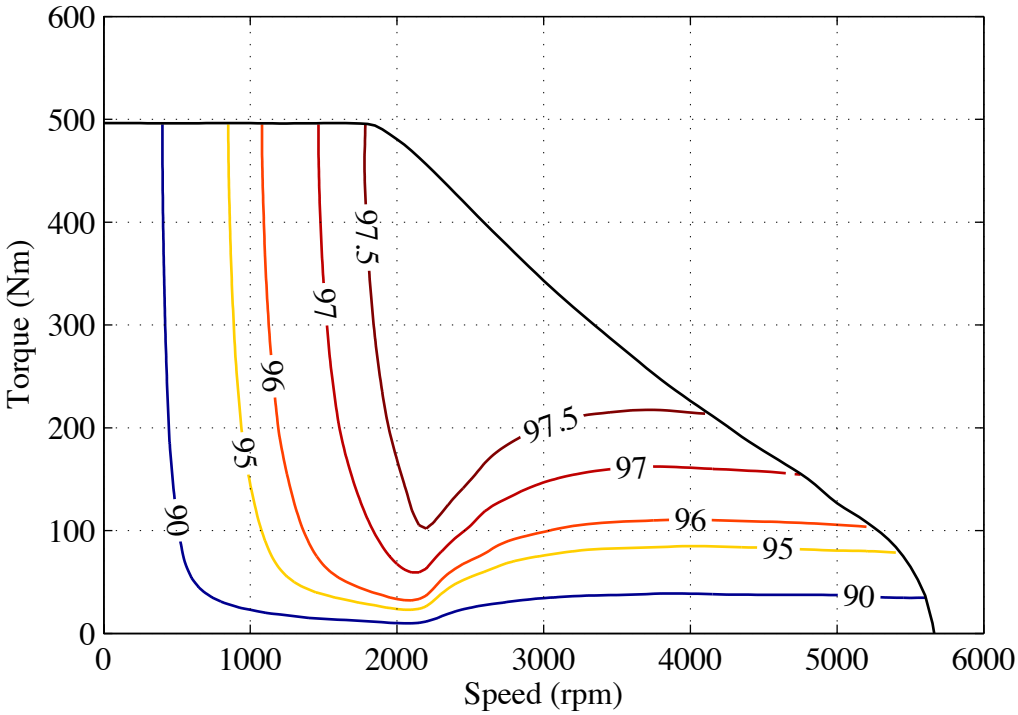

Figure A.7: BLDC-180 inverter efficiency map (contour values in %).

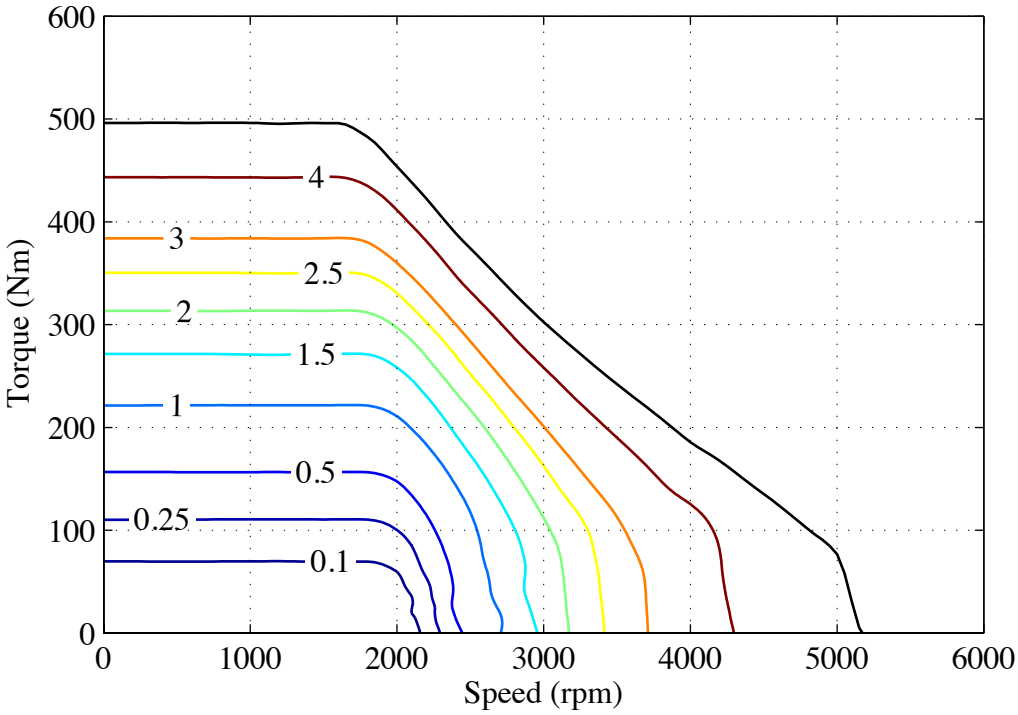

Figure A.8: BLAC winding loss map (contour values in kW).

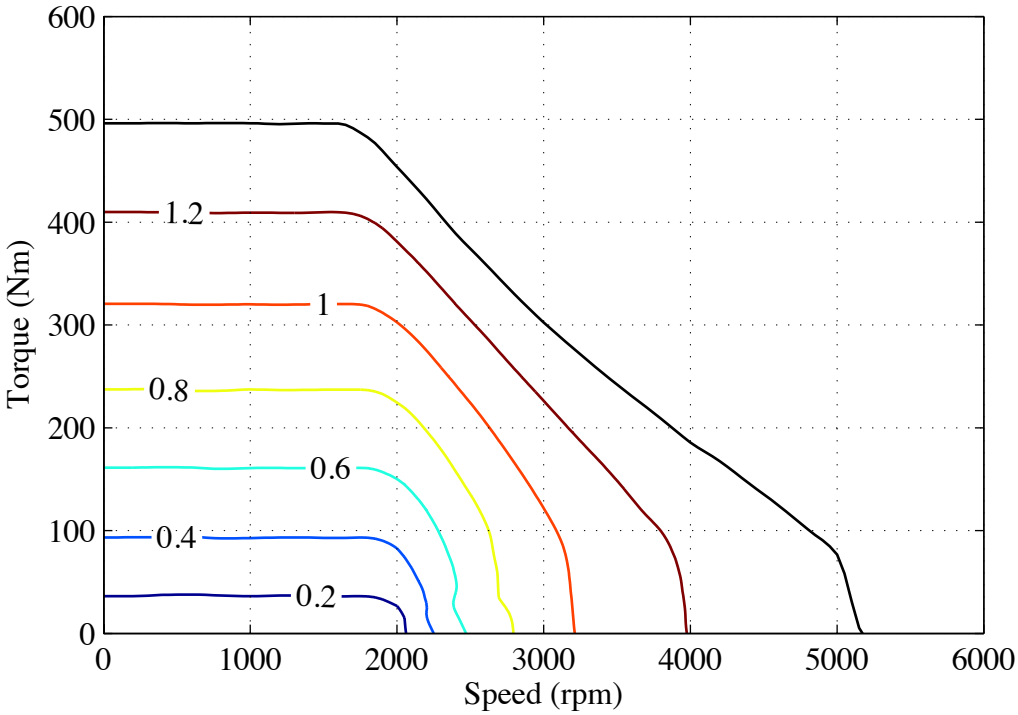

Figure A.9: BLAC inverter switching loss map (contour values in kW).

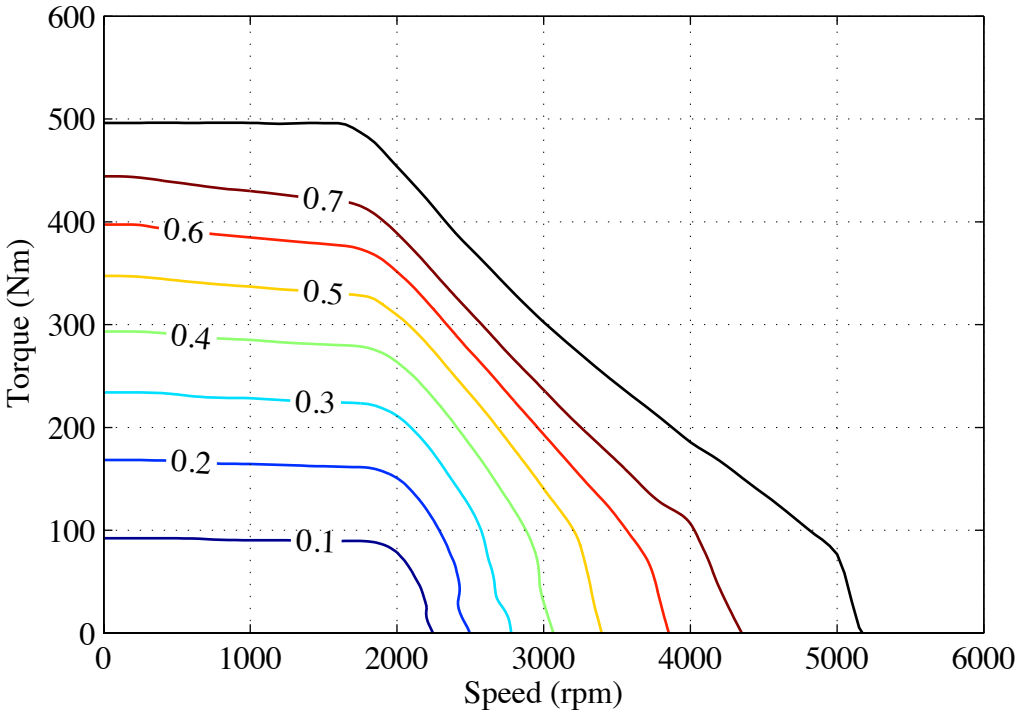

Figure A.10: BLAC inverter conduction loss map (contour values in kW).

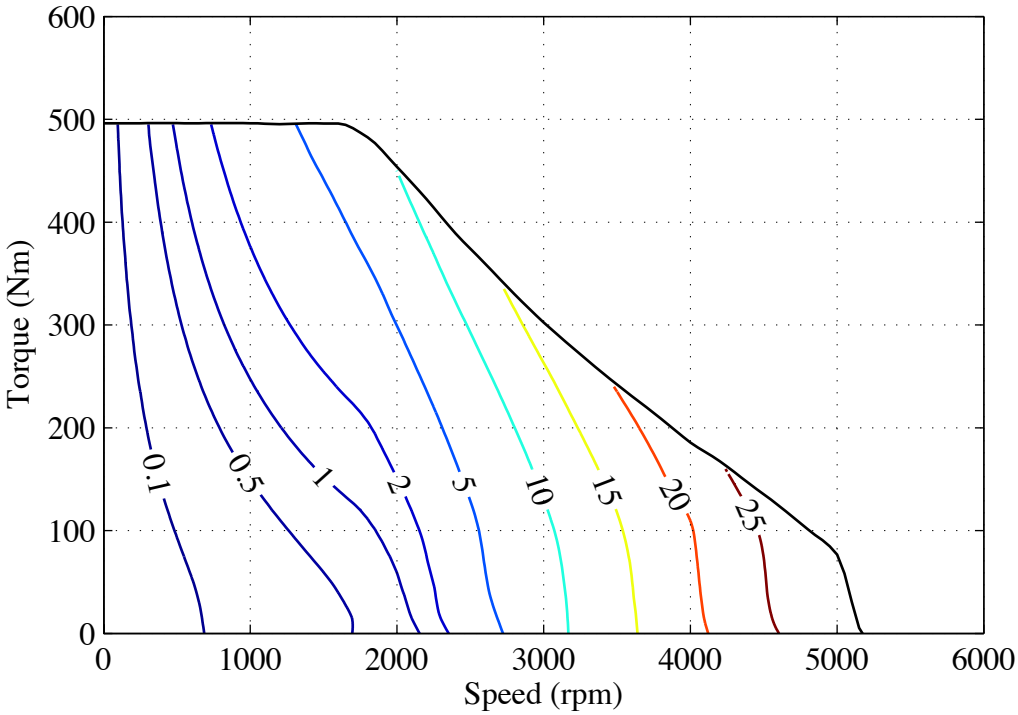

Figure A.11: BLAC eddy current loss map (contour values in kW).

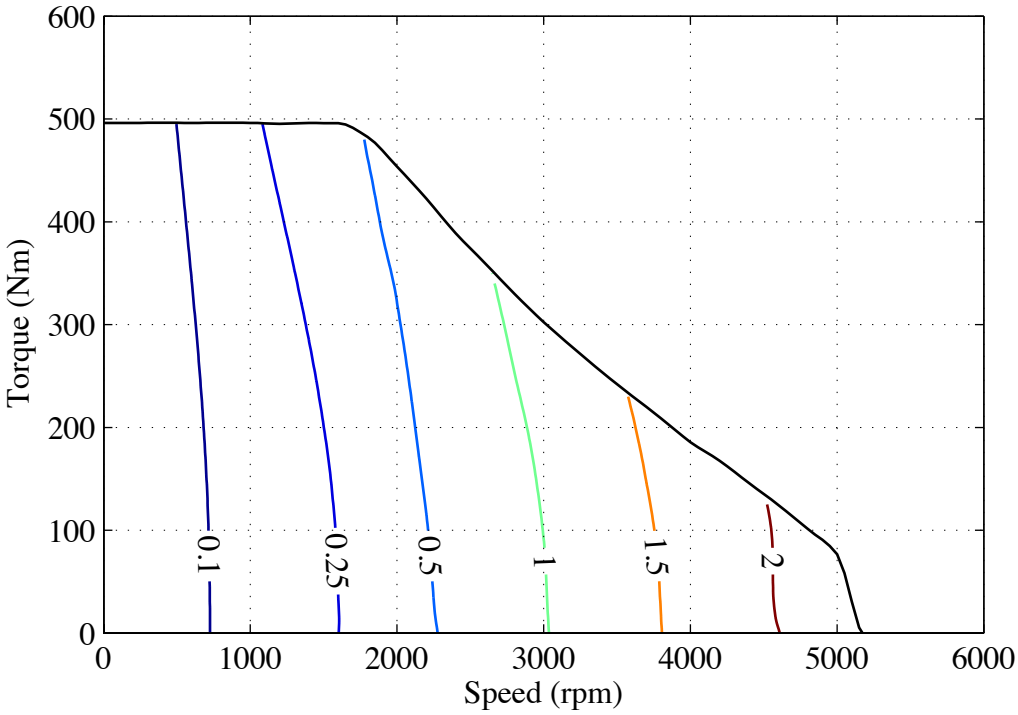

Figure A.12: BLAC hysteresis loss map (contour values in kW).

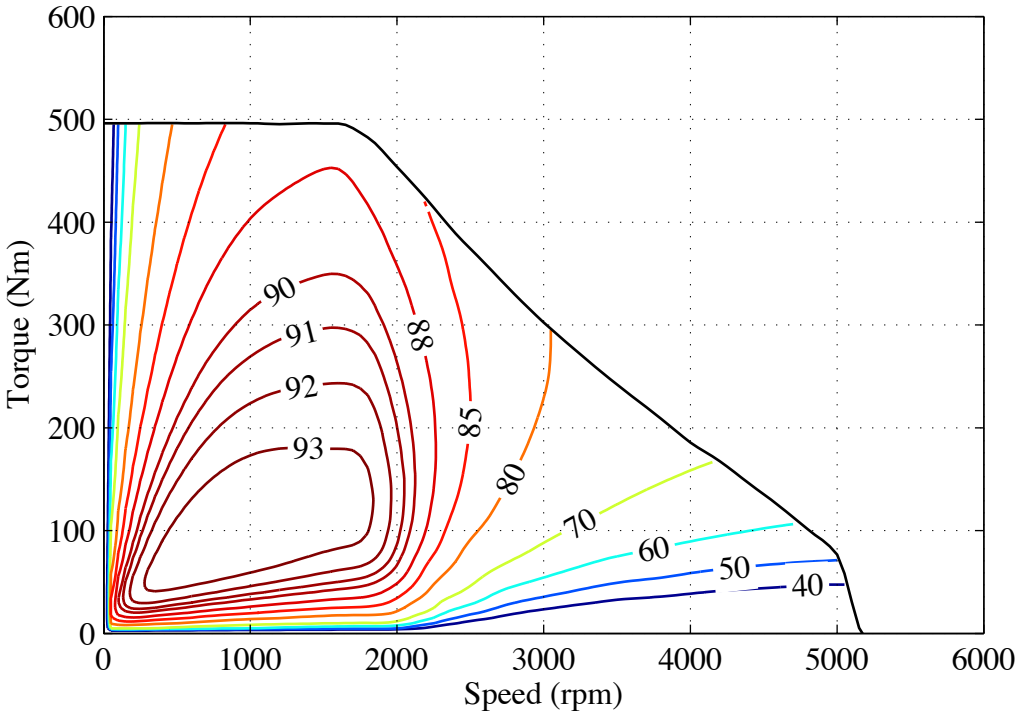

Figure A.13: BLAC motor efficiency map (contour values in %).

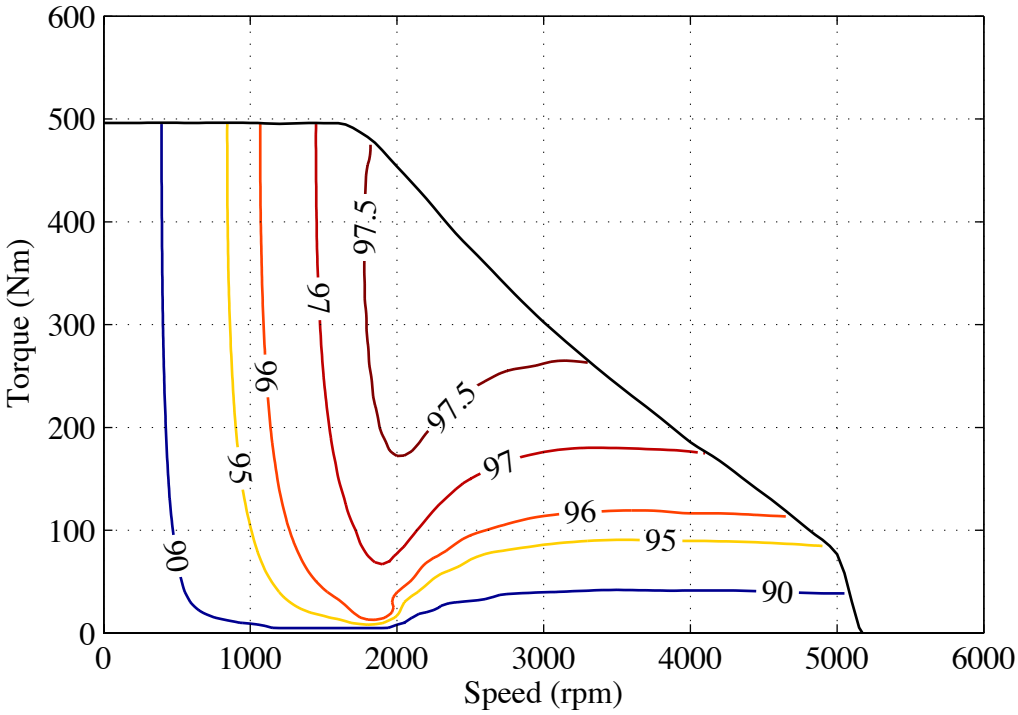

Figure A.14: BLAC inverter efficiency map (contour values in %).

B

Material Properties for Motor FEA

Table B.1: Conductivities of the YASA motor magnetic materials [2, 8, 9].

Material	Conductivity (S/m)
Rotor electrical steel	5.0×10^6
Somaloy 3P HR	384
N42SH NdFeB	6.25×10^5

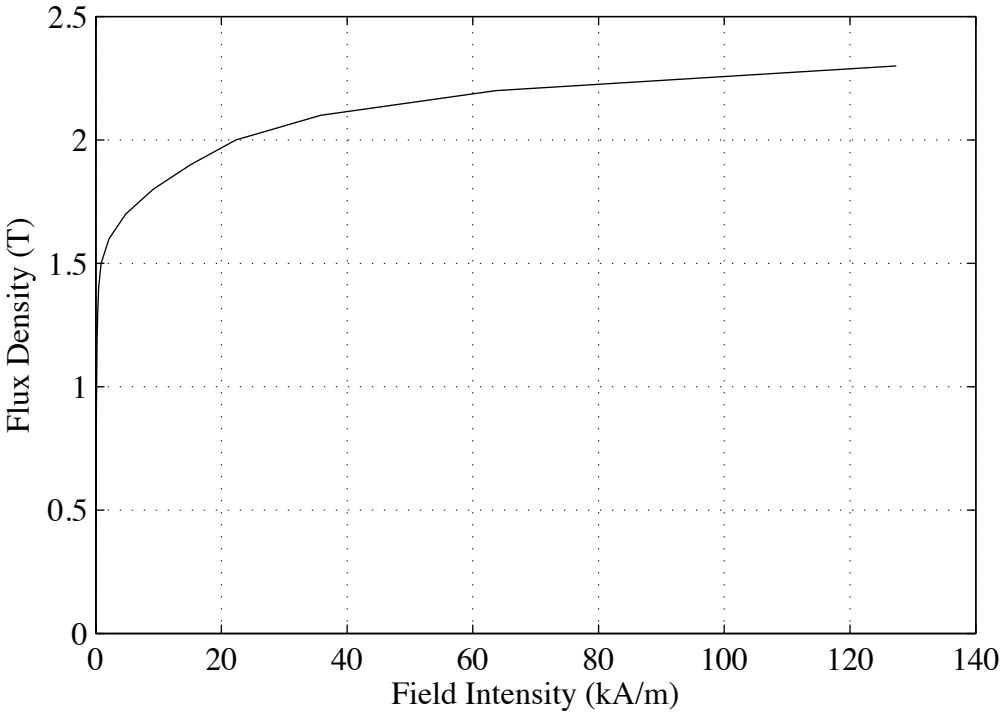

Figure B.1: Rotor silicon iron material B-H curve [8].

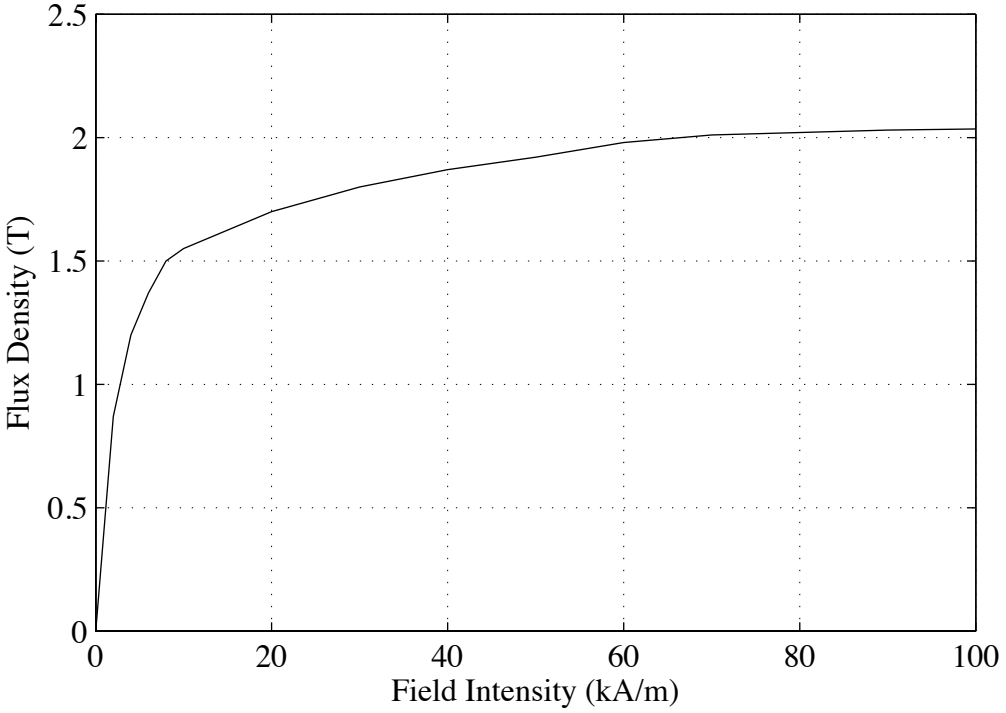

Figure B.2: Somaloy 3P HR (pole piece) material B-H curve [2].

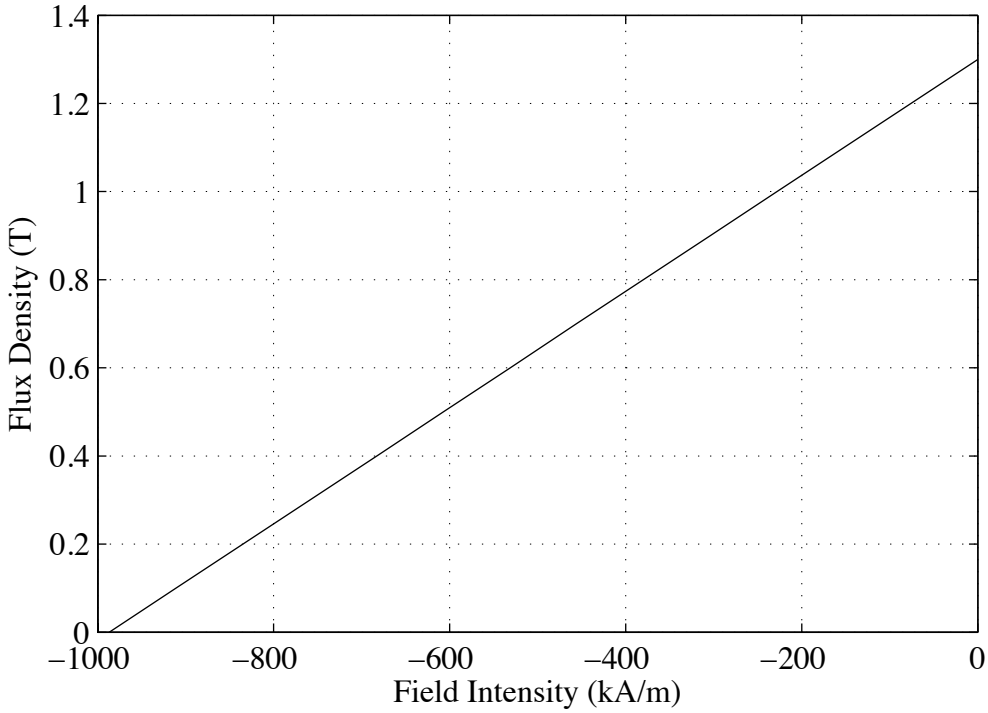

Figure B.3: N42SH NdFeB permanent magnet material B-H curve [9].

Bibliography

[1] International carbon flows: Automotive. Technical report, The Carbon Trust, May 2011. Available from: http://www.carbontrust.co.uk/publications/pages/publicationdetail.aspx?id=CTC792 [Accessed 16 August 2011].

[2] Hoganas. *Somaloy 3P HR SMC Datasheet*, 2007. Available from: http://www.hoganas.com/ [Accessed October 2007].

[3] R.S. Chokhawala, J. Catt, and B.R. Pelly. Gate drive considerations for IGBT modules. *Industry Applications, IEEE Transactions on*, 31(3):603 –611, May 1995.

[4] Ned Mohan, Tore M. Undeland, and William P. Robbins. *Power Electronics*. John Wiley and Sons, Inc., 3rd edition, 2003.

[5] T. Rekioua, F. Meibody Tabar, and R. le Doeuff. A new approach for the field-oriented control of brushless, synchronous, permanent magnet machines. In *Power Electronics and Variable-Speed Drives, 1991., Fourth International Conference on*, pages 46 –50, July 1990.

[6] K.S. Low, M.F. Rahman, and K.W. Lim. The dq transformation and feedback linearization of a permanent magnet synchronous motor. In *Power Electronics and Drive Systems, 1995., Proceedings of 1995 International Conference on*, pages 292 –296 vol.1, February 1995.

[7] California Environmental Protection Agency: Air Resources Board. Unified cycle driving schedule, December 1996. Available from: http://www.arb.ca.gov/msprog/obdprog/uccycle.doc [Accessed 10 September 2011].

[8] Vector Fields. *Opera-3D Reference Manual*, 2004.

[9] Magnet Applications Limited. *Magnet Technical Specification*, 2011. Available from: `http://www.magnetukonline.com/documents/technical%20specification.xls` [Accessed 6 August 2011].

[10] M.H. Westbrook, Institution of Electrical Engineers, and Society of Automotive Engineers. *The electric car: development and future of battery, hybrid and fuel-cell cars*. IEE power and energy series. Institution of Electrical Engineers, 2001.

[11] L. Guzzella and A. Sciarretta. *Vehicle propulsion systems: introduction to modeling and optimization*. Springer, 2005.

[12] J.G.W. West. DC, induction, reluctance and PM motors for electric vehicles. *Power Engineering Journal*, 8(2):77 –88, April 1994.

[13] T. Uematsu and R.S. Wallace. Design of a 100 kW switched reluctance motor for electric vehicle propulsion. In *Applied Power Electronics Conference and Exposition, 1995. APEC '95. Conference Proceedings 1995., Tenth Annual*, number 0, pages 411 –415 vol.1, March 1995.

[14] J.M. Miller. *Propulsion Systems for Hybrid Vehicles*. IEE Power and Energy Series. Institution of Engineering and Technology, 2004.

[15] T.J. Woolmer and M.D. McCulloch. Analysis of the yokeless and segmented armature machine. In *Electric Machines Drives Conference, 2007. IEMDC '07. IEEE International*, volume 1, pages 704 –708, 3-5 2007.

[16] Raser Technologies. *P-200 Motor: AC Induction Traction Motor*, 2011. Available from: `http://www.rasertech.com` [Accessed 19 August 2011].

[17] Semikron. *SKAI 3001GD12 1452 W Datasheet*, 2005. Available from: `http://www.eltron.pl/elektronika/semikron/pdf/systemy-mocy/`

systemy-specjalizowane/SKAI%203001GD12%201452%20W.pdf [Accessed 11 December 2009].

[18] The Engineering Toolbox. Resistivity, Conductivity and Temperature Coefficients for some Common Materials. Available from: http://www.engineeringtoolbox.com/resistivity-conductivity-d_418.html [Accessed 27 November 2010].

[19] The Engineering Toolbox. Metals and Alloys - Densities. Available from: http://www.engineeringtoolbox.com/metal-alloys-densities-d_50.html [Accessed 27 November 2010].

[20] Semikron. *Product Catalogue 2010/2011*, 2010. Available from: http://www.semikron.com/ [Accessed January 2011].

[21] Sensor Technology. *TorqSense RWT310/320 series Torque Transducer*, 2011. Available from: http://www.sensors.co.uk/files/dsm/Datasheet_RWT310-320.pdf [Accessed 29 August 2011].

[22] Testec Elektronik GmbH. *Active Differential Probe*, 2000. Available from: http://www.farnell.com/datasheets/22818.pdf [Accessed 1 October 2011].

[23] LEM. *Current Probe Model PR430*, 2001. Available from: http://www.farnell.com/datasheets/12567.pdf [Accessed 1 October 2011].

[24] Cleaner, More Efficient Vehicles: Reducing Emissions in Central and Eastern Europe. Technical report, Global Fuel Economy Initiative, May 2010. Available from: http://www.globalfueleconomy.org/Documents/Publications/wp3_cleaner_more_efficient_vehicles.pdf [Accessed 17 August 2011].

[25] Making cars 50% more fuel efficient by 2050 worldwide. Technical report, 50 By 50 Global Fuel Economy Initiative, 2009. Available from: http://

www.fiafoundation.org/50by50/documents/50BY50_report.pdf [Accessed 18 September 2011].

[26] M. Ehsani, Y. Gao, and J. M. Miller. Hybrid electric vehicles: Architecture and motor drives. *Proceedings of the IEEE*, 95(4):719–728, April 2007.

[27] M. Ehsani, Y. Gao, S. E. Gay, and A. Emadi. *Modern Electric, Hybrid Electric, and Fuel Cell Vehicles*. CRC Press, 2005.

[28] Investigation into the scope for the transport sector to switch to electric vehicles and plug-in hybrid vehicles. Technical report, Department for Business Enterprise & Regulatory Reform, October 2008.

[29] Amory B. Lovins and David R. Cramer. Hypercars, hydrogen, and the automotive transition. *International Journal of Vehicle Design*, 35(1/2):50–85, March 2004.

[30] C.C. Chan. The state of the art of electric, hybrid, and fuel cell vehicles. *Proceedings of the IEEE*, 95(4):704 –718, April 2007.

[31] A.E. Corbett and C. Mellors. Hybrid electric machines. *Machines and Drives for Electric and Hybrid Vehicles (Digest No: 1996/152), IEE Colloquium on*, pages 7/1–7/6, June 1996.

[32] A. Emadi, Young Joo Lee, and K. Rajashekara. Power electronics and motor drives in electric, hybrid electric, and plug-in hybrid electric vehicles. *Industrial Electronics, IEEE Transactions on*, 55(6):2237 –2245, June 2008.

[33] G. Maggetto and J. Van Mierlo. Electric and electric hybrid vehicle technology: a survey. *Electric, Hybrid and Fuel Cell Vehicles (Ref. No. 2000/050), IEE Seminar*, pages 1/1–111, 2000.

[34] C.C. Chan and Y.S. Wong. The state of the art of electric vehicles technology.

Power Electronics and Motion Control Conference, 2004. IPEMC 2004. The 4th International, 1:46–57 Vol.1, August 2004.

[35] Z.Q. Zhu and D. Howe. Electrical machines and drives for electric, hybrid, and fuel cell vehicles. *Proceedings of the IEEE*, 95(4):746 –765, April 2007.

[36] K. Asano, Y. Inaguma, H. Ohtani, E. Sato, M. Okamura, and S. Sasaki. High performance motor drive technologies for hybrid vehicles. *Power Conversion Conference - Nagoya, 2007. PCC '07*, pages 1584–1589, April 2007.

[37] Z.Q. Zhu and C.C. Chan. Electrical machine topologies and technologies for electric, hybrid, and fuel cell vehicles. In *Vehicle Power and Propulsion Conference, 2008. VPPC '08. IEEE*, pages 1 –6, September 2008.

[38] M. Zeraoulia, M.E.H. Benbouzid, and D. Diallo. Electric motor drive selection issues for HEV propulsion systems: A comparative study. *Vehicular Technology, IEEE Transactions on*, 55(6):1756 –1764, November 2006.

[39] Adam Aston. China's rare-earth monopoly. *Technology Review*, October 2010. Available from: `http://www.technologyreview.com/energy/26538/` [Accessed August 2011].

[40] Y.F. Shi, Z.Q. Zhu, and D. Howe. Torque-speed characteristics of interior-magnet machines in brushless AC and DC modes, with particular reference to their flux-weakening performance. In *Power Electronics and Motion Control Conference, 2006. IPEMC 2006. CES/IEEE 5th International*, volume 3, pages 1 –5, 14-16 2006.

[41] A.P. Wu and P.L. Chapman. Cancellation of torque ripple due to nonidealities of permanent magnet synchronous machine drives. In *Power Electronics Specialist Conference, 2003. PESC '03. 2003 IEEE 34th Annual*, volume 1, pages 256 – 261 vol.1, 15-19 2003.

[42] D.C. Hanselman. Minimum torque ripple, maximum efficiency excitation of brushless permanent magnet motors. *Industrial Electronics, IEEE Transactions on*, 41(3):292 –300, June 1994.

[43] D. Yousfi. Encoderless PM brushless drive for electric vehicle traction. In *Industrial Electronics, 2009. IECON '09. 35th Annual Conference of IEEE*, pages 3797 –3802, 3-5 2009.

[44] A.M. EL-Refaie, D.W. Novotny, and T.M. Jahns. A simple model for flux weakening in surface PM synchronous machines using back-to-back thyristors. *Power Electronics Letters, IEEE*, 2(2):54 – 57, June 2004.

[45] Tae-Suk Kwon and Seung-Ki Sul. A novel flux weakening algorithm for surface mounted permanent magnet synchronous machines with infinite constant power speed ratio. In *Electrical Machines and Systems, 2007. ICEMS. International Conference on*, pages 440 –445, October 2007.

[46] S. Williamson, M. Lukic, and A. Emadi. Comprehensive drive train efficiency analysis of hybrid electric and fuel cell vehicles based on motor-controller efficiency modeling. *Power Electronics, IEEE Transactions on*, 21(3):730 –740, May 2006.

[47] M. Negrea and M. Rosu. Thermal analysis of a large permanent magnet synchronous motor for different permanent magnet rotor configurations. In *Electric Machines and Drives Conference, 2001. IEMDC 2001. IEEE International*, pages 777 –781, 2001.

[48] A. Emadi, K. Rajashekara, S.S. Williamson, and S.M. Lukic. Topological overview of hybrid electric and fuel cell vehicular power system architectures and configurations. *Vehicular Technology, IEEE Transactions on*, 54(3):763 – 770, May 2005.

[49] Miaosen Shen, A. Joseph, Jin Wang, F.Z. Peng, and D.J. Adams. Comparison of

traditional inverters and z -source inverter for fuel cell vehicles. *Power Electronics, IEEE Transactions on*, 22(4):1453 –1463, July 2007.

[50] E. Levi. Multiphase electric machines for variable-speed applications. *Industrial Electronics, IEEE Transactions on*, 55(5):1893 –1909, May 2008.

[51] Carl Blake and Chris Bull. IGBT or MOSFET: Choose wisely. Technical report, International Rectifier, 2000. Available from: `http://www.irf.com/technical-info/whitepaper/choosewisely.pdf` [Accessed 17 August 2011].

[52] Microchip Technology Inc. *Brushless DC (BLDC) Motor Fundamentals*, 2003. Available from: `http://ww1.microchip.com/downloads/en/AppNotes/00885a.pdf` [Accessed 25 August 2011].

[53] Jamie Dunn. Determining MOSFET driver needs for motor drive applications. Technical report, Microchip Technology Inc., 2003. Available from: `http://ww1.microchip.com/downloads/en/AppNotes/00898a.pdf` [Accessed 17 August 2011].

[54] T. Finken, M. Felden, and K. Hameyer. Comparison and design of different electrical machine types regarding their applicability in hybrid electrical vehicles. In *Electrical Machines, 2008. ICEM 2008. 18th International Conference on*, pages 1 –5, September 2008.

[55] T.J. Woolmer and M.D. Mcculloch. Axial flux permanent magnet machines: A new topology for high performance applications. *Hybrid Vehicle Conference, IET The Institution of Engineering and Technology, 2006*, pages 27–42, December 2006.

[56] H.W. Beaty and J.L. Kirtley. *Electric Motor Handbook*. McGraw-Hill, 1998.

[57] R. Liu, P. Zheng, D. Xie, and L. Wang. Research on the high power density

electromagnetic propeller. *Magnetics, IEEE Transactions on*, 43(1):355 –358, January 2007.

[58] M. Mekhiche, S. Nichols, J.L. Kirtley, J. Young, D. Boudreau, and R. Jodoin. High-speed, high-power density PMSM drive for fuel cell powered HEV application. In *Electric Machines and Drives Conference, 2001. IEMDC 2001. IEEE International*, pages 658 –663, 2001.

[59] MWS Wire Industries. *Copper Magnet Wire: Material Safety Data Sheet*, July 2010. Available from: `http://www.mwswire.com/safetydata/cumagwire.pdf` [Accessed August 2011].

[60] S.M. Lukic and A. Emado. Modeling of electric machines for automotive applications using efficiency maps. In *Electrical Insulation Conference and Electrical Manufacturing Coil Winding Technology Conference, 2003. Proceedings*, pages 543 – 550, September 2003.

[61] C.R. Sullivan. Aluminum windings and other strategies for high-frequency magnetics design in an era of high copper and energy costs. *Power Electronics, IEEE Transactions on*, 23(4):2044 –2051, July 2008.

[62] K. Yamazaki, Y. Fukushima, and M. Sato. Loss analysis of permanent-magnet motors with concentrated windings - variation of magnet eddy-current loss due to stator and rotor shapes. *Industry Applications, IEEE Transactions on*, 45(4):1334 –1342, July 2009.

[63] L. Zheng, T.X. Wu, D. Acharya, K.B. Sundaram, J. Vaidya, L. Zhao, L. Zhou, K. Murty, C.H. Ham, N. Arakere, J. Kapat, and L. Chow. Design of a super-high speed permanent magnet synchronous motor for cryogenic applications. In *Electric Machines and Drives, 2005 IEEE International Conference on*, pages 874 –881, May 2005.

[64] W.G. Hurley, W.H. Wolfle, and J.G. Breslin. Optimized transformer design: inclusive of high-frequency effects. *Power Electronics, IEEE Transactions on*, 13(4):651–659, July 1998.

[65] C. Zwyssig, S.D. Round, and J.W. Kolar. An ultrahigh-speed, low power electrical drive system. *Industrial Electronics, IEEE Transactions on*, 55(2):577–585, 2008.

[66] Shen Wang, M.A. de Rooij, W.G. Odendaal, J.D. van Wyk, and D. Boroyevich. Reduction of high-frequency conduction losses using a planar litz structure. *Power Electronics, IEEE Transactions on*, 20(2):261 – 267, March 2005.

[67] P.H. Mellor, R. Wrobel, and N. McNeill. Investigation of proximity losses in a high speed brushless permanent magnet motor. In *Industry Applications Conference, 2006. 41st IAS Annual Meeting. Conference Record of the 2006 IEEE*, volume 3, pages 1514 –1518, October 2006.

[68] H. Polinder and M.J. Hoeijmakers. Eddy-current losses in the segmented surface-mounted magnets of a PM machine. *Electric Power Applications, IEE Proceedings -*, 146(3):261 –266, May 1999.

[69] H. Toda, Zhenping Xia, Jiabin Wang, K. Atallah, and D. Howe. Rotor eddy-current loss in permanent magnet brushless machines. *Magnetics, IEEE Transactions on*, 40(4):2104 – 2106, 2004.

[70] K. Yamazaki and S. Watari. Loss analysis of permanent-magnet motor considering carrier harmonics of PWM inverter using combination of 2-D and 3-D finite-element method. *Magnetics, IEEE Transactions on*, 41(5):1980 – 1983, May 2005.

[71] K. Yoshida, Y. Hita, and K. Kesamaru. Eddy-current loss analysis in PM of surface-mounted-PM SM for electric vehicles. *Magnetics, IEEE Transactions on*, 36(4):1941 –1944, July 2000.

[72] V. Navrapescu, M. Popescu, D.O. Kisck, G. Andronescu, and M. Kisck. Modelling of iron losses in salient pole permanent magnet synchronous motors. In *Power Electronics, 2007. ICPE '07. 7th Internatonal Conference on*, pages 352 –357, October 2007.

[73] You Guang Guo, Jian Guo Zhu, Zhi Wei Lin, and Jin Jiang Zhong. Measurement and modeling of core losses of soft magnetic composites under 3-D magnetic excitations in rotating motors. *Magnetics, IEEE Transactions on*, 41(10):3925 – 3927, 2005.

[74] K. Yamazaki, M. Shina, Y. Kanou, M. Miwa, and J. Hagiwara. Effect of eddy current loss reduction by segmentation of magnets in synchronous motors: Difference between interior and surface types. *Magnetics, IEEE Transactions on*, 45(10):4756 –4759, 2009.

[75] C. Mademlis, J. Xypteras, and N. Margaris. Loss minimization in surface permanent-magnet synchronous motor drives. *Industrial Electronics, IEEE Transactions on*, 47(1):115 –122, February 2000.

[76] Jia Hu, Yingli Luo, Mingji Liu, and Xiaofang Liu. Analysis of the iron loss of line start permanent magnet synchronous motor using time-stepping finite element method. In *Electrical Machines and Systems, 2008. ICEMS 2008. International Conference on*, pages 3237 –3240, October 2008.

[77] Z.Q. Zhu, K. Ng, N. Schofield, and D. Howe. Improved analytical modelling of rotor eddy current loss in brushless machines equipped with surface-mounted permanent magnets. *Electric Power Applications, IEE Proceedings* -, 151(6):641 – 650, November 2004.

[78] K. Atallah, D. Howe, P.H. Mellor, and D.A. Stone. Rotor loss in permanent-magnet brushless AC machines. *Industry Applications, IEEE Transactions on*, 36(6):1612 – 1618, November 2000.

[79] J. Nerg, M. Niemela, J. Pyrhonen, and J. Partanen. FEM calculation of rotor losses in a medium speed direct torque controlled PM synchronous motor at different load conditions. *Magnetics, IEEE Transactions on*, 38(5):3255 – 3257, September 2002.

[80] D.C. Jiles. A self consistent generalized model for the calculation of minor loop excursions in the theory of hysteresis. *Magnetics, IEEE Transactions on*, 28(5):2602 –2604, September 1992.

[81] J. Faiz and M.B.B. Sharifian. Core losses estimation in a multiple teeth per stator pole switched reluctance motor. *Magnetics, IEEE Transactions on*, 30(2):189 –195, March 1994.

[82] I. Junaid, J. Qudsia, and Byung il Kwon. Improved model of the iron loss for the permanent magnet synchronous motors. In *Electrical Machines and Systems (ICEMS), 2010 International Conference on*, pages 1246 –1251, October 2010.

[83] P. Sergeant, F. De Belie, L. Dupre, and J. Melkebeek. Losses in sensorless controlled permanent-magnet synchronous machines. *Magnetics, IEEE Transactions on*, 46(2):590 –593, February 2010.

[84] L. Ma, M. Sanada, S. Morimoto, and Y. Takeda. Iron loss prediction considering the rotational field and flux density harmonics in IPMSM and SynRM. *Electric Power Applications, IEE Proceedings* -, 150(6):747 – 751, November 2003.

[85] Cobham CTS Limited. Opera-3d: Hysteresis, February 2011. Available from: `http://www.cobham.com/about-cobham/aerospace-and-security/about-us/antenna-systems/kidlington/products/opera-3d/hysteresis.aspx` [Accessed August 2011].

[86] S.M. Hosseini, M. Agha-Mirsalim, and M. Mirzaei. Design and analysis of a novel disk permanent magnet generator. In *Power Electronics, Electrical Drives,*

Automation and Motion, 2006. SPEEDAM 2006. International Symposium on, pages 374 –378, May 2006.

[87] SKF. *SKF energy efficient bearings*, 2007. Available from: `http://www.skf.com/files/516191.pdf` [Accessed 6 February 2011].

[88] Ming Chen, An Hu, Bo Wang, and Yong Tang. Test of IGBT junction-case steady state thermal resistance and experimental analysis. In *Intelligent System Design and Engineering Application (ISDEA), 2010 International Conference on*, volume 2, pages 557 –560, October 2010.

[89] M.H. Bierhoff and F.W. Fuchs. Semiconductor losses in voltage source and current source IGBT converters based on analytical derivation. In *Power Electronics Specialists Conference, 2004. PESC 04. 2004 IEEE 35th Annual*, volume 4, pages 2836 – 2842 Vol.4, 2004.

[90] T.C. Green and B.W. Williams. Derivation of motor line-current waveforms from the DC-link current of an inverter. *Electric Power Applications, IEE Proceedings B*, 136(4):196 –204, July 1989.

[91] R.S. Chokhawala and S. Sobhani. Switching voltage transient protection schemes for high-current IGBT modules. *Industry Applications, IEEE Transactions on*, 33(6):1601 –1610, November 1997.

[92] A. Boglietti, P. Ferraris, M. Lazzari, and M. Pastorelli. Change of the iron losses with the switching supply frequency in soft magnetic materials supplied by PWM inverter. *Magnetics, IEEE Transactions on*, 31(6):4250 –4252, November 1995.

[93] R.S. Chokhawala, J. Catt, and L. Kiraly. A discussion on IGBT short-circuit behavior and fault protection schemes. *Industry Applications, IEEE Transactions on*, 31(2):256 –263, March 1995.

[94] M. Ciappa and W. Fichtner. Lifetime prediction of IGBT modules for traction applications. In *Reliability Physics Symposium, 2000. Proceedings. 38th Annual 2000 IEEE International*, pages 210 –216, 2000.

[95] Boyang Hu, S. Sathiakumar, and Y. Shrivastava. 180-degree commutation system of permanent magnet brushless DC motor drive based on speed and current control. In *Intelligent Computation Technology and Automation, 2009. ICICTA '09. Second International Conference on*, volume 1, pages 723 –726, October 2009.

[96] T. Kim and J. Yang. Control of a brushless DC motor/generator in a fuel cell hybrid electric vehicle. In *Industrial Electronics, 2009. ISIE 2009. IEEE International Symposium on*, pages 1973 –1977, July 2009.

[97] P.C. Sen. Electric motor drives and control-past, present, and future. *Industrial Electronics, IEEE Transactions on*, 37(6):562 –575, December 1990.

[98] Zheng Zedong, M. Fadel, and Li Yon Gdong. A high-performance control system of PMSM based on load torque observer. In *Power Electronics Specialists Conference, 2007. PESC 2007. IEEE*, pages 587 –592, June 2007.

[99] Keliang Zhou and Danwei Wang. Relationship between space-vector modulation and three-phase carrier-based PWM: a comprehensive analysis [three-phase inverters]. *Industrial Electronics, IEEE Transactions on*, 49(1):186 –196, February 2002.

[100] GE Industrial Systems. *SVM Space Vector Modulation: Improved output performance through advanced inverter control*, 2003. Available from: `http://www.lpsolutions-inc.com/resources/SVMSpaceVectorModulation.pdf` [Accessed 25 August 2011].

[101] A.R. Bakhshai, G. Joos, P.K. Jain, and Hua Jin. Incorporating the overmodulation

range in space vector pattern generators using a classification algorithm. *Power Electronics, IEEE Transactions on*, 15(1):83 –91, January 2000.

[102] Z.Q. Zhu, J.X. Shen, and D. Howe. Flux-weakening characteristics of trapezoidal back-EMF machines in brushless DC and AC modes. In *Power Electronics and Motion Control Conference, 2006. IPEMC 2006. CES/IEEE 5th International*, volume 2, pages 1 –5, August 2006.

[103] Haodong Yang, Zeyin Han, and Yangsheng Chen. Electromagnetic vibration of interior permanent magnet brushless motors under brushless DC and AC operation. In *Electrical Machines and Systems, 2009. ICEMS 2009. International Conference on*, pages 1 –6, November 2009.

[104] Jianjun Li, Yongxiang Xu, Jibin Zou, and Ruyi Liu. Rotor eddy-current loss of permanent magnet machine in brushless AC and DC modes, used for deep-sea HUV's propeller. In *Electrical Machines and Systems, 2009. ICEMS 2009. International Conference on*, pages 1 –4, November 2009.

[105] P. Kshirsagar and R. Krishnan. Efficiency improvement evaluation of non-sinusoidal back-EMF PMSM machines using field oriented current harmonic injection strategy. In *Energy Conversion Congress and Exposition (ECCE), 2010 IEEE*, pages 471 – 478, September 2010.

[106] P. Pillay and R. Krishnan. Application characteristics of permanent magnet synchronous and brushless DC motors for servo drives. *Industry Applications, IEEE Transactions on*, 27(5):986 –996, September 1991.

[107] N. Samoylenko, Qiang Han, and J. Jatskevich. Dynamic performance of brushless DC motors with unbalanced Hall sensors. *Energy Conversion, IEEE Transactions on*, 23(3):752 –763, September 2008.

[108] J.X. Shen, Z.Q. Zhu, and D. Howe. PM brushless drives with low-cost and low-resolution position sensors. In *Power Electronics and Motion Control Conference, 2004. IPEMC 2004. The 4th International*, volume 2, pages 1033 – 1038 Vol.2, 14-16 2004.

[109] Xu Zheng, Li Tiecai, Lu Yongping, and Guo Bingyi. Position-measuring error analysis and solution of Hall sensor in pseudo-sensorless PMSM driving system. In *Industrial Electronics Society, 2003. IECON '03. The 29th Annual Conference of the IEEE*, volume 2, pages 1337 – 1342 Vol.2, November 2003.

[110] Baumer Hübner GmbH. *AMG 71 Absolute Encoder*, July 2009. Available from: `http://www.baumerhuebner.com/pdf/amg71.pdf` [Accessed 27 July 2010].

[111] A.O. Di Tommaso and R. Miceli. A new high accuracy software based resolver-to-digital converter. In *Industrial Electronics Society, 2003. IECON '03. The 29th Annual Conference of the IEEE*, volume 3, pages 2435 – 2440 Vol.3, November 2003.

[112] M. Konghirun. A resolver-based vector control drive of permanent magnet synchronous motor on a fixed-point digital signal processor. In *TENCON 2004. 2004 IEEE Region 10 Conference*, volume D, pages 167 – 170 Vol. 4, November 2004.

[113] A. Consoli, G. Scarcella, and A. Testa. Industry application of zero-speed sensorless control techniques for PM synchronous motors. *Industry Applications, IEEE Transactions on*, 37(2):513 –521, March 2001.

[114] K.T. Chau, C.C. Chan, and Chunhua Liu. Overview of permanent-magnet brushless drives for electric and hybrid electric vehicles. *Industrial Electronics, IEEE Transactions on*, 55(6):2246 –2257, June 2008.

[115] F.G. Capponi, G. De Donato, and L. Del Ferraro. Brushless AC drive using an axial flux synchronous PM motor with low resolution position sensors. In *Power Electronics Specialists Conference, 2004. PESC 04. 2004 IEEE 35th Annual*, volume 3, pages 2287 – 2292 Vol.3, 20-25 2004.

[116] A. Lidozzi, L. Solero, F. Crescimbini, and A. Di Napoli. SVM PMSM drive with low resolution Hall-effect sensors. *Power Electronics, IEEE Transactions on*, 22(1):282 –290, January 2007.

[117] S. Morimoto, M. Sanada, and Y. Takeda. Sinusoidal current drive system of permanent magnet synchronous motor with low resolution position sensor. In *Industry Applications Conference, 1996. Thirty-First IAS Annual Meeting, IAS '96., Conference Record of the 1996 IEEE*, volume 1, pages 9 –14 vol.1, 6-10 1996.

[118] M.C. Harke, G. De Donato, F.G. Capponi, T.R. Tesch, and R.D. Lorenz. Implementation issues and performance evaluation of sinusoidal, surface-mounted PM machine drives with Hall-effect position sensors and a vector-tracking observer. *Industry Applications, IEEE Transactions on*, 44(1):161 –173, January 2008.

[119] L. Norum, W. Sulkowski, and L.A. Aga. Compact realisation of PWM-VSI current controller for PMSM drive application using low cost standard microcontroller. In *Power Electronics Specialists Conference, 1992. PESC '92 Record., 23rd Annual IEEE*, pages 680 –685 vol.1, June 1992.

[120] P. Pillay and R. Krishnan. Modeling of permanent magnet motor drives. *Industrial Electronics, IEEE Transactions on*, 35(4):537 –541, November 1988.

[121] Otmar Bitsche and Guenter Gutmann. Systems for hybrid cars. *Journal of Power Sources*, 127(1-2):8 – 15, 2004. Eighth Ulmer Electrochemische Tage.

[122] Magnet Applications. *Sintered Neodymium Iron Boron*, 2003. Available from:

http://www.magnetapplications.com/docs/sinteredndfeb.pdf [Accessed 1 October 2011].

[123] N. Bianchi, S. Bolognani, M.D. Pre, and G. Grezzani. Design considerations for fractional-slot winding configurations of synchronous machines. *Industry Applications, IEEE Transactions on*, 42(4):997 –1006, July 2006.

[124] B.K. Bose. A high-performance inverter-fed drive system of an interior permanent magnet synchronous machine. *Industry Applications, IEEE Transactions on*, 24(6):987 –997, November 1988.

[125] John D'Errico. Surface fitting using gridfit, July 2010. Available from: http://www.mathworks.de/matlabcentral/fileexchange/8998 [Accessed 7 September 2011].

[126] Yong Liu, Z.Q. Zhu, and D. Howe. Direct torque control of brushless DC drives with reduced torque ripple. *Industry Applications, IEEE Transactions on*, 41(2):599 – 608, March 2005.

[127] Jong-Woo Choi and Seung-Ki Sol. Design of fast-response current controller using d-q axis cross coupling: application to permanent magnet synchronous motor drive. *Industrial Electronics, IEEE Transactions on*, 45(3):522 –524, June 1998.

[128] F. Giulii Capponi, G. De Donato, L. Del Ferraro, O. Honorati, M.C. Harke, and R.D. Lorenz. AC brushless drive with low-resolution Hall-effect sensors for surface-mounted PM machines. *Industry Applications, IEEE Transactions on*, 42(2):526 – 535, March 2006.

[129] Enrico Cacciatori, Baptiste Bonnet, Nicholas D. Vaughan, Matthew Burke, David Price, and Krzysztof Wejrzanowski. Regenerative braking strategies for a parallel hybrid powertrain with torque controlled IVT. *Powertrain & Fluid Systems Conference & Exhibition, SAE International*, (2005-01-3826), October 2005.

[130] Research on quieter cars and the safety of blind pedestrians: A report to congress. Technical report, National Highway Traffic Safety Administration, U.S. Department of Transportation, 2009. Available from: http://www.nhtsa.gov/DOT/NHTSA/NVS/Crash%20Avoidance/Technical%20Publications/2010/RptToCongress091709.pdf [Accessed 24 May 2010].

[131] J. Poxon, P. Jennings, and M. Allman-Ward. Development of a hybrid electric vehicle (HEV) model for interactive customer assessment of sound quality. In *Hybrid and Eco-Friendly Vehicle Conference, 2008. IET HEVC 2008*, pages 1 –4, 8-9 2008.